

AD _____

GRANT NUMBER DAMD17-96-1-6283

TITLE: High Fidelity Electronic Display of Digital Mammographs

PRINCIPAL INVESTIGATOR: Michael J. Flynn, Ph.D.

CONTRACTING ORGANIZATION: Henry Ford Health Systems
Detroit, MI 48202-2689

REPORT DATE: October 1998

TYPE OF REPORT: Final

PREPARED FOR: Commander
U.S. Army Medical Research and Materiel Command
Fort Detrick, Frederick, Maryland 21702-5012.

DISTRIBUTION STATEMENT: Approved for public release;
distribution unlimited

The views, opinions and/or findings contained in this report are those of the author(s) and should not be construed as an official Department of the Army position, policy or decision unless so designated by other documentation.

20010122 012

REPORT DOCUMENTATION PAGE

Form Approved
OMB No. 0704-0188

Public reporting burden for this collection of information is estimated to average 1 hour per response, including the time for reviewing instructions, searching existing data sources, gathering and maintaining the data needed, and completing and reviewing the collection of information. Send comments regarding this burden estimate or any other aspect of this collection of information, including suggestions for reducing this burden, to Washington Headquarters Services, Directorate for Information Operations and Reports, 1215 Jefferson Davis Highway, Suite 1204, Arlington, VA 22202-4302, and to the Office of Management and Budget, Paperwork Reduction Project (0704-0188), Washington, DC 20503.

1. AGENCY USE ONLY (Leave blank)		2. REPORT DATE October 1998	3. REPORT TYPE AND DATES COVERED Final (3 Sep 96 - 2 Sep 98)	
4. TITLE AND SUBTITLE High Fidelity Electronic Display of Digital Mammographs			5. FUNDING NUMBERS DAMD17-96-1-6283	
6. AUTHOR(S) Michael J. Flynn, Ph.D.				
7. PERFORMING ORGANIZATION NAME(S) AND ADDRESS(ES) Henry Ford Health Systems Detroit, MI 48202-2689			8. PERFORMING ORGANIZATION REPORT NUMBER	
9. SPONSORING/MONITORING AGENCY NAME(S) AND ADDRESS(ES) Commander U.S. Army Medical Research and Materiel Command Fort Detrick, Frederick, Maryland 21702-5012			10. SPONSORING/MONITORING AGENCY REPORT NUMBER	
11. SUPPLEMENTARY NOTES				
12a. DISTRIBUTION / AVAILABILITY STATEMENT Approved for public release; distribution unlimited			12b. DISTRIBUTION CODE	
13. ABSTRACT (Maximum 200) We have investigated photoemissive structures which can achieve the required display performance of digital mammography. A design utilizing a thin glass faceplate supported by a glass microcapillary array was evaluated. The original objectives of this project was to model the performance of emissive structures and evaluate designs with high performance. With respect to performance modeling we have; 1) developed software to describe the electric field and the trajectories of electrons and used it to study the effect of the focusing plate electrode, 2) used electron/photon transport computations to characterize the electron backscattering from phosphor layers, and 3) developed a simulation code to study the luminance spread function of emissive structures and reported results for conventional CRT structures and for thin structures. With respect to the evaluation of potential designs we have; 1) constructed a vacuum subsystem and experimental chamber into which a cathode and emissive structure can be mounted, 2) designed, built and tested a unique cone shaped luminance probe that will measure spread function tails on actual emissive structures. 3) Identified electron charge deposition processes that limit the utility of the originally proposed method using microcapillary designs.				
14. SUBJECT TERMS Breast Cancer Mammography Display			15. NUMBER OF PAGES 379	
			16. PRICE CODE	
17. SECURITY CLASSIFICATION OF REPORT Unclassified	18. SECURITY CLASSIFICATION OF THIS PAGE Unclassified	19. SECURITY CLASSIFICATION OF ABSTRACT Unclassified	20. LIMITATION OF ABSTRACT Unlimited	

FOREWORD

Opinions, interpretations, conclusions and recommendations are those of the author and are not necessarily endorsed by the U.S. Army.

✓ Where copyrighted material is quoted, permission has been obtained to use such material.

✓ Where material from documents designated for limited distribution is quoted, permission has been obtained to use the material.

✓ Citations of commercial organizations and trade names in this report do not constitute an official Department of Army endorsement or approval of the products or services of these organizations.

NA In conducting research using animals, the investigator(s) adhered to the "Guide for the Care and Use of Laboratory Animals," prepared by the Committee on Care and use of Laboratory Animals of the Institute of Laboratory Resources, national Research Council (NIH Publication No. 86-23, Revised 1985).

NA For the protection of human subjects, the investigator(s) adhered to policies of applicable Federal Law 45 CFR 46.

✓ In conducting research utilizing recombinant DNA technology, the investigator(s) adhered to current guidelines promulgated by the National Institutes of Health.

✓ In the conduct of research utilizing recombinant DNA, the investigator(s) adhered to the NIH Guidelines for Research Involving Recombinant DNA Molecules.

✓ In the conduct of research involving hazardous organisms, the investigator(s) adhered to the CDC-NIH Guide for Biosafety in Microbiological and Biomedical Laboratories.

PI - Signature

Date

Table of Contents

- Pg. 1 - Introduction
- Pg. 3 - Body: Final Report
- Pg. 10- Conclusions
- Pg. 11- References
- Pg. 12- Appendix A, Bibliography of articles published
- Pg. 15- Appendix B, Copies of articles published

1 INTRODUCTION

This project involved the development of methods for "High Fidelity Electronic Display of Digital Mammographs". Cathodoluminescent medical image displays were considered including specialized cathode ray tubes and flat panel displays using cold cathode emitters and microvacuum cells (fig. 1). For field emitter display devices, a small cathode generates a regulated pulse of electrons which is accelerated across a vacuum gap to a photoemissive layer. The focus of the project was on the visual performance of the photoemissive layer.

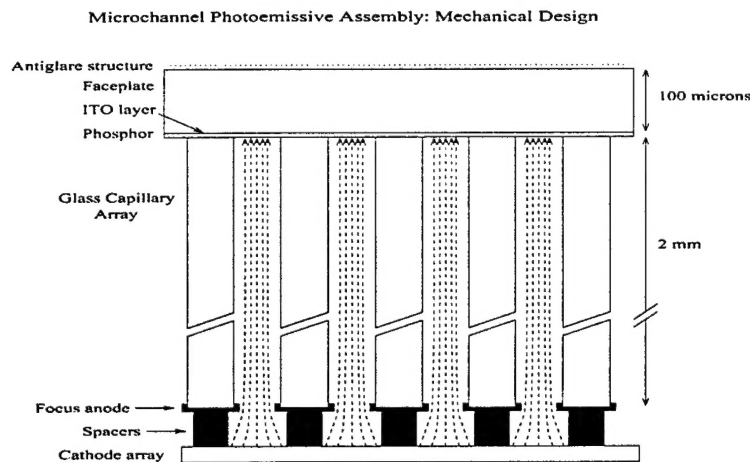


Figure 1: Photoemissive emissive structure model.

The objective of the project was to establish that advanced designs for the emissive structure of cathodoluminescent display devices can achieve the performance required for viewing computer images obtained from digital mammography systems. Conventional CRT devices are not capable of meeting the stringent display requirements of medical mammography because of the thick glass in the emissive structure. Microchannel photoemissive assemblies were investigated to determine if the needed display performance can be achieved.

In most display devices, image degradation can be traced to processes associated with the transport of light from the point of generation and to the optical properties of the emission surface. Transilluminated film, one of the highest fidelity display devices available, modulates the light intensity by diffusion in the layer of dense silver grains in the emulsion. This layer is

at the outer surface and separated only by a thin overcoat from the surface. Consequently, there is little lateral transport of light which would degrade contrast or resolution. Additionally, the overcoat has a rough surface causing diffuse scatter of ambient light and minimal surface glare.

A photoemissive assembly which generates light very near the surface and with a rough outer surface might produce the same high fidelity as obtained with transilluminated film. The general approach considered on this project involves the use of a glass microchannel plate with an overall thickness of 2 to 3 mm. As illustrated in fig. 1, electrons from the cathode elements are directed into the microchannels to a thin phosphor layer deposited on glass with a thickness of about 100 microns, i.e. similar to that of the cover plates used in conventional microscope slides. Structural rigidity is provided by the microchannel plate.

2 Body: Final Report

This project involved four technical objectives:

- Model electron trajectories in the display device.
- Model electron energy deposition in the emissive structure.
- Model light transport in the emissive structure.
- Compare experimental results with model calculations.

Successful results were obtained for the first three objectives. Difficulties in electron transport were identified as a part of objective 1 which prohibited successful testing as a part of objective 4. The specific results are reported in the following for each of these objectives.

2.1 Photoemissive performance modeling

The first three technical objectives involved the performance modeling of the the proposed emissive structure assembly. The simulation of device performance relates to 3 different aspects which differ both in the physical processes as well as in the applied methods:

- Predicting electron trajectories in the vacuum cell,
- Predicting electron energy deposition in the emissive layers, and
- Simulation of the light transport processes in the emissive structure.

For each aspect of performance modeling we describe in the following, the advancements and developments and results made during this project that contributed to obtaining significant insight on the performance of the proposed emissive structure design.

2.1.1 Modeling electron trajectories in vacuum cells

Methods

To study the effect of the capillary array on the electron trajectories, we developed a simulation code (ELECTRA) that computes the solution to the Poisson's equation using a finite-difference approach and an over-relaxation technique. For the analysis of the impact of the capillary structure, the full 3D solution may be obtained using a cylindrical coordinate system, by aligning the axis of symmetry with the axis of the capillary tube, when appropriate boundary conditions are used.

An important aspect of computing potential solutions in vacuum cells for the simulation of electron trajectories is the use of an appropriate mesh size. Large array sizes provide accuracy while increasing the computing time in a non-linear fashion with respect to array dimensions. To achieve good solutions for the electric potential, we implemented a 3-stage computation scheme (low-resolution, medium-resolution, and high-resolution). By computing the solution at each step, and using a bicubic spline technique to interpolate the expanded solution, we were able to significantly reduced the computing time for a given solution, and obtain convergence much faster.

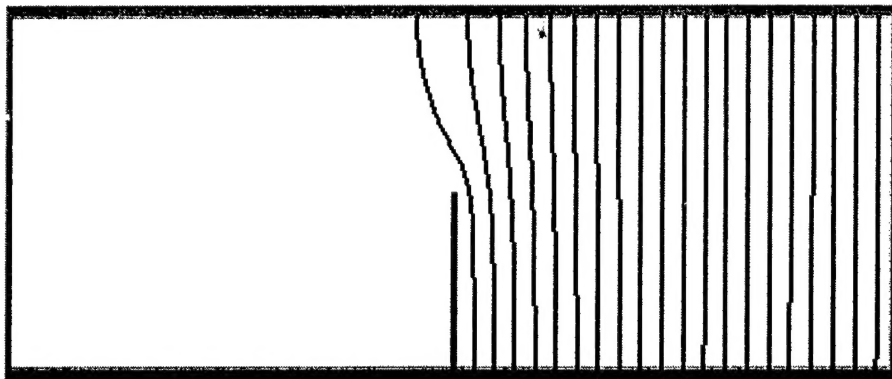


Figure 2: Isocontour plot for a region close to the focusing plate.

To determine when the iteration has converged to an acceptable solution, the residual at a given point in the solution array is reported. Typical values of 10^{-3} have shown to be acceptable criteria for the studied cases.

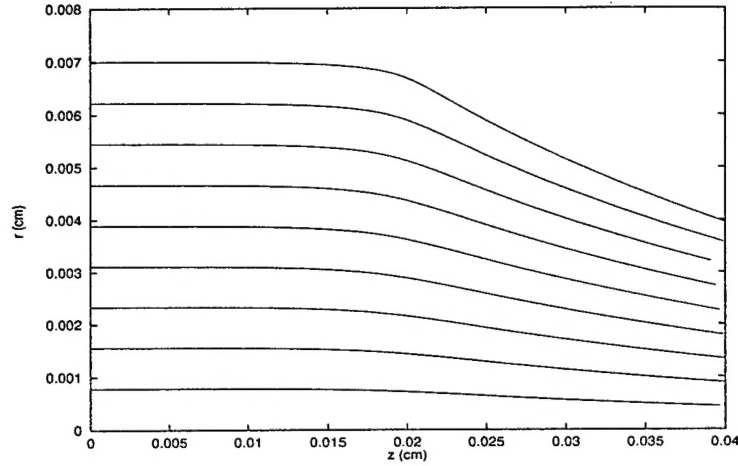


Figure 3: Electron trajectories generated with ELECTRA for a region close to the focusing plate.

The program generates electron trajectories using the Burlish–Stoer method to solve the equation of motion with adaptable time steps.[8] The results are presented in isocontour plots and trajectory data files (fig. 2 and 3).

Results

We applied ELECTRA to study the effect of the focusing plate electrode for the proposed design. For a 3 mm thick structure, a 1 mm thick microcapillary array with a 1 kV total acceleration voltage and focusing metal electrode at V_f was considered. The metal electrode enters the channel up to a diameter length, i.e. $50\ \mu\text{m}$. Electrons are assumed to be emitted from the cathode forming a parallel extended beam for normal incidence into the microcapillary array. This can be achieved with an emitting surface such as a field emitter cathode structure, or with a point emitter and appropriate electron optics components. The goal is to adjust V_f in order to alter the trajectories to direct the electrons into the tubes, while minimizing the impacts on the focusing electrode plate and on lateral tube walls (see next section for a discussion on secondary electron emission).

Problems encountered

A potential problem with the approach being used involves the charging of insulators in vacuum under electron bombardment which has been studied

by several authors. [6, 5, 1] When an energetic electron hits an insulator, multiple secondary electrons are generated. A fraction of them are directed back into the vacuum. This fraction is called "true" secondary electron emission. Energetic backscattered electrons can travel significant distances away from the initial landing site. The low-energy electrons however, can in some scenarios, be directed back against the surface, creating charge accumulation in the superficial layers of the insulator material. This surface charge density in turn changes the local electric fields, up to a point where a self-sustaining equilibrium is achieved. In this case, a secondary electron emission of 1 is required. When electric fields are parallel to the insulator surface, a net current can be observed which is explained by a hopping transport mechanism.[7]

Inside capillaries, the electric field is normally oriented parallel to the insulator surface. Two different electron paths are useful to consider. In the first, an energetic electron may hit directly the interior wall of the tube, before reaching the phosphor layer. Such an event will generate multiple less energetic secondary electrons that will eventually reach the anode. This condition is not favorable to an efficient electron energy to luminescence conversion, and thus its occurrence has to be minimized by using an appropriate voltage V_f . The second case relates to the backscattered electrons coming from the phosphor material that may hit the surfaces of the tube. In this case, the wide range of electron energies and angles of interaction will determine the ability of the system to reach the equilibrium point.

Similar scenarios are encountered in other technologies related to emissive displays. For instance, Micron Display Technologies, Inc. has recently reported the use of high aspect ratio glass posts for spacing the cathode structure from the anode layers. [3] The use of a thin resistive layer coated onto the inner walls of the tubes may constitute a solution to this problem, although a mechanism for controlling the resistivity of a thin layer, as well as a suitable coating technique have not been disclosed.

This problem was not recognized at the beginning of this project. The solution to the problem is likely to involve complex thin film surface coatings and is difficult to incorporate into simulation models.

2.1.2 Electron energy deposition modeling

Glare from backscattered electrons

Our laboratory previously developed an electron/photon transport code, SKEPTIC [4, 9], specifically intended to model low energy electron transport. We have used SKEPTIC to characterize the electron backscattering from the phosphor layer of an emissive structure. In CRT devices, the backscattered component that returns into the vacuum, may hit the phosphor layer at significant distances from the original landing site, and generate a diffuse signal. We have completed computations to document the effect of this backscattering on image glare. For this, we used actual layer material specifications including the aluminum conductive film on top of the phosphor grains, and the conductive coatings on the inside of the tube. We have used a typical broad band ZnO:Zn phosphor for the simulations. Preliminary results show that the tails of the line-spread function for incidence at the center will not affect significantly the image quality of the displayed data (fig. 4). However, in color CRTs, grille apertures or shadow masks may interfere the backscattered electrons and generate a more important and local degradation effect.

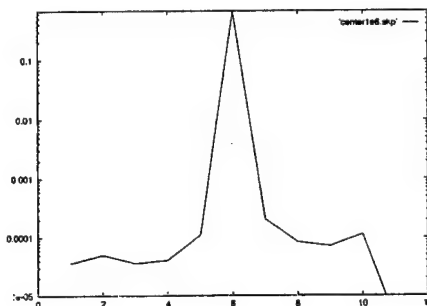


Figure 4: Line-spread function of backscattered electron diffuse signal for a typical monochrome CRT.

2.1.3 Modeling of light transport in emissive structures

We have developed a Monte Carlo simulation code (DETECT-II) to study the luminance spread functions of emissive structures. The unique features of the code, as well as the results for typical CRT and flat emissive display structures have been reported. [2].

In addition, simulation of degradation of image quality by glare using 2D Fast Fourier Transform over large image arrays (2048×2048) was performed. The application of this method to digital radiographs was described recently.

[2] We refer to the proceeding papers which are attached as appendices for a complete description of these methods and results.

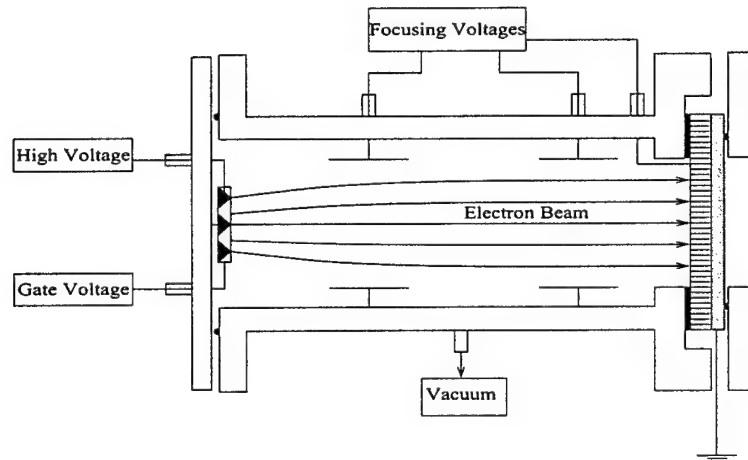


Figure 5: Test device assembly for testing photoemissive emissive structure.

2.2 experimental validation of simulation results

Following the original project plan, an experimental system was assembled to test emissive structures with an electron beam. The following describes this test system. Because of the secondary electron problem described above, successful experimental operation of a microcapillary emissive structure was not achieved.

During the project, it was found that existing devices to measure veiling glare in emissive structures would not provide the performance needed to evaluate high fidelity display devices. A specialized probe was designed and built. The performance of this probe has now been documented and it has been used to evaluate glare in CRT devices as well as new flat panel devices.

2.2.1 Experimental test system

The test system for emissive structures being built consists of a vacuum chamber with a cathode at one end and an emissive structure installed at the other end. Individual phosphors plates may be tested by placing a pattern on the back surface of the emissive structure to enable measurement of resolution

and glare. Used in the manner, the cathode needs only to produce a uniform beam of electrons with no dynamic pattern.

The the vacuum system has been completed all components are now installed in our laboratory. This includes a low vacuum mechanical pump, a high vacuum turbopump, high and low vacuum gauges, and an experimental chamber. The configuration of the subsystem is detailed in an attached appendix.

2.2.2 Glare performance measurements

Measurements of glare, particularly for systems with low glare, requires measurement systems which do not contribute to the observed glare. The measurements we proposed were to all be done with a CCD observation system. The lens used to couple the image to the sensor was found to have flare which prevented the evaluation of glare. The CCD was found to be adequate to characterize resolution and noise. For glare measurements we designed an optical probe for use with a laboratory photometer. The cone shaped luminance probe has been used to measure luminance spread function tails of actual emissive structures both in the test sytem and conventional display devices (fig. 6).

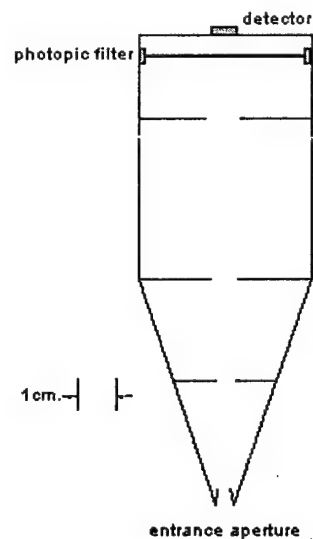


Figure 6: Cone-shaped probe for glare measurements.

3 CONCLUSIONS

During this project, we have developed practical simulation tools to characterize electron and optical transport in emissive structures. By using the simulation tools, we have advanced our understanding of the degrading effects of the luminance spread in thick emissive structures. The original concept of a capillary emissive microstructure was found to have significant problems with respect to secondary electron accumulation and a successful test was not accomplished. The reasons for this problem are understood. As a part of the project, new methods were developed to measure glare which have been reported in journal publications and used to characterize the glare of various medical imaging systems.

The use of FED display devices for medical applications including mammography remains of interest because of the attractive emissive distribution and potential for high brightness. However, manufacturing problems involving microvacuum integrity, electron focusing, stability, and brightness control have continued to be problematic. The seriousness of these problems has caused us to pursue other approaches for mammography as a part of our future research. Specifically, organic light emitting displays using thin film layers coated on TFT structures are now being studied. The light transport modeling developed on this project is specifically being applied to studies the light emission distributions from these devices.

References

- [1] C. Attard and J. P. Ganachaud. Study of the space charge induced by an electron beam in an insulating target ii. presentation of the results. *Physica Status Solidi*, 199:455–465, 1997.
- [2] A. Badano and M. J. Flynn. Image degradation by glare in radiologic display devices. In *SPIE Medical Imaging 1997: Image Display*, volume 3031, pages 222–231, 1997.
- [3] J. Browning, C. Watkins, and J. Alwan et al. Scaling of FED technology. In *International Display Research Conference 1997*, pages F–42, 1997.
- [4] M. J. Flynn, S. M. Hames, and S. J. Wilderman et al. Quantum noise in digital X-ray imaging detectors with optically coupled scintillators. *IEEE Transactions on Nuclear Science*, 1996. accepted for publication 2-19-96.
- [5] J. P. Ganachaud, C. Attard, and R. Renoud. Study of the space charge induced by an electron beam in an insulating target i. monte carlo simulation method. *Physica Status Solidi*, 199:175–184, 1997.
- [6] J. P. Ganachaud and A. Mokrani. Theoretical study of the secondary electron emission of insulating targets. *Surface Science*, 334:329–341, 1995.
- [7] B. H. W. Hendriks, G. G. P. van Gorkom, and N. Lambert et al. Modes in electron-hopping transport over insulators sustained by secondary electron emission. *Journal of Physics D: Applied Physics*, 30:1252–1264, 1997.
- [8] W. H. Press, S. A. Teukolsky, and W. T. Vetterling et al. *Numerical recipes in C*. Cambridge University Press, 1992.
- [9] S. J. Wilderman, S. M. Hames, and M. J. Flynn et al. Monte Carlo calculation of X-ray spectra emitted by various anode materials at low voltages. In *IEEE Nuclear Science Symposium NSS'94*, 1994.

Appendix A

DAMD17-96-1-6283
Publication and Presentations

PUBLICATIONS IN SCIENTIFIC JOURNALS:

1. Shtern F, Winfield D, Behlen F, Blume H, **Flynn MJ**, Hemminger B, Huang HK, Krupinski EA, Kundel H, Roehrig H, Shile PE, Sickles E, and Yaffe M: Report of the Working Group on Digital Mammography: Digital Displays and Workstation Design (Public Health Service's Office of Women's Health and National Cancer Institute), Academic Radiology, April 1999.
2. **Flynn MJ**, Badano A: Image Quality Degradation by Light Scattering in Display Devices, Journal of Digital Imaging, Vol 12, No 2 (May), pgs 50-59, 1999.
3. **Flynn MJ**, Kanicki J, Badano A, Eyler WR: High Fidelity Electronic Display of Digital Radiographs, accepted, Radiographics, scheduled for publication 11/99.
4. Badano A, **Flynn MJ**: A Method for Measuring Veiling Glare in High Performance Display Devices, manuscript submitted for publication in Applied Optics, [6/99].

SCIENTIFIC EXHIBITS

5. **Flynn MJ**, Kanicki J, Badano A, Eyler WR: High Fidelity Electronic Display of Digital Radiographs, 1997 RSNA scientific exhibit, certificate of merit award, invited for publication in Radiographics, (Abstract published in Radiology, 205(P) pg 616).

PUBLISHED PROCEEDINGS:

6. Badano A, **Flynn MJ**, Muka E, Compton K, Monsees T: The Veiling Glare Point-Spread Function of Medical Imaging Monitors, SPIE Medical Imaging: Image Display, Feb 1999, SPIE Proceedings Vol. 3658, pgs , 1999.
7. Badano A, Flynn MJ, Kanicki J: Small Spot Contrast Measurements in High Performance Displays, Conference record of the Soc. of Information Display (SID) 1999 Intern. Symposium, pg , May, 1999.
8. Badano A, **Flynn MJ**: Experimental Measurements of Glare in Cathode-Ray Tubes. SPIE Medical Imaging: Image Display, Feb 1998, SPIE Proceedings Vol. 3335, pgs 188-196, 1998.
9. Badano A, **Flynn MJ**: Monte Carlo Modeling of Glare in Cathode Ray Tubes for Medical Imaging, Conference record of the Soc. of Information Display (SID) 1998 Intern. Symposium, pg 1-4, May 1998.
10. Badano A, **Flynn MJ**: Image Degradation by Glare in Radiologic Display Devices, SPIE Medical Imaging: Image Display, Vol. 3031, pgs 222-231, 1997.

11. Badano A, **Flynn MJ**: Monte Carlo Modeling of the Luminance Spread Function in Flat Emissive Displays. Conference Record of the 1997 International Display Research Conference, Pg... Presented in Toronto, Sept 1997.
12. Badano A, **Flynn MJ**, Samei E, Kearfott KG: Performance of Low-Voltage Phosphors in Emissive Flat Panel Displays for Radiographic Applications. SPIE Medical Imaging: Image Display, Vol. 2707, pg. 312-321, 1996.

ABSTRACTS AND PRESENTATIONS AT PROFESSIONAL SOCIETY MEETINGS:

13. **Flynn MJ**, Badano A, Kanicki J: Contrast Reduction from Ambient Light for Film, CRT, and AM-LCD Display Devices, Presented at the 84th RSNA Annual Meeting, December 1998, (Abstract published in Radiology, 209 (P) pg 279).
14. **Flynn MJ**, Badano A, Kanicki J, Abileah A: Ambient Light Reflections in Electronic Radiology Display Devices, SPIE Medical Imaging: Image Display, Feb 1999, SPIE Conference Abstracts, Paper 3658-30, pgs 37, 1999. (Proceedings full article not submitted)

Appendix B

Report of the Working Group on Digital Mammography: Digital Displays and Workstation Design

March 9-10, 1998
Washington, DC

*Sponsored by
Public Health Service's Office on Women's Health
and
National Cancer Institute*

Editors

Faina Shtern, M.D.
USPHS—Office on Women's Health

Daniel Winfield, M.S.
Research Triangle Institute

Contributors

Fred Behlen, Ph.D.
University of Chicago

Elizabeth A. Krupinski, Ph.D.
University of Arizona

Hartwig Blume, Ph.D.
Phillips Medical Systems

Harold Kundel, M.D.
University of Pennsylvania Medical Center

Michael J. Flynn, Ph.D.
Henry Ford Health System

Hans Roehrig, Ph.D.
University of Arizona

Bradley Hemminger, Ph.D.
University of North Carolina

Peter E. Shile, M.D.
Mallinckrodt Institute of Radiology

H. K. Huang, D.Sc.
University of California at San Francisco

Edward Sickles, M.D.
University of California at San Francisco

Martin Yaffe, Ph.D., M.Sc.
University of Toronto

Acknowledgments

Daniel Sullivan, M.D.
National Cancer Institute

Wanda K. Jones, Dr.P.H.
USPHS—Office on Women's Health

Robert E. Wittes, M.D.
National Cancer Institute

Contents

Speakers and Panelists	ii
Introduction	1
Goals of the Joint PHS OWH/NCI Working Group	2
References	3
Session 1: Clinical and Technical Overview	4
Types of Digital Mammography Systems	4
Clinical Applications	5
Current Full-Field Digital Mammography Research	7
General Recommendations for Digital Mammography	8
Limitations of Current Display Workstations	9
Required Features of Display Workstations for Digital Mammography	9
Research Priorities	10
References	10
Session 2: Display Hardware for Soft-Copy Display	11
Cathode Ray Tube Monitors (CRT)	11
Liquid Crystal Displays (LCD)	13
Field Emission Displays (FED)	14
Organic Light Emitting Diode Displays (OLED)	14
Suitability for Digital Mammography	15
Research Priorities	16
References	17
Session 3: Computer Software and Workstation Design	18
Current State of the Art	18
Clinical State of the Art	18
Technical Overview of State of the Art	19
Image Preprocessing/Handling	19
Integration of CAD with Workstation Design	20
CAD and Observer-Controlled Post Processing	20
User Interface and Reading Environment	21
Research Priorities	22
References	23
Session 4: Image Perception and Workstation Design for Mammography	24
The Importance of Image Perception to Mammography	24
The Perception of Information Displayed on a Workstation	26
Models for Image Perception	27
Measuring Observer Performance: Accuracy and Process	27
Research Priorities	28
References	28

Speakers and Panelists

Chairs: Faina Shtern, M.D. U.S. Public Health Service, Office on Women's Health
Daniel Sullivan, M.D. National Cancer Institute, Diagnostic Imaging Program

Session 1: Clinical and Technical Overview

Speakers: Stanley Baum, M.D. University of Pennsylvania
Charles E. Putnam, M.D. Duke University Medical Center
Etta D. Pisano, M.D. University of North Carolina
Edward A. Sickles, M.D. University of California at San Francisco
Carl D'Orsi, Ph.D. University of Massachusetts
Martin J. Yaffe, Ph.D., M.Sc. University of Toronto

Panelists: Carl J. D'Orsi, M.D. University of Massachusetts Medical Center
R. Edward Hendrick, Ph.D. University of Colorado Health Sciences Center
Steve Horii, M.D. University of Pennsylvania Medical Center
Andrew Karellas, Ph.D. University of Massachusetts Medical Center
Harold L. Kundel, M.D. University of Pennsylvania Medical Center
John Lewin, M.D. University of Colorado Health Sciences Center
Richard M. Moore, M.D. Massachusetts General Hospital
Etta D. Pisano, M.D. University of North Carolina at Chapel Hill
Peter E. Shile, M.D. Mallinckrodt Institute of Radiology
Edward A. Sickles, M.D. University of California at San Francisco
Richard Slone, M.D. Mallinckrodt Institute of Radiology
Martin J. Yaffe, Ph.D., M.Sc. University of Toronto

Session 2: Display Hardware for Soft-Copy Display

Speakers: Hans Roehrig, Ph.D. University of Arizona
Dennis Bechis, Ph.D. National Information Display Laboratory
Bruce Gnade, Ph.D. Defense Advanced Research Projects Agency
Malcolm Thompson, Ph.D. dpiX, Incorporated
Albert Xthona Metheus Corporation

Panelists: Fred M. Behlen, Ph.D. University of Chicago
Ken Compton Clinton Electronics Corporation
Arthur H Firester, Ph.D. Sarnoff Corporation
David Gray G.E. Medical Systems
David J. Getty, Ph.D. BBN Corporation
John Huffman Silicon Graphics Corporation
Janet Keyes Lorad/Division of Trex Medical
Larry Partain, Ph.D. Varian Associates
Peter M. Steven, Ph.D. Dome Imaging Systems, Inc.
Rex Tapp OIS Optical Imaging Systems, Inc.

Session 3: Workstation Design

Speakers: Peter E. Shile, M.D. Mallinckrodt Institute of Radiology
H.K. Huang, D.Sc. University of California at San Francisco
Hartwig Blume, Ph.D. Philips Medical Systems
Martin J. Yaffe, Ph.D., M.Sc. University of Toronto
Maryellen L. Giger, Ph.D. University of Chicago
Shyh-Liang Lou, Ph.D. University of California at San Francisco
Bradley M. Hemmiger, M.S. University of North Carolina

Session 3: Workstation Design (continued)

Panelists:	Dev P. Chakraborty, Ph.D.	University of Pennsylvania
	Michael Flynn, Ph.D.	Henry Ford Health System
	Elizabeth Krupinski, Ph.D.	University of Arizona
	Seong K. Mun, Ph.D.	Georgetown University Medical Center
	Loren T. Niklason, Ph.D.	Massachusetts General Hospital

Session 4: Image Perception and Workstation Design for Mammography

Speaker:	Harold L. Kundel, M.D.	University of Pennsylvania Medical Center
-----------------	------------------------	---

Introduction

Breast cancer is the most commonly diagnosed cancer and the second leading cause of cancer deaths among American women. Today, one in eight women in this country will develop breast cancer. In spite of extensive research in breast cancer prevention and treatment, early detection of breast cancer through imaging remains the best hope that women currently have for effective treatment and reduced mortality. Conventional X-ray mammography, a mature technology providing high quality images at low radiation dose, has been shown to reduce mortality of breast cancer by about 30% in women older than 50 years of age and by about 17% in younger women. However, recent data indicate that many women have radiodense breast tissue, making conventional diagnosis problematic. Three out of four lesions detected by conventional mammography are benign, resulting in unnecessary biopsies and other medical procedures. These limitations in conventional mammography have created a strong incentive for the development of novel imaging technologies for improved early detection of breast cancer.

In 1991, National Cancer Institute (NCI) convened a conference devoted to the review and development of a research agenda for novel breast imaging technologies. This conference unanimously recommended digital X-ray mammography as the most promising research area for improved detection of early breast cancer in large-scale screening programs. Based on that recommendation, NCI established an International Digital Mammography Development Group (IDMDG), bringing together multiple leading academic and industrial institutions.¹ In addition, in early 1993, NCI staff developed and formulated the Federal Technology Transfer Program in Digital Mammography to identify and transfer digital imaging technologies originally developed for space, defense, intelligence, energy, and other communities to advance digital detectors, display systems, image analysis, transmission, and storage.² These extensive collaborations of multiple government agencies, industry, and academia facilitated comprehensive development and testing of digital mammography.

Encouraged by this experience, in early March 1996, the U.S. Public Health Service's Office on Women's Health (PHS OWH) established a Federal Multi-

Agency Consortium for Imaging and Other Technologies to Improve Women's Health (Consortium) to expand technology transfer. The membership of the Consortium includes but is not limited to the Food and Drug Administration, Health Care Financing Administration, Central Intelligence Agency, Department of Defense, Department of Energy, and National Aeronautics and Space Administration. The activities of this Consortium have been critical for sharing expertise, resources, and technologies by multiple government agencies for the advancement of breast imaging technologies for early detection of cancer, such as digital mammography; magnetic resonance imaging (MRI); ultrasound; nuclear medicine and positron emission tomography; and related image display, analysis, transmission, storage and minimally invasive diagnoses and treatments.³

The first priority recommended by the Consortium was to establish, evaluate, and implement a comprehensive inventory of the government-wide technology transfer opportunities. In May 1996, the PHS OWH held a conference entitled "New Frontiers in Image-Guided Breast Cancer Diagnosis and Treatment" that developed recommendations on the current and future scientific needs and technologic challenges in breast imaging. Based on these recommendations, the PHS OWH developed a problem statement that translated clinical needs in breast imaging into generic technical specifications in order to establish a common vocabulary between the medical community and engineers, physicists, and other scientists working on the development of advanced technologies for defense, space, intelligence, energy, and other applications. This problem statement was distributed to over 300 academic and industrial laboratories in search of technologies that may advance the current state of the art in breast image acquisition, display, analysis, management, and transmission. As the result of these efforts, about 100 technologies have been identified and incorporated into the development of the technologic inventory. About 50 technologies, judged as promising in their potential to advance breast imaging by the PHS OWH staff and peer review, were selected for presentation at a public conference entitled "Technology Transfer Workshop on Breast Cancer Detection, Diagnosis, and

Treatment" and sponsored by the Federal Multi-Agency Consortium. This workshop, convened on May 1-2, 1997, further facilitated technology transfer from DoD, CIA, DOE, NASA, and other agencies by fostering government-wide collaborations and public/private partnerships.³ In addition, this Federal Multi-Agency Consortium meeting developed recommendations for the scientific and technologic projects critical for advancement of novel breast imaging.

Based on these recommendations, in June 1997, PHS OWH issued a competitive contract solicitation that supported high priority multidisciplinary research in the development and clinical testing of novel breast imaging technologies. By September 1997, PHS OWH funded the following projects in the areas of digital mammography:

- 1) **Optimization of Soft Copy Display Parameters for Digital Mammograms**
Key Personnel: Shyh-Liang Lou, Ph.D., H. K. Huang, D.Sc., and Edward Sickles, M.D., of the University of California at San Francisco
- 2) **Computer Analysis of Mammography Phantom Images (CAMPI): An Application to the Optimization and Evaluation of a Full-Field Digital Mammography**
Key Personnel: Dev P. Chakraborty, Ph.D., of the University of Pennsylvania
- 3) **Multi-Center Clinical Evaluation of Digital Mammography**
Key Personnel: Etta Pisano, M.D., of the University of North Carolina and Martin J. Yaffe, Ph.D., M.Sc., and Donald Plewes, Ph.D., of the University of Toronto

The meeting of May 1997 clearly demonstrated that, while significant advances in the development of full-field digital detectors have been achieved, soft-copy display systems, although improved, remained the main roadblock to the clinical acceptance and implementation of digital mammography. Further extensive effort is required for the successful development, testing, and implementation of digital mammography displays and workstation design for image interpretation.

On March 9-10, 1998, in Washington, DC, the Public Health Service's Office on Women's Health and the National Cancer Institute convened a Joint Working

Group on Digital Mammography: Digital Displays and Workstation Design. The meeting was attended by over 100 scientific leaders representing clinical practice, academic research, government agencies and laboratories, and medical imaging and display system manufacturers. This paper describes findings and recommendations of this working group.

Goals of the Joint PHS OWH/NCI Working Group

- 1) Review the state of the art of display technologies including current and future clinical applications and technical challenges.
- 2) Outline research priorities in digital display technology and workstation design requiring further support.
- 3) Identify technical limitations and develop a problem statement seeking new or emerging technologies.

The Working Group meeting consisted of the following sessions:

Session 1: Overview Session set a common vocabulary between multidisciplinary medical and other participants (e.g., defense, intelligence, space, energy, and other communities) and focused on the overviews of the current and future needs for digital mammography displays and their impact on clinical practice and patient care.

Session 2: The Session on Hardware for Soft-Copy Displays provided an understanding of not only the current state of the art but also anticipated technical developments in both CRT-based and flat panel display technologies. This session analyzed a gap between the clinical requirements for digital mammography displays and emerging technologies foreseeable on the market in the near future. An industry panel discussion in this session considered issues related to practicality, manufacturability, and cost effectiveness that will influence market demand and implementation of digital mammography display systems.

Session 3: The Workstation Design Session established a framework for the overall system design for image interpretation, including user needs, physical constraints (space, response time, etc.).

hardware and software requirements, and overall system configuration. Scientific presentations further explored integration of image processing, computer aided diagnosis, and graphical user interfaces into a workstation design.

Evening Session: Working Group members met in the evening for a working session where they formulated consensus reports describing current state of the art and recommendations for the future priorities in research and development.

Session 4: The Human Perception Session addressed human visual perception as it relates to digital mammography displays and workstation design. The impact of human perception on display technical requirements were discussed, and the importance of psychophysical research emphasized.

Summary Session: During the Summary Session, co-moderators presented the consensus reports. The reports addressed (1) the current state of the art and fundamental clinical/technical roadblocks, (2) technical parameters required to meet current clinical needs, and (3) future priorities in technology development and related basic and clinical research.

Subsequent to the working group meeting, the session co-moderators, with input from their session participants, developed written summary reports. These summary reports have been incorporated into this article.

References

1. Shtern F. Digital mammography and related technologies: perspective from the National Cancer Institute. *Radiology* 1992; 183(3):629-630.
2. Winfield D, Silbiger M, Brown GS, et al. Technology transfer in digital mammography: report of the NCI/NASA workshop. *Investigative Radiology* 1994; 29(4):507-515.
3. Asher S, Shtern F, Winfield D, et al. Final report of the technology transfer workshop on breast cancer detection, diagnosis, and treatment. *Acad Radiol* 1998; (in press).

Digital mammography is a technique for radiography of the breast in which the screen-film X-ray image receptor used in conventional mammography is replaced by an electronic detector.¹ The detector absorbs X rays transmitted through the breast and produces an electrical signal proportional to the intensity of the X rays. This signal is converted to digital format and stored in computer memory to form the image. A key feature of digital mammography is that image acquisition, display, and storage are performed independently, allowing optimization of each. The digital image is formed as a two-dimensional matrix of square picture elements (pixels) of a fixed size, typically 0.04 to 0.1 mm on a side.² Therefore, it is a sampled representation of the pattern of X-ray transmission through the breast. Within each pixel, the image takes on a single value representing the brightness of the image, averaged over the area of the breast represented by that pixel. Similarly, the intensity of X rays is sampled by an analog-to-digital converter into a finite number (2^n) of levels, where n is referred to as the number of bits of precision to which the image is digitized. Typically, 12 to 14 bits of digitization are used, thereby producing 4,096 to 16,384 sampled intensity levels. Once the digital image is stored in computer memory, it can be displayed with contrast that is both independent of detector properties and adjustable by the viewer. This overcomes one of the greatest limitations of screen-film mammography—the fixed display scale, defined by the characteristic curve of the film.

Another important difference between screen-film mammography and digital mammography is that, in the former, the amount of radiation used to create the image is largely determined by the need for a screen to absorb enough energy to provide sufficient light to expose a film to the desired optical density. In digital mammography, the gain of the acquisition system can be controlled electronically and, therefore, the amount of radiation used can be chosen according to the required signal-to-noise ratio for the examination. This has implications for how optimum exposure techniques for digital mammography should be selected and provides opportunities for either improvement in image quality or else for dose reduction compared to screen-film mammography.

Types of Digital Mammography Systems

Currently, there are three types of dedicated digital mammographic systems under clinical evaluation. These are all based on a phosphor X-ray absorber and an optically sensitive photo-detector array that provides the image readout.

CCD-based area detector. The first practical systems for digital mammography were employed for producing small area (5 cm x 5 cm) digital images for guiding stereotactic breast biopsy. Such systems typically provide 1K x 1K images with 50 micron or 100 micron pixels. The detectors for these systems use an X-ray absorbing phosphor that is coupled to a smaller-area light-sensitive CCD array via demagnifying lenses or fiber-optic tapers. The CCD is a self-scanning device that provides an electronic readout of all the light-sensitive elements on a single wire. This output is then digitized to produce a high-resolution digital image. The CCDs are single crystalline silicon chips that typically cover an image field of less than 3 cm x 3 cm.

Although it is possible to use fiber-optic tapers with a greater demagnification factor to allow coverage of the entire breast, this is not a viable solution because it will result in very poor efficiency of transfer of the light to the CCD, resulting in a greatly reduced signal-to-noise ratio in the image. Instead, one company (Trex Medical) has built a detector for their digital mammography system that is formed as a large area X-ray phosphor coupled through 12 small-format modules, each consisting of a demagnifying fiber-optic taper and a small CCD. The sub-images from the modules are combined (stitched) in the computer to provide a single digital mammogram.

Amorphous silicon. Amorphous silicon provides another means for producing area detectors suitable for digital mammography. An array of photodiodes is deposited on a plate of amorphous silicon such that each element provides the signal for one pixel of the image. The diodes are covered by a suitable X-ray absorbing phosphor, such as cesium iodide, and the electric charges stored on the capacitance of each diode after X-ray exposure are read out through a network of switches and data lines. Another company (General Electric Medical Systems) has produced a

digital mammography system employing this type of detector with 100 micron pixel size.

Scanned-beam detectors. An alternative approach to large area detectors is to use a detector that is long and narrow, which is scanned in synchrony with a slot-shaped X-ray beam, across the entire breast, to build up a full image. In this way, current photo-optical technology can be used to provide the required spatial resolution, dynamic range, and signal-to-noise ratio for digital mammography. Because the image is acquired sequentially in a scanning system, the acquisition time is longer than for an area detector and there is greater heat loading on the X-ray tube per image. An offsetting advantage of scanned beam systems, however, is that, because only part of the volume of the breast is irradiated at any one time, it is more efficient than area systems in controlling the detrimental effects of scattered radiation at the image receptor.

In the scanning system developed by Fischer Imaging, the radiation beam is confined to a "slot" of dimensions approximately 22 cm by 10 mm at the detector. The detector is composed of several modules that are abutted end-to-end. Each consists of a strip of cesium iodide phosphor coupled to a time-delay integration (TDI) CCD array via a fiber-optic taper. Each CCD consists of a large number of columns and a smaller number of rows of light-sensitive elements. In TDI acquisition, as the detector is moved across the breast at constant speed, the charge collected in each element of the CCD, in response to the X-ray signal, is shifted down its column at the same speed as the scan motion, but in the opposite direction. When the charge packet reaches the last element in the CCD, the charge signals in the columns are read out. The image is acquired by scanning the fan X-ray beam and the slot detector across the breast in a direction parallel to the chest wall of the patient.

Clinical Applications

There are several clinical applications for which digital mammography can improve on the current state of the art with conventional film-screen imaging.

Near-real-time image display. This provides several advantages over conventional film mammography. (1) The time required between image acquisition and display can be reduced to a few

seconds, compared to the approximately 5 minutes required for image processing of a conventional film examination, thereby potentially increasing patient throughput and reducing the per capita cost of examination. (2) Day-to-day variability in automated film processors, which now requires careful monitoring including daily sensitometry / densitometry measurements, also ceases to be a problem since film processing is eliminated. (3) Percutaneous biopsy and lesion localization procedures are facilitated by the ability to visualize, in a few seconds rather than several minutes, needles as they are positioned within or immediately adjacent to suspect lesions (this application, using a 5 x 5 cm field of view, is already built into several stereotactic-guidance mammography systems).³ (4) With successful development of routine stereoscopic imaging, it may be possible to reduce or completely eliminate the need to perform recall mammography for summation artifacts (superimposition of normal breast structures, simulating breast masses), which account for up to one-third of recall examinations after mammographic screening.

Post-acquisition image enhancement. Signal processing techniques can be applied to the digitally acquired image to produce overall enhancement or to increase the conspicuity of specific mammographic findings. (1) Window and level controls can be manipulated, after image acquisition, to portray the entire breast with proper intensity and increased contrast, thereby providing a greatly expanded gray scale to facilitate visualization of important findings that otherwise might be obscured by display within the toe or shoulder of the characteristic film curve. (2) Enlargement (magnification) and unsharp masking techniques can make more readily visible such tiny structures as breast microcalcifications. (3) Other edge enhancement manipulations can highlight border contours in similar fashion to that produced by xeroradiography. (4) Noise suppression techniques can render more readily perceptible certain types of low-contrast objects, such as noncalcified masses having indistinct margins. (5) Intensity equalization techniques can be applied to clearly portray in a single image structures that usually are difficult to see on conventional film mammograms, such as the skin and subcutaneous tissues. (6) Digital systems also have the capability to overcome some underexposure and overexposure conditions and display fully interpretable mammograms despite what otherwise would be considered unacceptable image quality.

Image archival, storage, and retrieval. A major advantage of digital over conventional film imaging is its ability to conveniently archive, store, and retrieve images. This electronic archival process can permit substantial cost savings, especially for high-volume operations, despite the initial large expenditure for digital equipment. The cost of physical storage of films is eliminated, and personnel costs involved in image archival and retrieval are markedly reduced. Finally, digital data storage is much more rapid and reliable than film-based methods. This is particularly noticeable when prior studies are needed for comparison. Retrieval time is usually measured in seconds rather than minutes, hours, or days. Furthermore, one will only rarely encounter the situation in which digital examinations are misfiled, lost, damaged in storage, or signed out to another location.

Teleradiology applications. Electronic transfer of digital images to remote viewing sites can be accomplished almost as rapidly as occurs between the standard display workstation and computer storage. Numerous activities utilizing teleradiology have been devised, many of which are clearly applicable to mammography practice. (1) Radiologists who work in several different offices or hospitals will be able to monitor and interpret examinations that are carried out in a nearby or even distant location or locations. (2) Mammography screening in mobile units will be made more efficient not only by overcoming the need to transport films from the site of examination to the site of interpretation, but also by permitting image interpretation while patients are still available for repeat or additional exposures. (3) Teleradiology can be used to facilitate second-opinion interpretation, in effect making world-class mammography expertise immediately accessible to community-practice radiologists. (4) Digital image transmission can be the cornerstone upon which multisite teaching conferences are built, from applications as simple as the simultaneous conduct of teaching rounds among the nearby hospitals that participate in a residency training program to intercontinental multi-institution conferences supported by satellite transmission of digital mammograms.

Dual-energy subtraction imaging. Dual-energy subtraction mammographic techniques are based on the principle that, if both high and low kVp exposures are taken using the same radiographic projection, some breast structures will exhibit greater absorption

of low-energy compared with high-energy photons, depending upon atomic composition. Thus, if there is no patient motion between exposures, one digital image can be electronically subtracted from the other, causing common elements (those that do not exhibit differential absorption) to cancel out completely. In this fashion, dual-energy subtraction mammography has the potential to increase the conspicuity of selected subtle findings, not only by showing some low contrast objects with increased clarity but especially by removing the superimposed "clutter" of background breast structures. This is particularly useful in demonstrating the tiny calcifications that can be the earliest indicator of a breast cancer, because the relatively high atomic number of calcium results in increased absorption of low-energy photons.

Tomosynthesis. In conventional tomography, the X-ray source and film move in opposite directions during exposure, so that radiographic features in only one plane of the image remain in sharp focus. However, conventional tomography of the breast is not practical since one exposure is necessary for each imaged plane, resulting in a high total radiation dose. Tomosynthesis involves exposures made as the X-ray tube moves in an arc above a stationary object (breast) and image receptor. Images must be obtained from multiple different angles to permit reconstruction of any plane in the breast that is parallel to the image receptor, but this can be accomplished with digital mammography at a total radiation dose similar to that of a single film mammogram. Recent development of a full-field digital detector that is flat now makes breast tomosynthesis practical in the clinical setting.⁴ The ability to see through overlying areas of dense benign fibroglandular tissues may permit improved detection of early breast cancer and more accurate characterization of benign and malignant lesions.

Computer-aided image analysis. There already has been considerable success in developing computer-executed algorithms that detect abnormal findings on mammograms. Most such attempts have been directed at the identification of clustered microcalcifications, although several computer programs also have been written to detect spiculated breast lesions. Current applications are designed to indicate suspect findings by superimposing arrows, circles, or boxes in appropriate locations on digitized mammograms. The most successful of these programs presently are capable of identifying about

85% of targeted mammographic lesions, but also on average falsely indicate approximately one suspect area in each image.

If clinical utility is demonstrated (maintenance of essentially 100% sensitivity, especially if including poorly defined masses and densities), these computer-based applications will be widely used by radiologists as second-interpretation devices to avoid missing identifiable mammographic abnormalities. Especially if false-positive identifications are substantially reduced, this approach will be much less expensive than double readings done by another radiologist. However, it is unlikely that computer-aided detection (CAD) programs will be used in the United States for the first-pass interpretation of digital mammography screening examinations, sending only those cases with suspect findings on to a radiologist for definitive interpretation. This is because neither the providers of the CAD software nor the radiologists who use the software would be willing to accept potential malpractice related to missed cancers.

Computer-aided image interpretation programs also are being developed to further characterize already detected lesions, to determine whether subsequent management should involve biopsy or less invasive procedures. Again, these efforts have been directed principally at the analysis of clustered microcalcifications. Applications begin by quantitating the digital data within suspect lesions that already have been flagged either by radiologists or by computer detection programs. Formulas then are used to describe a wide variety of lesion characteristics; for calcifications these include not only the standard parameters assessed by radiologists (particle size, number, density, distribution, and shape) but also several more complex measures of calcific particle irregularity (for example, compactness, eccentricity, coefficient of convexity, elongation). Finally, numeric scores derived for these various parameters are weighted by pre-determined algorithms and combined to yield a likelihood of malignancy index, upon which management decisions can be based. Currently, the most successful of the calcification characterization programs operate at levels of diagnostic accuracy that usually approximate but occasionally even exceed those of expert mammographers. For other types of suspect lesions, today's computer-aided diagnosis programs are less fully developed.

Computer-aided instruction. Rapid, inexpensive, computer-based storage of digital mammography examinations facilitates the creation and utilization of computer-aided instruction packages, since selected sets of images can be readily catalogued and retrieved for display. The simplest application represents the digital counterpart to the conventional film mammography learning file. This involves an organized library of interesting case material (digital mammograms), supplemented by hard-copy text descriptions of mammographic findings, suggested interpretation, pathologic correlation, additional discussion, and literature reference material for each case or group of cases. Large numbers of mammography cases can be stored on a single optical disk. In a somewhat more sophisticated system, the text material itself is stored electronically, so that cases can be viewed with equal ease either in random sequence (as unknown cases) or in sequences organized either by diagnosis or by specific mammographic finding.

Instructional programs have been developed to provide the user with response-driven self-instruction modules, in which incorrect answers trigger the display of remedial material and additional questions before subsequent cases can be viewed.⁵ Such systems can track the progress of individual users, compiling grades and documenting that proficiency has been achieved.

The most ambitious instructional packages will interface directly with the day-to-day interpretation of digital mammograms. Such systems would be activated at the request of the radiologist, whenever specific mammographic features are described by the radiologist or determined by a computer-aided characterization program. In either circumstance, a particular mammographic feature would call up related image and text materials from expert learning databases, to compare with the case under consideration. Thus, the radiologist could view pathology-proved cases in which mammograms display similar if not identical radiographic findings. Embedded text also could suggest strategies for further evaluation and interpretation of the mammographic findings.

Current Full-Field Digital Mammography Research

The manufacturers that developed each of the types of full-field digital mammography systems described

Table 1-1. Clinical sites at which prototype full-field digital mammography units currently are in use for investigational studies

Equipment Manufacturer	Medical Center
Fischer Imaging	University of Toronto University of California, San Francisco University of North Carolina, Chapel Hill Brooke Army Medical Center Thomas Jefferson University
General Electric	University of Colorado University of Massachusetts Massachusetts General Hospital University of Pennsylvania
Trex Medical	University of Virginia University of California, Los Angeles Good Samaritan Hospital, Long Island

previously have installed prototype units at several clinical sites (Table 1-1). A variety of investigational studies are currently being carried out at these sites, for a wide range of purposes. Studies designed to demonstrate degrees of safety and effectiveness of digital mammography compared to conventional film mammography are being conducted by each equipment manufacturer to secure approval from the Food and Drug Administration to market their devices for general use.

Of greater scientific value are more sophisticated studies being done at single sites or groups of sites, designed to assess the sensitivity and specificity of clinical images taken of the same women using both digital and conventional film mammography units. Such a large-scale screening trial is under way at the Universities of Colorado and Massachusetts, which will use ROC analysis to indicate the current capability of digital mammography in the detection of clinically occult breast cancer. A telemammography study is underway at the University of California San Francisco, designed to demonstrate whether digital mammography can successfully provide: (1) real-time consultation by off-site expert mammographers for on-site general radiologists conducting diagnostic mammography examinations and (2) accurate and

time-efficient off-site interpretation and management by expert mammographers of diagnostic examinations simultaneously performed by on-site general radiologists using conventional film mammography. IDMDG also was assembled, involving many of the sites and all of the equipment listed in Table 1-1. Originally, NCI supported individual institutional clinical testing of digital mammography by the IDMDG. More recently, PHS OWH funded a 250-patient pilot study that has been undertaken by eight participating institutes of the IDMDG to facilitate multicenter clinical evaluation of digital mammography and its diagnostic value in high-risk women. This pilot research will be followed by a 2,500-patient study that will explore the accuracy of digital mammography in both screening and diagnostic settings. Results from the various scientific studies described above should be available in the next two to three years.

General Recommendations for Digital Mammography

For a number of reasons, the potential advantages of digital mammography can probably best be realized by interpretation from soft-copy display. Soft-copy display allows convenient and dynamic manipulation

of the image display to obtain optimal presentation of information. In addition, there is the opportunity to eliminate the cost of hard-copy film and the associated time, complexity, and waste disposal problems of film processing.

Limitations of Current Display Workstations

Currently there are numerous impediments to the use of soft-copy display for digital mammography. These include deficiencies in the speed with which images can be loaded and presented on the display as well as inconvenience or inappropriateness of the human-computer interface of existing commercial systems. Most systems provide only rudimentary control of the lookup table, relating digital signal value and display brightness with such functions as linear clipping and scaling (window and level). More flexible lookup tables that provide nonlinear lookup tables are likely to improve image display and make more optimum use of the characteristics of the display device.

Generally, most displays do not have an adequate pixel matrix size to display the complete digital mammogram at full spatial resolution. There is also concern about whether the contrast resolution and display luminance of available hardware is adequate. There is controversy over this issue in that some scientists believe that performance of current systems is sufficient if image viewing takes place under appropriate conditions (e.g., very low ambient light).

Required Features of Display Workstations for Digital Mammography

The system should have the capability of displaying up to eight images simultaneously. These would include the standard four views of the breast for both the current and a previous examination. Image "hanging" should be automatic and customized to the preferences of the particular radiologist, with the possibility of override (moving or flipping images) when necessary. Images should load rapidly and it should be possible to retrieve other examinations from the archive quickly and efficiently, when it is desired to make comparisons.

The images should appear initially with a gray-scale rendition that is near-optimal, so that image

interpretation can be accomplished with minimal need for user interaction in manipulating images. The viewer should be able to change the display characteristics easily when this is required.

The system should incorporate an image navigation strategy that provides convenient availability of the full degree of acquired spatial resolution of the images, while maintaining the anatomical context provided by an overview of the entire examination. Using overlays or another strategy, it should be possible to superimpose annotation information or CAD information on the mammograms and to black out nonanatomic information that may distract the radiologist.

To make full use of the digital nature of the images, the system should provide easy-to-use image manipulation tools, such as contrast, brightness, image reordering, selection of regions of interest, magnification, and other methods to provide quantitative measurements from the image. Since at least some type of hard-copy record may be required on occasion, the workstation should provide a preview of how any such printed mammogram would appear, so that the lookup table could be tuned to provide the most useful image before printing.

For practicality, the workstation must be compliant with the digital imaging and communications in medicine (DICOM) standard, and it should be possible to display digital mammograms from all DICOM-compliant acquisition systems, including those produced by other vendors. The workstation should be able to accommodate alternative acquisition schema that may provide complementary information (e.g., CAD, stereotaxy, tomosynthesis, digital subtraction angiography, dual energy subtraction, etc). Workstation design also should facilitate interfacing of the digital system with radiology/ hospital information systems (RIS/HIS).

The system should also support quality control functions for the digital mammography acquisition system as well as for soft- (and hard-) copy displays, and to facilitate quantitative use of digital image data for quality control testing. This would allow objective testing of imaging performance and could reduce some of the costs currently associated with quality control.

Research Priorities

- | | |
|--------------------------|---|
| Short term | <ul style="list-style-type: none">• Develop improved quality control procedures for soft-copy displays. |
| Intermediate term | <ul style="list-style-type: none">• Conduct performance-based studies on optimal technical parameters for digital displays, including contrast resolution, spatial resolution, display luminance, data compression, time efficiency, cost efficiency, accuracy, etc.• Improve display controllers to provide greater speed of image manipulation, application of nonlinear lookup tables, image zooming, and rehanging, etc.• Develop an improved understanding of design factors for the image reading environment.• Study how to optimize the human user interaction (ergonomics). |
| Long term | <ul style="list-style-type: none">• Explore alternative display technologies.• Develop of education and testing methods to instruct radiologists in the use of digital display systems. |
-

References

1. Feig SA, Yaffe MJ. Digital mammography, computer-aided diagnosis, and telemammography. *Radiol Clin North Am* 1995; 33:1205-1230.
2. Karellas A, Harris LJ, D'Orsi CJ. Small field digital mammography with 2048 x 2048 pixel charge-coupled device. *Radiology* 1990; 177:288.
3. Dershaw DD, Fleischman RC, Liberman L, Deutch B, Abramson AF, Hann L. Use of digital mammography in needle localization procedures. *AJR* 1993; 161:559-562.
4. Niklason LT, Christian BT, Niklason LE, et al. Digital tomosynthesis in breast imaging. *Radiology* 1997; 205:399-406.
5. Cao F, Sickles EA, Huang HK. Interactive digital breast imaging teaching file. *RSNA EJ* 1997; 1:26.

Session 2: Display Hardware for Soft-Copy Display

Only direct-view display technologies capable of high brightness and high spatial resolution are considered to be candidates for mammography display. Projection technologies suffer from large space requirements and limitations to their dynamic range from veiling glare and ambient light. Head-mounted displays are not suitable, due to user fatigue and discomfort in prolonged daily use.

The principal candidate technologies for mammography image display are:

- Laser-printed film
- Cathode Ray Tube monitors (CRT)
- Liquid Crystal Displays (LCD)
- Field Emission Displays (FED)
- Organic Light Emitting Diode Displays (OLED)

Characteristics are summarized in Table 2-1.

Laser-Printed Film

Film has the combination of high spatial resolution, luminance, and contrast ratio that makes it the "gold standard" for display quality. Specialized laser film printers with 40-micron pixels are required to print digital mammograms with normal size. Conventional laser film printers with 80-micron pixels can display full detail by magnifying the image size. Luminance is effectively limited only by the intensity of the backlight. Mammographic film viewers are as bright as 1,000 foot-Lamberts (ft-L). Light transmitted through film has been measured at 520 ft-L. The contrast ratio of 800:1 ensures that limits of the human vision system and elsewhere in the imaging chain will determine the effective dynamic range.

The disadvantages of film are self-evident. It is a static medium that cannot take advantage of interactive image manipulation. More significant is the cost of producing and handling film images. Digital mammography introduces significant additional equipment costs, and savings related to film costs will be essential if the benefits of digital mammography are to be obtained by a broad segment of the American population.

Cathode Ray Tube Monitors (CRT)

CRT monitors are the reigning soft-copy display technology today. Manufacturing processes have

been fine-tuned after years of volume production for the consumer entertainment and computer markets. Monitors with 5 million addressable pixels (2,000 x 2,500) are available from several manufacturers today; units nearing eight million pixels (2,500 x 3,000) are just beginning to appear commercially.

Maximum luminance and dynamic range of CRT displays are significantly lower than those of the conventional film-light box.¹⁻⁶ Peak luminance up to approximately 200 ft-L is available on 5-megapixel monitors today. Brightness levels as high as 400 ft-L have been achieved in experimental monitors. Typically, higher luminance is attended by degradation of the modulation transfer function (MTF), limiting the effective spatial resolution.

The MTFs of CRTs are anisotropic: whereas they reach values of 30 to 40% at the Nyquist frequency in the vertical direction, the MTFs are limited to 10 to 20% at the Nyquist frequency in the horizontal direction. The MTF in both directions is limited by the spot size and point spreading effects. These effects are nearly isotropic and increase in magnitude as luminance increases. The MTF in the horizontal direction is further limited by the bandwidth of the video electronics. Eight-megapixel displays today particularly suffer from degradation of the MTF in the horizontal direction, as the 800 megahertz bandwidth is difficult to achieve for the final stage of amplification, which drives the electron gun's grid. High luminance levels require higher output voltages from this final amplifier. Since high amplifier bandwidth is difficult to achieve at higher voltages, the requirement for high brightness further limits the achievable resolution on the CRT monitor.

The contrast ratio of CRT monitors is limited by veiling glare, which results primarily from scatter of light in the CRT's faceplate. Although a dynamic range of 10,000:1 can be demonstrated with measurements of uniform fields, the veiling glare imposes a limit on the dynamic range that can be displayed within any one picture to perhaps 200:1.¹⁻³ The contrast ratio of CRT monitors is further affected by ambient light, which reflects off the surface of the phosphor and raises the luminance in the "dark" or "black" portion level. This effect may be diminished by use of a darkened faceplate, but such faceplates

Table 2-1. Characteristics of current soft-copy display technologies

	Availability	Resolution (matrix size)	Luminance (ft-L)	Contrast ratio	Volume market drivers	Advantages	Problems
Laser- printed film	Now	4,000 x 5,000	520	800:1	Consumer, entertainment	Long familiarity, proven diagnostic capability	Operational cost, archive, communication
CRT	Now	2,500 x 3,000	120	200:1	Consumer, entertainment, computers	Relatively low cost	Noise, veiling glare
LCD	Year 2000 production, 8-bit, high fidelity monochrome	2,500 x 3,000 or more	>500	300:1	Laptop and desktop computers	Low glare, low reflection	Contrast dependent on viewing angle
FED	Year 2000-2002; experimental	2,500 x 3,000 or more	?	?	Hand-held devices, automotive, consumer electronics	High brightness, wide viewing angle	Manufacturing process, noise
OLED	Year 2003-2008; experimental	?	?	?	?	Potentially high brightness, wide viewing angle	Operating life, materials

reduce light output and require higher beam current for higher luminance at the phosphor. Minimization of surface reflection requires use in a very dark room, which is often not practical in the clinical care setting.

Spatial noise characteristics of CRT monitors derive largely from phosphor granularity, which affects the threshold contrast for human observers.^{6,7} High-efficiency phosphors desirable for high luminance from a given beam current are usually mixtures of two components, which increase phosphor's granularity. Single-component phosphors such as P45 are therefore usually preferred for medical imaging applications.

The major drawback of CRTs is the fact that, even for the display of static images, a scanning electron beam is required, writing the information (the image) serially up to 70 times per sec onto the CRT's faceplate.

Liquid Crystal Displays (LCD)

Active matrix liquid crystal displays (AM-LCD) are a familiar component of laptop computers, which provide the volume market for the development of new technology and manufacturing processes. Similar to film, AM-LCD devices are transilluminated devices whose brightness is determined by the intensity of the backlight. Also similar to film, the AM-LCD can be manufactured to absorb ambient light and viewed in rooms with high illumination. However, previous available devices have had severe variations in brightness as a function of viewing angle, which can even lead to contrast reversal. Since medical image interpretation requires low contrast detection at many gray levels, this performance limitation has previously ruled out use of these devices for clinical diagnosis. The viewing angle problem is now well understood, and several recent developments have established much improved consistency as a function of viewing angle.

Most AM-LCD devices use a thin layer (about 5 to 10 μm) of nematic liquid crystal material with the molecular direction or director aligned in the display plane. Boundary layers (the alignment layers) are used to orient the molecules on one surface with a specific angular orientation. The angular orientation of the alignment layers are different for the front and back side (typically 90 degrees), such that a helical twist of the nematic liquid crystal is created (twisted nematic [TN]). To make a display device using this

TN structure, a polarizing film is used to filter the light incident on the back side. The polarization direction then rotates by 90 degrees when traversing the TN material.

A second polarizing filter, oriented 90 degrees to the first, is then placed on the front side of the TN cell. The LC molecules distant from the boundaries can change their orientation when an external field is applied. A variation in transmission through the TN-LC cell is established by perturbing the orientation of the directors in the cell with an electric field and altering the orientation of the light polarization with respect to the front polarizing filter. The electric field for each pixel is controlled by active matrix thin film circuits commonly made from amorphous silicon transistors fabricated on glass substrates.

The viewing angle problem with conventional LCD devices results from the perturbation of the director orientation by the electric field being in the direction of the surface normal. At intermediate gray levels, the directors are tilted obliquely in the display plane, and the intensity of light transmitted becomes a function of the incident angle relative to the director orientation.⁸

For higher electric fields the director becomes predominantly normal to the surface and the light deflection is reduced. At certain viewing angles, the expected reduction in brightness reverses and an increase in brightness occurs.

Three notable approaches have recently been introduced to reduce the viewing angle artifact.⁸

- **Retarder films:** Negative birefringence films are placed at the entrance or at the exit (or both) of the LC structure.^{14, 15}
- **Multidomain TN LCDs:** For each pixel, two, four, or more subpixels each with a different orientation in the alignment layers are employed.^{10, 16}
- **In plane switching (IPS):** Electrode pairs are positioned on the side of the LCD pixel structure such that the electric field rotates the director in the plane of the display.¹³

Retarder films provide global correction but, because of the complex and varying director configurations, do not provide a full solution. Multidomain designs

with two or four cells provide some averaging of the artifact and are being widely used in the new generation of wide viewing angle AM-LCD devices that will reach the market in late 1998. IPS is particularly attractive in that it resolves the artifact problem at its source by maintaining the director orientations in the display plane. Electric fields are typically provided by interdigitated electrodes formed on the entrance side of the structure.⁸ A multitude of combinations or variations of these approaches are now being considered and have great potential for high fidelity applications.¹⁰⁻¹²

Essentially all AM-LCD devices currently manufactured provide full color images. These devices have additional color filter layers that degrade optical contrast performance and reduce brightness. Specifically, color devices have three TN cells for each pixel, with each cell covered by a different color filter. For high quality color, the narrow spectral bandpass of the filters is associated with low transmission. Operation of the device to produce shades of gray is done by setting each cell to a balanced brightness. However, substantially brighter gray levels can be achieved by eliminating the color filters with the added benefit of a threefold increase in the number of pixels and improved optical properties. Manufacturing of monochrome devices with large area, high pixel density, and square pixels will be important to utilize this technology for mammography.

Field Emission Displays (FED)

Field emission displays have phosphor screens behind which is a matrix of microvacuum cells such that each pixel has its own cathode.¹⁹

For most devices, the cathode consists of a large array of low work function emitter microtips.^{17, 20} Electrons are accelerated through the small vacuum cell to impinge on the cathodoluminescent phosphor layer. FEDs are similar to CRTs in that electrons are emitted from a cathode and accelerated toward the phosphor through a vacuum cell. However, they typically form the image in a line scan and thus do not have the problems associated with raster scanned devices. They are notable for their high brightness capability and good emission characteristics (i.e., a Lambertian angular distribution with very good viewing angle attributes). Numerous companies (Pixtech, Micron, Canon, Raytheon, Candescent, FED Corp., Futaba, and Motorola) will fabricate FED

devices in 1998 for applications in small mobile and avionic devices.

Several problems with FED technology raise questions as to whether high fidelity devices suitable for mammography are feasible. Pixel brightness variations resulting from electron emission nonuniformities and low reliability of the cathode have been reported for prototype designs. Low voltage phosphors consume less power but have low efficiency and rapid saturation due to high current density. However, the longer phosphor lifetime and lower driver costs of a high voltage phosphor are complicated by an increase in flashover risk, more stringent surface degasification requirements, a need for wider vacuum gaps, and high aspect ratio spacers.

While significant problems exist, the large amount of industrial development occurring with these devices may eventually result in very high performance devices.¹⁸

Organic Light Emitting Diode Displays (OLED)

Among display technologies, electroluminescence represents an all-solid-state approach that provides the most direct conversion of electrical energy into light. Efficiency and performance characteristics depend strongly on materials and fabrication processes used. Electroluminescent displays (EL) use a phosphor under the influence of an electric field to generate light. Electroluminescence occurs in two forms: injection EL (light release upon recombination of minority and majority carriers), and high field EL (emission is due to impact excitation by accelerated charge carriers). Thin film EL devices are made up of a stack of conductors and dielectrics with a phosphor in the center. The thin films are deposited onto a glass substrate. A black thin film layer may be incorporated at the bottom of the structure to provide contrast enhancement. Thin film transistors can be used to address EL for high resolution, low cost devices.

Rapid advances have recently been made in the development of electroluminescent materials. Different doping elements have been used with a ZnS host, providing a wide range of emission spectra with typical efficiencies up to 5 lm/W (ZnS:Mn, ZnS:TbF₃, ZnS:Mn, TbF₃, SrS and CeF₃). White monochrome emission can be obtained by mixing red-green and blue-green phosphors with high

efficiencies. Another promising design concept has recently been reported, consisting of a multilayer stacked structure with organic EL materials with increased efficiency and full-color capabilities.²¹

An attractive feature of thin film inorganic EL is the very steep luminance vs. voltage slope which occurs above a threshold. This, along with a fast phosphor time response, allows for a direct addressing of large arrays. The low voltage threshold and similar steep curve characteristics that have been reported for organic EL materials are of particular note since inexpensive driver circuits may be employed.^{22, 23} Organic materials with high luminous efficiency (up to 12 lm/W), low driving voltage requirements, and fast response times have recently been described. Needs for improved performance relate to chemical structure of organic thin films, organic-metal contacts, organic-organic layers interface, device structure, nonradiative recombination losses, and electrical degradation. Materials include complex metallic compounds with aromatic rings, such as anthracene. In early stages of development, organic EL presents electrical reliability issues such as electrochemical instabilities with formation of radical species, contacts degradation, encapsulation (needed because of air and humidity sensitivity), and low thermal tolerance.

The low voltage and high efficiency of the organic devices has made them of particular interest. Since they operate like an array of light-emitting diodes, they have been referred to as organic light-emitting diodes (OLED) displays. They are regarded as the technology having the most promising long range potential but requiring significant materials research.

Suitability for Digital Mammography

The state of the art of current display technologies is sufficient for soft-copy display in digital mammography, provided that software functions are provided to overcome limitations of:

- Spatial resolution
- Limited luminance
- Dynamic range.

Digital mammography examinations produce data sets immensely larger than can be presented or perceived at one time. A standard mammographic examination at 50 micron pixel size generates four images of 4,000 x 5,000 pixels each, each pixel

comprising 10 to 12 bits. A screening study will usually be compared to a prior exam, and these eight images are the data set the radiologist must interpret.

It is not necessary to have displays showing 4,000 x 5,000 pixels for each image. Human visual acuity is limited by the density of cones in the retina's fovea: they are spaced at about 2 microns, resulting in an angular resolution of about 1 arc-min arc for the typical eye-lens.²⁴ At a viewing distance of 50 cm, the object resolution is then 121 microns. A total of 2,048 of these pixels add up to a vertical image dimension of 11.5 inches, little more than the typical size of a mammogram. To see finer detail than this on film, observers get closer, often with the use of a magnifying glass. An electronic magnifying glass or zoom feature can accomplish the same function just as effectively on soft-copy display, provided it is ergonomically designed and essentially instantaneous in operation.

While zoom and magnification functions can effectively overcome limitations of spatial resolution, limitation of dynamic range is more difficult to mitigate. Wide dynamic range contributes a richness of perceived information that cannot be recovered with gray scale window and level adjustments. High display luminance enables wide perceived dynamic range, particularly in the presence of ambient light.

Current display technologies for 2,500 x 3,000 images are suitable for digital mammography if computer graphic magnifications are employed, provided that such displays prove to have MTFs better than present 2,000 x 2,500 displays. Such a display in landscape format would allow two images to be displayed on each monitor and thus eight images on a four-monitor workstation.

Computer processing can help to overcome some display limitations. High frequency enhancement helps compensate for display MTF and different threshold contrast. Equalization of brightness near the skin line reduces the dynamic range required. Still, the limited contrast of devices may reduce observer performance in diagnostic mammography. Objective data on display performance for diagnostic tasks is lacking. Every practical image processing measure must be taken to compensate for the limited dynamic range of the soft-copy display device.

The suitability of the display technologies for digital mammography is summarized below.

Laser-printed film. The standard of image quality. Suitable for use from a clinical viewpoint, but not a viable long-term solution because of the cost and the operational issues of hard-copy imaging.

CRT monitors. Spatial resolution is adequate provided that proper magnification tools are provided by the workstation software. Brightness and dynamic range are limiting factors but can be partly overcome through image processing, including but not limited to enhancement of tissue visibility near the skin line. If the needed software functions are provided, modern high brightness monitors are highly likely to be sufficient for primary interpretation of digital mammography.

LCDs. Monochrome units with adequate spatial resolution will be available shortly. Luminance is very high, and contrast when viewed on-axis is better than CRT monitors. Its major drawback is the degradation of contrast ratio with increasing viewing angle. The extent to which this will affect diagnostic performance is unknown. High performance gray scale LCD technology is mature enough to be evaluated in comparison to CRT for mammography.

FEDs and OLEDs. Both FED and OLED are promising technologies that offer potential for high brightness flat panel displays with wide viewing angle, when and if the present manufacturing and materials science problems are resolved. FED and OLED have demonstrated potential and should be encouraged as future alternative display technologies.

Research Priorities

Short term

- Conduct studies to determine the relation between the visibility of early signs of breast cancer and digital display performance parameters.
- Update the body of work related to CRT evaluation.
- Conduct new research to evaluate display technology (particularly new generation CRTs and LCDs) for mammographic imaging objectively.

Intermediate term

- Develop and test perception models appropriate for mammographic imaging to enable optimization of display characteristics without lengthy and prohibitively costly trial-and-error. Work should begin immediately, as development and testing may require a number of years.
- Correlate the short-term research proposed above with the development of these models.

Long term

- Develop high resolution display technologies providing high spatial and contrast resolution, high luminance, high dynamic range and wide viewing angle at reasonable cost.
 - Research materials and device structures for new display technology:
 - Techniques for manufacturing FEDs
 - Long life, high luminance OLED materials.
 - Monitor and assess advances in commercial display technology and potential spin-offs from nonclassified defense, aerospace, and intelligence developments.
-

References

1. Blume H, Roehrig H, Ji T-L, Browne M. Very high-resolution monochrome CRT displays: how good are they really? *SID Digest* 1991; 91:355-358.
2. Blume H, Roehrig H, Ji T-L. Very high-resolution CRT display systems: update on state of the art of physical and psychophysical performance. *SID Digest* 1992; 92:699-702.
3. Blume H, Roehrig H, Ji T-L. High-resolution high-brightness CRT display systems: update on the state of the art. *SID Digest* 1994; 94:219-222.
4. Weibrecht M, Spekowius G, Quadflieg P, Blume H. Image quality assessment of monochrome monitors for medical soft copy display. *SPIE* 1997; 3031:232-244.
5. Roehrig H, Blume H, Ji T-L, Browne M. Performance test and quality control of cathode ray tube displays. *J Digital Imaging* 1990; 3:134-145.
6. Ji T-L, Roehrig H, Blume H, Seeley G, Browne M. Physical and psychophysical evaluation of CRT noise performance. *Proc SPIE* 1991; 1444:136-150.
7. Roehrig H, Blume H, Ji T-L, Sundareshan MK. Noise of CRT display systems. *Proc SPIE* 1993; 1897:232-245.
8. Bos P, Werner K. Viewing angle improvements for LCDs. *Inform Display* 1997; 13(11):26-30.
9. Chen CJ, Lien A, Nathan MI. 4x4 and 2x2 matrix formulations for the optics in stratified and biaxial media. *Journal of the Optical Society of North America* 1997; 14(11):3125-3134.
10. Hoke CD, Mori H, Bos PJ. An ultra wide viewing angle STN-LCD with a negative birefringence compensation film. *Proc of the Intern Display Research Conf* 1997; 21-24.
11. Nam MS, Wu JW, Choi YJ, et al. Wide viewing angle TFT-LCD with photo-aligned four-domain TN module. *SID Digest* 1997; 97:933-936.
12. Wakemoto H, Asada S, Kato N, et al. An advanced in-plane switching mode TFT-LCD. *SID Digest* 1997; 97:929-932.
13. Masutani Y, Tahata S, Hayashi M, et al. Novel TFT array structure for LCD monitors with in-plane switching mode. *SID Digest* 1997; 97:15-18.
14. Miyashita T, Yamaguchi Y, Uchida T. Wide viewing angle display mode using bend-alignment liquid crystal cell. *Japanese Journal of Applied Physics* 1995; 34: L177-L179.
15. Mori H, Bos PJ. Application of a negative birefringence film to various LCD modes. *Proc of the Intern Display Research Conf* 1997; M88-M97.
16. Schadt M, Sieberle H, Schuster A. Optical patterning of multidomain LCD with wide viewing angle. *Nature* 1996; 381:212-215.
17. Brodie I, Schwoebel PR. Vacuum microelectronic devices. *Proc of the IEEE* 1994; 82(7):1006-1034.
18. Derbyshire K. Beyond AMLCDs: field emission displays? *Solid State Technology* 1994; Nov.
19. Gray HF. The field emitter display. *Information Digest* 1993; March 9-14.
20. Utsumi T. Vacuum microelectronics: What's new and exciting. *Proceedings of the IEEE* 1991; 82(7):1006-1034.
21. Burrows PE, Shen Z, Forrest SR. Saturated full color stacked organic light emitting devices. *Proc Intern Display Research Conf* 1997.
22. Seidler PF, Haskal EI, Curioni A, et al. Lithium-aluminum cathodes for organic light-emitting diodes. *Proc Intern Display Research Conf* 1997.
23. Sturm JC, Sturm CC. Integrated organic light emitting diode structures using doped polymers. *Proc Intern Display Research Conf* 1997.
24. Rose A. *Vision: human and electronic*. New York, NY: Plenum Press, 1973.

Session 3: Computer Software and Workstation Design

Current State of the Art

Over the past decade, substantial resources have been directed at the development of digital X-ray detection systems for mammographic imaging. Currently there are several companies with full-field-of-view digital mammography systems seeking FDA approval for marketing. In order to obtain this approval, manufacturers need to show equivalence in diagnostic accuracy and dosage between current screen-film technology and digitally acquired images printed onto laser film. However, it is anticipated that direct digital acquisition of mammographic data will ultimately offer more than just a replacement for screen-film technology. It is a technology that should lead to improved diagnostic accuracy. This is possible due to the fact that, unlike screen film technology, digital mammography uncouples the detection and display processes, allowing for manipulation of the image data to enhance the conspicuity of mammographic abnormalities prior to display. It is believed that, in order for the radiologists to take full advantage of the many potential computer manipulations of digitally acquired mammographic data, soft-copy display of images will be essential.

It appears that approval for marketing of full-field-of-view digital mammographic detection systems is nearly at hand. However, issues concerning soft-copy display of images from these systems are only beginning to be addressed and they present significant challenges. Issues include the enormous size of mammographic image datasets and the wide range of visibly detectable gray levels needed to appreciate minimal differences in X-ray attenuation between normal and abnormal breast tissue. In principle these issues are solvable; however, there are severe cost constraints on this market that may hinder research on solving these problems. Reimbursement rates for mammographic interpretation are low and often considered a loss-leader of radiologic imaging. As a result mammography is one the most efficiently run areas of any radiology department. The interpretation process with current screen-film technology has already been designed for the most efficient use of radiologists' time. Any soft-copy display technology will have to compete with this already highly efficient, cost restricted process. Radiology soft-copy display systems are only a

fraction of a much larger global market for soft-copy displays and, unfortunately, mammography occupies only a small portion of the market for radiologic equipment. Hence the market forces to move this technology forward in mammography are weak. In sponsoring this workshop, the PHS OWH and the NCI have stepped forward to identify roles that NIH might take in helping to mature this technology toward its clinical acceptance and implementation. Session 3 of this workshop addressed the issue of workstation design, summarizing current state of the art, identifying gaps in understanding and technology, and prioritizing a research and development agenda.

Clinical State of the Art

Speed, simplicity, and intuitive image review are essential components of a clinically acceptable workstation for mammography. There are currently no soft-copy workstations that would be acceptable to radiologists as a replacement for today's film and light box technology for mammography. However, several existing laboratory systems are exploring and defining key features that will be important to the clinically acceptable soft-copy workstation.^{6, 11, 14} There are two environments, screening and diagnostic, in which mammography is performed, and workstation designs need to take into account radiologists' needs in both environments.

In the screening environment, speed and ease of image review are of paramount importance. In this setting, two views of each breast (craniocaudal and mediolateral oblique views) from the current exam are compared to the same views from a prior year. Not infrequently, there is also the need to compare the current exam to multiple prior years. Thus, at a minimum, a soft-copy workstation must be capable of displaying at least eight different images (two views of each breast, current and prior). With current detector technology, this means that workstation must be capable of handling a minimum of 320 Mbytes of raw image data per examination. On a light box, the arrangement of films allows for symmetry comparisons between opposite breasts, confirmation of findings on both the craniocaudal and oblique views, and assessment of interval changes with prior exams. With current mammography film multiviewers, these eight projections can all be viewed at the same time, such that only simple head

and eye movements are required by the radiologist to make these various comparisons. The images are then reviewed a second time, using a magnifying glass to aid identification of microcalcifications and architectural distortion and to help characterize morphological features of soft tissue masses and calcifications. Although a lot happens in the review of a screening mammogram, the perceptual skills of the radiologists are highly trained at these tasks, and they can typically be completed in about one minute. Positioning of the next patient exam on the multiviewer takes a fraction of a second, and workstations will need to be able to handle near-instantaneous presentation of image data for the next patient.

In the diagnostic environment, speed and ease of use of the soft-copy workstation are similarly important.² However, film arrangement and manipulation are much more variable than in screening, and are likely to present more of a challenge to technology and system developers than will be required for the screening mammography workstation. Images that will require viewing will include the standard craniocaudal and mediolateral oblique views, prior mammographic exams, tailored mammographic views (e.g., straight mediolateral, magnification, spot compression, rolled, and implant displacement views), as well as images from other modalities (ultrasound, MRI), and new imaging techniques (digital tomosynthesis). Further complicating the display issue is that the same images will also need to be viewed subsequent to imaging processing used to enhance the conspicuity of specific findings (e.g., architectural distortion). Not only does the manner in which radiologists view all these images differ from radiologist to radiologist, but also for an individual radiologist the viewing pattern will vary from case to case. To replace the mammographic view box, workstations will have to permit the radiologists to navigate through hundreds of megabytes of data at speeds approaching those of the head and eye movements of the radiologist.

Technical Overview of State of the Art

Current state-of-the-art computer technology is believed to be adequate for implementation of functional, acceptable clinical workstations. Although the storage needs for a breast imaging exam will be greater than that of any other radiologic imaging technology, use of an optical disc, tape, and lossless data compression (3-5:1 ratios) will permit

storage of several years of raw image data for any single patient. When needed these data can be transferred from storage media via high speed ATM and Gigabit Ethernet communication networks³ into the workstation. Quick access to a large amount of data will be essential. Systems using large amounts of DRAM⁷ or video RAM¹⁴ have been designed to permit the radiologist to gain near instantaneous access to these large datasets. However, less expensive solutions, such as more direct data transfer pathways or software optimization for existing data transfer schemes could be implemented. Image boards that convert 12 and 16 bit data down to 10 or 8 bit data are currently on the market and will facilitate rapid data manipulation at the workstation. For image viewing, 2K x 2.5 K video monitors are currently being used in prototype digital mammography workstations, and with the proper image handling and manipulation tools are thought to be adequate for first generation workstations. The precise number of CRTs needed in a workstation requires further study. However, one¹⁴ and two^{6,11} 2.0 x 2.5 K monitors have been used in prototype workstations for screening mammography.

As with other radiologic imaging modalities, standards have been developed for handling image and image related demographic data (DICOM [NEMA 97] and HL7 [HL7 94]). Use of these standards in digital breast imaging is obviously essential, as mammography workstation will need to tap into existing picture archiving and communication, radiology information, and hospital information systems. Prototype workstations that use these standards have already been developed that connect to existing PACS, RIS, and HIS.⁹

Despite the fact that current display technologies are considered adequate for the first generation of mammographic workstations, there are a number of technologies on the horizon that could markedly enhance soft-copy display, not only in mammography but radiology in general. These include such technologies as LCDs, which have a higher luminance than currently used CRTs, and 20 megapixel displays (as opposed to currently used 5 megapixel displays) which may come to the market in the future.

Image Preprocessing/Handling

Image processing is an area that is critical to the success of soft-copy workstations not only for mammography, but also for other projection

radiographic techniques such as bone and chest.¹³ Some of the issues are the same regardless of body part being imaged; others are specific to mammography. For soft-copy displays in general, it is important to define a "default image," which will have identical perceptual characteristics regardless of the system on which it is being displayed. This is important, as not only do CRT characteristics change from one manufacturer to another, but identical models of CRT's differ from one another as they come off the production line and as they are used. Thus, if the fidelity of the image is to be maintained so that it has an identical appearance regardless of the manufacturer or age of the workstation, workstation-specific processing will be necessary to achieve this.

Mammography-specific image processing includes methods for enhancing the conspicuity of pathologic findings. Unlike many areas of radiology, there are relatively few features that are used by the radiologists to detect and assess breast abnormalities. These include mass shape and margins, calcification morphology and distribution, and architectural distortion. Algorithms that enhance the conspicuity of these features hold great promise for increasing the sensitivity and specificity of mammography. In addition, one of the hoped for benefits of digital mammography is improved visualization of pathology in the mammographically dense breast. With current screen-film techniques, dense breast tissue is known to obscure even clinically obvious cancer. However, digital mammography permits image acquisition to be uncoupled from image display, allowing the acquired data to be manipulated in ways that may permit better assessment of the mammographically dense breast.

Other software techniques that will be critical to the success of mammography workstations is the use of "computer intelligence" to help the radiologist sort through the enormous amounts of data that digital acquisition and processing will present to the radiologists. This includes intelligent pre-hanging of individual images from a study, and perhaps intelligent strategies for navigating through the vast amounts of image data. These intelligent hanging and navigation schemes will need to take into account work flow that is common to all radiologists as well as the individual radiologist's specific work habits.

Integration of CAD with Workstation Design

CAD (computer-aided diagnosis) in mammography is the detection of a potential abnormality or the diagnosis of an abnormality made by a radiologist who takes into consideration the output from a computer analysis of the mammogram.^{3,4} CAD is being used to aid radiologists in both the screening and diagnostic mammography settings. Output from CAD programs include localization of potential abnormalities, indications of the likelihood of malignancy, and more controversially, quantitative risk assessment based on the mammographic density of the breast. Many observer performance studies have shown that the use of computer output improves radiologists' performance in mammographic detection and classification tasks.^{1,10} However, integration of CAD into the daily practice of radiology is far from routine. One reason includes barriers to its easy use. Current programs are designed for digitized film mammograms, and the digitization process is cumbersome and time consuming. Direct digital mammography should greatly facilitate CADs use, and modifications to existing software to accommodate the image characteristics of direct digital data is not anticipated to be a significant barrier.

As a result of the potential impact of CAD on mammographic practice, design of soft-copy workstations will need to take into account how to efficiently implement the use of CAD in both screening and diagnostic workups. This includes interface design issues, such as when and how CAD output is used by the radiologist, and the form of that output (graphical, text, or both). As with other areas of workstation design, CAD needs to be fast and easy to use and will almost certainly need to accommodate user-specific preferences.

CAD and Observer-Controlled Post Processing

The theme of simplicity and ease of use for the interpreting radiologists will also need to guide the integration of signal post-processing into mammographic workstation design, as has been noted many times above. Once post-processing algorithms have been developed that highlight the conspicuity of specific mammographic findings, the method of controlling use of these algorithms and the

presentation layout of resulting images will need to be carefully thought out and tested. In all likelihood, strategies to control the use of post-processing and layout presentation will be different in the screening and diagnostic environments.

One control strategy that is being contemplated is the use of CAD to guide the presentation of images based on the type of pathology that is identified by CAD. In the screening environment, high sensitivity is obviously desirable, although there is a direct relationship between the sensitivity and the number of false positives presented to the interpreting radiologists. Likewise, in the diagnostic environment, high specificity is desirable, but this comes at the expense of false negatives. Workstation adjustments for individual radiologist's sensitivity and specificity preferences will be necessary in both environments.

Regardless of any predefined strategy for controlling the use of post-processing algorithms and image layout, it is inevitable that some amount of user control will be necessary. Specific tools that radiologists will want to use will include those that permit rearrangement of images, image zoom-and-scroll, image magnification, image equalization, and near instantaneous application of pathology-specific enhancement algorithms. It is important to realize, however, that the clinically successful workstation will likely require minimal, if any, need for user controlled image manipulation for most cases.

User Interface and Reading Environment

Even with hardware and software that might realize the much hoped for improvements in diagnostic accuracy that digital mammography may offer, if radiologists' ability to get at this information is not intuitive and easy, clinical acceptance of this technology will be problematic. As with current screen-film and light box technology, the radiologists' attention and eyes need to be primarily focused on reviewing and assessing the images, not on manipulating and processing them. The clinically successful workstation will be one that packages all the necessary hardware and software components into a workstation that allows radiologists to spend their time looking at the images.¹⁴

Last, but not least, an understanding of the need to strictly control ambient lighting in the workstation area is needed. This is already a critical issue in mammographic reading rooms and will become more so if soft-copy workstations replace light box technology. Detection of subtle differences in shades of gray are essential to the identification of pathology in a mammographic image of the breast. Any level of ambient lighting in the reading area hinders the human eye's ability to detect these differences. Since current CRT technology cannot match the absolute luminance levels of film light boxes or the range of visibly detectable gray levels that can be achieved with current screen-film on light boxes, low ambient light levels in the soft-copy reading area will be even more critical than they already are to the detection and characterization of mammographic abnormalities.²

Research Priorities

Short term

- Model radiologists' viewing and work patterns in both screening and diagnostic environments so that critical parameters of work flow can guide workstation design. Time is an essential model variable.
- Develop image management and navigation software based on the above modeling.
- Define default soft-copy images (initial view and visually enhanced images) with respect to contrast resolution, spatial resolution, maximum luminance, background luminance, and system contrast. DICOM standards should be accommodated in defining default display performance.
- Develop CRT-specific compensations to permit fidelity of default images (i.e., default images should be the same regardless of specific display device). To achieve this, display specific processing needs to be studied to compensate for: absolute luminance, luminance nonuniformity, veiling glare, dynamic range, distortion, noise, modulation transfer, luminance range, and acquired image size.
- Use above findings and existing state-of-the-art technologies to assemble soft-copy workstations for digital mammography in both screening and diagnostic environments. Evaluate impact on diagnostic accuracy, time efficiency, cost, reader fatigue, and satisfaction of search in both screening and diagnostic environments.*
- Develop quality control techniques to assure fidelity of standard images regardless of specific displays.

Intermediate term

- Develop and evaluate feature specific enhancement algorithms (e.g., calcifications, masses, and architectural distortion).
- Further develop CAD algorithms for both the screening and diagnostic environments. Expand work on current algorithms to increase sensitivity and specificity and to decrease false positives. Modify current algorithms to accommodate direct digitally acquired mammographic data.
- Investigate user preference issues with respect to CAD and user directed image processing and manipulation tools.
- Incorporate above work on feature-specific image processing, CAD and user control issues into efficient and easily used soft-copy workstation. Evaluate impact on diagnostic accuracy, time efficiency, cost, reader fatigue, and satisfaction of search in both screening and diagnostic environments.
- Model and evaluate network support needed to incorporate digital mammography in full functioning radiology department.
- Evaluate utility, image quality, and methods of image compression for storage and data transfer.

Long term

- Research perception modeling and assessment techniques to more rapidly and less expensively evaluate new image processing algorithms and changes in soft-copy display technology (e.g., monitor brightness, monitors with higher and more uniform modulation transfer) on observer performance in radiology.
- Evaluate and incorporate new display technologies into mammographic workstations.

*A few members in the working group felt that, if first generation workstations are evaluated without CAD, they may fail and, thus, incorporation and evaluation of CAD in first generation workstations is crucial.

References

1. Chan HP, Doi K, Vyborny CJ, et al. Improvement in radiologists' detection of clustered microcalcifications on mammograms: the potential of computer-aided diagnosis. *Invest Radiol* 1990; 25(10):1102-1110.
2. Cho PA, Huang HK. Architecture and ergonomics of imaging workstations. In: Hendee WR, Wells PNT, eds. *The perception of visual information* (2nd ed.). New York, NY: Springer, 1997; 343-358.
3. Doi K, Giger ML, Nishikawa RM, Schmidt RA, eds. *Digital Mammography '96: Proceedings of the 3rd International Workshop of Digital Mammography*. New York, NY: Elsevier, 1996.
4. Giger ML, MacMahon H. Image processing and computer-aided diagnosis. In: Greenes RA, Bauman R, eds. *Radiologic clinics of North America*. Saunders Publishing Co., 1996; 565-596.
5. Health Level Seven, Inc. *Health level seven: an application protocol for electronic data exchange in healthcare environments (Version 2.2)*. Ann Arbor, MI: Health Level Seven, Inc., 1994.
6. Hemminger BM, Dillon A, Pisano ED, Johnston RE. Demonstration of a soft-copy display system for digital mammography. *Radiology* 1997; 205(P):473.
7. Hemminger BM. Design of useful and inexpensive radiology workstations. *S/CAR: Symposia Foundation*, 1992; 615-624.
8. Huang HK, Wong AWK, Zhu X. Performance of asynchronous transfer mode (ATM) local area and wide area networks for medical image transmission in clinical environment. *J Comp Med Imag & Graphics* 1997; 21(3):165-173.
9. Huang HK, Wong AWK, Lou SL, et al. Clinical experience with a second generation PACS. *J Digital Imag* 1996; 9(4):151-166.
10. Jiang Y, Nishikawa RM, Wolverton DE, et al. Malignant and benign clustered microcalcifications: automated feature analysis and classification. *Radiology* 1996; 198(3):671-8.
11. Lou SL, Sickles EA, Huang HK, et al. Full-field direct digital telemammography: technical components, study protocols, and preliminary results. *IEEE Trans on Inform Tech Biom* 1997.
12. National Electrical Manufacturers Association. *Digital imaging and communications in medicine (DICOM) (PS3-1996)*. Rosslyn, VA: NEMA, 1997.
13. Reiker GG, Blume HR, Slone RM, et al. Filmless digital chest radiography within the radiology department. *Proc SPIE* 1997; 3035:355-368.
14. Shile PE, Fujii T, Ramamurthy V, Blaine GJ, Cox JR, Jost RG. Observer productivity reading full-field-of view digital mammograms: an evaluation of a soft-copy workstation supported by a high-capacity high performance display buffer. *Proc SPIE* 1997; 3035:287-290.

Session 4: Image Perception and Workstation Design for Mammography

This statement starts with a review of the sources of error in mammography. We indicate that at least half of the errors are due to faulty image perception. We then describe some of the principles of perception and show how understanding them can benefit mammography. The research that is needed to achieve these benefits is outlined. In the short term it is important to understand display system and environment tradeoffs that affect the detection and discrimination of abnormalities in mammography and to use this information to improve user interfaces. The long term goal is to develop predictive models that allow calculation of how to improve human performance by changes in images, detectors, displays, and the environment.

The Importance of Image Perception to Mammography

Mammography is a definitive diagnostic procedure. The mammographic exam whether it is film or digitally based is and will be the primary diagnostic procedure for breast cancer detection screening. Other imaging modalities such as MRI, ultrasound, or nuclear medicine are used primarily to aid in the diagnosis of breast cancer. A negative mammogram returns the woman to routine screening and a missed cancer becomes a missed opportunity for early treatment.

About half of the cancers missed at screening mammography are missed for perceptual reasons.

The actual number of cancers missed in the usual clinical practice is unknown. Cancers can be missed because the imaging technique has failed to record them adequately or because the reader either does not

see the cancer or sees it and decides that it is something else. These can be simply classified as technological, perceptual, and interpretational errors, respectively.

Bird et al.¹ analyzed 77 cancers that were missed during screening a population of about 77,000 women.² The results shown in Table 4-1 indicate that 43% of the misses were perceptual, meaning that the cancer was recorded in the image but not seen.

A review of 575 screening-detected cancers and 102 interval cancers found in the Canadian National Breast Cancer Screening Study showed that 46% of the screening-detected cancers and 34% of the interval cancers had a previous image that showed the cancer not reported on the initial reading.³ The data are shown in Table 4-2.

There is also a very large variation in cancer detection performance among radiologists. Beam et al. gave 108 radiologists a mammography reading test consisting of 79 screening mammograms.⁴ The results are summarized in Table 4-3. The median sensitivity of 80% indicates that on average 20% of the cancers known to be visible in the images were missed. In addition, note the wide variation in performance as shown by the minimum and maximum values.

These data indicate that observer error is an important issue for mammography and that methods for minimizing observer error should be incorporated into imaging systems. This is why so much effort has been put into CAD.

Table 4-1. Reason for mammographic false negatives in cases with a histological diagnosis of breast cancer within one year of screening from Bird et al.¹

Reasons for Missed Breast Cancer	Number	Percentage
Misinterpreted	40	52
Overlooked	33	43
Suboptimal Technique	4	5

Table 4-2. Reason for mammographic false negatives in histologically proved cancers, Canadian National Breast Cancer Screening Study³

	Screen cancers		Interval cancers	
	No.	Pct.	No.	Pct.
Total number of cancers	575		102	
Total number of missed cancers	218		94	
Observer errors				
- One screen before detection	100	46	35	37
- Screen at time of detection	28	13	NA	
Technological errors				
- One screen before detection	28	13		
Occult at time of screening	62	28	59	63

Table 4-3 Summary measures of diagnostic accuracy among 108 U.S. radiologists reading randomly selected test set of 79 screening mammograms reported by Beam et al.⁴

	Median	Minimum	Maximum
Sensitivity %	80	47	100
Specificity %			
- Normal	95	37	100
- Benign	60	13	100
ROC Curve Area	0.84	0.74	0.95

The Perception of Information Displayed on a Workstation

The purpose of workstations is to transfer image information from the display surface to the human perceptual system.^{5,6} The efficiency of the transfer is influenced by (1) the matching of the physical properties of the display to the visual system, (2) the working environment, (3) the computer interface, and (4) the expertise of the observer.

Matching the physical properties of the display to the visual system.

- **Image size and spatial resolution:** The effects of display size and pixel size on the detectability of abnormalities on mammograms have not been clearly determined. Mammographers typically use magnifying lenses when searching mammograms for microcalcifications. On a workstation this activity must be accomplished by a zoom and rove operation.
- **Image luminance and tone scale:** The ability of the visual system to detect a difference in luminance or contrast sensitivity has been extensively studied. It depends upon a number of factors, including the type of stimulus and the adapting luminance.⁷ The basic situation is shown in the following figure. When the adaptation luminance is low (the image and the environment is dark), the contrast threshold (C_T) changes rapidly with the luminance. This is called the Rose-DeVries Region after the two investigators who independently modeled contrast sensitivity when the eye was photon limited. At higher luminance levels the contrast sensitivity is independent of changes in the adapting luminance. This is called the Weber region after the investigator who first established this. The thick line shows the contrast threshold when the eye is fully adapted at each luminance. The thin line shows the contrast threshold in the darker part of the image when the eye is adapted at one level (10 fL in the diagram). When viewing a variegated scene with alternating dark and light regions, the eye can never fully adapt, especially to the dark areas. Consequently objects in the dark areas are harder to see.
- **Perceptually linearized gray scale:** One approach to improving contrast perception in the portions of the image where contrast sensitivity is

increased is to adjust the gray scale in the image to more closely match the performance of the visual system. The idea is to produce a gray scale transfer function that converts equal changes in the digital input values to produce equal levels of perceived contrast over the entire luminance range of the monitor. This is done by modeling the human contrast sensitivity curve and using it to define a gray scale transfer function.⁸ A perceptually linearized monitor yields better performance (detection of masses and microcalcification clusters in mammograms) than a monitor that has not been perceptually linearized. Krupinski and Roehrig compared performance when a monitor was linearized using the Barten curve versus performance with a default nonlinearized tone scale.⁹

Performance, as measured by ROC Az, was significantly higher when the monitor was perceptually linearized. Monitor luminance (80 fL Vs 140 fL) did not influence detection performance to a significant degree. Eye-position recording indicated that there may be some influence of monitor luminance on overall viewing time - average viewing times with the higher luminance monitor were shorter than with the lower luminance monitor. Tone scale had little influence on viewing time.

The working environment. The contrast on the display is due to both the light from the CRT phosphor and reflected light from the environment. The adaptation level of the eye is determined by the light from the display and extraneous light from other sources in the environment. It has been shown that excess light from unmasked portions of the display and the ambient illumination can decrease the detectability of microcalcifications on mammograms.¹⁰ This effect is due to both loss of display contrast and decreased visual contrast sensitivity.

The computer interface. The arrangement of the images on the display, the use of image processing tools, and the control of the computer interface have not been studied carefully enough in mammography. The success or failure of a workstation may depend more on the way it functions than on the quality of the images. Time and motion studies are an important and efficient way to design proper and useful computer human interfaces.¹¹ These principles have been applied to workstations for other imaging applications.¹²

The expertise of the observer. Knowledge and experience clearly play a role in the interpretation of mammograms. Familiarity with the image content and the task influence diagnostic performance and the way that readers search the images. Krupinski found that readers with more experience tended to detect lesions earlier in search than readers with less experience; but readers with less experience tended to spend more time overall searching the images and covered more image area than those with more experience.¹³ Nodine et al. also observed that experienced readers are characterized by speed and efficiency.¹⁴

Models for Image Perception

It is impossible to test clinically every change in an imaging system. The solution is to develop a model that will predict how system changes will affect performance. These models have the following form.

$$\text{detectability} = \frac{(\text{target properties}) * (\text{system properties})}{(\text{system noise})}$$

Decision theory models have been developed that relate the performance of an ideal observer on a specific task to the physical properties of the image.¹⁵

¹⁷ Models can be used to predict how changes in the physical properties of the imaging system (contrast, unsharpness, noise) will affect performance. This type of modeling is currently being extended to include backgrounds that are very similar to those found in mammograms.

Measuring Observer Performance: Accuracy and Process

When comparing film versus workstation viewing of radiographic images, a number of factors relating to

process and accuracy can be evaluated. The most important question that must be addressed is whether diagnostic accuracy using a workstation is at least as good as that when viewing film images. There are accepted measures of diagnostic accuracy that can and should be used in an objective assessment of observer performance. Although receiver operating characteristic (ROC) studies can be time-consuming and laborious, they do measure diagnostic performance reliably and they also permit valid statistical comparisons between viewing modalities. Other measures, such as sensitivity and specificity, and positive and negative predictive value are also accepted objective measures of diagnostic performance that can be derived without doing an ROC based study; however, they are biased by differences in the use of diagnostic criteria and by the prevalence of abnormality. Other measures and alternatives to ROC analysis (e.g., alternative forced-choice protocols) also exist and can be used as objective measures of observer performance. Subjective measures are useful and informative, but should not be used as the sole means of deciding whether one display modality is better than another. Subjective assessments of image quality should always be accompanied by objective measures of performance.

Measures of the process of reading images are also important because they are the determinants of efficiency and fatigue. These measures include viewing time, number of operations performed during viewing, times associated with viewing particular parts of a display, such as the time spent looking at the diagnostic image versus the menu on a computer display, and times associated with different diagnostic decisions. The time spent viewing various parts of the image and specific diagnostic decision times can be estimated from eye-position recordings.

Research Priorities

Short term

- Conduct psychophysical studies of the effect of display parameters on detection and discrimination of diagnostic features in mammograms:
 - Determine the effects of major display parameters on human detection and discrimination of diagnostic features in mammograms. This includes studies of spatial resolution, luminance, contrast range, system noise, ambient illumination and glare.
 - Phantom studies are appropriate, but the relationship between performance on the phantom and performance on real imagery must be established. It is highly likely that the most useful results will be derived from studies of hybrid images consisting of realistic backgrounds that have well-characterized abnormalities added to them.
 - Preference studies may be used in a complementary fashion but should not be used in lieu of objective metrics, such as receiver operating characteristic (ROC) parameters, forced choice parameters, observer signal-to-noise ratio measures, or sensitivity and specificity.
- Conduct time and motion studies on the performance of image reading tasks in mammography:
 - Develop models of the workflow of the radiologist during image reading tasks. Include as metrics the time to perform operations and the number of independent operations required to complete a task. The accuracy of models should be verified by comparison to the actual radiologist performance. Eye position studies can be helpful for defining where attention is directed during various tasks. These data will be useful for the system designer working on the display interface.

Intermediate term

- Determine the effect of image navigation and different display protocols on the detection and discrimination of diagnostic features in mammograms:
 - With film on an alternator, numerous images both present and past, can be viewed simultaneously in their entirety, and a magnifying glass can be used to detect microcalcifications. With monitors, the number of images displayed at full resolution is limited and a magnifying glass does not have the same effect with the monitor as with film because the actual pixels become visible. Some display protocols will be more fatiguing than others and may even affect diagnostic performance if they are too tedious and complicated.

Long term

- Develop computational models for predicting human detection and discrimination performance using real mammograms:
 - Testing every change in the physical parameters of an imaging system on decision outcome is not feasible. A predictive model would be much more useful, and scientific effort should be expended on model development.
- Study the effects of fatigue and vigilance during screening tasks:
 - In the general screening environment the detection of an actual lesion is a relatively rare event. Vigilance is required at all times by the mammographer in order to avoid missing these rare events. Although vigilance and fatigue have been well studied in areas such as the detection of targets using radar, the topic has not been studied well in radiology. The added factors of viewing images on a monitor and diverting attention from the diagnostic to the menu or other icons on the monitor may prove to be important factors.

References

1. Bird RE, Wallace TW, Yankaskas BC. Analysis of cancers missed at screening mammography. *Radiology* 1992; 184:613-617.
2. Bird RE. Low-cost screening mammography: report on finances and review of 21,716 consecutive cases. *Radiology* 1989; 171:87-90.
3. Baines CJ, McFarlane DV, Miller AB. The role of the reference radiologist: estimates of inter-observer agreement and potential delay in cancer detection in the national breast cancer screening study. *Invest Radiol* 1990; 25:971-976.
4. Beam CA, Layde PM, Sullivan DC. Variability in the interpretation of screening mammograms by U.S. radiologists. *Arch Intern Med* 1996; 156:209-213.
5. Kundel HL. Visual perception and image display terminals. *Radiol Clin N Am* 1986; 24(1):69-78.
6. Arenson RL, Chakraborty DP, Seshadri SB, Kundel HL. The digital imaging workstation. *Radiology* 1990; 176:303-315.
7. Heinemann E. The relation of apparent brightness to the threshold for differences in luminance. *Journal of Experimental Psychology* 1961; 61:389-399.
8. Blume H, Hemminger BM. Image presentation in digital radiology: perspectives on the emerging DICOM display function standard and its application. *Radiographics* 1997; 17:769-777.
9. Krupinski E, Roehrig H. Influence of monitor luminance and tone scale on observer detection performance. *Medical Imaging 98: Image Perception* 1998; 3340.
10. Kimme-Smith C, Haus AG, DeBruhl N, Bassett LH. Effects of ambient light and view box luminance on the detection of calcifications in mammography. *AJR* 1997; 168:775-778.
11. Card S, Moran T, Newell A. The psychology of human-computer interaction. Hillsdale, NJ: Erlbaum, 1983.
12. Beard DV, Hemminger BM, Perry JR, et al. Interpretation of CT studies: single-screen workstation versus film alternator. *Radiology* 1993; 187:565-569.
13. Krupinski E. Influence of experience on scanning strategies in mammography. *Medical Imaging 96: Image Perception* 1996; 2712:95-101.
14. Nodine C, Kundel H, SC. L, Toto L. 1996. The nature of expertise in searching mammograms for masses. *Medical Imaging 96: Image Perception* 1996; 2712:89-94.
15. Burgess A. Image quality, the ideal observer, and human performance of radiologic detection tasks. *Academic Radiology* 1995; 2:522-526.
16. Wagner RF, Brown DG. Unified SNR analysis of medical imaging systems. *Phys Med Biol* 1985; 30:489-518.
17. Barrett HH, Denny J, Wagner RF, Meyers KJ. Objective assessment of image quality II: Fisher information, Fourier crosstalk and figures of merit for task performance. *J Opt Soc Am* 1995; A12:834-852.

Image Quality Degradation by Light Scattering in Display Devices

Michael J. Flynn and Aldo Badano

Veiling glare and ambient light reflection can significantly degrade the quality of an image on a display device. Veiling glare is primarily associated with the diffuse spread of image signal caused by multiple light scattering in the emissive structure of the device. The glare ratio associated with a test image with a 1-cm-diameter black spot is reported as 555 for film, 89 for a monochrome monitor, and 25 for a color monitor. Diffuse light reflection results from ambient light entering the display surface and returning at random emission angles. The diffuse reflection coefficient (luminance/illuminance, 1/sr) is reported as 0.026 for film, 0.058 for a monochrome monitor, and 0.025 for a color monitor with an antireflective surface coating. Both processes increase the luminance in black regions and cause contrast reduction. Specular reflections interfere with detail in the displayed scene. The specular reflection coefficient (luminance/luminance) is reported as 0.011 for film, 0.041 for a monochrome monitor, and 0.021 for a color monitor with an antireflective coating.

Copyright © 1999 by W.B. Saunders Company

KEY WORDS: display, image quality, glare, reflection, contrast.

RADIOGRAPHIC DISPLAYS are designed to convey the visual information in an image to an observer. To achieve this goal, light is generated or modulated in intensity within structures that may have multiple layers. Light photons have numerous opportunities for scattering when traveling through these layers to the human visual system receptors. In some cases, light scattering can improve image quality. For instance, in emissive electronic devices, multiple scattering of light within a phosphor layer produces a quasi-Lambertian angular emission distribution that makes the display brightness independent of the viewing angle. In other situations, scattering processes degrade image quality.

From the Department of Diagnostic Radiology, Henry Ford Health System, Detroit, MI, and the Nuclear Engineering and Radiological Sciences Department, University of Michigan, Ann Arbor, MI.

Supported in part by a US Army Breast Cancer research grant (DAMD17-96-1-6283).

Address reprint requests to Michael J. Flynn, PhD, Radiology Research (2F), Henry Ford Health System, 1 Ford Pl, Detroit, MI 48202.

*Copyright © 1999 by W.B. Saunders Company
0897-1889/99/1202-0002\$10.00/0*

This article addresses the deleterious effects of light scattering in display devices with respect to veiling glare and to ambient light reflections. A review of the physics and characteristics of such effects is presented, and the differences between currently available medical imaging cathode-ray tubes (CRTs) and flat panel displays (FPDs) are noted.

Veiling glare is primarily associated with the diffuse spread of light caused by multiple scattering processes in display devices. For example, in CRTs, the thick faceplate of the vacuum bulb causes multiple internal reflections that result in unwanted veiling glare. The observed result is a low-frequency degradation of image quality perceived as a reduction in contrast. This phenomenon is present in all imaging systems and has been studied in detectors,¹⁻³ in lenses,⁴ and in the human eye.^{5,6}

Ambient reflections from room lights can contaminate the primary luminous signal of the display device. The display reflectance generally is considered as a superposition of specular and diffuse components. Specular reflections are mirror-like reflections that superimpose a highly structured pattern on the desired image. The diffuse component causes a uniform added background that affects the blackness of the device and reduces contrast. The luminous intensity in the room where radiographic display devices are used varies greatly, from the relatively dark radiology reading room to bright rooms associated with areas of patient care. Thus, the degradation of image quality from ambient lighting is a function of both the ambient illumination of the display device and the relative ambient reflection for both specular and diffuse components.

Minimizing the effect of light scattering on image quality is of particular importance in radiography because of the wide signal range and low noise inherent in the recorded image. Transilluminated radiographic film provides a display with a wide range of luminance and little deleterious light scattering. However, when radiographic images are displayed using electronic devices, the quality observed often is degraded owing to light scattering that contaminates dark regions of the image. Herein we report measured results for veiling glare and ambient reflection, which can be used to estimate

the potential for high-quality display. The results for several CRT devices are compared with measurements made using radiographic film.

VEILING GLARE

Radiographic images displayed using transilluminated film do not suffer significantly from degradation by veiling glare. Modulation of the luminance occurs within a very thin emulsion layer containing darkened grains. Although extensive scattering occurs, the small thickness prevents light photons from traveling laterally over distances that would degrade image quality.

In general, CRT display devices are not able to maintain veiling glare to the low levels associated with radiographic film. In CRTs, the emissive structure is designed to direct all light rays toward the viewer. This is achieved by placing a highly reflective backing in the vacuum side of the phosphor layer. Light generated in the phosphor grains must then travel through a thick faceplate where multiple scattering events occur before the light reaches the human eye. The limited absorption of light by the phosphor layer encourages multiple scattering of photons within the faceplate. Lateral light diffusion in CRT emissive structures causes luminance spread functions with tails that extend over the entire viewable area. This diffuse component over large areas degrades the maximum contrast capabilities of the device.

In addition to the optical scattering in emissive structures, veiling glare is caused by backscattering of electrons and from light leakage through aluminum-layer nonuniformities (cracks and holes). In color tubes, the black matrix that separates the phosphor dots contributes to color purity and reduces the lateral spread of light. As a consequence, the electronic contribution to veiling glare is known to be larger than the optical component, particularly for tubes with a shadow mask design.⁷⁻⁹ In general, the optical veiling glare of color CRT devices is less than that of monochrome devices, but the contributions from backscattered electrons are greater.

In FPD devices, the thin pixelated structures used to generate the image signal produce veiling glare effects that are significant only at short ranges and are not important at long distances from bright fields. For instance, in liquid crystal displays, light diffusion (referred to as optical cross-talk) is localized mostly to adjacent pixels and is associated

primarily with resolution loss.¹⁰ FPD devices typically have thin cover plates, which limit lateral spread from multiple internal scattering.¹¹

Characterization of Veiling Glare

The degradation of contrast resulting from veiling glare can be described by measuring the luminance level in the center of a dark spot caused by a bright ring with a given radius and with small radial thickness. The relative luminance at the center as a function of the radius of the ring can be defined as the ring response function. For shift-invariant systems, the ring response function is equivalent to the one-dimensional image point-spread function expressed as the number of photons that emerge toward the viewer at a given distance from the point source. The increase in luminance in dark regions of an image is associated with light originating at points within bright regions. For a large circular bright field with a dark circular region in the center (such as in Fig 1), the central luminance can be related to the integral of the veiling glare ring response function from the radius of the dark region to the radius of the bright region (Fig 2).

Using light transport Monte Carlo simulation techniques, the ring response function of display devices can be computed by tracking individual light photons coming from a point source. The number of photons that exit the emissive structure from within a ring area and within a specified solid angle is related to the total number of photons. Using this approach, the trade-offs between display brightness and veiling glare have been investigated.^{12,13} The predictions show that reduction of the ring response function tails can be achieved by increasing faceplate glass absorption or by using absorptive black matrix between monochrome phosphor dots.^{11,14}

The veiling glare ring response function of CRTs has extended tails and can have peaks associated with the geometric dimensions of the emissive structure. A computed ring response function is shown in Fig 2. By convolving a dark spot test pattern with a ring response function typical of conventional CRTs, the resulting degradation can be illustrated. The pattern on the right side of Fig 1 depicts the expected reduction in contrast. The diffuse component is observed clearly in the image data profiles shown below the image. This increase

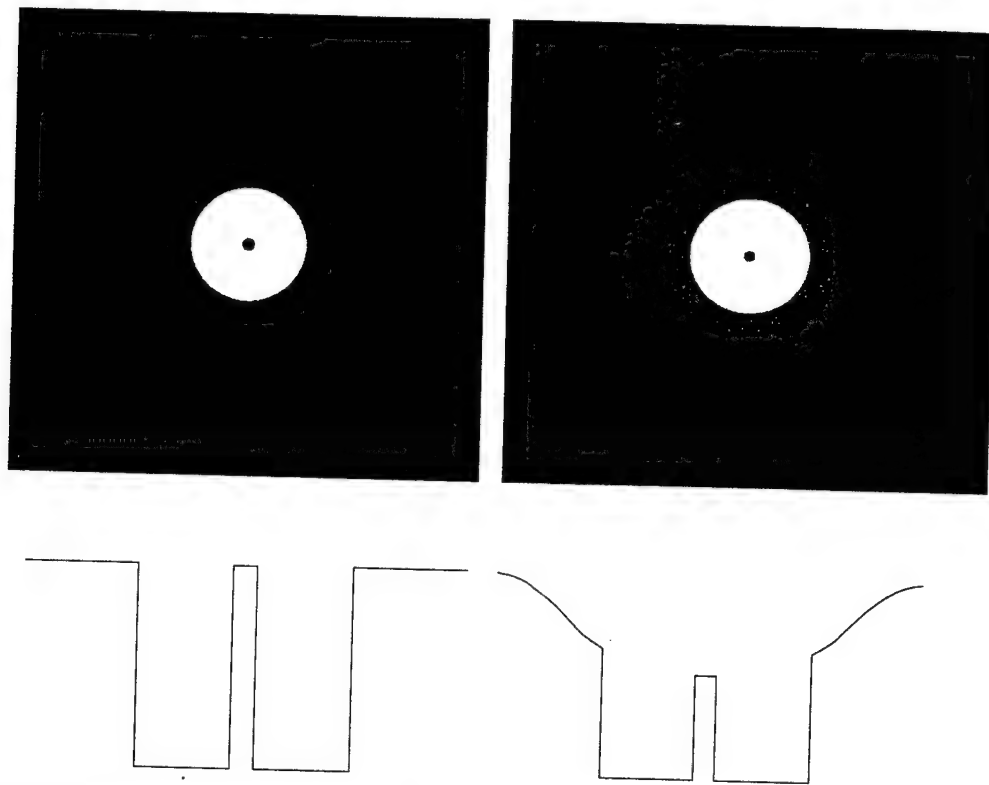


Fig 1. Effect of veiling glare on test patterns with small dark regions. The curves depict a center data row from the above images. A diffuse background component is shown that reduces the ratio of the luminance in the bright region relative to the luminance in the dark spot, ie, the glare ratio defined as L_{\max}/L_{\min} .¹⁴

of luminance in the dark regions is associated with degradation of contrast.

Measurement of Veiling Glare

To date, no published standard defines experimental techniques to measure the veiling glare charac-

teristics of display devices. Generally, the ratio of maximum luminance to minimum luminance (contrast ratio) is measured for a specific test pattern.^{8,15} Investigators from the National Institute of Standards and Technology have reported results using black squares of varying size on a white back-

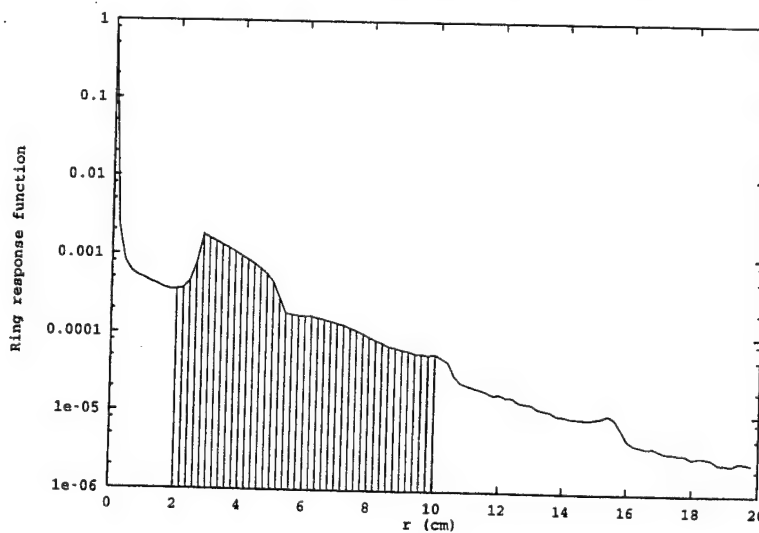


Fig 2. A typical ring response function for a monochrome CRT that has been computed using Monte Carlo simulation techniques. The integration over the ring area from 2 to 10 cm represents the contribution to the luminance of a 2-cm radius dark spot from a 10-cm bright region.

ground.¹⁶ Differences in the shape and relative size of dark and bright regions in the test pattern produce different results and prevent comparison of the veiling glare characteristics of display devices. In addition, especially for liquid crystal displays, the use of a contrast ratio can lead to confusion because often it is computed by measuring bright and dark luminance levels using uniform fields.

For experimental measurements of the veiling glare characteristics of a display device, a useful test pattern is a small black circular spot surrounded by a bright circular region. The glare ratio for this test pattern can be defined as the ratio of the luminance in the center, measured without the dark spot, to that measured with the dark spot present. However, the measured glare ratio will be different for test patterns with different radii for the dark and bright regions. If the glare ratio is measured for many different dark region radii, the ring response function can be obtained by differential analysis. Measurements with a single test pattern are more typically used to compare the veiling glare characteristics of different display devices.

Measurement of the low luminance signal in the dark region of a test pattern is difficult because light coming from the surrounding bright region can directly enter the probe. The human visual system is particularly good at viewing information in dark regions surrounded by bright fields. As such, the eye is an excellent detector, with little intrinsic veiling glare. The lack of veiling glare is in part attributable to a reduced directional sensitivity in the retina to obliquely incident light coming from

light scattered near the eye lens.^{5,6,17} Conventional camera systems with lenses have significant intrinsic veiling glare ($\sim 1\%$ to 2%), which is caused by light scattering in the optical components, particularly at lens interfaces and aperture edges.^{4,18} For camera lenses, the veiling glare often is referred to as flare.

We previously reported the performance characteristics of a luminance probe designed to measure the glare ratio of circular test patterns having very small black regions (Fig 3). A highly collimated probe with no lens is used to minimize contamination from bright surrounding regions. Using this probe, glare ratios greater than 1,000 can be measured reliably. The probe has been used to demonstrate the minimal veiling glare of transilluminated film using circular test patterns having a film density range of about 3. The results reported in this article were achieved using a probe similar in design to that used in our previous work¹⁹ but with additional collimation and a high gain detector (model SHD-033; International Light Inc, Newbury Port, MA).

AMBIENT LIGHT REFLECTIONS

Radiographic films have a coating on the emulsion layer that greatly reduces specular reflections. Because this coating is in contact with the emulsion layer, the optical characteristics of the image are not affected. The diffuse reflectance is relatively modest because the blackened grains in the emulsion layer will absorb a certain fraction of light. Although diagnostic interpretations are done in

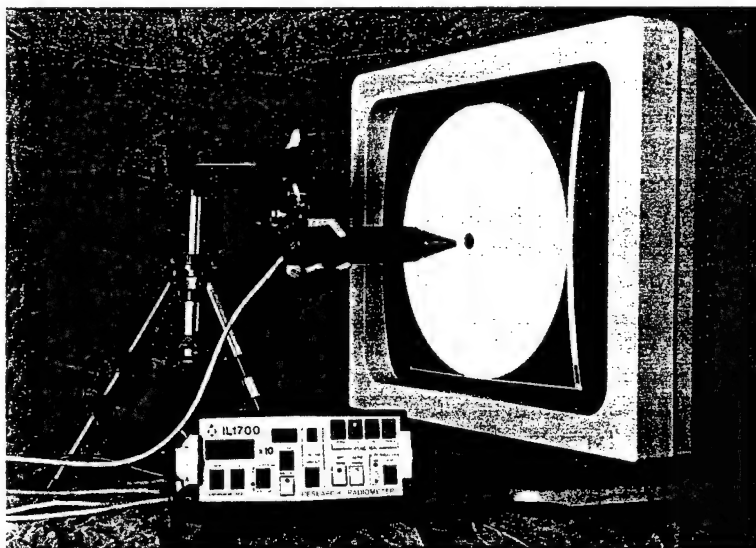


Fig 3. Photometric probe for measuring veiling glare characteristics. A highly collimated probe is used, with a photodiode detector and light filter to measure the luminance in a black spot without signal contamination from the surrounding bright region.

rooms with specially arranged dim lighting, radiographic film still can be viewed relatively well in bright rooms, as often is required in areas of patient care such as the emergency room.

Because of the nature of CRT emissive structures, a large fraction of the light that illuminates the device is reflected either at the first surface or from multiple internal scattering. A rough surface coating cannot be used because it will blur the image detail owing to the thick glass faceplate. Light that enters the faceplate and strikes the phosphor layer encounters a structure that, by design, has high diffuse reflectance. The phosphor structure consists of small grains in a binder with a reflective backing. Similar to radiographic screens, this structure is designed for good light emission with little absorption. Thus, the monochrome CRT devices used for high-resolution radiographic display typically have very poor characteristics with respect to both specular and diffuse reflection of ambient light. This has forced the use of very dark rooms for diagnostic interpretation and has severely handicapped the deployment of electronic imaging systems in patient care areas.

To dampen specular reflections, antireflective (AR) structures can be used. AR coatings typically consist of several thin film layers designed to reduce the reflectance of the front surface by increasing the light transmission into the faceplate. Normally, AR coatings also include a conductive layer that dissipates the static generated at the front surface and helps maintain a dust-free surface.^{20,21} The reflections from AR coatings can have a color shift when illuminated with a broad-spectrum light source because of the wavelength dependency of the thin film response. However, by decreasing the reflection of incident light, AR coatings may increase diffuse reflections because more light enters the faceplate. The effectiveness of AR coatings is a compromise between the specular and diffuse components of ambient light reflection.

To reduce diffuse reflectance, CRTs may use an absorptive faceplate that will attenuate light that may scatter several times in the glass. For a faceplate with a transmittance of 1/2, the diffuse reflections will be reduced by at least a factor of 1/4 because the reflected light will travel through the glass twice. Typically, more reduction is found because of the oblique directions that the reflected light may travel and because of multiple internal scattering. However, this reduction comes at the

expense of a reduction in display brightness of 1/2. In color monitors, the black matrix material between phosphor cells is of considerable benefit in absorbing incident light without reducing brightness. Thus, the design of color monitors is advantageous from the standpoint of both veiling glare and ambient reflection. However, to date, black matrix phosphor technologies have not been used with high-brightness monochrome phosphors.

Ideally, a display device will have an AR coating and a design that specifically absorbs ambient light. New flat-panel display devices offer opportunities for the absorption of ambient light that are not possible with CRTs. New active matrix liquid crystal display devices are being designed to optimize the absorption of ambient light for use in sunlit applications such as for avionic devices.²² New devices may be able to achieve better ambient light reflection performance than is currently experienced with radiographic films.

Characterization of Display Reflections

The reflectance of display devices can be characterized by separate components involving specular and diffuse light scattering. Specular reflections produce distinct virtual images at the display surface that mirror luminous objects in the room. The reflected luminance L_s can be related to the source luminance L_s by $R_s = L_s/L_s$, where R_s is the dimensionless specular reflectance coefficient. Specular reflections can severely degrade image quality in specific regions by adding interfering structured signal to the image content and by causing localized regions of contrast reduction.

Ambient illumination of the display surface also will produce diffuse reflections with no detail and similar intensity over the entire screen. Typically, light photons will strike the display surface and emerge with a broad angular distribution caused by surface roughness and multiple scattering processes. Diffuse reflections can be characterized by a coefficient defined as $R_D(\theta, \phi) = L_D(\theta)/I(\phi)$, where $L_D(\theta)$ is the diffusely reflected luminance measured at the angle θ from the surface normal, and $I(\phi)$ is the illuminance at the surface from light impinging at an angle ϕ . Because of the units associated with measures of luminance (nit) and illuminance (lux), $R_D(\theta, \phi)$ has units of 1/sr. For an ideal Lambertian reflector, $L_D(\theta)$ is independent of θ and the reflection coefficient is only a function of the illumination angle, $R_D(\phi)$. If the illumination of the surface

is from many directions, as is the case in a room, the illuminance will have differential contributions from different directions, such that

$$I = \int_0^{90} I(\phi) d\phi,$$

where $I(\phi)d\phi$ is the differential illuminance averaged over all azimuthal angles. The diffuse reflection coefficient that is specific to a particular lighting condition can be defined as

$$R_D(\theta) = L_D(\theta)/I,$$

where $R_D(\theta)$ is a weighted average of $R_D(\theta, \phi)$, which depends on the angular distribution of illumination.

Measurement of Display Reflections

Methods for measuring reflection coefficients have been the focus of recent efforts.²³⁻²⁶ Although test methods have been proposed as part of an international standard,²⁷ the defined experimental techniques have been found to be not repeatable and unreliable because of variations in instrumentation response and light source geometry.²⁸ Kelley et al²⁹ and Becker²⁵ recently suggested that for FPD devices, difficulties can arise when reflections fall in the intermediate area between specular and diffuse. They propose using the bidirectional reflection distribution function (BRDF) to fully describe the performance in any ambient lighting condition. The BRDF is a function of both source and observer directions and is equivalent to $R_D(\theta, \phi)$.

For measurement of specular reflection, a small uniform source of light can be used to create a specularly reflected image on an otherwise black display surface located in a dark room. To minimize the diffuse component, the area of the light source should be as small as possible. We have used a small spot lamp with a white luminous area of about 5 cm in diameter. Using a spot photometer, the luminance of the reflected image is related to the luminance of the light source when directly viewed. We have used a Minolta (Ramsey, NJ) LS110 spot photometer, which measures luminance in a 1/3 degree spot. Typical values for the reflection angles include 15° and 30°, at distances ranging from 50 to 100 cm. Because most displays are viewed from a direction near the surface normal, we have made measurements with the light source and the spot photometer at 15° from the central point of the display.

The diffuse reflection from display devices is measured by illuminating the display device in an off condition with a diffuse source.* Others have used various lamps at different positions in a dark room.^{27,28} Inconsistent measures result in part from variations in illumination that come from the walls, objects, and persons in the room. We have used a 40 × 40 × 40-cm box with white reflective sides and two compact fluorescent lamps located at the back corners (Fig 4). Luminance is measured in a normal direction through a hole in the back of the box with a spot photometer. Illuminance is measured with a small illuminance probe placed on the surface of the display. The measured luminance per illuminance is reported as lumens/sr/m² (ie, cd/m² or nit) per lumens/m² (ie, lux), which has units of 1/sr. This test device creates, in effect, a reproducible white room that can be taken to different locations for comparison measurements. The angular distribution of illumination from this test device is representative of that found in patient care areas.

RESULTS

In this article, we describe experimental techniques for measuring the degradation in image quality caused by light scattering in display devices. A method for measuring the veiling glare ratio using circular test patterns and a specifically designed luminance probe is presented in the section on measuring veiling glare. Practical experimental techniques to measure specular and diffuse reflection coefficients are delineated in the section on measuring display reflections. In this section, we report experimental results for a monochrome CRT (24 in, model M24L; Image Systems, Minnetonka, MN) and a color CRT (19 in, model Super-Scan Elite 751; Hitachi, Monitor Division, Westwood, MA). The results are compared with data obtained for transilluminated radiographic film using the same experimental techniques.

Measurements of veiling glare were carried out using two dark-spot test patterns having a bright 32-cm circular field with 1-cm and 2-cm central dark spots. For measuring the glare characteristics of radiographic film, the test patterns were digitally printed on film using a laser printer (Kodak Ekta-

*For devices that rely on changes in transmission to modulate the luminance of the scene (ie, transilluminated film, liquid crystal displays), measurements of diffuse reflections with fields at different luminance levels are required.

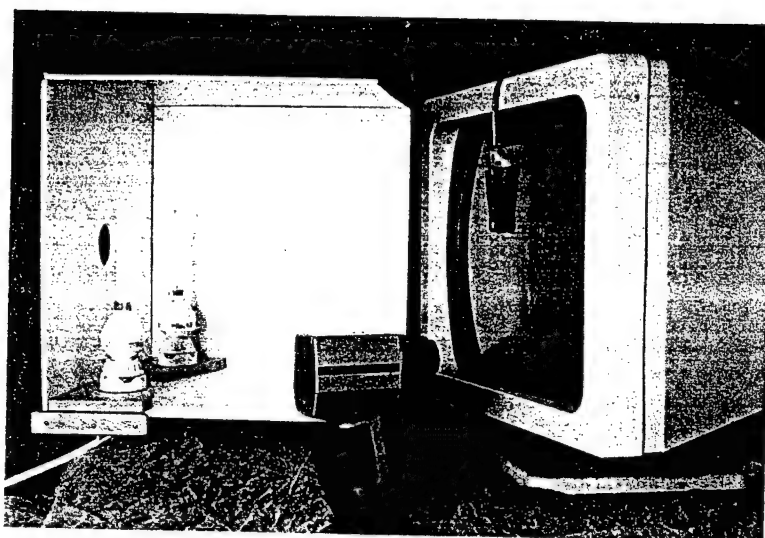


Fig 4. Test device for measuring diffuse reflection coefficients consisting of a $40 \times 40 \times 40$ -cm box with white reflective sides and two compact fluorescent lamps located at the back corners. The front side of the box has been removed for illustration purposes. Luminance is measured in a normal direction through a hole in the back of the box with a spot photometer. Illuminance is measured with a small illuminance probe placed on the surface of the display.

scan Laser Printer, model XLP; Eastman Kodak Co, Rochester, NY). The optical density in the test pattern films was 2.84 in the dark spot and 0.08 in the bright region, producing relative luminance values of 575. The same test patterns were displayed in the CRTs as $1,024 \times 1,024$ images, with the monitor contrast control adjusted to maximum. The monitor brightness control was set to the minimum level and then increased until the luminance measured for a full dark field increased relative to the value observed with the unit turned off. The brightness was then slightly reduced from this point. The monitor full-field dark luminance was recorded and used to correct subsequent measurements. All veiling glare measurements were made with the entrance of the photopic probe less than 1 mm from the surface of the display. Table 1 shows the results on veiling glare ratio for both 1-cm and 2-cm dark-spot test patterns.

As discussed previously, the diffuse reflection

Table 1. Veiling Glare Ratios for Test Patterns Having 32-cm Bright Circular Fields and Dark-Spot Diameters of 1 and 2 cm

Dark Spot Diameter (cm)	Radiographic Film	Monochrome CRT	Color CRT
1	555 ± 2	89.0 ± 0.6	25.0 ± 0.1
2	546 ± 1	125.8 ± 0.6	44.0 ± 0.1

NOTE. For film, the measured values are near those expected from the film density of the black spot, ie, a glare ratio of 575. Error estimates are based on the standard deviation of 20 consecutive measurements. The 24-in monochrome monitor (Image Series M24L) demonstrates significant glare from optical scattering. The 19-in color monitor (Hitachi SuperScan Elite 751), with even more veiling glare, is typical of monitors used on modern graphic arts workstations.

coefficient is specific to the angular distribution of illumination associated with particular measurement conditions. When using the experimental technique described in this work, the obtained result corresponds to $R_D(0) = L_D(0)/I$, with I being the total illuminance at the display surface. The illuminance probe used records incident light with a broad angular response (International Light Inc, model SCL110). Table 2 shows the diffuse and specular coefficients for all three display types.

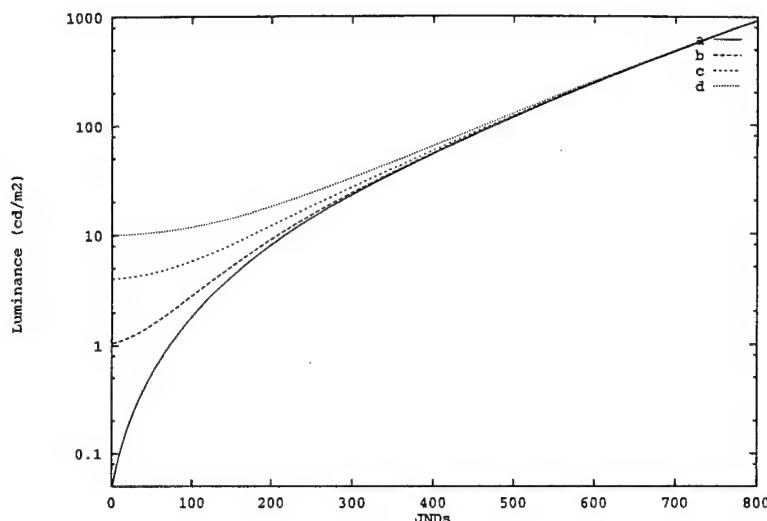
When measuring diffuse reflections from radiographic film, attention must be given to the optical density values in the image because they affect the light diffusion characteristics of the device. For instance, R_D measured for film with a typical chest radiograph was 0.026 1/sr. When using the same technique with a 1-cm dark-spot veiling glare test pattern, the result was 0.020 1/sr. The difference is associated with ambient light, which is transmitted to the view box and reflected back. This dependence of R_D with the image luminance pattern is not observed in CRTs, where measurements are performed with the display turned off.

Table 2. Specular and Diffuse Reflection Coefficients for Film and CRTs

Display	R_s	R_D (1/sr)
Radiographic film	0.011 ± 0.001	0.0264 ± 0.0002
Monochrome CRT	0.041 ± 0.001	0.0582 ± 0.0002
Color CRT	0.021 ± 0.001	0.0251 ± 0.0002

NOTE. The reflection properties of the color monitor are better because of an AR coating and the black matrix in the phosphor layer. Random errors are estimated from the standard deviation of 10 consecutive measurements.

Fig 5. (a) Standard display function curve shown as log-luminance versus image value in units of just noticeable visual differences (JNDs).^{31,32} A unit change in the JND variable causes a luminance change equal to the contrast threshold at the indicated luminance level. Curves b, c, and d depict the effect of adding a background luminance level of 1, 4, and 10 cd/m^2 . A significant reduction of contrast for small image values is indicated by the small slope of this curve for high background levels.



DISCUSSION

At high luminance, a function that maps an image value to brightness such that the logarithm of the luminance is linearly proportional to the image value will produce a uniform perception of contrast at all brightness levels. This occurs because the human vision system perceives contrast as a relative change in luminance ($\Delta L/L$) for sufficiently bright scenes. However, for many display systems, the dark regions of the scene occur at a luminance level so low that the contrast response of the human observer is poor.³⁰ To compensate for this, the relative contrast ($\Delta L/L$) at low luminance can be increased relative to that at high luminance. An industry standard display curve that maps image values to luminance can be used to obtain a uniform perception of brightness in both dark and bright regions of an image.^{31,32} This relationship is shown in Fig 5, where it can be seen that the slope of the curve relating log-luminance to image value is greater at low luminance. This standard display curve is based on psychovisual models of experiments that measure the threshold contrast of a small test pattern on a uniform background to establish the contrast for which the test pattern can just be detected. The luminance difference associated with this contrast threshold often is referred to as the just noticeable difference (JND) in luminance, and the standard display curve often is plotted in units of JNDs, which are taken to be proportional to display values.

Many systems will calibrate the display device luminance response curve such that it follows the display standard curve based on measurements

made with no ambient illumination. However, when such a system is used in a reading room, the ambient illumination will add a constant luminance to the display response owing to diffuse reflections. To illustrate the effect of diffuse reflections on image quality, we have plotted the expected curve when a background luminance of 1, 4, or 10 cd/m^2 is added to the normal display luminance (Fig 5). For the monochrome monitor tested for this work with a diffuse reflection coefficient of about 0.06 l/sr , an added luminance of 6 cd/m^2 results from an illuminance of 100 lux, which is typical of common office lighting. The significant reduction in the slope of the curves for low image values, which are at a luminance of 1 cd/m^2 for the monochrome monitor, is associated with a significant reduction in the perceived contrast. Ideally, the added luminance should not be greater than 20% of the minimum luminance of the display device. For example, a display with a luminance range of 3 to 300 cd/m^2 could be used in a room with 100-lux ambient illumination if $R_D \leq .006 \text{ l/sr}$. For film viewed in a luminance range of 20 to 2000 cd/m^2 , no significant degradation occurs if $R_D \leq .04 \text{ l/sr}$.

The image quality degradation associated with specular reflections is notably different from that associated with diffuse reflection or veiling glare. Although similar contrast reduction occurs where specular reflections contribute to display luminance, the detailed patterns of the specular reflection are more problematic. The specific pattern of a reflection may overlay complex structures in the image scene and reduce the conspicuity of diagnos-

tic features. Additionally, there is a belief that the presence of these added features in the image and the human observer's need to separate reflection artifacts from image information contribute to visual fatigue.

Veiling glare adds luminance in dark regions of an image in amounts that vary according to the spatial distribution of bright regions. This added luminance locally decreases contrast and can degrade the detection of low-contrast structures. The specific effect is different for each image. Particularly problematic are scenes such as the lateral chest view that can have very dark lung regions surrounded by a large bright field. In general, displays with a glare ratio greater than 200 when measured with a 1-cm circular dark-spot test patterns will have little contrast degradation from

veiling glare. A display with a glare ratio of less than 100 will have poor image quality for certain images.

To date, much attention has been paid to the resolution and brightness required of a display device for application in medical radiography. Herein we have described how veiling glare and ambient reflections associated with current CRT technology may seriously affect the quality of a displayed radiograph relative to the quality seen with transilluminated radiographs. Therefore, systems with very good resolution and brightness may not be suitable for diagnostic application because of these optical limitations. The serious problems relating to veiling glare and ambient reflections perhaps have not been adequately acknowledged to date.

REFERENCES

1. Zeman HD, Hughes EB, Otis JN, et al: Veiling glare of a linear multichannel Si(Li) detector. *Proc SPIE* 535:214-221, 1985
2. Swank RK: Calculation of modulation transfer functions of x-ray fluorescent screens. *Appl Optic* 12:1865-1870, 1973
3. Caruthers E: Monte Carlo studies of image spread by x-ray image intensifiers. *Proc SPIE* 535:140-147, 1985
4. Matsuda S, Nitoh T: Flare as applied to photographic lenses. *Appl Optic* 11:1850-1856, 1972
5. Beckman C, Nilsson O, Paulsson L-E: Intraocular light scattering in vision, artistic painting, and photography. *Appl Optic* 33:4749-4753, 1994
6. Spencer G, Shirley P, Zimmerman K, et al: Physically-based glare effects for digital images. *Computer Graphics Proceedings, Annual Conference Series SIGGRAPH 95*, 1995, pp 325-334
7. van Oekel JJ: Improving the contrast of CRTs under low ambient illumination with a graphite coating. *Proceedings of the Society for Information Display*, 1995, pp 427-430
8. de Vries GC: Contrast-enhancement under low ambient illumination. *Proceedings of the Society for Information Display*, 1995, pp 32-35
9. van Oekel JJ, Severens MJ, Timmermans GMH, et al: Improving contrast and color saturation of CRTs by Al_2O_3 shadow mask coating. *Proceedings of the Society for Information Display*, 1997, pp 436-439
10. Kobayashi K, Masutani Y, Nakashima K, et al: IPS-mode TFT-LCDs for aircraft applications. *Proceedings of the Society for Information Display*, 1998, pp 70-73
11. Badano A, Flynn MJ: Monte Carlo modeling of the luminance spread function in flat panel displays. *International Display Research Conference*, 1997, pp 382-385
12. Badano A, Flynn MJ, Samei E, et al: Performance of low-voltage phosphors in emissive flat panel displays for radiologic applications. *Proc SPIE* 2707:312-321, 1996
13. Badano A, Flynn MJ: Monte Carlo modeling of glare in cathode-ray tubes for medical imaging. *Proceedings of the Society for Information Display*, 1998, pp 495-498
14. Badano A, Flynn MJ: Image degradation by glare in radiologic display devices. *Proc SPIE* 3031:222-231, 1997
15. Blume H: Very-high-resolution CRT display systems. *Proceedings of the Society for Information Display*, 1992, pp 699-702
16. Boynton PA, Kelley EF: Accurate contrast-ratio measurements using a cone mask. *Proceedings of the Society for Information Display*, 1997, pp 823-826
17. Stiles WS, Crawford BH: The luminous efficiency of rays entering the eye pupil at different points. *Proc R Soc London* 122:428-450, 1937
18. Boynton PA, Kelley EF: Measuring the contrast ratio of displays. *Information Display* 11:24-27, 1996
19. Badano A, Flynn MJ: Experimental measurements of glare in cathode-ray tubes. *Proc SPIE* 3335:188-196, 1998
20. Tong HS, Prando G: Hygroscopic ion-induced antiglare/antistatic coating for CRT applications. *Proceedings of the Society for Information Display*, 1992
21. Ono Y, Ohtani Y, Hiratsuka K, et al: A new antireflective and antistatic double-layered coating for CRTs. *Proceedings of the Society for Information Display*, 1992
22. Brinkley R, Xu G, Abileah A, et al: Wide-viewing-angle AMLCD optimized for gray-scale operation. *Proceedings of the Society for Information Display*, 1998, pp 471-474
23. Lloyd CJ, Mizukami M, Boyce PR: A preliminary model of lightning-display interaction. *J Illuminating Engineering Soc* 25:59-69, 1996
24. Jones GR, Kelley EF, Germer TA: Specular and diffuse reflection measurements of electronic displays. *Proceedings of the Society for Information Display*, 1996, pp 203-206
25. Becker ME: Evaluation and characterization of display reflectance. *Displays* 19:35-54, 1998
26. Lindfors M: Accuracy and repeatability of the ISO 9241-7 test method. *Displays* 19:3-16, 1998
27. ISO: Technical report 9241-7: Ergonomic requirements for office work with visual display terminals, 1997
28. Umezumi N, Nakano Y, Sakai T, et al: Specular and diffuse

reflection measurement feasibility study of ISO 9241 part 7 method. Displays 19:17-25, 1998

29. Kelley EF, Jones GR, Germer TA: Display reflectance model based on the BRDF. Displays 19:27-34, 1998

30. Peli E, Yang J, Goldstein R, et al: Effect of luminance on suprathreshold contrast perception. J Optical Soc America A 8:1352-1359, 1991

31. ACR/NEMA Working Group XI: Greyscale display function standard, draft version 1.2. Technical report, ACR/NEMA, March 1997

32. Blume H, Hemminger BM: Image presentation in digital radiology: Perspectives on the emerging DICOM display function standard and its application. Radiographics 17:769-777, 1997

HIGH FIDELITY ELECTRONIC DISPLAY OF DIGITAL RADIOGRAPHS

Michael J. Flynn, Ph. D., Jerzy Kanicki, Ph. D.,
Aldo Badano, Ph. D., William R. Eyler, M. D.* †

Dec. 04, 1998: Manuscript submitted to *Radiographics*
Feb. 02, 1999: Accepted pending revisions by *Radiographics*
May 05, 1999: Revised manuscript returned to *Radiographics*

SUMMARY

This article summarizes the desired performance requirements for radiologic electronic display devices, and reviews current cathode-ray tube and emerging flat panel display technologies.

May 5, 1999

*MJK, AB and WRE from the Department of Diagnostic Radiology, Henry Ford Health System, Detroit, MI. JK and AB from the Center for Integrated Microsystems, University of Michigan, Ann Arbor, MI. Corresponding author: Dr. Michael J. Flynn, Radiology Research (2F), Henry Ford Health System, 1 Ford Place, Detroit, MI, 48202, phone: (313) 874-4483, fax: (313) 874-4494, email: mikef@rad.hfh.edu.

†This work was partially supported by a U.S. Army Breast Cancer research grant (DAMD17-96-1-6283).

Abstract

A fully digital radiographic system requires high fidelity electronic display devices that preserve diagnostic quality. Current cathode-ray tube (CRT) monitors do not meet desired performance criteria for displaying radiographs and have excessive size, weight and power consumption. Recent developments in flat panel display technology (in particular active-matrix liquid crystal displays, field-emission displays, and organic light emitting displays) suggest that high fidelity, light weight displays will be available in the near future. This paper defines high fidelity display requirements based on the performance limits of the human visual system. Next, a summary of the limitations of CRTs is presented. Finally, flat panel display technologies being developed to replace CRTs are described, and their potential for high display quality is reviewed.

Introduction

The display of radiographic images using electronic devices is now common within diagnostic radiology and within referring medical services. However, the quality of digital images displayed on electronic devices is typically less than the quality observed with printed films. For electronic displays to fully replace radiographic film, their diagnostic performance needs to be similar or superior to film. In this paper, we consider the limitations of the observer (the human visual system) in order to define those aspects of display quality that are important for interpreting diagnostic radiographs. Display device performance requirements for parameters such as luminance range, contrast, resolution and surface reflections are defined and minimum device requirements for radiologic applications are suggested. Display devices including cathode-ray tubes (CRTs) and flat panel technologies are then considered with respect to their potential for meeting these requirements.

Display performance

For a display device with ideal performance, both image quality and observer performance are constrained by human visual system limitations. Data from psycho-visual experiments can be used to establish the performance of a high fidelity device which can stimulate the human visual system over its full range of response. These visual performance requirements can then be used along with radiologic application requirements to specify device parameters such as luminance range, gray-scale mapping functions, contrast, resolution and display size. In this section, well-known characteristics of the human visual system are reviewed and used to define high fidelity display device performance.

Luminance Range

The neural response of photoreceptors in the eye is known to be linear at low light levels and to saturate at higher levels [1, 2]. In addition, psycho-visual experiments have been used to describe the adaptation of the human visual system to the average luminance of the scene observed [3, 4].* Using electrophysiological observations and computer simulations, Normann [5] and Baxter [6] have reported on the relationship between photoreceptor sensitivity and image processing at neural centers for visual tools involving the detection of low-contrast radiological features in non-uniform backgrounds. The sensitivity response function for the complete visual system can be approximately described by an expression of the form $P = L/(L + S)$ [7], where

*Luminance is a photometric measurement unit reflecting the brightness of a small region on a display surface. The SI unit of brightness is the nit, which is a candela per square meter (cd/m^2). 1 cd/m^2 is equal to 0.2919 foot-lambert (fL).

P is the photoreceptor response, L is the retinal luminous intensity, and S represents a constant that conforms with the state of adaptation. This relationship was first introduced as part of Hecht's photochemical theory of photoreceptor response [8], and has been confirmed experimentally by other investigators [1]. Figure 1 depicts the measured rate of neuronal signals for different adaptation states using the above general expression with illustrative numerical values.

When the observer is adapted to a particular average luminance, the change in neuronal response associated with a small change in relative luminance is a biologic contrast response, $\Delta P/(\Delta L/L)$. This biological response is maximal near the average luminance and is markedly reduced for regions in the scene with higher or lower luminance, as shown in Figure 2. In general, displaying images using a wide luminance range produces improved quality due to high physical contrast (large $\Delta L/L$ for a specific image intensity change).[†] However, the perceived contrast results from the physical contrast modified by the observer's biological response, $\Delta P = \Delta L/L \times \Delta P/(\Delta L/L)$. Thus, when an observer is focused on a specific region which contains a wide range of luminance, contrast perception is reduced in the bright and dim areas relative to the average luminance for which the eye is adapted

When focused on a position in the image, the foveal field of the eye where acuity is high is about 2 cm in diameter (500 mm viewing distance). This region will have an average luminance, \bar{L} , and may contain details with high contrast. Considering all positions in the image that the observer might inspect, the range of average luminance values in these regions should be less than 80 ($\bar{L}_{max}/\bar{L}_{min} \leq 80$) in order for the

[†]In this work, contrast is defined using the Michelson definition: $C = (L_{max} - L_{mean})/L_{mean}$ [9].

adapted visual system to maintain satisfactory biologic contrast response at each position (i.e. in excess of 35% of the maximum response). While the relation between the scene in the surrounding field and adaptation for a point of focus is complex[10], the overall size of the field which contributes to adaptation is probably about 100 mm (500 mm viewing distance) in diameter.

To support contrast values up to 1.0 within the foveal region, a device should be capable of displaying high spatial frequency with a modulation of $\pm 50\%$ at positions in the image where the average luminance is either \bar{L}_{max} or \bar{L}_{min} . Thus the full luminance range for individual pixels of the device must be greater than 240 ($L_{max}/L_{min} \leq 240$). For transilluminated films, this corresponds to an optical film density range from .30 to 2.20 for the average values within foveal regions and an optical film density range from 0 to 2.5 for all pixels. This is consistent with the common practice of interpreting regions above a density of 2.2 with the aid of a "bright light". Note however, that the base optical density of film, 0.15, does limit the negative modulation of contrast at low luminance.

Gray-Scale and Contrast

The physical contrast required to detect a test pattern having a sinusoidal variation in luminance over a uniform background can be described by a visual contrast sensitivity function that depends on luminance and spatial frequency as well as other parameters of secondary influence [11]. In psychophysics, sensitivity is related to detection and usually defined as the reciprocal of the contrast threshold. At a spatial frequency of 1 cycle per mm where the observer has good response, the contrast threshold is nearly

constant at high luminance and is higher below 10 cd/m^2 (see Figure 3) [12].

When medical images are displayed, the image values are modified by display processing to produce presentation values (P-Values) which are converted to digital driving levels (DDL) to establish the luminance for each pixel. The display processing may involve window and level adjustment or more complex processing as is often done with digital radiographs. At high luminance where the threshold contrast ($\Delta L/L$) is constant, a gray-scale map for which $\log(\text{luminance})$ is proportional to the P-Values will produce uniform contrast. However, for many display systems, the dim regions occur at a luminance where the contrast threshold is poor [13]. A gray-scale map can be defined such that each increment in P-Value causes a just noticeable difference increment (JND) in luminance [14, 15]. This relationship is shown in Figure 4. Devices with a maximum luminance of 1200 cd/m^2 and a minimum luminance of 5 cd/m^2 are associated with 680 JNDs. For such a device, 680 gray levels or more with the correct luminance value will produce optimal image quality. Systems with fewer gray levels may produce noticeable artifacts appearing as contour lines. If the same image information is mapped to a less bright display device, the number of available JNDs decreases (see Table 1) and the image appears with reduced perceived contrast.

Resolution

The visual contrast sensitivity is a strong function of spatial frequency. For typical viewing distances, the response is best at a frequency of about 0.5 to 1.0 cycles per mm [16]. Although radiographic film typically is associated with a pixel array of 4000×5000 for $35 \times 43 \text{ cm}$ size, a display device with a maximum spatial frequency

of 3 cycles per mm [†] will present all the information that a human observer can perceive. This can be provided, even in a diagonal direction, with a pixel size of 120 μ m. Interestingly, sensitivity is reduced at low frequency causing radiologists to back away from an image to observe large features.

Increasingly, digital radiographs are being recorded successfully on regions smaller than the conventional 35 \times 43 cm size. A display size of 30 \times 36 cm corresponds to a 2500 \times 3000 array of 120 μ m pixels. This display size, combined with a regional image zoom function will provide a high fidelity workstation.

Ambient Light Reflections

The luminous intensity and the spatial distribution of light sources in rooms where electronic devices are utilized to display radiographic images can vary significantly. The observed image quality is always affected by the scattering of ambient light in the direction of the viewer. With radiographic film, these reflections are highly dampened and diffused due to a thin emulsive layer with absorbent dark grains coated on the front surface. High fidelity electronic displays should have diffuse angular emission while minimizing ambient light reflections.

When using electronic display devices, the display reflectance can be generally described as a superposition of specular and diffuse components. The diffuse component adds a uniform background luminance that reduces substantially the observed contrast in dim regions. In general, diffuse ambient reflections should contribute a luminance that is no larger than 20% of L_{min} which is 10% of \bar{L}_{min} . Diffuse re-

[†]Display resolution is defined as the maximum spatial frequency of the device. This is equal to $0.5/P$ where P is the pixel size.

flectance can be dampened with absorptive faceplates and black matrix designs. In a room producing an illuminance of 40 lux (as may be found in diagnostic reading rooms within a radiology department), a display device having 0.025 cd/m²/lux diffuse reflection coefficient will noticeably decrease the contrast only in regions with a luminance less than 5 cd/m². Typical values for the diffuse reflection coefficient of radiographic film are 0.02 to 0.03 cd/m²/lux. Monochrome medical imaging CRTs can have coefficients as low as 0.018 cd/m²/lux and advanced AMLCD designs can have coefficients below 0.01 cd/m²/lux. Display devices intended for use in areas of high illumination (100 to 300 lux in patient care areas) need very low diffuse reflection coefficients or high L_{min} to achieve high fidelity (.01 to .033 for L_{min} of 5 cd/m²).

The image quality degradation introduced by the specular component is associated with the overlay of structured luminous patterns onto the radiologic image that affects the detection of diagnostic features. Moreover, the addition of reflected patterns can cause visual fatigue. To reduce specular reflections, anti-reflective (AR) coatings and rough surfaces can be employed. Most medical display devices now have advanced AR coatings which also reduce static charge buildup on the display surface. These coatings should have a specular reflection coefficient which keeps high contrast from illuminated objects below the contrast threshold (Table 2).

Display Specifications

The foundations of the above discussion rely on simple models of perception of detail by the human visual system. When considering the complex nature of the visual system and the perception processes, limitations of the presented approach arise. For

instance, when subtle details are displayed in radiographic images, structured luminance levels outside the foveal field are likely to impact the observer performance. Recent research efforts utilizing complex backgrounds suggest that human performance is markedly degraded by the presence of surrounding patterns [17-19]. In spite of this, the above discussion results in a useful guide for defining device requirements for radiologic displays.

In Table 2, the image quality specifications for three radiographic display qualities are summarized. Film quality display is defined as one having all the attributes of transilluminated medical radiography film. A high fidelity display is one that has all of the image quality that can be perceived by the human visual system. It is expected that magnification, and contrast and brightness adjustments are done using computer software. We have additionally defined a good quality device suitable for certain clinical functions. This quality is typical of the specialized CRTs now used in medicine.

Cathode-ray tubes

To date, CRTs are the only choice for an electronic display device in the radiology practice. Improved designs have only recently allowed higher brightness, increased resolution and better contrast. In this Section, a review of CRT technology is presented, focusing on design aspects that affect display quality.

Design Characteristics

In a CRT, electrons are accelerated within the large vacuum bulb with a high voltage of up to 30 kV. The beam scans the plate in a raster fashion, exciting the cathodoluminescent phosphor with a small beam spot (see Figure 5). To reduce mechanical stress, thick glass is used for the funnel and plate. For 74 cm diagonal bulbs with relatively flat faceplate, 13.7 mm thick glass is normally used.

Typical CRT emissive structures consist of a cathodoluminescent material (phosphor) deposited onto a glass faceplate panel as a powder layer. In color tubes, a light absorbent, carbon based black matrix separates the RGB phosphor dots for color purity. A sub-micron reflective layer of Al is overlaid on top of the phosphor to conduct the incoming electron current and maximize light output towards the viewer. For that purpose, a filming material is used to assure a smooth, continuous and highly reflective film.

Figure 6 shows a scanning electron microscope image of the emissive structure of a monochrome CRT, where multiple layers of phosphor grains can be observed under the thin Al coating. The glass faceplate can absorb up to 70% of the direct light. The increased absorption that occurs for light scattered within the faceplate reduces

light diffusion, thus improving contrast. In addition, glass faceplates may have a rough surface on the vacuum side to reduce specular reflections. A photograph of the interior surface of a CRT faceplate sample after the Al and phosphor layers were removed is shown in Figure 7.

To obtain adequate brightness, a high-current beam is deflected, while maintaining a small focal spot that is related to the display resolution. The thick faceplate causes image quality degradation by glare, and contributes to the weight of the device.

Veiling Glare

Glare is the diffuse spreading of light that results from multiple scattering processes in emissive display devices resulting in low frequency degradation of image quality (perceived as contrast reduction). This phenomenon is present in all imaging systems and has been studied for detectors [20-24] and for the human eye [25-28].

Light rays generated in the phosphor grains must undergo multiple scattering events before escaping the emissive structure and eventually being detected by the observer. Light diffusion in the emissive structure multiple layers causes luminance spread functions with tails that extend up to a distance of 20 cm. When displaying images with wide luminance range, this diffuse component over large areas degrades the maximum contrast capabilities of the device.

Recently, efforts to model glare in emissive displays have been conducted using a light transport Monte Carlo simulation code [29-32]. Figure 8 shows the simulated luminance spread functions for a 16 mm thick faceplate with and without black matrix (BM). The plots illustrate the reduction of the tails that can be achieved by increasing

faceplate glass absorption or by using BM. Other solutions that have recently been implemented in commercial devices involve the use of pigmented or filtered phosphors.

In Figure 9, the effect of glare degradation has been simulated. The circular test pattern used to measure veiling glare characteristics in electronic devices has been convolved with a point-spread function typical of conventional CRTs. The pattern on the right depicts the expected reduction in contrast. The diffuse component is clearly observed in the image data profiles shown below.

Another source of image quality degradation in CRTs comes from light leakage through Al layer non-uniformities (cracks, holes). Particularly for color tubes, electron backscattering in the emissive structure and in components such as aperture grilles and shadow masks has been identified as additional source of veiling glare, responsible for reduction in contrast and poor color saturation [33-35].

It is useful to define the veiling glare ratio as the luminance in a full bright field to the luminance in a central dark spot of a given diameter. However, the quantitative relationship between this ratio and image quality degradation for radiographics images is not well understood. We estimate that good performance display devices require glare ratios greater than 150 for a black spot diameter of 1 cm and that high fidelity display devices should have a glare ratio near 400.

Phosphors

Cathodoluminescent phosphors convert energy deposited by energetic electrons to light (see Figure 10). Electrons penetrate a cover layer and travel into individual phosphor grains. Light then scatters within the emissive structure until escaping from

the display surface. The total luminous efficiency is computed as a linear combination of efficiencies and a photopic correction K_λ : $\epsilon = K_\lambda \epsilon_e \epsilon_p \epsilon_g$, where ϵ_e is the energy deposition efficiency, ϵ_p is the energy quantum efficiency, and ϵ_g is the escape efficiency. For typical devices, ϵ is 20.8 lm/W for P104 phosphors and 13.5 lm/W for P45. The improved efficiency of P104 results from a mixture of three different phosphors grains. However, this significantly increases the granularity of regions with nominally uniform brightness as compared with devices using the P45 phosphor.

Total display brightness is a function of the electron beam power (p_l , W), the display area (a_l , m²), and the luminous efficiency (ϵ , lm/W),

$$L = \frac{\epsilon p_l}{\pi a_l}.$$

For example, a CRT with a display area of 0.3×0.4 m, a 1 mA electron beam accelerated to 20,000 V (20 W), and a phosphor emissive layer with an efficiency of 10 lm/W will have a display brightness of 530 cd/m². To achieve the same display brightness, a system with a P45 phosphor thus requires an increased beam current relative to a system with a P104 phosphor. An increase in beam spot size is associated with this increase in beam current unless improved electron focusing optics are employed. However, the relatively high granularity of P104 phosphors along with their more limited lifetime have made P45 the preferred phosphor material for medical CRT systems.

Current models of eye-brain function indicate that humans depend on display brightness for interpreting contrast and detail in a scene. Color is evaluated from separate eye receptors and interpreted as a low resolution difference signal (R-G and Y-B). It is commonly believed that inspection of detailed scenes as found in medical

radiography is best done with a display having a broad light spectrum perceived as white and various shades of gray. Figure 11 shows highly magnified recordings of a uniform gray region (5 mm in diameter) from three CRT devices depicting differences in color formation and noise characteristics.

Active-Matrix Liquid Crystal Displays

Recent improvements in size, contrast ratio, and viewing angle have established active-matrix liquid crystal displays (AMLCD[§]) as practical devices for computer workstations and candidates for radiologic applications. In this section, the fundamentals of such devices are presented, and current engineering challenges are outlined.

Liquid Crystal Displays

When the molecule orientation within a liquid crystal (LC) is altered by the application of an electric field, the optical characteristics of the LC change. This electro-optical effect is used in liquid crystal displays (LCD) to modulate light transmission. Light is emitted from the back-light and directed to the front through the LC cell. The transmission is associated with the state of polarization of the light as it passes through the polarizer films and LC layer. In an AMLCD, the switch between ON and OFF states is controlled by a thin-film transistor (TFT) deposited onto the glass substrate (see Figure 12).

As shown in Figure 13, multiple layers are needed to effectively modulate display luminance. Overall transmission is poor (6-8%) for full color TFT-LCDs, and up to 24% for monochrome designs, thus requiring high efficiency back-lights. Full ON and OFF states ("black" and "white") have typically good angle of view. Yet, for intermediate gray levels the emission distribution is severely affected due to the optical anisotropy of the LC cell. Other problems include gate signal distortion for large area displays (described in next section), lifetime, and temperature sensitiv-

[§]AMLCD is an industry term for active-matrix liquid crystal display.

ity. Amorphous Si:H TFT-LCDs are now larger with higher resolution and improved gray-scale. Large color AMLCDs up to 41 cm in diagonal having QSXGA resolution (2560×2048), and brightness up to 250 cd/m^2 have been developed [36].

AMLCD Technological Trend

To use AMLCD in medical applications, the viewing angle, brightness, contrast ratio, and number of gray levels must be improved. Since light transmitted through the LC cell can follow paths with different lengths and directions, the overall transmission depends on its emission angle. A more uniform angular distribution of light emission can be achieved if molecular alignment is varied, in a controlled manner, in sub-regions ("domains") within individual pixels [37, 38]. Figure 14 illustrates typical improvements in viewing angle characteristics for a multi-domain design. Other solutions that have been implemented are: in-plane switching [39, 40], and optically negative birefringent compensation plates [41, 42].

Transmitted light intensity is limited by polarizers, color filters, and other layers, as well as by the fraction of transparent pixel area ("aperture ratio"). One method to improve aperture ratio is to reduce the indium tin oxide (ITO) pixel electrode to bus line separation. Figure 16 and 15 show a TFT design with overlap between ITO and bus lines [43]. As the gate signal reaches the other end of the gate line conducting path, it suffers a time constant of about $\tau = RC$. This delay limits display size and resolution. For large area high resolution displays, Cu or Al metalization must be used [44].

By improving the polarizers, reducing the dispersion of pigments in color filters,

and by adding a black matrix layer, current twisted-nematic mode LCDs have realized high pixel contrast ratio of 100, viewed from normal incidence. For low power consumption, improvements in transmission, efficiency of the back-light, and driving circuit power requirements have also been demonstrated. These devices can effectively absorb ambient light and reduce reflections, as has been demonstrated for military applications [45].

Thin Emissive Technologies

Among the developing flat panel technologies, field emission displays (FEDs) and electroluminescent devices have confirmed auspicious attributes. In this section, a discussion of the current state-of-the-art is given, and notable aspects of these technologies are summarized.

Field Emission Display Technology

FEDs are similar to CRTs in that electrons are emitted from a cathode and accelerated towards the phosphor through a vacuum cell. Instead of using thermionic emission, electrons are emitted by a cold pixel electron source that typically consists of a large array of low work function emitter micro-tips. Electrons are accelerated through a vacuum cell to impinge on a cathodoluminescent phosphor.

A schematic cross-section of a typical FED is depicted in Figure 17. Instead of using a diode arrangement with a small gap between the emitter and the phosphor screen, a focus electrode can be incorporated to decrease beam spot size and increase resolution [46]. While most FEDs use metallic micro-tips, amorphous diamond has

shown good current-voltage characteristic, however, the emission mechanism is not well understood.

Most FED designs must be evacuated to low pressures (10^{-7} torr) to prevent contamination and deterioration of the electron emitters. Large display sizes thus need spacers to prevent bending of the faceplate. In low voltage designs, small spherical spacers can be used. For high voltage operation with large gaps, high aspect ratio spacers are being developed [47].

FED faceplates usually consists of a thin glass panel, a conductive layer, and a cathodoluminescent phosphor (e.g., $Y_2O_3:Eu$, $SrGaS_4:Eu$, $ZnS:Cu,Al$, $Gd_2O_2S:Tb$). When compared to thick emissive structures typical of CRTs, thin faceplates are capable of low veiling glare due to more frequent light absorption by the phosphor layer [31]. For low voltage approaches, transparent conductive oxides (e.g., ITO) are used instead of Al. In general, phosphor efficiency is greater at high voltages. Devices with high voltage designs will have large spacers and focused electron beams.

Pixel brightness variations due to electron emission non-uniformities and low reliability of the cathode have been reported for prototype designs. Recently, active elements such as metal-oxide semiconductor field effect transistor (MOSFET) have been employed to control and stabilize the emission current of field emission arrays [48]. Low voltage phosphors consume less power but are less efficient and saturate rapidly due to high current density (~ 0.1 mA/cm²), making high voltage designs look more promising. Devices with long lifetime and low driver cost are challenged by an increase in flash-over risk, more stringent surface de-gasification requirements, wider vacuum gaps and spacer uniformity.

FED advantages include wide temperature and humidity range, wide viewing angle, Lambertian emission (CRT-like), and potential for high brightness and contrast. Numerous companies have announced FED products for 1999, but are all interested in color rather than monochrome (black and white) displays.

Electroluminescent Devices

Among display technologies, electroluminescence represents an all solid state approach that provides the most direct conversion of electrical energy into light. Their efficiency and performance characteristics depend strongly on the materials and fabrication processes used. EL devices use a phosphor under the influence of an electric field to generate light.

As shown in Figure 18, thin film electroluminescent devices are made up of a stack of conductors and dielectrics deposited onto a substrate [49]. One attractive feature of thin film inorganic EL is a very steep luminance versus voltage slope above threshold, as seen in Figure 19. This, along with a fast phosphor time response, allows for direct addressing using thin film transistor arrays.

Recently, good light emission, fast response and extended lifetime have been reported for amorphous and crystalline organic thin film stacked diodes deposited on glass and flexible substrates [50-53]. With vertically stacked pixel architecture, these devices allow for color tuning [54, 55]. Different organic materials have been used, providing a wide range of emission spectra with typical efficiencies up to 15 lm/W, although white emission from single organic layers has not been reported [56-58]. Using transparent organic layers, devices with high transmission in the visible spectral

region have been developed [59]. Organic light-emitting diodes (OLEDs) made with organic semiconductors with the processability of conventional polymers are currently being investigated [60, 61].

Improvements are still needed in the chemical structure of the organic thin films, organic-metallic contacts, organic-organic layers interface, and in the understanding of non-radiative recombination losses and electrical degradation. In early stage of development, OLEDs present reliability issues such as electro-chemical instabilities with formation of radical species, contact degradation, encapsulation (needed due to air and humidity sensitivity), and low thermal tolerance [50, 62, 53, 63].

To obtain good gray-scale in large sizes, an active-matrix array that delivers controlled current levels to the pixel OLED is needed. This is unique since AMLCD array technologies have been required to deliver a control voltage to control light transmission. Pixel designs for OLED displays thus require more than 1 TFT per pixel [64].

Summary

Successful integration of digital radiography in medicine will require high fidelity electronic displays. Current CRT systems do not meet the desired performance and have excessive volume, weight and power consumption. Recent developments in flat panel display technology suggest that high fidelity, light weight displays will be available in the near future. Large size AMLCD devices have been demonstrated. High brightness can be easily achieved with bright back illumination. Further developments in optical design for monochrome displays should provide high fidelity and improve the angular dependencies of the gray-scale. FED devices have attractive emission distribution and potential for low veiling glare. This technology needs to be extended to a large area and problems with cathode aging and non-uniformity have to be contemplated. OLED displays represent a simple and potentially inexpensive display technology with the ability to achieve high image quality. However, extensive research and development is required to achieve suited large area manufacturing methods.

Acknowledgments

The authors wish to acknowledge Ed Muka, MS, of the Mallinckrodt Institute of Radiology for discussions on CRT quality and glare. The assistance of Wayne Pitchford of Henry Ford Health Systems in obtaining SEM images of CRT phosphors is greatly appreciated.

References

- [1] Baylor DA, Fuortes MGF. Electrical responses of single cones in the retina of the turtle. *Journal of Physiology* 1970; 207:77-92.
- [2] Norman RA, Werblin FS. Control of retinal sensitivity: light and dark adaptation of vertebrate rods and cones. *Journal of General Physiology* 1974; 63:37-61.
- [3] Hecht S, Hsia Y. Dark adaptation following light adaptation to red and white lights. *Journal of the Optical Society of America* 1945; 35:261-267.
- [4] Norman RA, Perlman I. The effects of background illumination on the photoreponses of red and green cones. *Journal of General Physiology* 1979; 286:491-507.
- [5] Normann RA, Baxter BS, Ravindra H, et al. Photoreceptor contributions to contrast sensitivity: Applications in radiological diagnosis. *IEEE Transactions on Systems Man and Cybernetics* 1983; SMC-13:944-953.
- [6] Baxter B, Ravindra H, Normann RA. Changes in lesion detectability caused by light adaptation in retinal photoreceptors. *Investigative Radiology* 1982; 17:394-401.
- [7] Glantz RM. Visual adaptation: a case of nonlinear summation. *Vision Research* 1972; 12:103-109.
- [8] Hecht S, Hsia Y. Relation between visual acuity and illumination. *Journal of General Physiology* 1928; 11:255-281.
- [9] Michelson AA. *Studies in Optics*. The University of Chicago Press, 1962.

- [10] Makous WL. Fourier models and the loci of adaptation. *Journal of the Optical Society of America A* 1997; 14:2323–2345.
- [11] Kelly DH. Visual contrast sensitivity. *Optica Acta* 1997; 24:107–129.
- [12] Barten PGJ. Physical model for the contrast sensitivity of the human eye. *Proceedings of the SPIE* 1992; 1666:57–72.
- [13] Peli E, Yang J, Goldstein R, et al. Effect of luminance on suprathreshold contrast perception. *Journal of the Optical Society of America A* 1991; 8:1352–1359.
- [14] Digital Imaging and Communications in Medicine (DICOM), Part 3.14 (proposed), Grayscale Standard Display Function. Tech. rep., National Electrical Manufacturers Assoc., 1998.
- [15] Blume H, Hemminger BM. Image presentation in digital radiology: perspectives on the emerging DICOM display function standard and its application. *Radiographics* 1997; 17:769–777.
- [16] Owsley C, Sekuler R, Siemsen D. Contrast sensitivity throughout adulthood. *Vision Research* 1983; 23:689–699.
- [17] Burgess AE, Li X, Abbey CK. Visual signal detectability with two noise components: anomalous masking effects. *Journal of the Optical Society of America A* 1997; 14:2420.

- [18] Eckstein MP, Ahumada AJ, Watson AB. Visual signal detection in structured backgrounds. II. Effects of contrast gain control, background variations, and white noise. *Journal of the Optical Society of America A* 1997; 14:2406–2421.
- [19] Snowden RJ, Hammett ST. The effects of surround contrast on contrast thresholds, perceived contrast and contrast discrimination. *Vision Research* 1998; 38:1935–1945.
- [20] Seibert JA, Nalcioglu O, Roeck W. Characterization of the veiling glare PSF in X-ray image intensified fluoroscopy. *Medical Physics* 1984; 11:172–179.
- [21] Bromberg N, Bickford J. Veiling glare in the imaging chain. *Proceedings of the SPIE* 1984; 454:387–391.
- [22] Swank RK. Calculation of modulation transfer functions of X-ray fluorescent screens. *Applied Optics* 1973; 12:1865–1870.
- [23] Caruthers E. Monte Carlo studies of image spread by X-ray image intensifiers. *Proceedings of the SPIE* 1985; 535:140–147.
- [24] Zeman HD, Hughes EB, Otis JN, et al. Veiling glare of a linear multichannel Si(Li) detector. *Proceedings of the SPIE* 1985; 535:214–221.
- [25] Paulsson LE, Sjostrand J. Contrast sensitivity in the presence of a glare light. *Investigative Ophthalmology* 1980; 19:401–406.
- [26] Stiles WS. The effect of glare on the brightness difference threshold. *Proceedings of the Royal Society of London* 1929; B104:322–351.

- [27] Beckman C, Nilsson O, Paulsson LE. Intraocular light scattering in vision, artistic painting, and photography. *Applied Optics* 1994; 33:4749-4753.
- [28] Spencer G, Shirley P, Zimmerman K, et al. Physically-based glare effects for digital images. *Computer Graphics Proceedings Annual Conference Series SIGGRAPH 95* 1995; 325-334.
- [29] Badano A, Flynn MJ, Samei E, et al. Performance of low-voltage phosphors in emissive flat panel displays for radiologic applications. *Proceedings of the SPIE* 1996; 2707:312-321.
- [30] Badano A, Flynn MJ. Image degradation by glare in radiologic display devices. *Proceedings of the SPIE* 1997; 3031:222-231.
- [31] Badano A, Flynn MJ. Monte Carlo modeling of the luminance spread function in flat panel displays. *International Display Research Conference* 1997; 382-385.
- [32] Badano A, Flynn MJ. Monte Carlo modeling of glare in cathode-ray tubes for medical imaging. *Proceedings of the Society for Information Display* 1998; 495-498.
- [33] van Oekel JJ. Improving the contrast of CRTs under low ambient illumination with a graphite coating. *Proceedings of the Society for Information Display* 1995; 427-430.
- [34] de Vries GC. Contrast-enhancement under low ambient illumination. *Proceedings of the Society for Information Display* 1995; 32-35.

- [35] van Oekel JJ, Severens MJ, Timmermans GMH, et al. Improving contrast and color saturation of CRTs by Al_2O_3 shadow mask coating. Proceedings of the Society for Information Display 1997; 436-439.
- [36] Schleupen K, Alt P, Andry P, et al. High-information-content color 16.3"-desktop-AMLCD with 15.7 million a-Si:H TFTs. International Display Research Conference 1998; 187-190.
- [37] Nam MS, Wu JW, Choi YJ, et al. Wide-viewing-angle TFT-LCD with photo-aligned four-domain TN mode. Proceedings of the Society for Information Display 1997; 933-936.
- [38] Chen J, Bos PJ, Bryant DR, et al. Four-domain TN-LCD fabricated by reverse rubbing or double evaporation. Proceedings of the Society for Information Display 1995; 868-868.
- [39] Masutani Y, Tahata S, Hayashi M, et al. Novel TFT-array structure for LCD monitors with in-plane switching mode. Proceedings of the Society for Information Display 1997; 15-18.
- [40] Wakemoto H, Asada S, Kato N, et al. An advanced in-plane switching mode TFT-LCD. Proceedings of the Society for Information Display 1997; 929-932.
- [41] Hoke CD, Mori H, Bos PJ. An ultra-wide-viewing angle STN-LCD with a negative-birefringence compensation film. International Display Research Conference 1997; 21-24.

- [42] Mori H, Bos PJ. Application of a negative birefringence film to various LCD modes. International Display Research Conference 1997; M88-M97.
- [43] Lan JH, Kanicki J. Planarization technology of a-Si:H TFTs for AM-LCDs. Proceedings of the SPIE 1998; 3421:170-182.
- [44] Kim JH, Kanicki J, den Boer W. Aluminum gate metallization for AMLCDs. Materials Research Society 1997; 471:111-116.
- [45] Brinkley R, Xu G, Abileah A, et al. Wide-viewing-angle AMLCD optimized for gray-scale operation. Proceedings of the Society for Information Display 1998; 471-474.
- [46] Tang CM, Swyden TA. Beam collimation from field-emitter arrays with linear planar lenses. Proceedings of the Society for Information Display 1997; 115-118.
- [47] Browning J, Watkins C, Alwan J, et al. Scaling of FED technology. International Display Research Conference 1997; F-42.
- [48] Yokoo K, Arai M, Kawakami M, et al. Emission characteristics of JFET-based field emitter arrays. 1997 55th Annual Device Research Conference Digest. IEEE Electron Devices Society, 1997; 152-153.
- [49] Tang CW, VanSlyke SA. Organic electroluminescent diodes. Applied Physics Letters 1987; 51:913-915.
- [50] Sheats JR, Antoniadis H, Hueschen M, et al. Organic electroluminescent devices. Science 1996; 273:884-8.

- [51] Shen Z, Burrows PE, Bulovic V, et al. Three-color, tunable, organic light-emitting devices. *Science* 1997; 276:2009–2011.
- [52] Takada N, Tsutsui T, Saito S. Strongly directed emission from controlled-spontaneous- emission electroluminescent diodes with europium complex as an emitter. *Japanese Journal of Applied Physics* 1994; 33:L863–6.
- [53] Wakimoto T, Yonemoto Y, Funaki J, et al. Stability characteristics of quinacridone and coumarin molecules as guest dopants in the organic LEDs. *Synthetic Metals* 1997; 91:15–19.
- [54] Burrows PE, Shen Z, Forrest SR. Saturated full color stacked organic light emitting devices. *International Display Research Conference* 1997; 318–321.
- [55] Sheats JR. Stacked organic light-emitting diodes in full color. *Science* 1997; 277:191–2.
- [56] Chen LC, Nguyen TP, Wang X, et al. Multilayer light-emitting diodes using poly(p-phenylene vinylene) copolymer. *Synthetic Metals* 1998; 94:239–243.
- [57] Hebner TR, Sturm JC. Local tuning of organic light-emitting diode color by dye droplet application. *Applied Physics Letters* 1998; 73:1775–1777.
- [58] Niko A, Tasch S, Meghdadi F, et al. White light and RGB-electroluminescence by light-color-conversion. *Opt Materials* 1998; 9:188–191.
- [59] Bulovic V, Gu G, Burrows PE, et al. Transparent light emitting devices. *Nature* 1996; 380.

- [60] Moerner WE. Polymer luminescence: those blinking single molecules. *Science* 1997; 277:1059-1060.
- [61] He Y, Gong S, Hattori R, et al. High performance organic polymer light-emitting heterostructures. *Applied Physics Letters* 1999; 74.
- [62] Bernsten A, Croonen Y, Liedenbaum C, et al. Stability of polymer LEDs. *Opt Materials* 1998; 9:125-133.
- [63] Sheats JR, Roitman DB. Failure modes in polymer-based light-emitting diodes. *Synthetic Metals* 1998; 95:85-79.
- [64] Stewart M, Howell RS, Pires L, et al. Polysilicon VGA active matrix OLED displays - Technology and performance. *Interntl Electron Devices Meeting* 1998; 871-874.
- [65] Sezan MI, Yip KL, Daly SJ. Uniform perceptual quantization: applications to digital radiology. *IEEE Transactions on Systems Man and Cybernetics* 1987; SMC-17:622-634.
- [66] Bos P, Werner K. Viewing-angle improvements for LCDs. *Information Display* 1997; 13:26-30.
- [67] Sturm JC, Wu CC. Integrated organic light emitting diode structures using doped polymers. *International Display Research Conference* 1997; F11-F18.
- [68] Yoshimi M. Current topics in amorphous materials: Physics and Technology. *Elsevier Science*, 1993; 415-420.

List of Figures

- 1 Stimulus response relationship and light adaptation. The profile of the response function was approximated using an expression of the form $P = L/(L + S)$ [6], where P is the photoreceptor response, L is the retinal intensity, and S is a parameter that represents the state of adaptation. Same incremental changes in stimulus cause different response according to the adaptation state. 36
- 2 Biologic contrast response of the human visual system. The curve was obtained by differentiating the photoreceptor response. The perception of contrast deteriorates rapidly as the intensity of the stimulus is increased or decreased with respect to the optimum response coordinate. 37
- 3 For a particular spatial frequency in the signal, the contrast threshold of the human visual system can be plotted as a function of luminance. While constant at higher luminance values, the threshold deteriorates at low luminance, which is known as the Weber-Fechner law [65]. . . 38

4	Standard display function curve shown as luminance versus display pixel value (PV) [14, 15]. A unit change in PV causes a luminance change equal to the contrast threshold at the indicated luminance level. The upper curve depicts the effect of diffuse ambient light reflection for a display device having a $0.01 \text{ cd/m}^2/\text{lux}$ diffuse reflection coefficient in a room producing 100 lux. The difference between the standard curve and the modified curve becomes small for regions where the luminance is greater than 5 cd/m^2	39
5	Cross-section illustrating the relative dimensions of a typical cathode-ray tube bulb.	40
6	Scanning electron microscope image of a CRT faceplate sample. The phosphor layers were exposed using a scalpel scratch. The width of the image corresponds to $50 \mu\text{m}$. Debris from the sample preparation process can be seen on top of the Al layer.	41
7	CRT faceplate core showing the inner surface after removal of the phosphor and Al layers. This roughness causes internal reflections at the interior surface to have a diffuse angular distribution.	42
8	Point-spread function of two CRT emissive structure designs. Curve (a) represents a typical monochrome CRT with no faceplate glass absorption. When black matrix is combined with an absorption of 0.2 cm^{-1} (curve (b)) the magnitude of the tails of the point-spread function (PSF) is reduced significantly, increasing the available display contrast.	43

- 9 Effect of contrast degradation in glare test patterns. The curves depict a center data row from the above images, showing the diffuse background component that reduces the glare ratio (defined as L_{max}/L_{min} [30]).

44

- 10 Cross-section of typical CRT emissive structure. Light generated in the phosphor layer by electron impact scatters in the different components until its fate is determined. The processes can be described by three efficiencies. First, the incident electron beam will deposit energy into the phosphor with an efficiency ϵ_e , which relates the energy of the incoming electrons to the deposited energy in the phosphor. Secondly, the energy deposited by the electrons into the phosphor is converted to light photons in the luminescence sites with a quantum efficiency ϵ_p . Once the light is generated, it diffuses and eventually reaches the viewer by escaping the structure with an efficiency ϵ_g , which is dependent on light emission characteristics, spatial distribution of emitted photons, and relative dimensions of the emissive structure components. The complex light transport that takes place may consist in several possible processes which include reflection and refraction at the surfaces, and scattering and absorption in the medium. 45

11	Photos of CRT phosphors: (a) Some high brightness phosphors (notably P104) contain a mixture of phosphors with different colors and often produce a noisy image. (b) Phosphors which naturally emit a broad spectrum (such as P45) typically have reduced luminous efficiency. (c) Color monitors rely on simultaneous stimulation of red, green, and blue phosphors to simulate a white or gray emission. To date, high luminosity white phosphor screens with black matrix have not been commercially available.	46
12	Cross-section illustration of an active-matrix liquid crystal display. The liquid crystal cell that modulates light intensity according to the driving voltages, is confined by multi-layer structures.	47
13	In a liquid crystal display, light is transmitted through several layers. Overall transmission is only 6-8% for color designs. The absence of color filters in monochrome designs can elevate this up to 24%.	48
14	Improvement in viewing angle for a multi-domain liquid crystal display (adapted from [66, 38]. Because anisotropies in the liquid crystal configuration are averaged over all domains, the emission angular distribution is enhanced. Ideally, emitted light should approach a Lambertian distribution.	49
15	Pixel structure showing the transmissive area (aperture) of a TFT high aperture ratio design for an active-matrix liquid crystal display (AMLCD).	50

16	Thin film transistor design with overlap between ITO and bus line having a higher pixel aperture ratio in an active-matrix liquid crystal display (AMLCD) design.	51
17	Typical field emission display (FED) cross-section illustrating the sharp emitters and the structures that confine the microvacuum cell.	52
18	A typical electro-luminescent (EL) display cross-section showing the film arrangement needed for a display device, although layers for specific designs may differ.	53
19	Attained luminance (L) versus driving voltage for organic and inorganic electro-luminescent devices (adapted from [67, 68]). High luminance devices based upon organic light-emitting materials can be achieved using low voltage drivers which are relatively inexpensive.	54

List of Tables

1	Just noticeable differences for display devices having different maximum luminance and the same luminance range (240).	55
2	Display requirements for medical imaging.	56

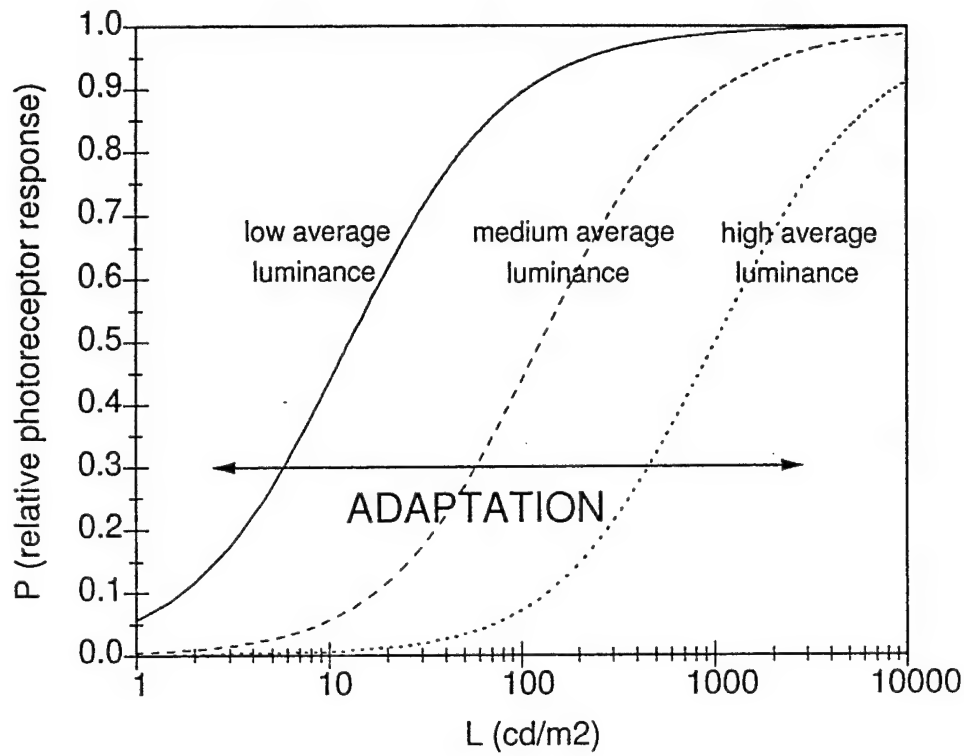


Figure 1: Stimulus response relationship and light adaptation. The profile of the response function was approximated using an expression of the form $P = L/(L + S)$ [6], where P is the photoreceptor response, L is the retinal intensity, and S is a parameter that represents the state of adaptation. Same incremental changes in stimulus cause different response according to the adaptation state.

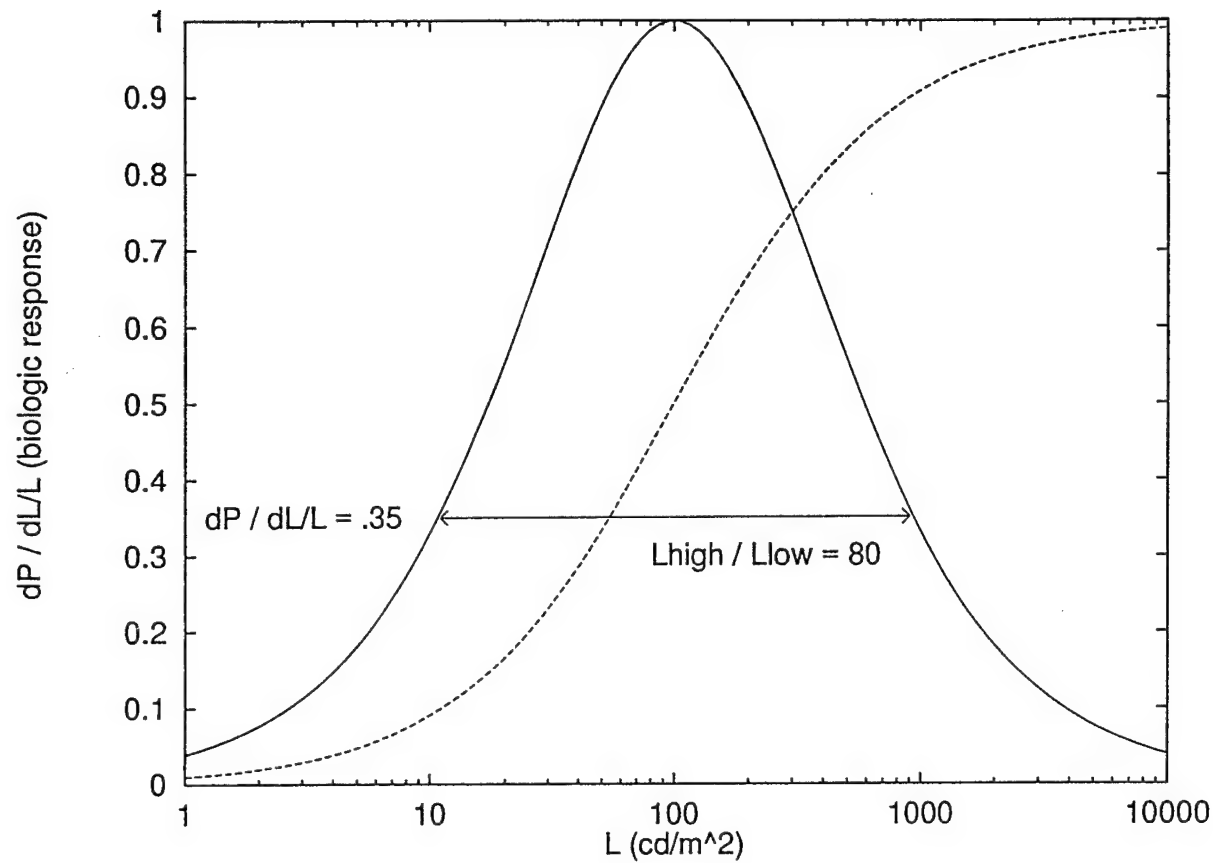


Figure 2: Biologic contrast response of the human visual system. The curve was obtained by differentiating the photoreceptor response. The perception of contrast deteriorates rapidly as the intensity of the stimulus is increased or decreased with respect to the optimum response coordinate.

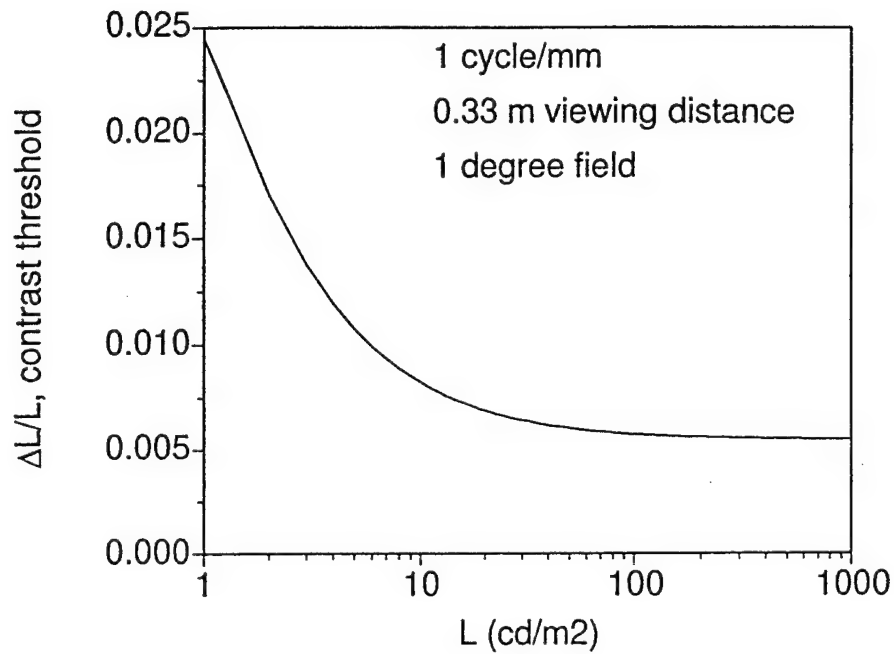


Figure 3: For a particular spatial frequency in the signal, the contrast threshold of the human visual system can be plotted as a function of luminance. While constant at higher luminance values, the threshold deteriorates at low luminance, which is known as the Weber-Fechner law [65].

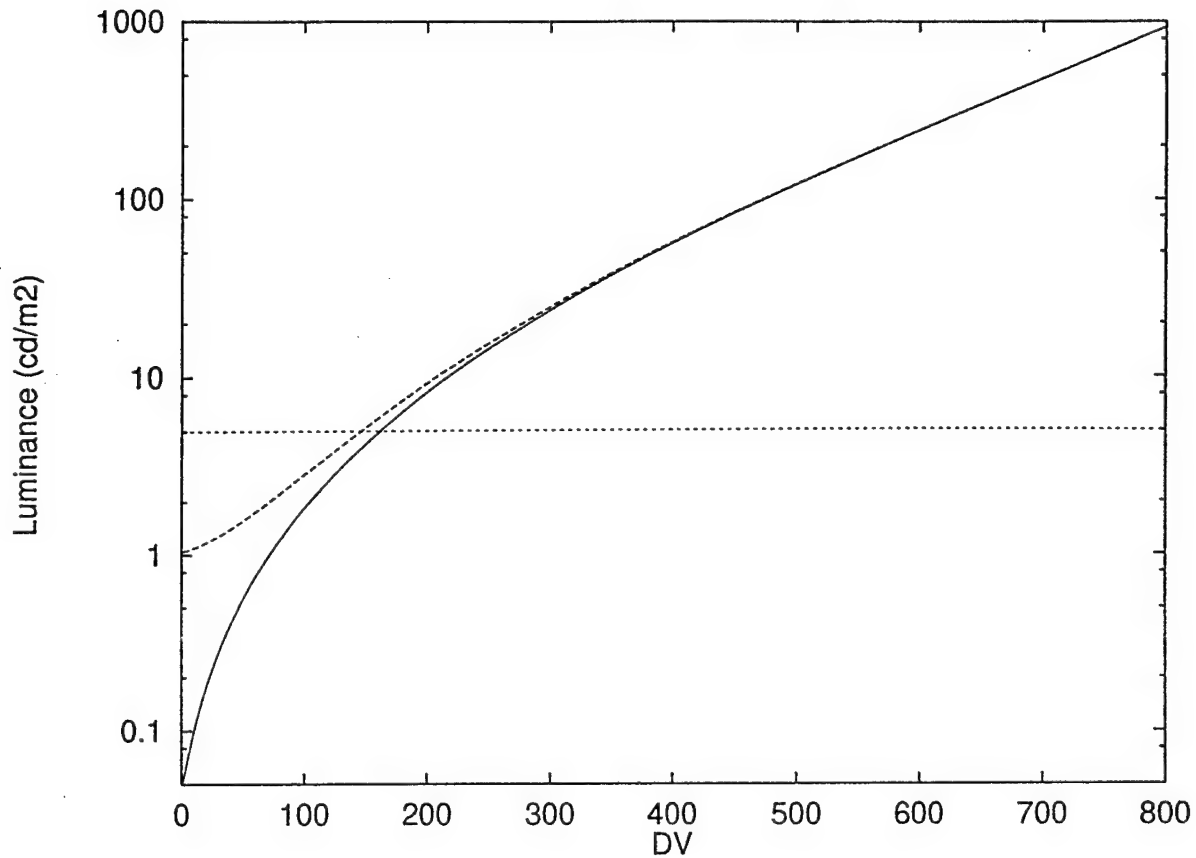


Figure 4: Standard display function curve shown as luminance versus display pixel value (PV) [14, 15]. A unit change in PV causes a luminance change equal to the contrast threshold at the indicated luminance level. The upper curve depicts the effect of diffuse ambient light reflection for a display device having a $0.01 \text{ cd/m}^2/\text{lux}$ diffuse reflection coefficient in a room producing 100 lux. The difference between the standard curve and the modified curve becomes small for regions where the luminance is greater than 5 cd/m^2 .

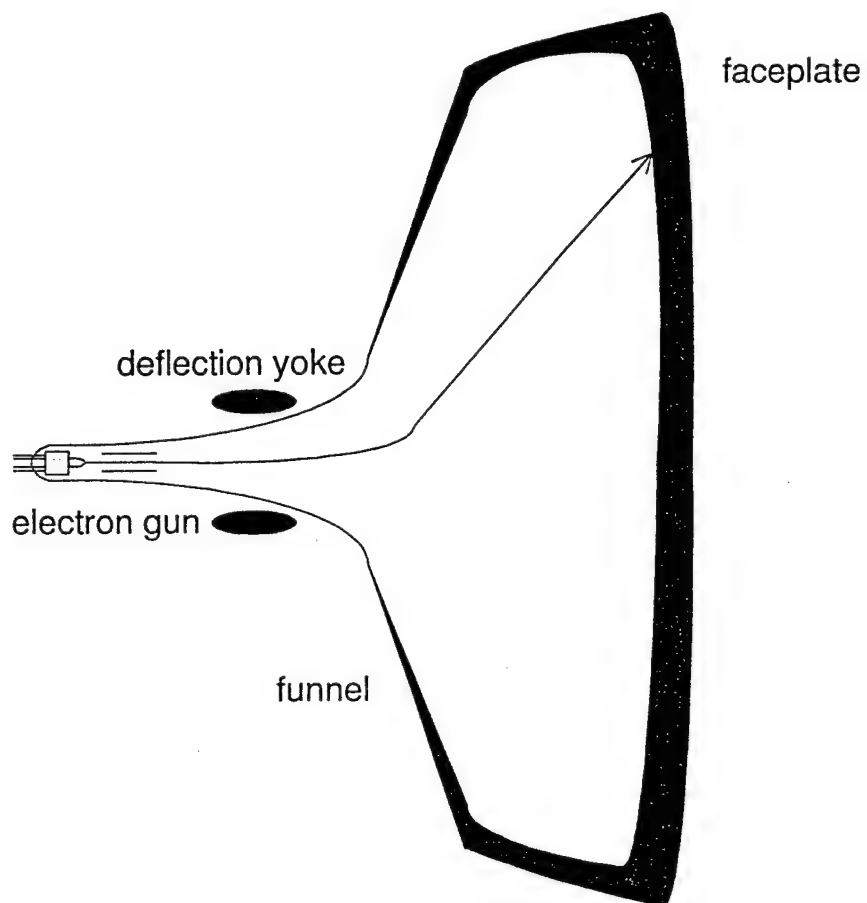


Figure 5: Cross-section illustrating the relative dimensions of a typical cathode-ray tube bulb.

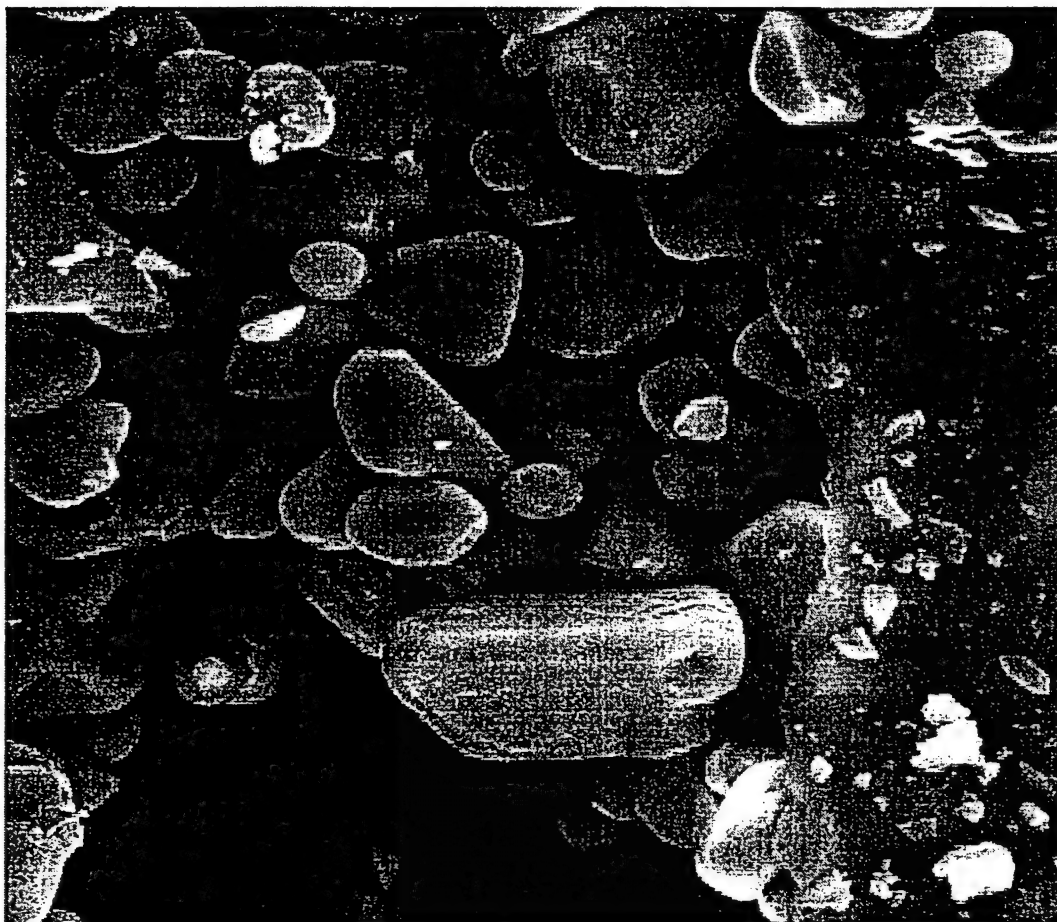


Figure 6: Scanning electron microscope image of a CRT faceplate sample. The phosphor layers were exposed using a scalpel scratch. The width of the image corresponds to 50 μm . Debris from the sample preparation process can be seen on top of the Al layer.

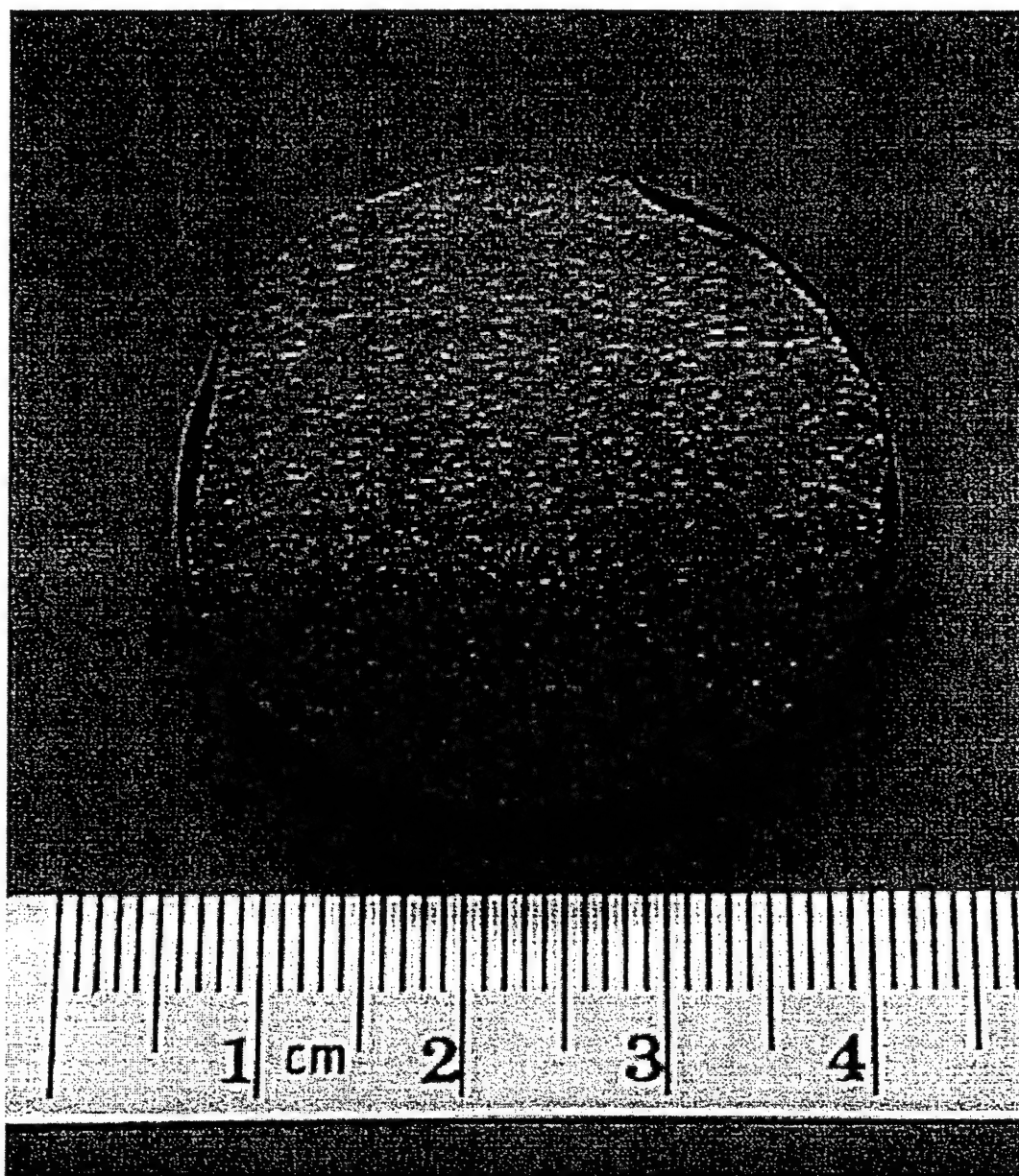


Figure 7: CRT faceplate core showing the inner surface after removal of the phosphor and Al layers. This roughness causes internal reflections at the interior surface to have a diffuse angular distribution.

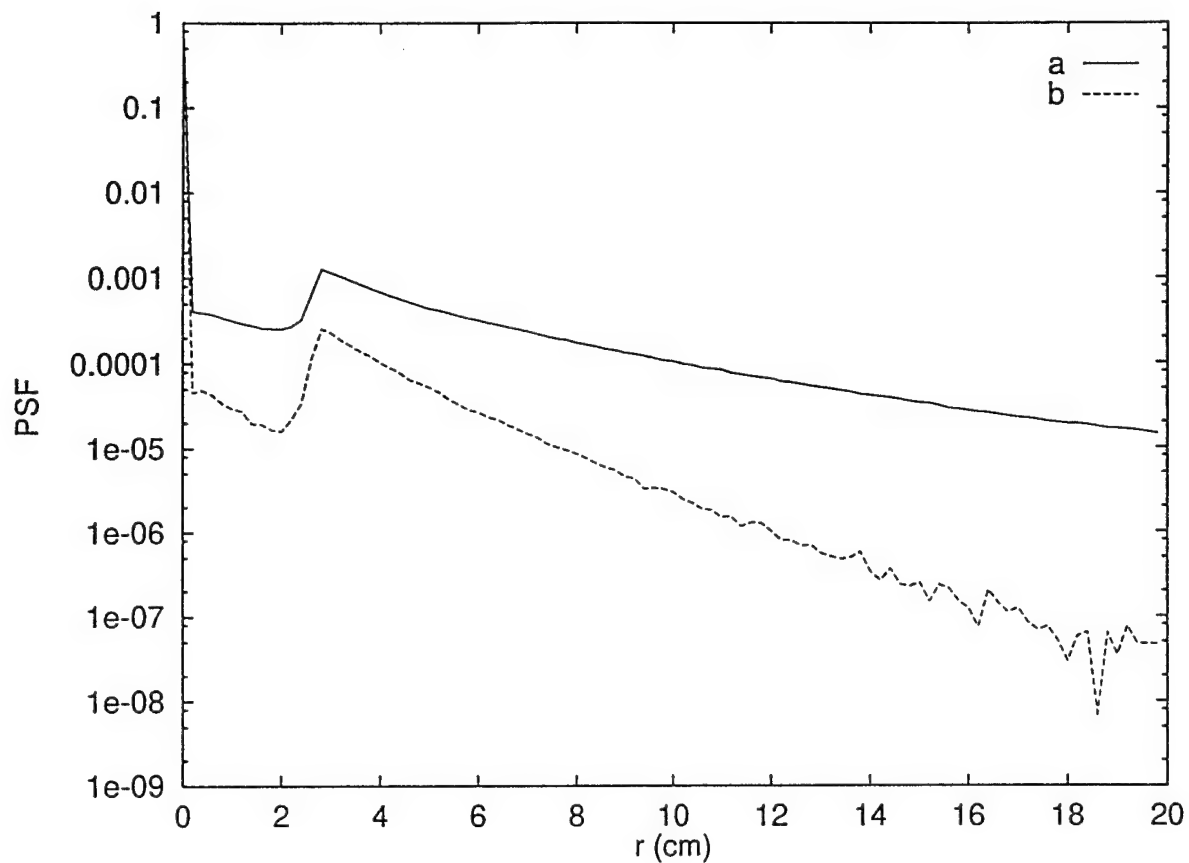


Figure 8: Point-spread function of two CRT emissive structure designs. Curve (a) represents a typical monochrome CRT with no faceplate glass absorption. When black matrix is combined with an absorption of 0.2 cm^{-1} (curve (b)) the magnitude of the tails of the point-spread function (PSF) is reduced significantly, increasing the available display contrast.

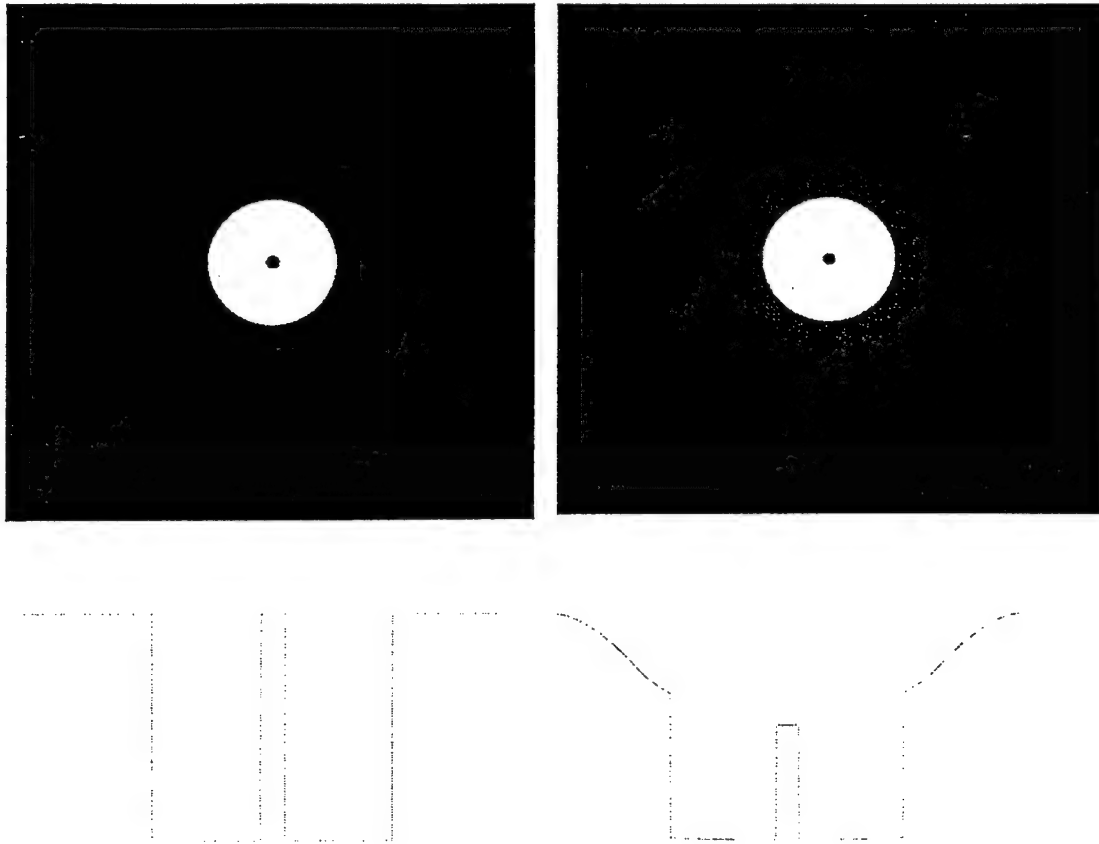


Figure 9: Effect of contrast degradation in glare test patterns. The curves depict a center data row from the above images, showing the diffuse background component that reduces the glare ratio (defined as L_{max}/L_{min} [30]).

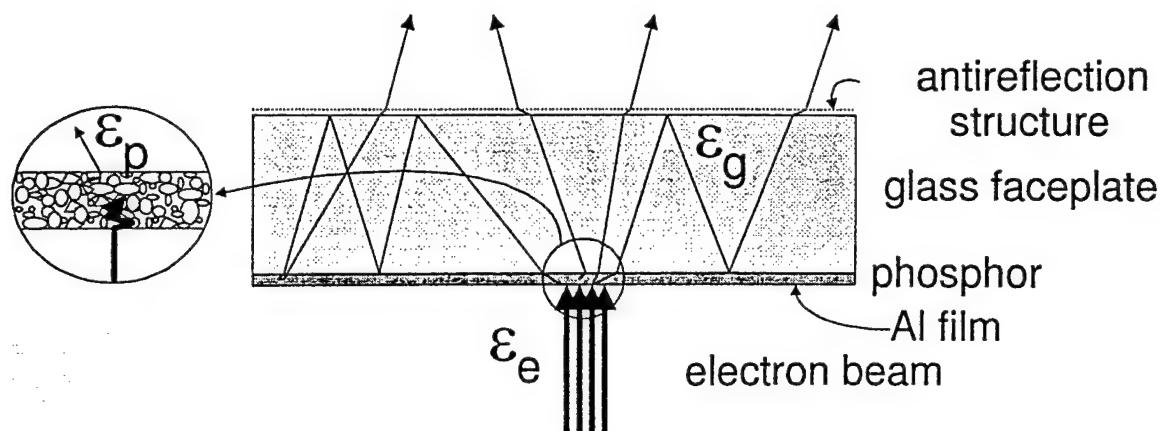


Figure 10: Cross-section of typical CRT emissive structure. Light generated in the phosphor layer by electron impact scatters in the different components until its fate is determined. The processes can be described by three efficiencies. First, the incident electron beam will deposit energy into the phosphor with an efficiency ϵ_e , which relates the energy of the incoming electrons to the deposited energy in the phosphor. Secondly, the energy deposited by the electrons into the phosphor is converted to light photons in the luminescence sites with a quantum efficiency ϵ_p . Once the light is generated, it diffuses and eventually reaches the viewer by escaping the structure with an efficiency ϵ_g , which is dependent on light emission characteristics, spatial distribution of emitted photons, and relative dimensions of the emissive structure components. The complex light transport that takes place may consist in several possible processes which include reflection and refraction at the surfaces, and scattering and absorption in the medium.

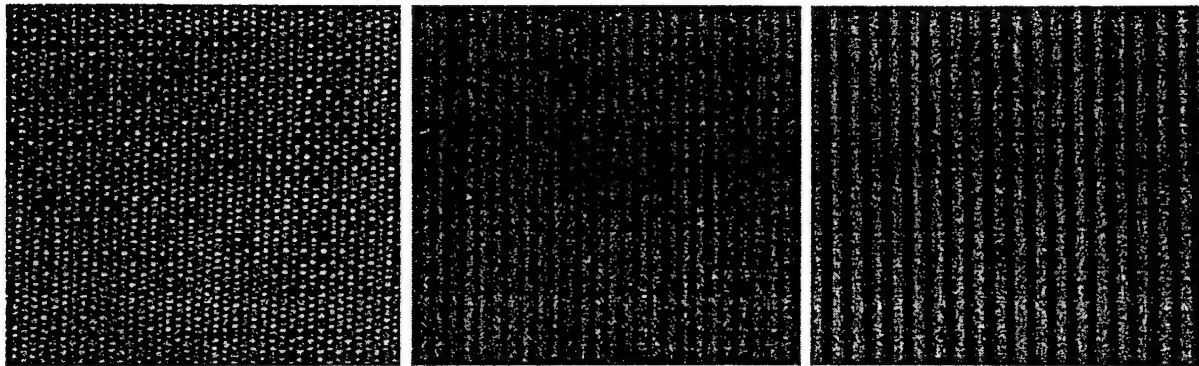


Figure 11: Photos of CRT phosphors: (a) Some high brightness phosphors (notably P104) contain a mixture of phosphors with different colors and often produce a noisy image. (b) Phosphors which naturally emit a broad spectrum (such as P45) typically have reduced luminous efficiency. (c) Color monitors rely on simultaneous stimulation of red, green, and blue phosphors to simulate a white or gray emission. To date, high luminosity white phosphor screens with black matrix have not been commercially available.

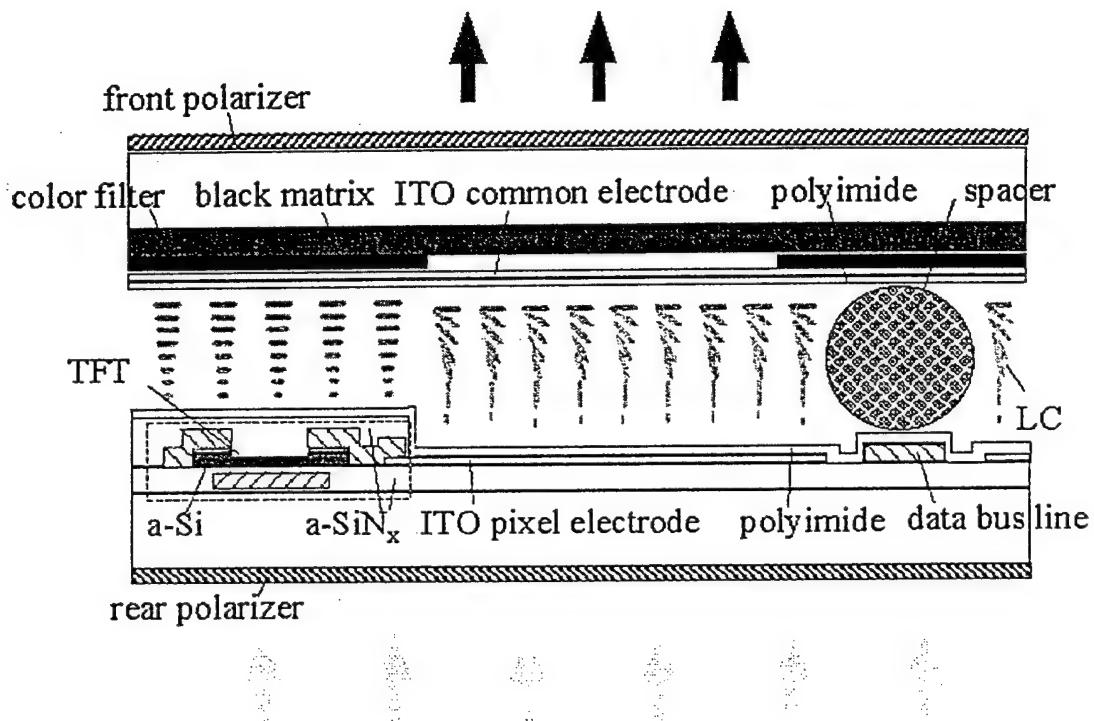


Figure 12: Cross-section illustration of an active-matrix liquid crystal display. The liquid crystal cell that modulates light intensity according to the driving voltages, is confined by multi-layer structures.

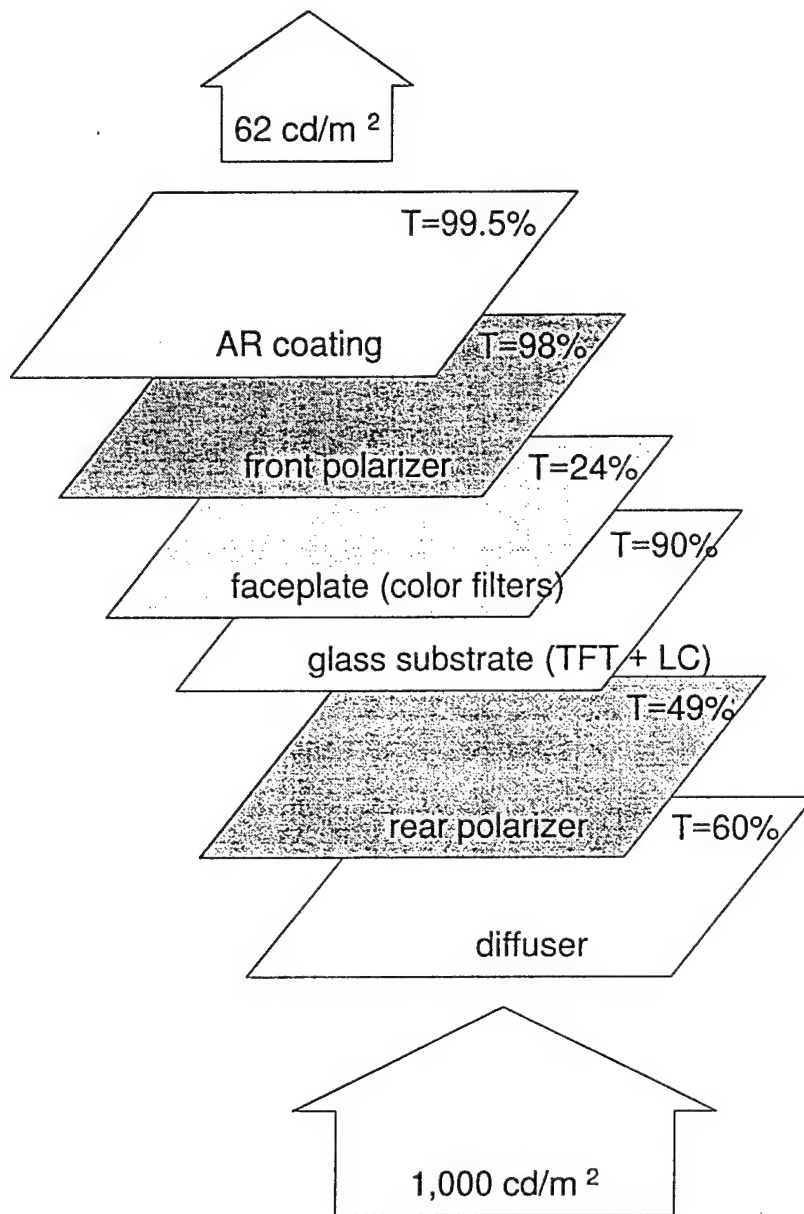


Figure 13: In a liquid crystal display, light is transmitted through several layers. Overall transmission is only 6-8% for color designs. The absence of color filters in monochrome designs can elevate this up to 24%.

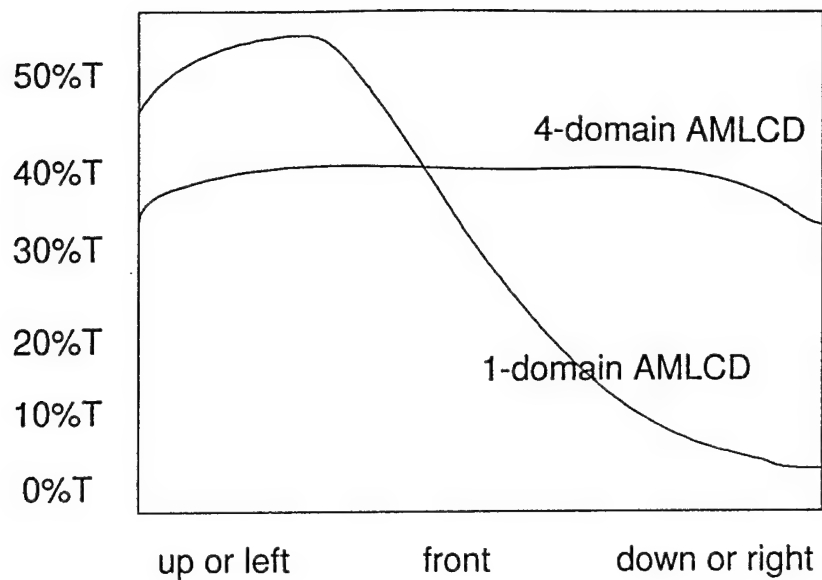


Figure 14: Improvement in viewing angle for a multi-domain liquid crystal display (adapted from [66, 38]). Because anisotropies in the liquid crystal configuration are averaged over all domains, the emission angular distribution is enhanced. Ideally, emitted light should approach a Lambertian distribution.

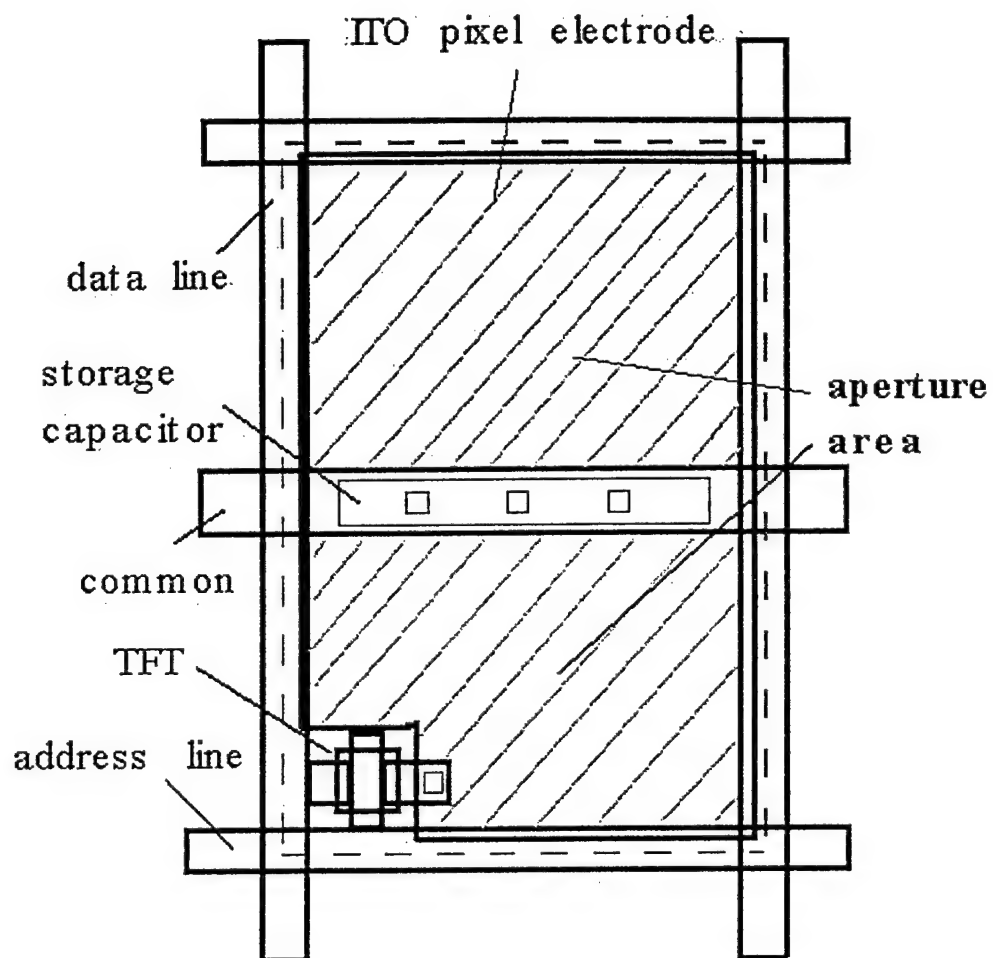


Figure 15: Pixel structure showing the transmissive area (aperture) of a TFT high aperture ratio design for an active-matrix liquid crystal display (AMLCD).

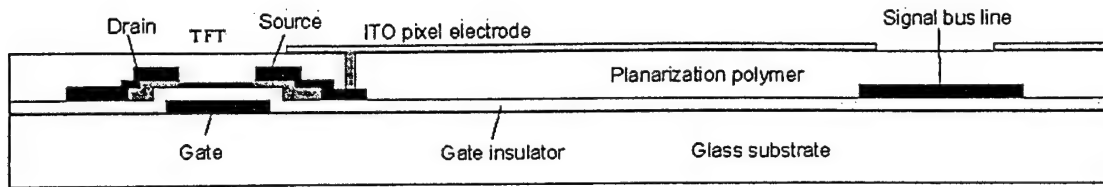


Figure 16: Thin film transistor design with overlap between ITO and bus line having a higher pixel aperture ratio in an active-matrix liquid crystal display (AMLCD) design.

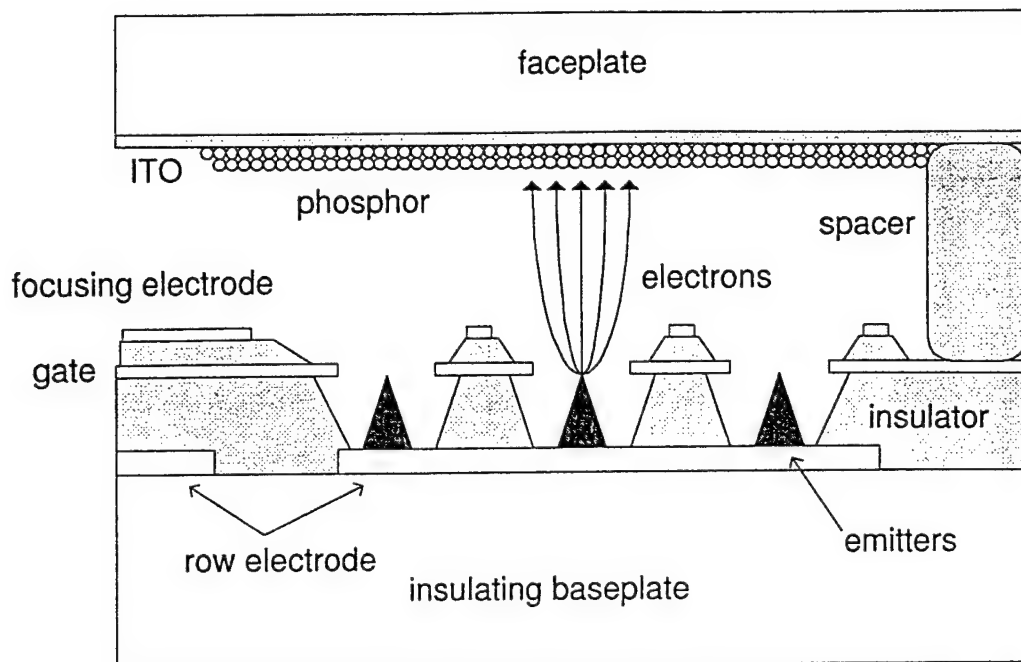


Figure 17: Typical field emission display (FED) cross-section illustrating the sharp emitters and the structures that confine the microvacuum cell.

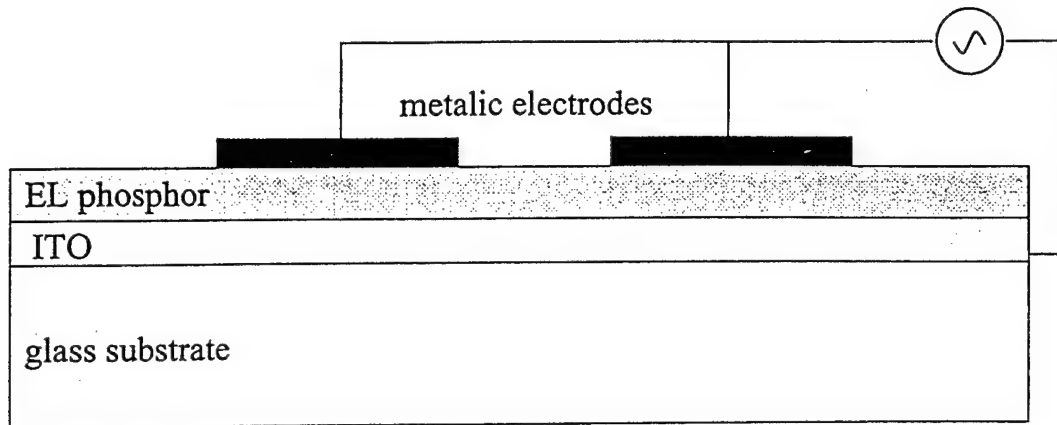


Figure 18: A typical electro-luminescent (EL) display cross-section showing the film arrangement needed for a display device, although layers for specific designs may differ.

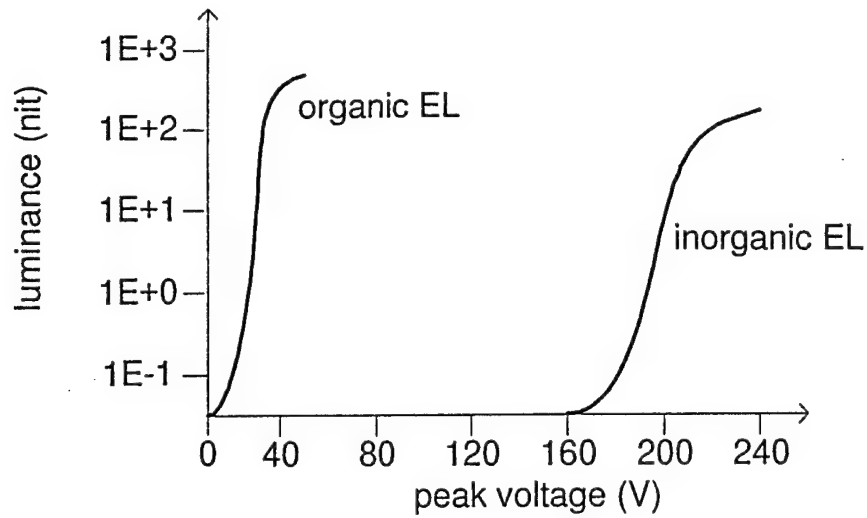


Figure 19: Attained luminance (L) versus driving voltage for organic and inorganic electro-luminescent devices (adapted from [67, 68]). High luminance devices based upon organic light-emitting materials can be achieved using low voltage drivers which are relatively inexpensive.

Table 1: Just noticeable differences for display devices having different maximum luminance and the same luminance range (240).

L_{low} (cd/m ²)	L_{high} (cd/m ²)	JNDs
0.5	120	450
1	240	530
2	480	600
5	1200	680
10	2400	730

Table 2: Display requirements for medical imaging.

Specification	Film Quality Display	High Fidelity Display	Good Display
Size	35×43 cm ^a	30×36 cm	24×30 cm
Pixels	4000×5000	2500×3000	1200×1500
Pixel size	0.08 mm	0.12 mm	0.20 mm
Refresh rate	static	static - 80 Hz	static - 80 Hz
Maximum luminance	2000 cd/m ²	1000 cd/m ²	240 cd/m ²
Minimum luminance	1 cd/m ²	4 cd/m ²	1 cd/m ²
Gray-scale levels ^b	≥ 850	≥ 680	≥ 530
Emission	Lambertian	Lambertian	Lambertian
Color	monochrome ^c	monochrome	monochrome
Veiling glare ratio ^d	> 1000	400	150
Large area distortion	< 0.1 %	2 %	2 %
Diffuse reflectance	0.025 nit/lux	0.02 nit/lux	0.03 nit/lux
Specular reflectance	0.024 nit/nit	0.002 nit/nit	0.005 nit/nit
Viewing angle ^f (vertical)	full	± 45°	± 30°
Viewing angle ^f (horizontal)	full	± 60°	± 45°

^a 43×35 cm is a standard size for radiographic detectors. Displays should have a horizontal/vertical aspect ratio of about 0.8.

^b The log-luminance versus pixel value relationships should follow a perceptually linear profile based on the DICOM standard.

^c General preference in the field has been for displays with a white to slightly blue color. Most film bases are tinted blue.

^d Contrast ratio defined with test pattern images consisting of a 1 cm centered dark circular spot, surrounded by a bright field.

^f Full stated contrast ratio and luminance performance is to be maintained within the required viewing angle. No contrast inversion is allowed.

A method for measuring veiling glare in high performance display devices

Aldo Badano and Michael J. Flynn

When this work was performed, both the authors were with the Department of Diagnostic Radiology, Henry Ford Health System, Detroit, MI 48202, and Department of Nuclear Engineering and Radiological Sciences, University of Michigan, Ann Arbor, MI 48109. AB is now with the Center for Integrated Microsystems, University of Michigan, 2360 Bonisteel Blvd., Ann Arbor, MI 48109, phone (734) 6151519, fax (734) 9360347, email badano@umich.edu.

Abstract

An experimental method for measuring the veiling glare characteristics of display devices is presented. The measured veiling glare ratio is taken to be the luminance in the surrounding bright field divided by the luminance in a dark circle. The method is based on a collimated conic probe that minimizes the signal contamination from bright surroundings allowing measurements of very low luminance in a circular dark spot of a test pattern. A correction factor computed with test patterns having opaque spots is introduced. The factor is expressed as a bi-variate function of the dark spot radius and the distance between the probe and the emissive surface. The uncertainty introduced by the method was studied by measuring veiling glare test patterns printed on radiographic film for which the transmission of the dark spots was determined experimentally. Performance characterization measurements show that signal contamination is less than 10^{-4} of the bright field surrounding a dark circle. Our results show that veiling glare ratios in the order of a few hundreds can be measured with this method with an uncertainty of a few percent, and ratios of about 10^3 can be reported within 10%. Finally, the method is demonstrated by

measuring veiling glare ratios for a high performance monochrome CRT display.

Key words: Veiling glare, contrast ratio, display device, dark spot measurement.

© Optical Society of America, 1992.

1. Introduction

There is a significant need to improve the performance of display devices in high fidelity applications such as medical imaging, graphic arts, and industrial inspection. A wide luminance range (5-1,000 cd/m²) with minimal image quality degradation due to luminance spread is required for low contrast details to be visible. However, the image quality of electronic display devices is often limited by extensive veiling glare that causes a low-frequency degradation resulting in contrast reduction. In cathode-ray tubes (CRTs), veiling glare is caused by multiple light scattering in the thick glass faceplate,^{1,2} by back-scattered electrons in the vacuum tube,³⁻⁶ and by light leakage through non-uniformities in the reflective coating. New flat panel technologies employing discrete pixel designs generally have less veiling glare than CRT devices.⁷ Veiling glare has otherwise been studied in other components of the imaging chain, such as for detectors⁸⁻¹¹ and lenses,¹² and for the human eye.^{13,14}

Several groups have suggested that the veiling glare characteristics of display devices be measured using test patterns with rectangular fields of different sizes at low luminance surrounded by bright regions.^{15,4} However, the radial symmetry of the veiling glare processes suggests that a test pattern with circular targets is more appropriate. In this paper, we define a luminance point spread function with radial dependency and use this function as a basis for performing experimental measurements using circular test patterns.

For measuring veiling glare in high performance display devices, a collimated probe capable of measuring very low luminance values in a small dark region surrounded by a large bright field is required. Multiple light reflections in detector optics can substantially alter the measured low luminance value in the dark spot. The measurement error amounts to 1-3% of the bright field intensity for low-flare lenses with anti-reflective coatings.¹² When

measuring a test pattern for which the bright field luminance is 500 times the dark spot luminance (i.e., a contrast ratio of 500), the measured contrast ratio will only be 83 if the detector records 1% of the bright field in the dark region. For veiling glare measurements this light leakage should be less than 0.01%, which results in a contrast ratio of 476 for the preceding example.

In this paper, we describe a collimated probe that minimizes contamination from very bright neighboring regions. The probe has been specifically designed to measure veiling glare using a test pattern with a circular dark spot of varying diameter. Details pertaining to the optical design and construction of the probe are reported. By measuring test patterns digitally printed on radiographic film, the response attributes of the detection assembly have been established. Finally, the method is demonstrated by measuring the veiling glare characteristics of a monochrome medical imaging CRT.

2. Analytic model for veiling glare

The contrast degradation caused by veiling glare can be described by a normalized continuous point spread function $P(r, \theta)$.[†] This function describes the luminance (cd/m²) at (r, θ) resulting from a point source of light with unit intensity, 1 cd, located at $r = 0$. The units of the point spread function, $P(r, \theta)$, are thus m⁻². It is useful to assume that $P(r, \theta)$ is shift-invariant and radially symmetric. The veiling glare, $L_g(x, y)$, produced in a display by an image with a primary luminance of $I(x, y)$ can then be estimated using a convolution integral:

$$L_g(x, y) + I(x, y) = \iint I(x', y') P(r') dx' dy' \quad (1)$$

[†]In principle, $P(r, \theta)$ may also have a wavelength dependence associated with light transport processes. This is particularly true when anti-reflection coatings or tinted optical components are used. In this paper, we address only monochromatic devices and ignore any wavelength dependence.

where $r' = \sqrt{(x - x')^2 + (y - y')^2}$, and both $L_g(x, y)$ and $I(x, y)$ have units of cd/m^2 . Our use of the point spread function is equivalent to classical definitions,¹⁶ although the function is typically used to describe short range blur associated with resolution and not the long range processes associated with veiling glare.⁸

To model test patterns consisting of a centered black circular region surrounded by a circular region of uniform luminance, I_o , it is useful to define the ring response function, $R(r)$, as:

$$R(r) = \int_0^{2\pi} P(r, \theta) r d\theta = 2\pi r P(r), \quad (2)$$

where $R(r)$ has units of m^{-1} . This function describes the luminance at $(0, 0)$, in cd/m^2 , produced by an infinitely thin ring source of light having a total intensity of 1 cd distributed uniformly over a distance of $2\pi r$. The luminance in the center of the dark spot is given by:

$$L_g = L_g(0, 0) = I_o \int_{r_d}^{r_l} R(r) dr \quad (3)$$

where r_d is the radius of the black circle and r_l is the radius of the luminous surrounding region.

In this paper, we define the veiling glare ratio (G) as I_o/L_g , a function that depends on the two radii associated with the test pattern, $G(r_d, r_l)$. In practice, we have considered the dependence of G on r_d when r_l is constant, $G(r_d)$. If experimental measurements are made with a set of test patterns having a black circle of varying radius, r_i where $i = 1, 2, \dots, n$, and the same radius r_l for the luminous region (see Figure 1), the measured set of glare ratios, G_i , provides information describing both the short and long range characteristics of veiling glare. Notably, two measurements with different black circles can easily be related to the integration of the ring response function between the two different radii of the black circles:

$$\frac{1}{G_i} - \frac{1}{G_{i+1}} = \int_{r_i}^{r_{i+1}} R(r) dr. \quad (4)$$

If $R(r)$ is slowly varying over this range of radii, we can use this expression to numerically estimate $R(r)$ from a full set of measurements of G_i (for i varying from 0 to r_l).

3. A collimated probe and luminance detector

To determine the veiling glare ratio of a display device, the luminance from small circular dark spots needs to be accurately measured. To develop a luminance probe with minimal response from surrounding bright regions, a collimated design with multiple baffles was employed. The device is based on a high-gain Si photo-diode sensor with an active area of about 5.7×5.7 mm, a photopic filter, and a research radiometer (SHD 033 sensor, IL 1700 radiometer, International Light Inc., Newburyport, MA). A standard barrel (40 mm diameter and 70 mm long) into which baffles can be positioned using threaded parts is attached to the sensor. A conic probe fabricated on a lathe from aluminum rod is placed at the end of this barrel. The assembled components are shown in Figure 2.

The probe tip is designed to minimize the amount of light scattered from the probe back to the emissive structure. As shown in Figure 3, the probe entrance aperture has a diameter of 9 mm. The interior of the tip is shaped with a reverse cone geometry creating a pointed entrance aperture. The inclination of the interior walls of the inner tip minimizes the amount of light reflecting back to the display faceplate. The external conic shape of the probe reflects light coming from bright regions away from the display surface. An angle between the walls of the cone and the display surface normal of 15° allows central measurements in 380 mm diagonal displays.

The surface characteristics of the first few millimeters of internal wall at the probe tip was thought to have a major impact on the reduction of scattered light that contaminate dark spot measurements. For this reason, both highly reflective and diffuse absorptive surface finishings were evaluated. The comparison showed that a highly specular surface at the inside front end resulted in a lower dark spot luminance. The specular surface was realized by polishing about 3 mm of the interior wall of the tip with very fine grit polishing paper.

Light entering the probe at oblique angles is trapped by interior baffles and chambers. A series of four baffles of about 4 mm diameter creates a highly collimated response. Baffle positions and aperture diameters were determined using manual design methods. Figure 4

shows drawings that illustrate three aspects of the optical design. The principal rays that define the detector active area are depicted in Figure 4(a). The detector is directly exposed to only a portion of the back surface of each aperture as shown in Figure 4(b). Each aperture is very thin to reduce light scattering from the edges. Light entering at oblique angles, Figure 4(c), is reflected off the interior walls of the probe that are not viewed by the detector. Significant signal contamination is prevented by the large number of scattering events from absorptive surfaces required to reach the detector through the multiple apertures.

The probe assembly was accomplished by a sequential procedure of painting and aperture bonding for each of four chambers. All interior walls except for the reversed conic tip are coated with a black absorptive paint (KRYLON, Ultra Flat Black 1602) to effectively dampen light reflected inside the probe. Interior baffle apertures were fabricated by attaching small, thin perforated disks of black anodized aluminum on either machined ledges in the conical end or on standard aperture holders screwed into the barrel. The bonding of baffles and apertures was performed using a two-part black epoxy. The specially machined conical end was attached to a standard baffle which, in turn, was attached to the end of the barrel. Finally, the external surface was polished and black anodized to provide a specular absorptive surface.

All apertures were originally made with the same diameter (4 mm). However, when the probe was assembled, apparent light diffraction was observed by looking at a small dark spot in a bright field with the eye in the position of the sensor. It was determined that scattering from the edge of the second aperture was responsible for the interference pattern. This effect was successfully eliminated by slightly increasing the diameter of the second aperture to 4.1 mm.

4. Experimental methods

In this Section, we describe the experimental procedures used to test the performance of the proposed method to measure veiling glare in display devices. Correction factors are

introduced by using opaque spots and spots of known transmission with negligible veiling glare.

A. Probe response versus spot diameter

The response characteristics of the probe can be determined by measuring the luminous signal from test patterns having an opaque spot which emulated a device with no veiling glare. For dark spot diameters smaller than the field of view of the probe, the measured luminance is associated with direct light striking the detector. For larger diameters, the luminance is caused by scattered light originating in the bright regions that enters the probe after multiple reflections. It is this contamination in the signal that limits the performance of the method. The amount of signal contamination for this probe is a function of both the dark spot radius (r_d) and the distance between the probe and the emissive surface (d).

To characterize the performance of the proposed method, veiling glare test patterns having a 320 mm diameter bright circular field with varying dark spot diameters were printed on 35×43 cm transparent ESTAR film with a laser printer (KODAK Ektascan, model XLP). The transilluminated patterns do not suffer degradation of image quality by veiling glare. Much light scattering occurs in the film, but is locally confined to the thin emulsion containing absorptive grains that modulate luminance. The optical density in the dark circles was supplemented with black absorptive paper glued to the film back side (next to the illuminator) to obtain negligible transmittance through the spot.

The test patterns were back-illuminated in a dark room with a fluorescent lamp illuminator used for viewing radiographic film. The maximum luminance in the bright field of the test patterns was about 2,040 cd/m². Black velvet was used to cover the detector assembly to shield the films from reflections coming from objects in the room. Measurements were performed using test patterns in a fixed location aligned with the probe axis, for values of r_d from 0 to 10 mm, and distances d of 2, 10, and 20 mm. A correction factor was then computed as a bi-variate function $\zeta(r_d, d)$, expressed as a fraction of the bright field intensity.

The correction factor ζ represents the dark signal contamination due to scattered light. A corrected veiling glare ratio (G_{corr}) can then be computed from measured values (G_{meas}) as follows,

$$G_{corr}(r_d, d) = G_{meas}(r_d, d) \frac{1}{1 - \zeta(r_d, d)G_{meas}(r_d, d)}. \quad (5)$$

Using this expression, a criteria for the application of the correction can be established. For example, for a device capable of a contrast ratio of 300, a maximum correction of 1% due to light leakage is obtained for ζ less than 3.3×10^{-5} .

B. Measurements for a display with no veiling glare

The same test patterns used in the performance characterization experiment were utilized to understand how the proposed method performs when measuring veiling glare ratios in a test environment similar to a display device with no glare and low luminance. In this case, no additional absorption was employed in the dark target resulting in a film transmission of about 0.003. The transmission of the dark spot was determined by measuring the relative signal using a bright view-box masked with black absorptive paper with a centered hole of about 3 mm in diameter. The transmission $T_d(d)$ was computed as the ratio of the luminous signal when the hole was centered in the dark spot, to the signal for the same test pattern with no dark circular spot (i.e., a full bright circular field). Although the printing parameters were identical, the transmission values for film patterns with different dark spot diameter varied due to variations in film development conditions. The luminous signal resulting from the transmission through the film was subtracted from the measured luminance to estimate the veiling glare (L_g).

To simulate display devices, the luminance in the bright region of the test patterns was reduced to be similar to the luminance found in high performance monitors. A film with uniform optical density was placed inside the illuminator between the lamps and the diffuser to obtain a bright field luminance of 170 cd/m². Measurements were performed with test patterns having dark spot radii varying from 4 to 80 mm. The measurements

were intentionally made at distances different than those used to measure the light leakage correction (i.e., 5 and 15 mm versus 2, 10, and 20 mm) to assess the performance of the correction.

C. Measurements for a monochrome CRT

To illustrate the application of the method for devices having veiling glare, measurements were performed for a monochrome medical imaging CRT (Image Systems, 24 inches diagonal, model M24L). Test patterns with varying spot diameter were displayed as images with 1000×1000 pixels (see Figure 1). With the contrast control set to the maximum level, the monitor brightness control was increased from the minimum level until the full dark field luminance was greater than the value observed with the unit powered off. The brightness was then slightly reduced from this point, and the luminance of a full black field recorded (L_d). The veiling glare measurements were made with the entrance of the collimated probe at a total distance of 14 mm from the emissive layer (estimated using laser reflection technique). The probe entrance was at 1 mm from the surface of the display. The distance d was determined by adding the distance between the probe tip to an estimate of the faceplate thickness based on laser reflection measurements. The thickness was measured to be 13 mm resulting in a total distance d of 14 mm. Measurements were performed with test patterns of many radii varying from 4 to 160 mm.

5. Results

In this Section, we present results obtained for opaque spots, for spots with known luminance, and finally, for a medical imaging monochrome CRT.

A. Probe response versus spot diameter

Figure 5 depicts the light leakage in test patterns with perfectly black spots measured at distances of 2, 10 and 20 mm. The measured data points are expressed as a fraction of the measured signal for a uniformly bright field. The recorded measurements for small radii define the collimated region of direct path light response with a width of 10% of the maximum equal to 2.5 to 3.5 mm radius. For values of the correction factor ranging from about 3×10^{-5} to 10^{-3} , the correction decreases exponentially with increasing spot radius. For a distance of 2 mm, the data asymptotically approaches a value of about 3×10^{-5} . At relative response values of 3×10^{-5} , the noise of the luminance detector measured with the probe aperture blocked was less than 10% of the signal (i.e., 1 pA).

The relative response at large radii represents a correction factor ζ that can be used to adjust the dark luminance values recorded in actual devices according to Equation 5. To provide a practical mechanism for computing corrected glare ratios (G_{corr}), a surface fitting was performed for $\zeta(r_d, d)$ for correction factors ranging from 3×10^{-5} to 10^{-3} . A second degree polynomial expression with cross terms was obtained for the logarithmic values of the correction using a least-square fitting technique (MAPLE V, Waterloo Maple Inc.). The polynomial expression used for the correction factor is

$$\log \zeta(r_d, d) = 0.00339 d^2 - 0.0778 d - 0.435 r_d - 0.00120 r_d d^2 + 0.0371 r_d d - 1.85 \quad (6)$$

where r_d and d are expressed in mm. Figure 6 shows the experimental data points for the measured signal contamination along with the polynomial function $\zeta(r_d, d)$ for the distances d used in the experiment. Data is presented for the region of radii and distances where the function is defined, namely, $3 \times 10^{-5} < r_d < 10^{-3}$, and $3 \text{ mm} < d < 10 \text{ mm}$. The results predicted using Equation 5 agree well with the experimental points.

B. Measurements for a display with no veiling glare

For measurements performed using veiling glare test patterns with known dark spot transmission, the measured dark signal (L_{meas}) was interpreted as

$$L_{meas}(r_d) = L_g(r_d) + [T_d(r_d) + \zeta(r_d, d)]L_b \quad (7)$$

where L_g is the contribution associated with veiling glare, and L_b is the luminance in the uniform bright field. For an ideal detector ($\zeta = 0$) and perfectly black targets ($T_d = 0$), L_{meas} is identical to L_g . In this case, due to negligible veiling glare contribution for radiographic film, and a priori knowledge of the values for $T_d(r_d)$ and $\zeta(r_d, d)$, L_{meas} is expected to be zero and can thus be related to the uncertainty introduced by the method in the estimation of G .

The same relationship described by Equation 7 can be expressed in terms of veiling glare ratios as,

$$\frac{1}{G_{corr}(r_d)} = \frac{1}{G_{meas}(r_d)} - T_d(r_d) - \zeta(r_d, d), \quad (8)$$

where G_{meas} is the measured uncorrected veiling glare ratio. Again, for a perfect detector and true black spots, G_{meas} is equal to G_{corr} .

Figure 7 shows the inverse of the corrected veiling glare ratio, as defined in Equation 8, for radiographic film at 5 and 15 mm distance between the probe and the film surface. For both distances, $1/G$ is within ± 0.00012 for dark spot radii larger than 5 mm. Since in these experimental conditions veiling glare is negligible, these results represent the measurement error for the method.

C. Measurements for a monochrome CRT

For CRT measurements, an equation similar to Equation 8 was used to correct for the black luminance:

$$\frac{1}{G_{corr}(r_d)} = \frac{1}{G_{meas}(r_d)} - \frac{L_d(r_d)}{L_b} - \zeta(r_d, d) \quad (9)$$

Figure 8 shows the corrected veiling glare ratios for the medical imaging CRT. For a radius of 5 mm, G_{corr} is equal to 130. The data were numerically differentiated to obtain the ring response function discrete values (see Equation 4). Figure 9 shows the computed ring response function $R(r)$. At short distances, $R(r)$ has a plateau with magnitude equal to $5 \times 10^{-4} \text{ mm}^{-1}$. At about a radius of 20 mm, the magnitude drops to about $2 \times 10^{-5} \text{ mm}^{-1}$. This value remains approximately constant up to the large radius measured for this monitor. A small increase in the magnitude of the tail can be observed as the radius increases which suggests that $P(r)$ decreases with less than a $1/r$ dependency (see Equation 2). The ring response function may also be influenced by the edges in the CRT faceplate that can act as partial reflectors.

6. Discussion

The human visual system is very effective at observing images having a very large luminance range. The perception of brightness is generally understood to be logarithmically proportional to luminance¹⁷ and capable of adapting to different average luminance in the observed scene.^{18,19} Additionally, the human visual system performs well when observing the luminance of dark regions surrounded by bright fields. The very low intrinsic veiling glare of the eye is primarily determined by the retina which has reduced sensitivity to obliquely incident light associated with scattering events in the lens.^{14,13,20} A high quality display device thus requires a veiling glare ratio of 400 or more for relatively small dark spots.²¹

We have described an experimental method capable of measuring the large veiling glare ratios characteristic of high performance display devices. A luminance probe with very low light leakage has been developed for use with this method. Using this probe, we have demonstrated that measurements of very low luminance in small dark spots can be performed even when the surrounding field is 1,000 times brighter.

The method described is applicable to very small dark spots. The minimum spot diameter that can be measured using this method depends on the distance between the entrance

aperture of the probe and the emissive surface due to the imperfect collimation provided by the design. A good approximation for the minimum spot diameter for a given distance d' can be obtained by computing the value of r_d for which $\zeta(r_d, d')$ is equal to 10^{-3} . Minimum dark spot size thus have radii from 3 to 6 mm for measurement distances from 2 to 20 mm.

Using a display device with negligible veiling glare, we have shown for the distances considered that the uncertainty in the method is below 10^{-4} for $1/G$. The method can thus be used for measuring glare ratios up to 10^3 with an error of less than 10%. Furthermore, when this measurement method is applied to construct the ring response function associated with veiling glare (as described in Equation 4), the error introduced by the method is small enough to allow features in $R(r)$ to be clearly observed. While the probe and method described in this work were developed to measure veiling glare from light transport processes, contributions to glare from other sources (i.e., electron back-scattering and frequency response of the drive amplifier) cannot be discriminated.

Measurement artifacts caused by multiple scattering in lenses prevents their use for measuring veiling glare. Other investigators have used masking techniques (including flat and conic black masks) to shield the lens and camera from the bright regions when performing similar measurements.^{22,23} Flat masks perform better when placed adjacent to the emissive surface. For CRT devices, cone masks have proven useful due to the reflection of light away from the thick faceplate.

We have compared the performance of the method described in this paper to results obtained using a black conic mask. An LS110 spot photometer (MINOLTA Co., Ramsey, New Jersey), with a $1/3^\circ$ acceptance angle, was used with a close up lens (No.135) to observe a 2 mm spot from a distance of 450 mm. A black cone with a 4 mm radius entrance aperture, 20° degree full cone angle, and 350 mm in length was constructed using darkened radiographic film with the glossy surface of the film towards the outside of the cone. The interior surface was covered, before rolled to conic form, with a light-absorptive paper (Edmund Scientific Company, Barrington, New Jersey). The conic mask was centered over a 5 mm radius dark spot at distances of 2 mm, 10 mm, and 20 mm. The glare ratios

measured for test patterns having known dark spot transmission using a display with no anticipated veiling glare (i.e., the transilluminated film condition described in Section 4B with a maximum luminance of about 2,000 cd/m²) are shown in Table 1. The performance of the conic mask is poor at all distances measured, and worsens with increasing distance d . Observation of the test patterns through the conic mask revealed that light reflected at the entrance tip is responsible for the contamination of the dark luminance measurement. The results for 10 and 20 mm show that the conic mask method is not appropriate for measuring the veiling glare of high performance CRTs. At these distances between the cone tip and the emissive surface, and for the high glare ratios of interest in this work (about 400), the conic mask method fails to accurately determine G due to significant contamination of the dark luminance measurement.

As detailed in Section 5, the performance of the collimated probe permits the accurate measurement of veiling glare ratios for 5 mm radius dark spot test patterns even with 20 mm between the emissive surface and the probe tip.

The authors wish to thank Ed Muka (Mallinckrodt Institute of Radiology) and Ed Kelley (NIST) for their useful comments on the manuscript draft. This work was supported in part by U.S. Army Breast Cancer research grant DAMD17-96-1-6283.

References

1. E. B. Gindele, B. R. Gandhi, and S. L. Shaffer, "A non-linear CRT system simulation model," *Proceedings of the Society for Information Display* pp. 785-788 (1990).
2. A. Badano and M. J. Flynn, "Image degradation by glare in radiologic display devices," *Proceedings of the SPIE* **3031**, 222-231 (1997).
3. J. R. Mansell and A. W. Woodhead, "Contrast loss in image devices due to electron back-scattered from the fluorescent screen," *Journal of Physics D: Applied Physics* **16**, 2269-2278 (1983).
4. G. C. de Vries, "Contrast-enhancement under low ambient illumination," *Proceedings of the Society for Information Display* pp. 32-35 (1995).
5. J. J. van Oekel, "Improving the contrast of CRTs under low ambient illumination with a graphite coating," *Proceedings of the Society for Information Display* pp. 427-430 (1995).
6. J. J. van Oekel *et al.*, "Improving contrast and color saturation of CRTs by Al_2O_3 shadow mask coating," *Proceedings of the Society for Information Display* pp. 436-439 (1997).
7. A. Badano and M. J. Flynn, "Monte Carlo modeling of the luminance spread function in flat panel displays," *International Display Research Conference* pp. 382-385 (1997).
8. J. A. Seibert, O. Nalcioğlu, and W. Roeck, "Characterization of the veiling glare PSF in X-ray image intensified fluoroscopy," *Medical Physics* **11**, 172-179 (1984).
9. H. D. Zeman *et al.*, "Veiling glare of a linear multichannel Si(Li) detector," *Proceedings of the SPIE* **535**, 214-221 (1985).
10. E. Caruthers, "Monte Carlo studies of image spread by X-ray image intensifiers," *Proceedings of the SPIE* **535**, 140-147 (1985).

11. N. Bromberg and J. Bickford, "Veiling glare in the imaging chain," *Proceedings of the SPIE* **454**, 387-391 (1984).
12. S. Matsuda and T. Nitoh, "Flare as applied to photographic lenses," *Applied Optics* **11**, 1850-1856 (1972).
13. C. Beckman, O. Nilsson, and L.-E. Paulsson, "Intraocular light scattering in vision, artistic painting, and photography," *Applied Optics* **33**, 4749-4753 (1994).
14. G. Spencer *et al.*, "Physically-based glare effects for digital images," *Computer Graphics Proceedings, Annual Conference Series SIGGRAPH 95* pp. 325-334 (1995).
15. H. Blume, "Very-high-resolution CRT display systems," *Proceedings of the Society for Information Display* pp. 699-702 (1992).
16. K. Rossmann, "Point-spread function, line-spread function, and modulation transfer function: Tools for the study of imaging systems," *Radiology* **93**, 257-272 (1969).
17. D. A. Baylor and M. G. F. Fuortes, "Electrical responses of single cones in the retina of the turtle," *Journal of Physiology* **207**, 77-92 (1970).
18. R. A. Norman and F. S. Werblin, "Control of retinal sensitivity: light and dark adaptation of vertebrate rods and cones," *Journal of General Physiology* **63**, 37-61 (1974).
19. R. A. Norman and I. Perlman, "The effects of background illumination on the photoreponses of red and green cones," *Journal of General Physiology* **286**, 491-507 (1979).
20. W. S. Stiles and B. H. Crawford, "The luminous efficiency of rays entering the eye pupil at different points," *Proceedings of the Royal Society of London* **122**, 428-450 (1937).
21. M. J. Flynn *et al.*, "Flat panel display technology for high performance radiographic imaging," *Proceedings of the SPIE* **2431**, 360-371 (1995).
22. P. A. Boynton and E. F. Kelley, "Measuring the contrast ratio of displays," *Information Display* **11**, 24-27 (1996).

23. P. A. Boynton and E. F. Kelley, "Accurate contrast-ratio measurements using a cone mask," Proceedings of the Society for Information Display pp. 823-826 (1997).

List of Figures

1	Computer graphic patterns for veiling glare. During the measurements, the bright circular field diameter is maintained constant while the dark spot diameter is varying from 0 up to the bright field diameter.	21
2	Photopic probe and IL 1700 research radiometer for measurements of veiling glare ratio.	22
3	Schematic drawing of the collimated probe showing dimensions in cm and the relative position of apertures and baffles.	23
4	Design drawings for the photopic probe showing aspects of the optical design.	24
5	Experimentally measured probe response values as a function of the opaque spot radius for 2, 10, and 20 mm distance between the tip of the probe and the emissive surface. The factor is expressed as a fraction of the bright region signal. The bright circular region was 320 mm in all cases.	25
6	Experimental data points plotted along with correction function ζ curves for 2, 10, and 20 mm distance d . The range of values showed represents the area where the function $\zeta(r_d, d)$ is defined, namely, $3 \times 10^{-5} < r_d < 1 \times 10^{-3}$, and $3 \text{ mm} < d < 10 \text{ mm}$. The error bars represent a standard deviation of 20 consecutive measurements recorded at each point with the photometer. . . .	26
7	Inverse veiling glare ratios measured for test patterns on radiographic film at a distance of 5 and 15 mm. The values for $1/G$ were computed by subtracting the known G_d and the correction factor ζ (see Equation 8) for each dark spot diameter. Due to the veiling glare characteristics of radiographic film, the small values of $1/G$ for radii greater than 10 mm relate to the error introduced by the method.	27
8	Veiling glare ratio for a medical imaging CRT measured at a distance of 1 mm from the faceplate surface.	28

9	Ring response function for the medical imaging CRT. The magnitude of the tails caused by light transport processes that occur in the display emissive structures can be measured using this approach.	29
---	---	----

List of Tables

- 1 Experimental veiling glare ratios for test patterns printed on film with known dark spot transmission, measured with the collimated probe presented in this paper and with a method based on a conic mask. The true value of G was determined to be 478.6 based on optical density measurements using a film densitometer. Measurement errors are estimated from the standard deviation of 10 consecutive measurements. 30

FIGURES

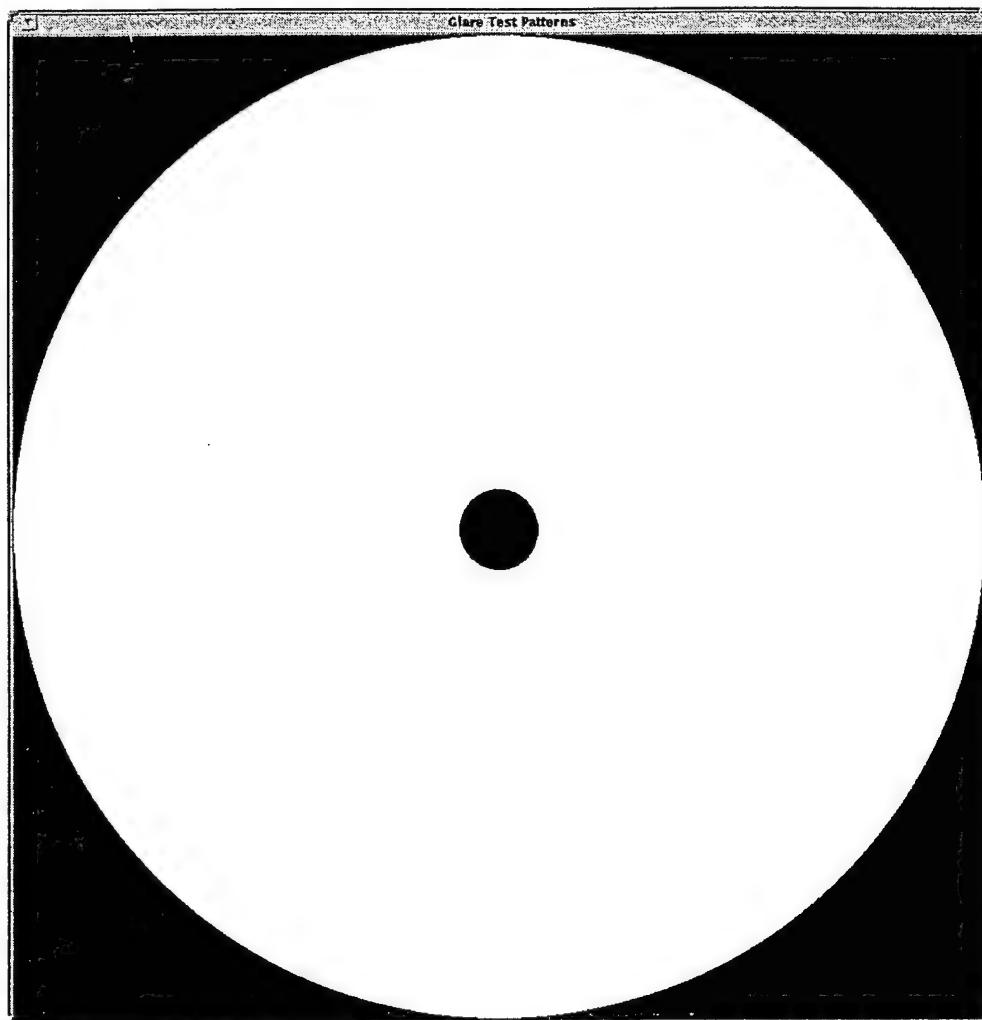


Fig. 1. Computer graphic patterns for veiling glare. During the measurements, the bright circular field diameter is maintained constant while the dark spot diameter is varying from 0 up to the bright field diameter.

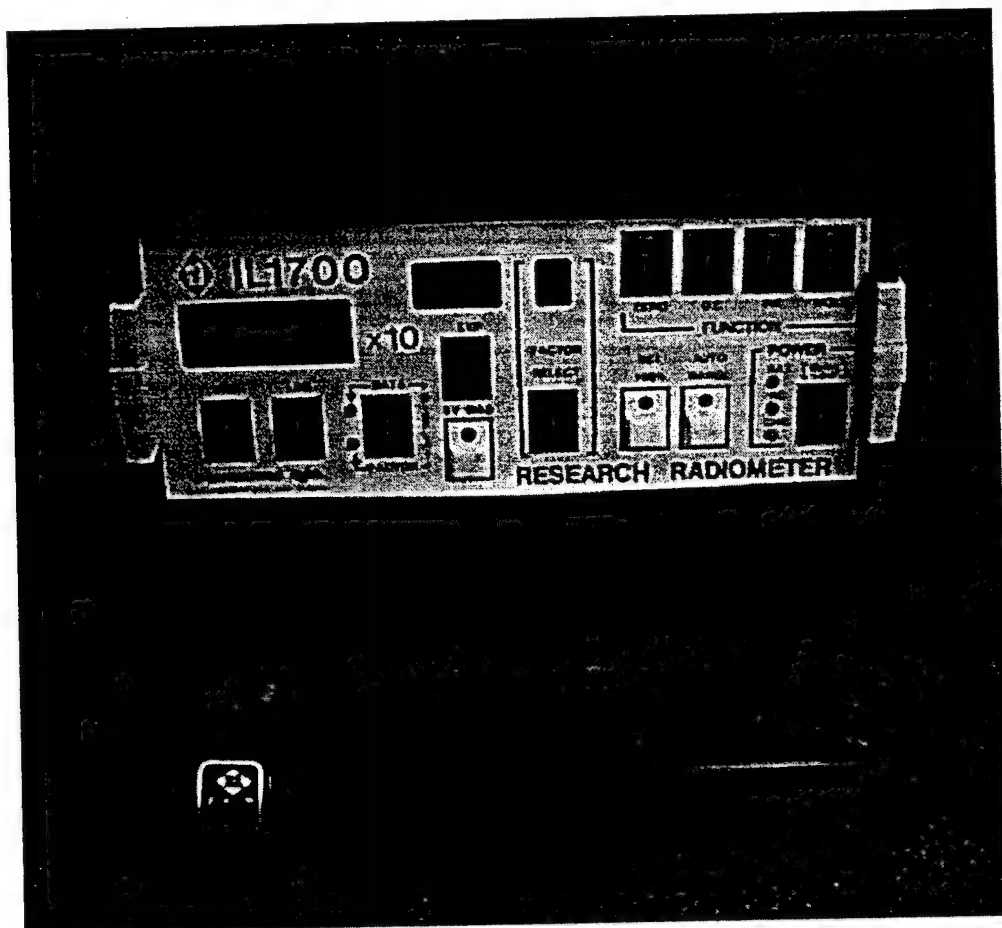


Fig. 2. Photopic probe and IL 1700 research radiometer for measurements of veiling glare ratio.

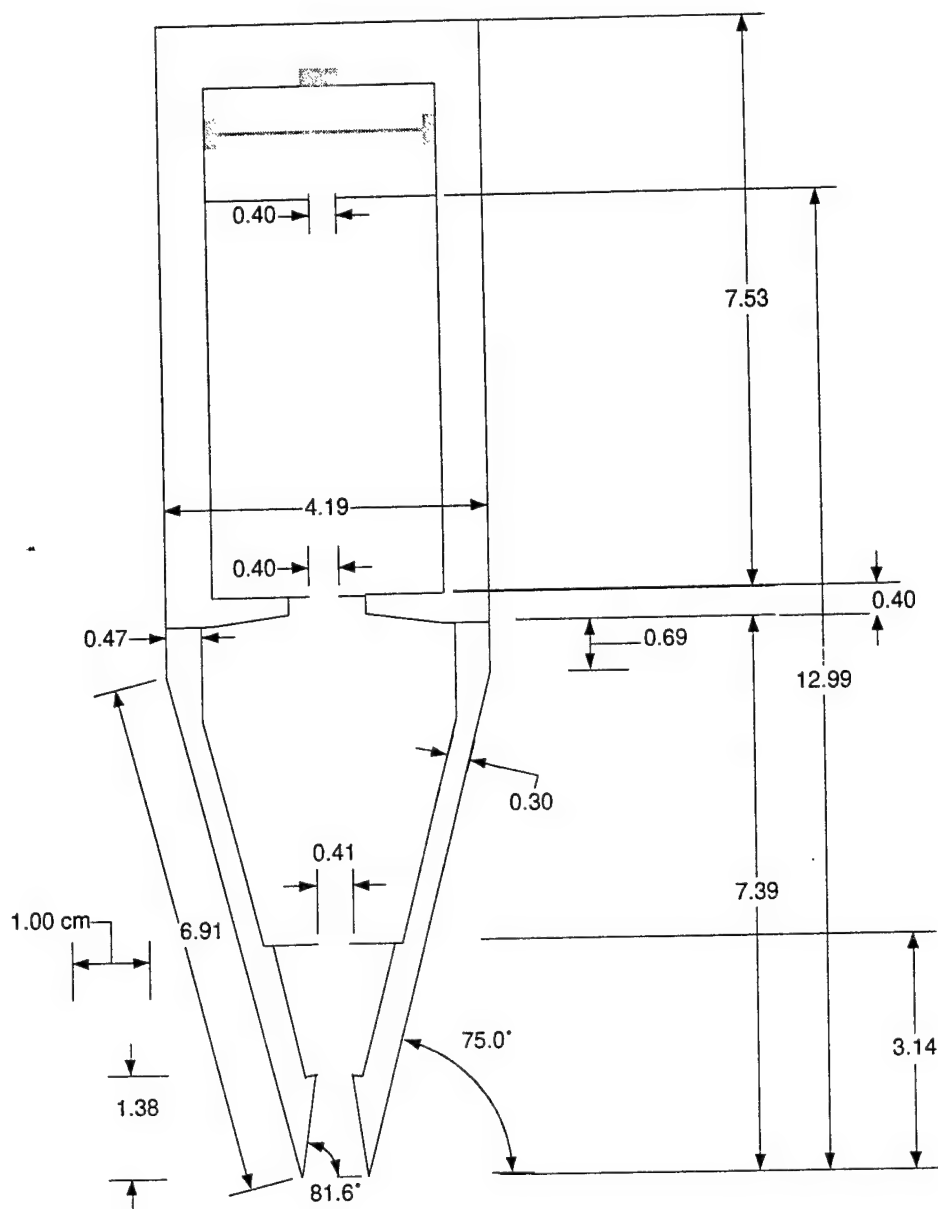
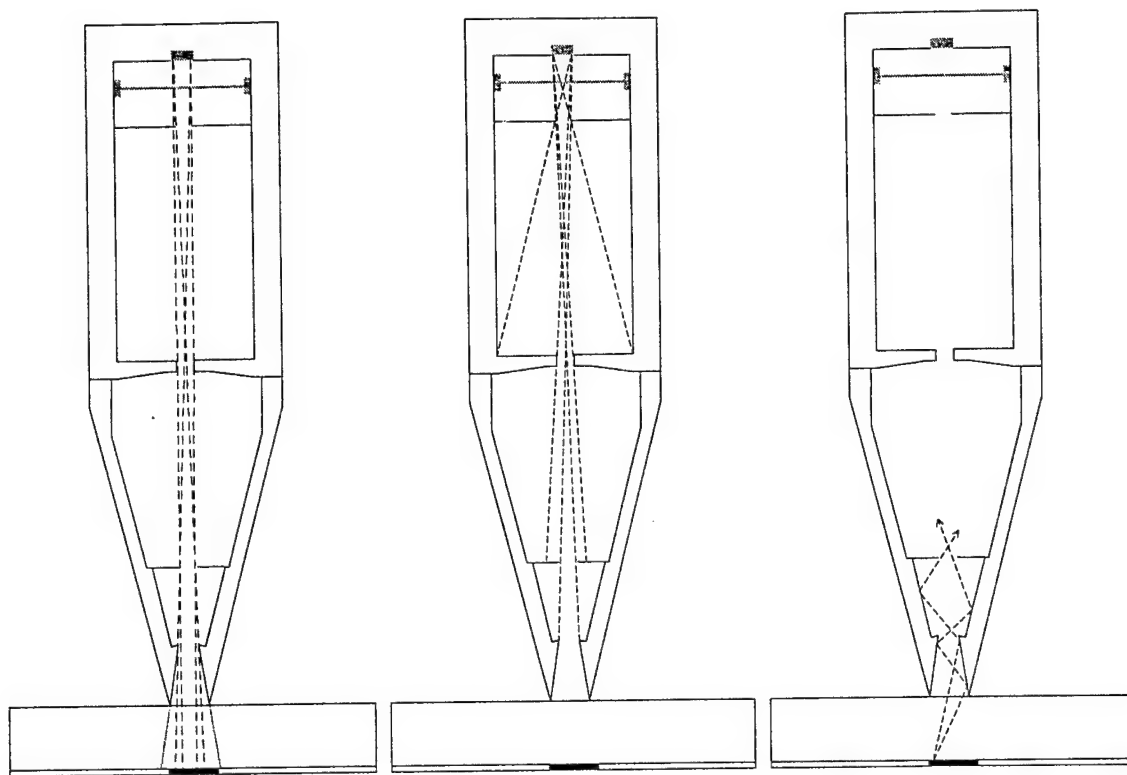


Fig. 3. Schematic drawing of the collimated probe showing dimensions in cm and the relative position of apertures and baffles.



(a) Principal rays that define the detector direct field of view.

(b) Baffle positioning and back surfaces viewed by the detector.

(c) Scattered rays absorbed by multiple reflections in the conic probe.

Fig. 4. Design drawings for the photopic probe showing aspects of the optical design.

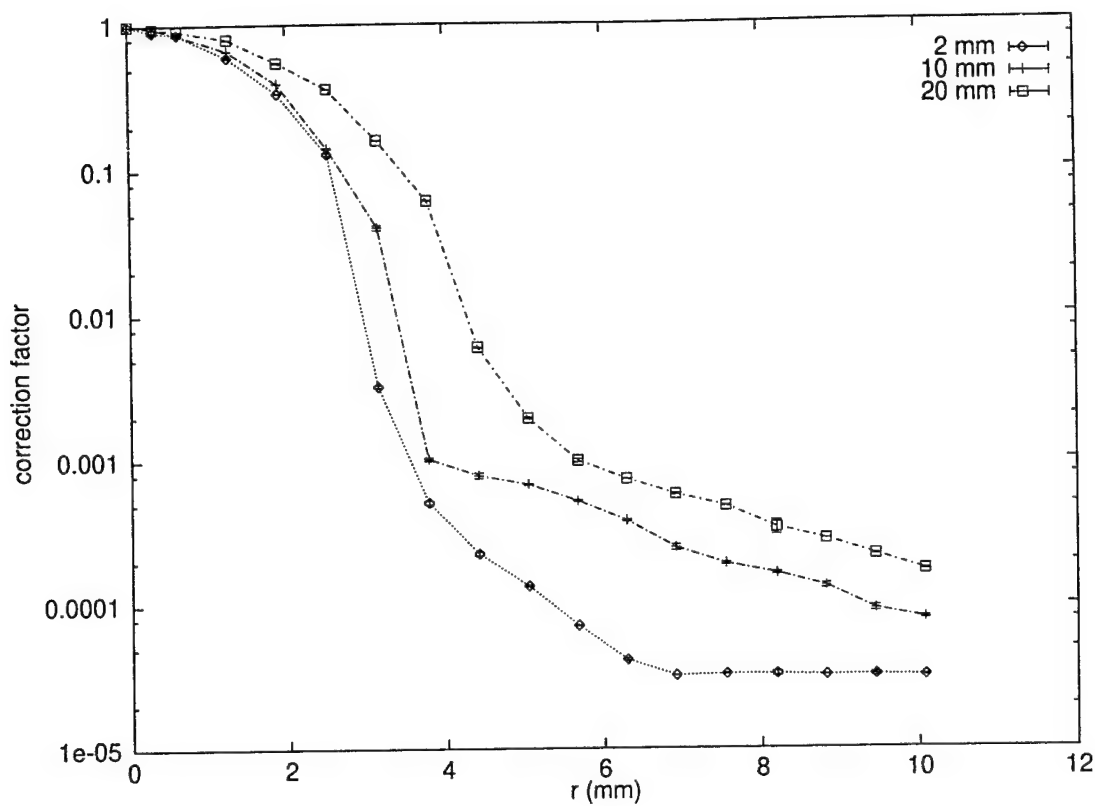


Fig. 5. Experimentally measured probe response values as a function of the opaque spot radius for 2, 10, and 20 mm distance between the tip of the probe and the emissive surface. The factor is expressed as a fraction of the bright region signal. The bright circular region was 320 mm in all cases.

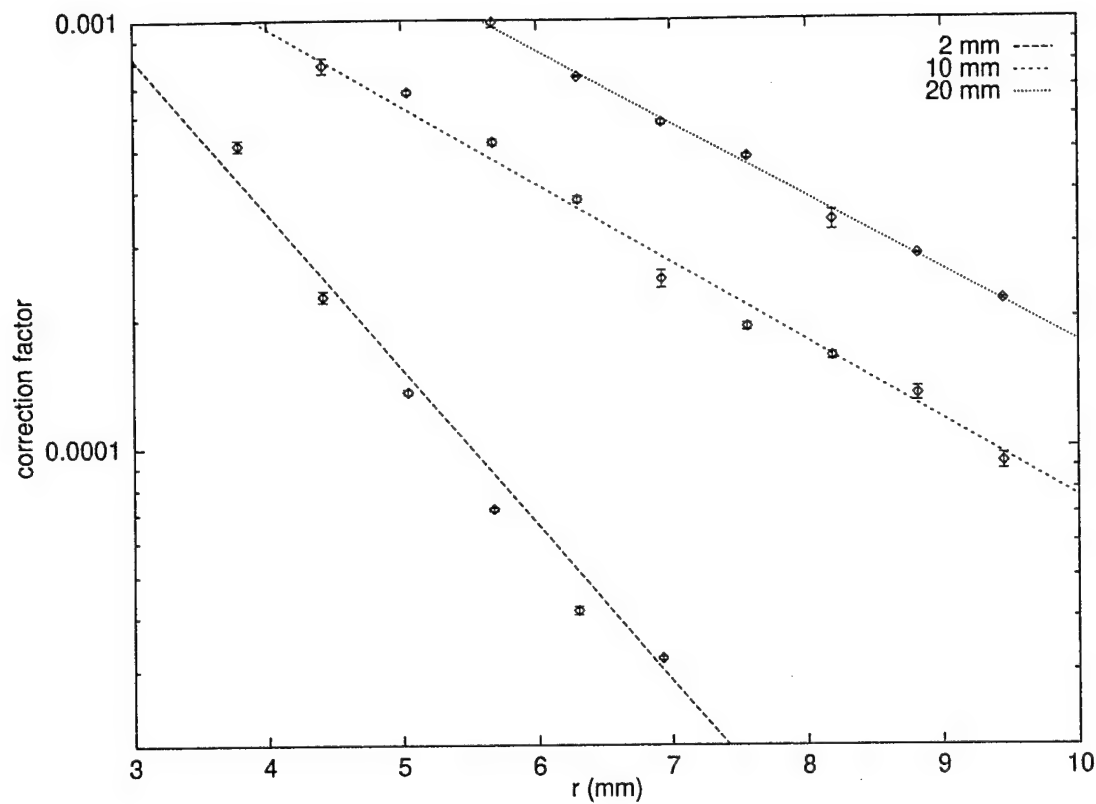


Fig. 6. Experimental data points plotted along with correction function ζ curves for 2, 10, and 20 mm distance d . The range of values showed represents the area where the function $\zeta(r_d, d)$ is defined, namely, $3 \times 10^{-5} < r_d < 1 \times 10^{-3}$, and $3 \text{ mm} < d < 10 \text{ mm}$. The error bars represent a standard deviation of 20 consecutive measurements recorded at each point with the photometer.

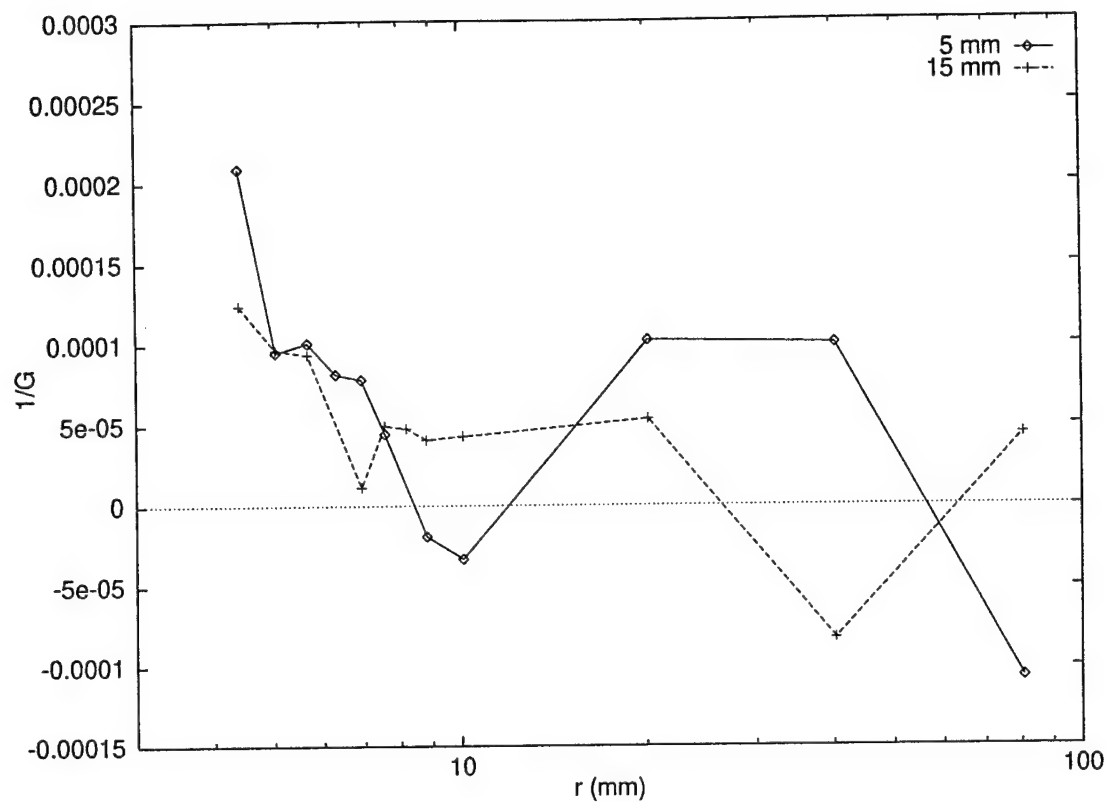


Fig. 7. Inverse veiling glare ratios measured for test patterns on radiographic film at a distance of 5 and 15 mm. The values for $1/G$ were computed by subtracting the known G_d and the correction factor ζ (see Equation 8) for each dark spot diameter. Due to the veiling glare characteristics of radiographic film, the small values of $1/G$ for radii greater than 10 mm relate to the error introduced by the method.

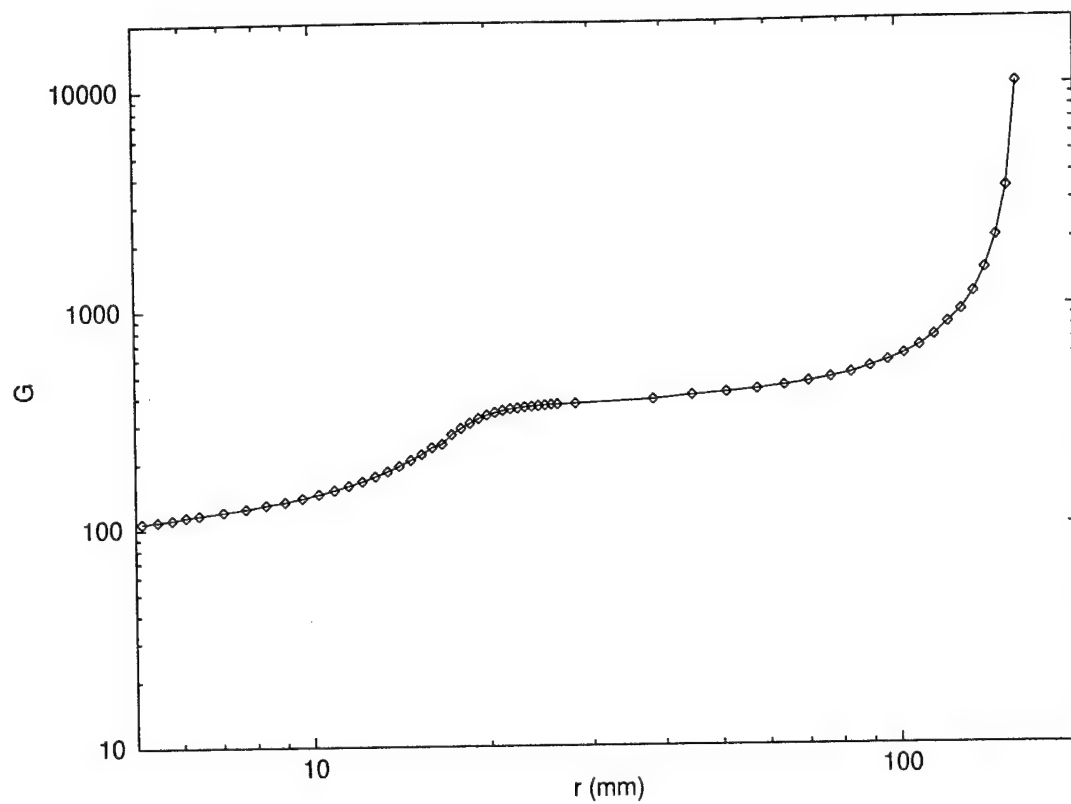


Fig. 8. Veiling glare ratio for a medical imaging CRT measured at a distance of 1 mm from the faceplate surface.

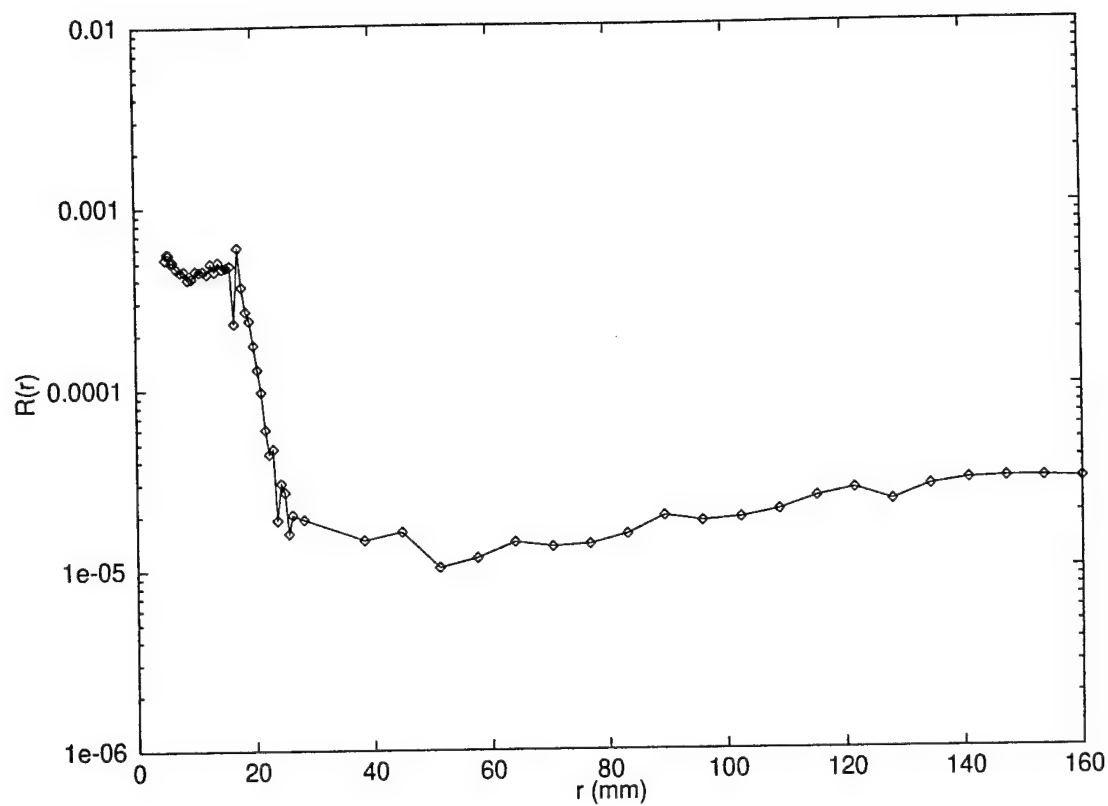


Fig. 9. Ring response function for the medical imaging CRT. The magnitude of the tails caused by light transport processes that occur in the display emissive structures can be measured using this approach.

TABLES

Table 1. Experimental veiling glare ratios for test patterns printed on film with known dark spot transmission, measured with the collimated probe presented in this paper and with a method based on a conic mask. The true value of G was determined to be 478.6 based on optical density measurements using a film densitometer. Measurement errors are estimated from the standard deviation of 10 consecutive measurements.

d (mm)	2	10	20
G with conic mask	373 ± 26	161 ± 12	106 ± 9
G with collimated probe	474 ± 1	474 ± 1	479 ± 1

HIGH FIDELITY ELECTRONIC DISPLAY OF DIGITAL RADIOGRAPHS

Michael J. Flynn ^{1,2}, Jerzy Kanicki ³,
Aldo Badano ^{1,2}, William R. Eyler ¹

¹ Department of Diagnostic Radiology, Henry Ford Health System

² Nuclear Eng. and Radiological Sciences Dept., University of Michigan

³ Display Technology and Manufacturing Center, University of Michigan



This exhibit will:



- ♦ Define high fidelity display requirements which are based on the performance limits of the human visual system.
- ♦ Summarize the design limitations of cathode-ray tube (CRT) monitors and identify methods being used to improve CRT performance.
- ♦ Review flat panel display technologies being developed to replace CRTs (active matrix liquid crystal, field emission and electroluminescence), and evaluate their potential for high display quality.

Scientific Exhibit presented at the 83rd Scientific Assembly and Annual Meeting
of the Radiological Society of North America, November 1997.

Certificate of Merit Award winner.

Invited for publication in Radiographics.

Note: The quality of the images shown in this paper print may not appropriately reflect the illustrated principle, since they were designed to be displayed with radiographic film in a bright viewbox.

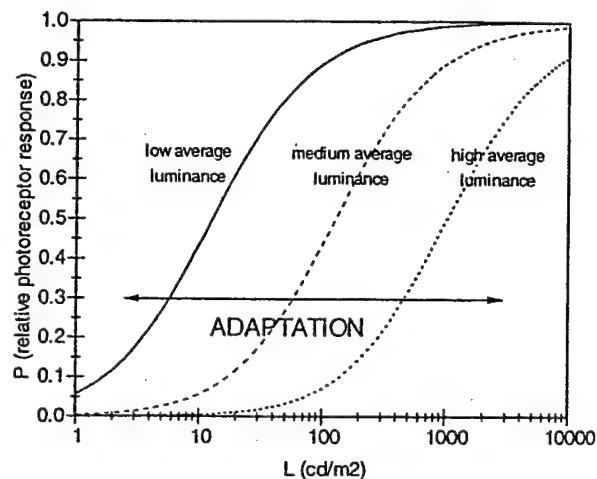
LUMINANCE RANGE

DISPLAY BRIGHTNESS MEASURES

Luminance is a photometric measurement unit reflecting the brightness of a small region on a display surface. The SI unit of brightness is the nit, which is a candela per square meter (cd/m^2). 1 Cd/m^2 is equal to 0.2919 foot-lambert (fL).

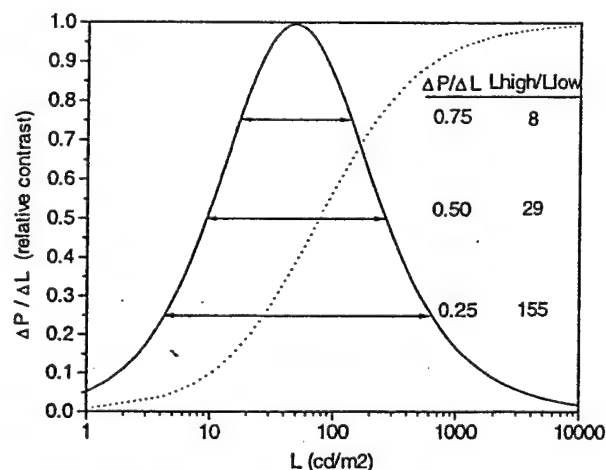
VISUAL ADAPTATION

The human visual system will adjust its response to accommodate the average luminance of the scene observed. Animal experiments have been used to describe this adaptation.^{1,2} Illustrated to the right is the measured rate of neuronal signals for individual nerve channels connecting the eye to the brain.



CONTRAST RESPONSE

When the observer is adapted to a particular average luminance, the change in neuronal rate associated with a small change in luminance is a biologic indication of contrast response. This response is maximal near the average luminance and is markedly reduced for regions in the scene with higher or lower luminance.



DISPLAY LUMINANCE RANGE

The display of intensity information over a wide range of luminance results in images with high contrast (large $\Delta L/L$ for a given image intensity change). However, the luminance range is limited by the observer contrast response.

WHAT RANGE OF BRIGHTNESS SHOULD A RADIOLOGIC DISPLAY HAVE?

Display luminance should be within a range of 100 ($L_{\text{high}}/L_{\text{low}}$) to maintain good contrast response. In order to display contrast up to 0.5 ($\Delta L/L$) at these limits, the maximum luminance should be 200 times brighter than the minimum luminance.

[1] R. A. Norman and I. Perlman. J. Gen. Physiol., 286:491-507, 1979.

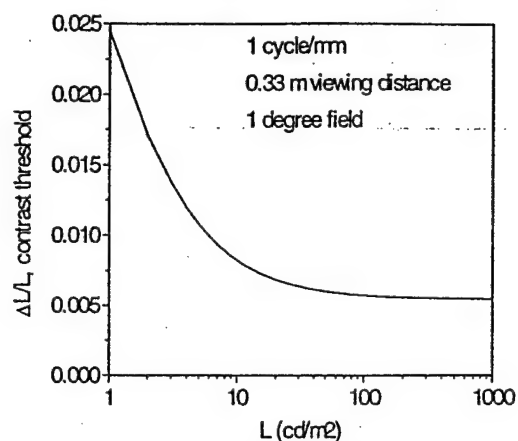
[2] R. A. Norman and F. S. Werblin. J. Gen. Physiol., 63:37-61, 1974.

GREYSCALE AND CONTRAST

The contrast of a test pattern is defined as the relative change in luminance, $\Delta L/L$, and not as the absolute change in luminance.

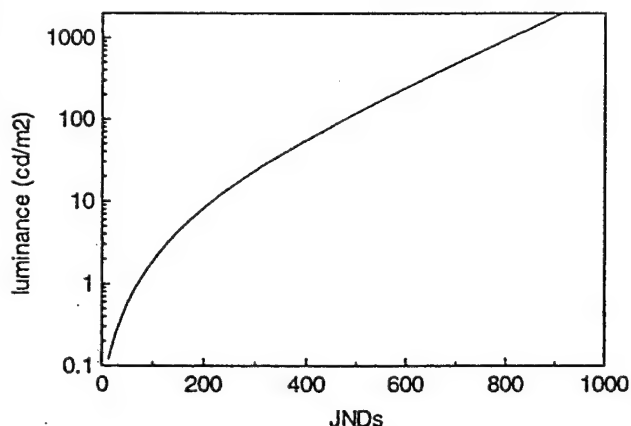
CONTRAST THRESHOLD

Psychovisual experiments have established how much contrast is required to detect a test pattern having a sinusoidal variation in luminance ($\Delta L/L$) superimposed on a uniform background. The threshold contrast is dependent on luminance and spatial frequency as well as other parameters of secondary influence. At a spatial frequency of 1 cycle/mm where the observer has good response, the contrast threshold is nearly constant at high luminance and is poorer below 10 cd/m^2 (see figure on the right).²



LINEAR PERCEPTION OF CONTRAST

Digital images are displayed with a greyscale that maps the image value (IV) to display luminance. At high luminance where the threshold contrast ($\Delta L/L$) is constant, a greyscale map for which $\log(\text{luminance}) = \text{IV}$ will produce uniform contrast. However, for many display systems, the dim regions occur at a luminance where the contrast threshold is poor. A greyscale map can be defined such that each increment in IV causes a just noticeable difference in luminance (see the figure at the left)². For a display with a maximum luminance of 1000 cd/m^2 and a minimum luminance of 5 cd/m^2 there are about 600 just noticeable difference increments (JNDs).



WHEN IS QUANTUM NOISE VISIBLE?

For digital radiography, quantum noise often exceeds the contrast threshold and is visually apparent. For the noise power spectra associated with typical computed radiography systems, the noise amplitude exceeds the visual threshold (0.007 at 100 cd/m^2) when the noise-equivalent quanta (NEQ) is equal to about 80,000 and the image is displayed using a transformation curve having a gamma of 2.0. This occurs with 1.5 mR exposure to a CR plate (80 kVp filtered beam).

WHAT SHOULD THE MAXIMUM LUMINANCE OF A DISPLAY BE?

For a display system with a luminance range of 200, a maximum luminance of 1000 cd/m^2 provides good contrast performance.

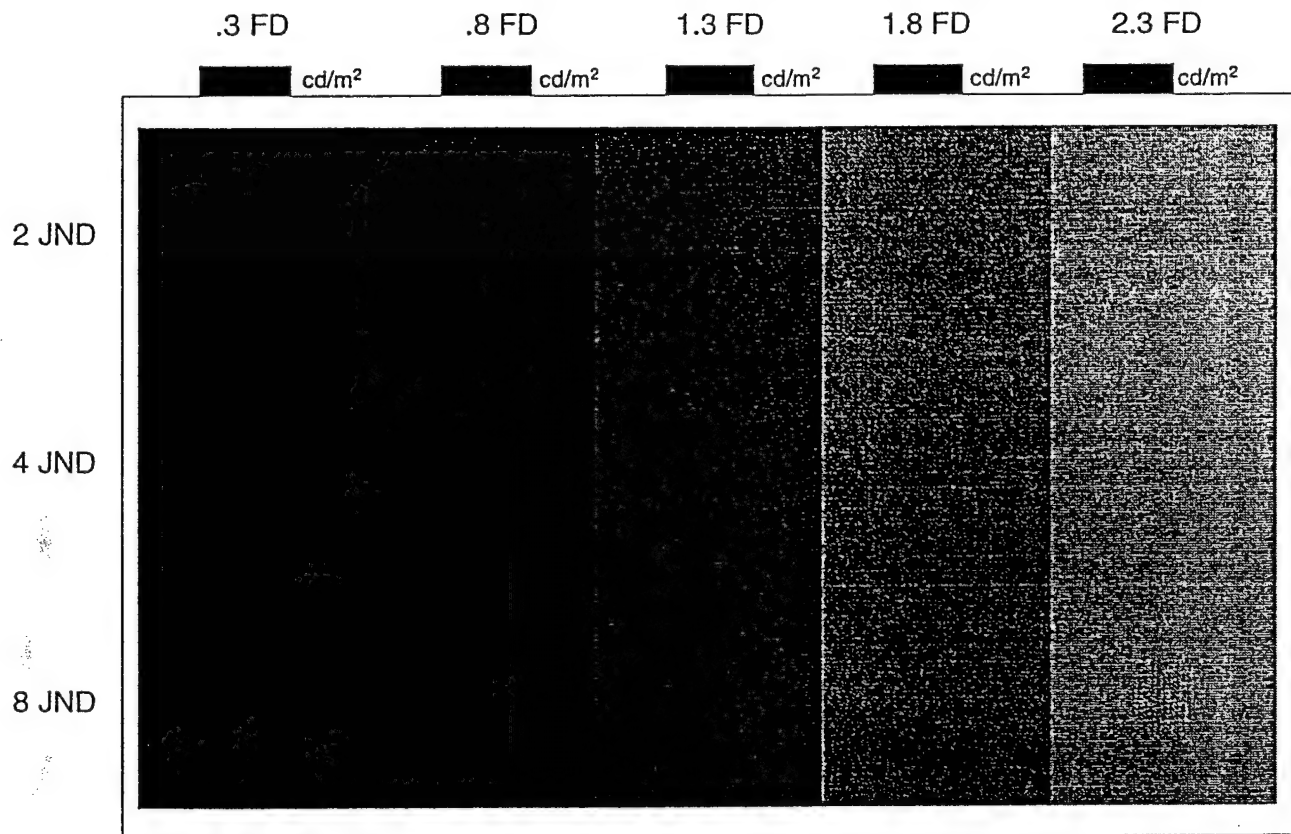
L_{low} (cd/m²)	L_{high} (cd/m²)	JNDs
0.5	100	430
1	200	500
2	400	567
5	1000	630
10	2000	700
20	4000	740

[1] P. G. J. Barten, Proceedings of SPIE vol. 1666, 1992.

[2] ACR/NEMA, Greyscale display function standard, ACR/NEMA Working Group XI, Working Draft Version 1.2, March 27, 1997.

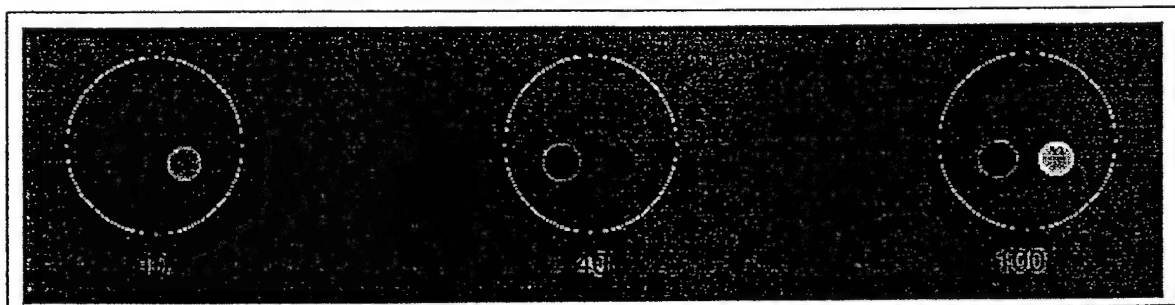
LINEAR PERCEPTION

Display systems typically use a greyscale for which the log of the display luminance and thus the relative contrast, $\Delta L/L$, is proportional to the signal value. Transilluminated film has this characteristic. Because the contrast response of the human eye is not as good at low luminance, the dark portions of an image will have poor contrast unless the display enhances contrast in these regions. In the test pattern below, contrast at a film density (FD) of 2.3 has been increased by 73% relative to that at a density of .3 using the linear perception greyscale described at the left.



DYNAMIC RANGE

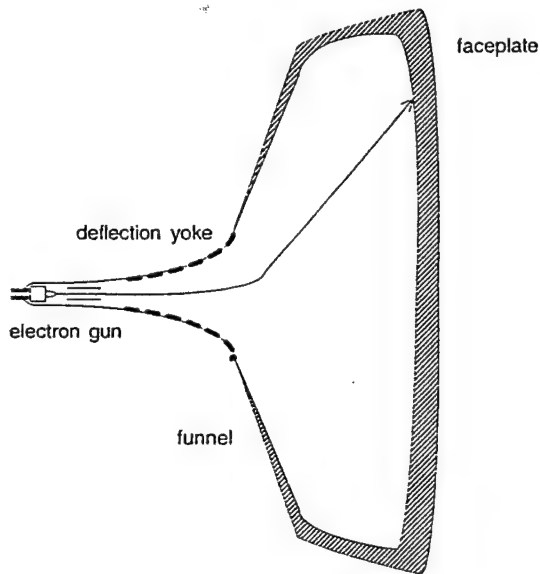
In the example above, the large size of the test pattern allows the eye to adapt to the luminance in each of the subregions. The region of foveal response and eye adaptation is primarily located in a region of 3 cm diameter. Within this region, contrast at high or low luminance relative to the average may be reduced by the limited range of neuronal signal between the eye and the brain. In the three regions below the luminance dynamic range $L_{\text{high}}/L_{\text{low}}$ is 10, 40, and 100.



CRT DEVICES

Although CRT is a mature technology, improvements in device performance are presently being sought. Active research topics include advanced electron gun and deflection lens design, emissive structures, and shadow mask coatings.

DESIGN CHARACTERISTICS



Electrons are accelerated within the large vacuum bulb with a high voltage of up to 30 kV. The beam scans the plate in a raster fashion, exciting the cathodoluminescent phosphor with a small beam spot. To reduce the stress, thick glass is used for the funnel and plate. For a relatively flat faceplate with 29" diagonal bulbs, 13.7 mm thick glass is typically used.²

GENERAL PROBLEMS

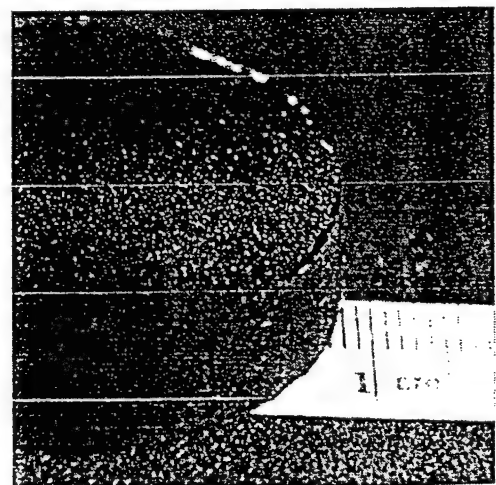
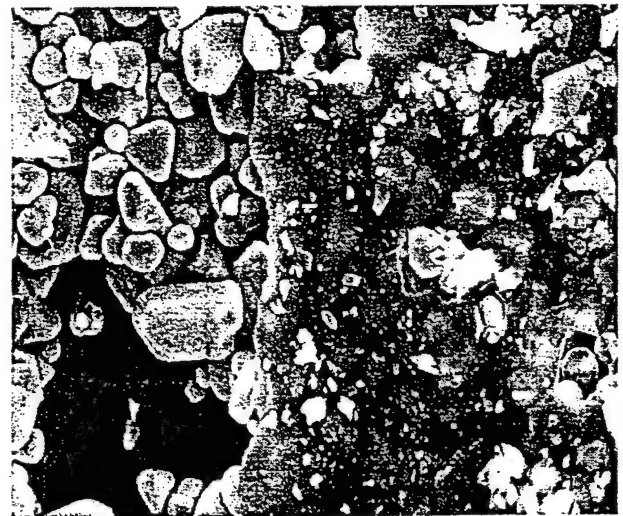
To obtain adequate brightness, high current beam is deflected, while maintaining a small focal spot that is related to the display resolution. The thick faceplate results in image quality degradation by glare, and contributes to the weight of the device.

EMISSIVE STRUCTURE COMPONENTS

- Typical CRT emissive structures consist of a cathodoluminescent material (phosphor) deposited onto a glass faceplate panel as a powder layer. In color tubes, a highly light absorbent, carbon based black matrix separate the RGB phosphor dots for color purity.

- A sub-micron thin layer of Al is overlayed on top of the phosphor to conduct the incoming electron current and maximize light output towards the viewer. For this, a filming material is used to assure a smooth, continuous and highly reflective film. The top figure on the right shows a scanning electron microscope image of the emissive structure of a monochrome CRT, where multiple layers of phosphor grains can be observed under the thin Al coating.

- The glass faceplate can absorb up to 37% of the direct light improving contrast, and may have a rough surface on the vacuum side to reduce specular reflections. The bottom figure on the right shows a photograph of the interior surface of a CRT faceplate sample after the Al and phosphor layers were removed.



[1] A. Badano, E. Samei, M. J. Flynn and K. J. Kearfott, SPIE Medical Imaging, 1996.
[2] A. Imamura, T. Ikoma, H. Makio, K. Kikuchi, SID'92 Digest.

GLARE

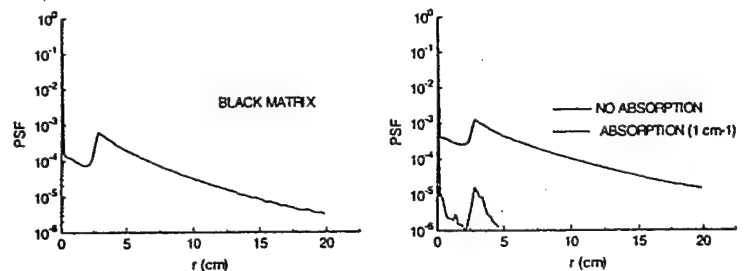
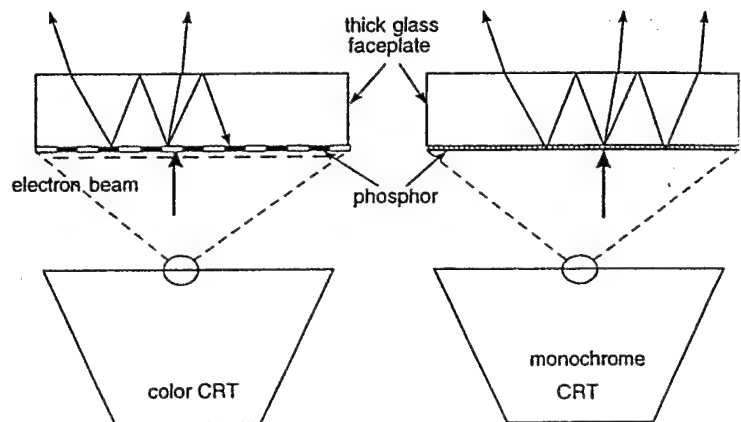
Glare is a diffuse spreading of light that results from multiple scattering processes in emissive display devices. Low frequency degradation of image quality (perceived as contrast reduction) is observed when no glare reduction features are employed in the device design.

LUMINANCE SPREAD IN FACEPLATE

Light rays generated in the phosphor grains must undergo multiple scatterings before escaping the emissive structure and eventually being detected by the observer. Light diffusion in the emissive structure multiple layers results in luminance spread functions with tails that extend up to a distance of 20 cm. When wide luminance range images are displayed, this diffuse component over large areas degrades the maximum contrast capabilities of the device.

POINT-SPREAD FUNCTION CHARACTERISTICS

The figure on the right shows luminance spread functions for a 16 mm thick faceplate with and without black matrix (BM), computed with a light transport Monte Carlo code (DETECT-II).¹ The plots illustrate that reduction of the tail of the functions can be achieved by increasing faceplate glass absorption or by using BM.^{1,2}

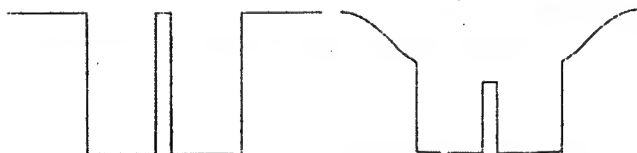
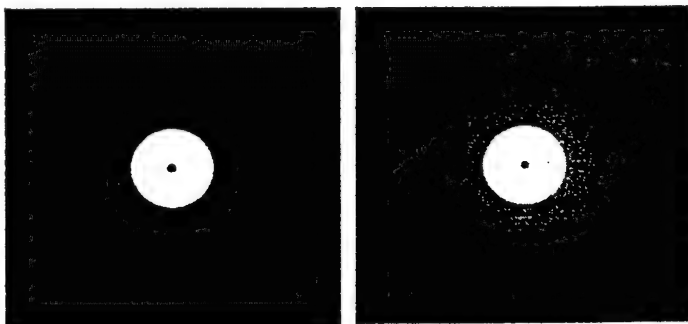


CONTRAST REDUCTION BY GLARE

On the left, the effect of glare degradation has been simulated. The circular test pattern (non degraded) has been convolved with a point-spread function typical of conventional CRTs. The pattern on the right depicts the expected reduction in contrast. The diffuse component is clearly observed in the image data profiles shown below.

OTHER CONTRIBUTING FACTORS

Another source of image quality degradation in CRTs can come from Al layer non-uniformities (cracks, holes) that may result in light leakage. In addition, electron backscattering in the emissive structure and in components such as aperture grille and shadow mask has been identified as responsible for a reduction in contrast and poor color saturation.^{3,4}

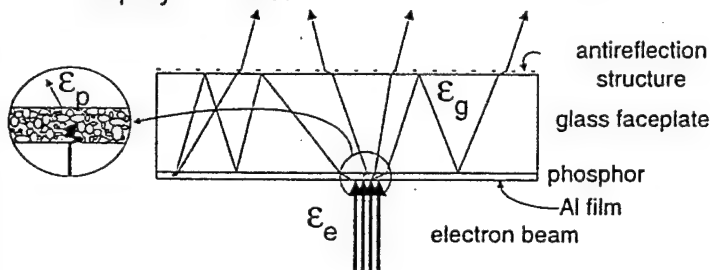


- [1] A. Badano, and M. J. Flynn, SPIE Medical Imaging, 1997.
- [2] A. Badano, and M. J. Flynn, International Display Research Conference, 1997.
- [3] J. J. van Oekel, SID'95 Digest.
- [4] G. C. de Vries, SID'95 Digest.

CRT PHOSPHORS

LUMINOUS EFFICIENCY

Cathodoluminescent phosphors convert energy deposited by energetic electrons to light. Electrons penetrate a cover layer and travel into individual phosphor grains. Light then scatters within the emissive structure until escaping from the display surface.



The total luminous efficiency is computed as a linear combination of efficiencies and a photopic correction $K\lambda$.

$$E_l = K\lambda \cdot \epsilon_e \cdot \epsilon_p \cdot \epsilon_g$$

- ϵ_e energy deposition efficiency
- ϵ_p energy quantum efficiency
- ϵ_g escape efficiency

For typical devices, E_l is 20.8 lm/W for P104 phosphors and 13.5 lm/W for P45.

DISPLAY BRIGHTNESS

Total display brightness is a function of the electron beam power (p_i , W), the display area (a_i , m^2), and the luminous efficiency (E_l , lm/W).

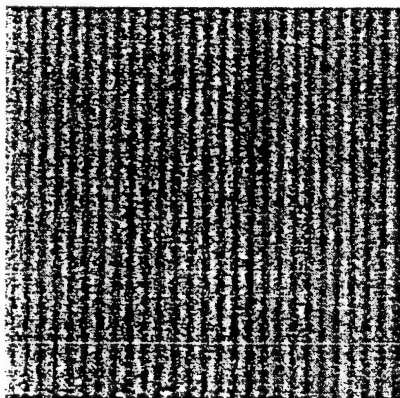
$$L = \frac{E_l \cdot p_i}{\pi \cdot a_i}$$

For example, a CRT with a display area of 0.3 m by 0.4 m, an 1 mA electron beam accelerated to 20,000 V (20 W), and a phosphor emissive layer with an efficiency of 10 lm/watt will have a display brightness of 530 cd/ m^2 .

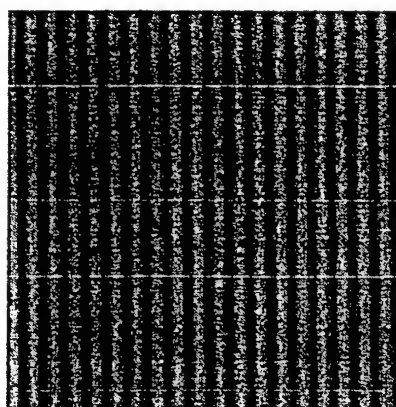
COLOR OR GREY

Current models of eye-brain function indicate that humans depend on display brightness for interpreting contrast and detail in a scene (ref). Color is evaluated from separate eye receptors and interpreted as a low resolution difference signal (R-G and Y-B). It is generally thought that medical radiographic inspection of detailed scenes as encountered in medical radiography is best done with a display having a constant broad light spectrum perceived as white and various shades of grey.

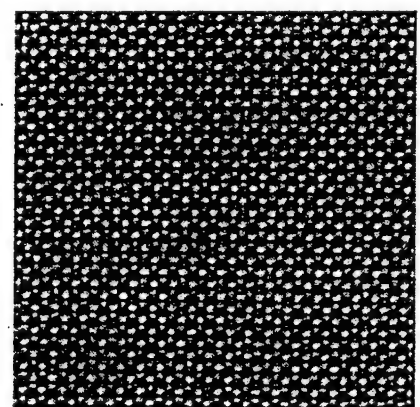
Illustrated below are highly magnified recordings of a uniform grey region (5 mm diameter) from 3 CRT devices:



A. Some high brightness phosphors, notably P104, contain a mixture of phosphors with different color and often produce a noisy image.



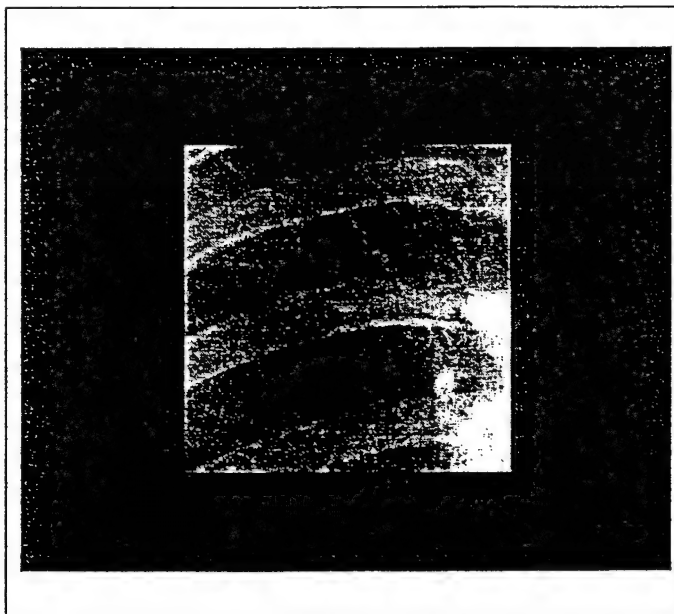
B. Phosphors which naturally emit a broad spectrum, such as P45, typically have reduced luminous efficiency.



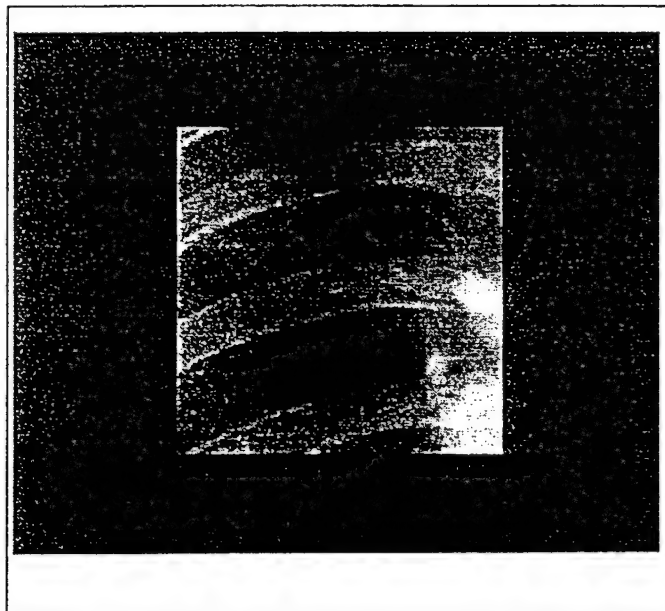
C. Color monitors rely on simultaneous stimulation of red, green, and blue phosphors to simulate a white or grey emission. To date, the color matrix technology has not been exploited by loading each cell with a high luminosity white phosphor.

DEGRADATION BY NOISE, GLARE AND LOW LUMINANCE

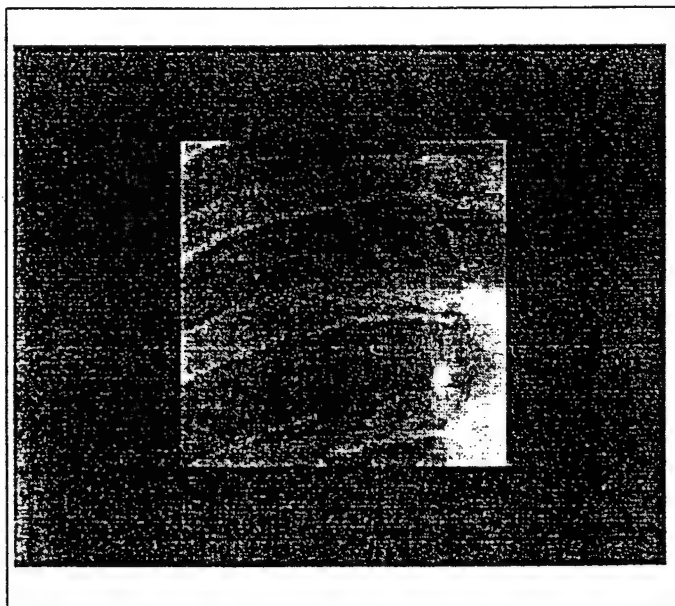
ORIGINAL QUALITY: This image was extracted from the digital radiography data of a chest study obtained using a storage phosphor system having a $200\text{ }\mu\text{m}$ pixel size. It is printed with 80% size reduction using a typical radiographic greyscale. The maximum density in the lung of the image is about 2.0. The minimum luminance for display with this exhibit is thus about 10 cd/m^2 .



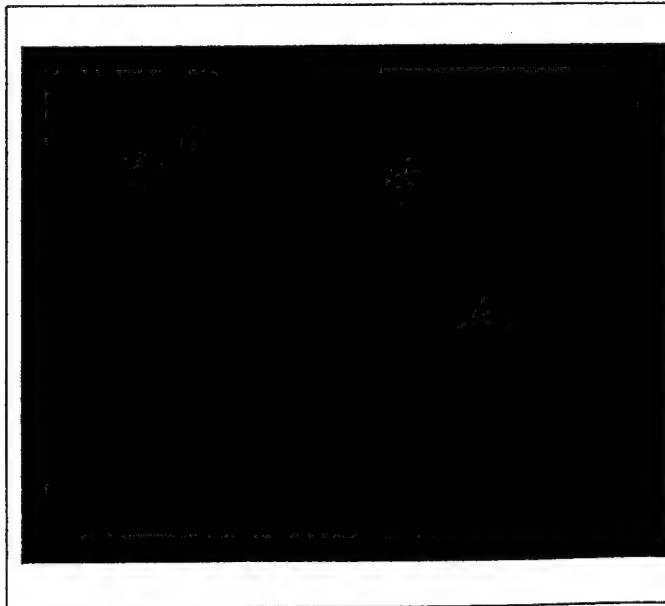
NOISE: Noise simulating phosphor granularity has been added to degrade the quality of this image. The added noise has a fluctuation of about 5 percent (± 1 std. dev.) corresponding to a noise equivalent quanta of $10,000\text{ \#/mm}^2$.



GLARE: The effects of glare have been simulated by adding a constant quantity of luminance to all regions of this image. This is done by converting film density to luminance, adding a constant, and converting back to luminance. The amplitude of the glare degrading this image is 30 cd/m^2 .



LOW LUMINANCE: Finally, we have simulated the appearance of a display with low luminance by increasing the film density of the exhibit page. If the exhibit backlight has a luminance of $2,000\text{ cd/m}^2$, the maximum luminance of the display that this image would appear on would be about 125 cd/m^2 .

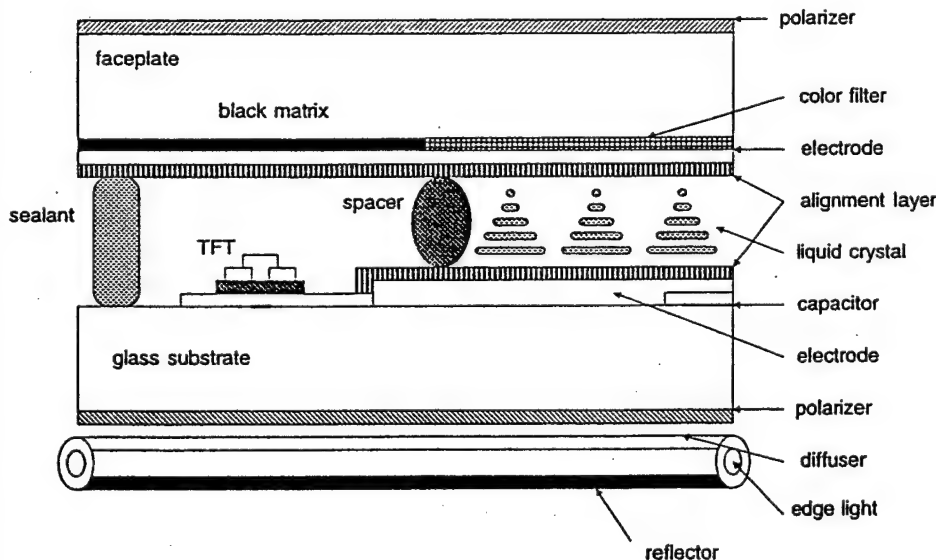


AMLCD DEVICES

AMLCD is an industry term for active-matrix liquid crystal display.

OVERVIEW

When the molecule orientation within a liquid crystal (LC) is changed by the application of an electric field, the optical characteristics of the LC cell change. This electro-optical effect is used to modulate light transmission in LCDs. Light is emitted from the backlight, directed to the front and transmitted through the LC cell (see drawing below). The transmission is thus associated with the state of polarization of the light as it passes through the polarizer films and LC layer. In an active-matrix LCD, the switch between ON- and OFF-state is controlled by a thin-film transistor deposited onto the glass substrate.

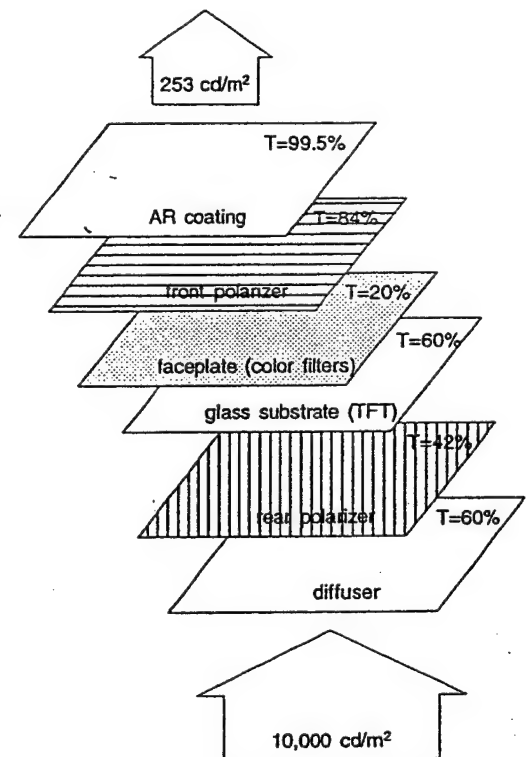


STATUS

a-Si:H TFT-LCD displays are now larger with higher resolution and increased grey scales. Different companies have produced full color AMLCDs up to 1 m (40") in diagonal having SXGA resolution (1280 x 1024), and brightness up to 250 cd/m².

GENERAL PROBLEMS

- As shown in the diagram below, multiple layers are needed to effectively modulate display luminance. Overall transmission is poor with values from 3 to 5% for full color TFT-LCDs, and up to 15 % in monochrome (black and white) designs. High efficiency backlights are needed for a high brightness displays.
- LCs are optically anisotropic. Full ON- and OFF-states ("black" and "white") have typically good angle of view. However, for intermediate greylevels the emission distribution is severely affected.
- Other problems include gate signal distortion for large area displays, lifetime, and temperature sensitivity.

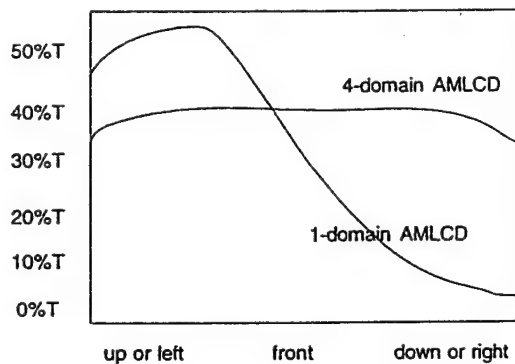


AMLCD TECHNOLOGICAL TREND

To use AMLCD in medical applications, the viewing angle, brightness, contrast ratio, and number of grey levels must be improved.

WIDENING OF THE VIEWING ANGLE

Since light transmitted through the LC cell can follow paths with different lengths and directions, the effective transmission depends on its emission angle, as seen in the figure below. Solutions that provide a more uniform response include: optically negative compensation plate, half-tone method, optically compensated birefringence mode utilizing a bent alignment cell (π -cell). The figure below illustrates typical improvements with a multidomain design.



IMPROVING DISPLAY BRIGHTNESS

Transmitted light intensity is limited by the polarizers, color filters, and other layers. It is also restricted by the geometric aperture ratio of the pixel cell. One method to improve pixel electrode aperture ratio is to reduce the ITO pixel electrode to bus line separation (see figure on the right). The figure on the bottom of this page shows a TFT design with overlap between ITO and bus lines.

LARGER SIZE AND HIGHER RESOLUTION

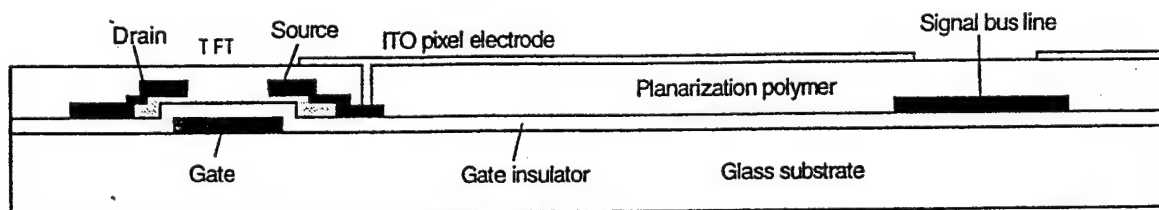
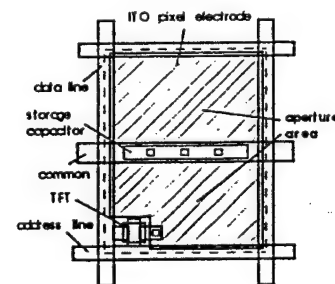
As the gate signal reach the other end of the gate line conducting path, it suffers an time delay of about $\tau=RC$. This limits display size and resolution. For large area high resolution displays, Cu or Al metalization must be used. Monochrome displays 13" in size, with 3072 x 2048 pixel array, and pixel pitch of 90 μm have been developed.

INCREASE OF CONTRAST

Currently, the twisted-nematic mode is widely being used in LCDs. It has realized a high pixel contrast ratio of 100:1, viewed from the front. This has been attained by improving the polarizers, reducing the dispersion of pigments in color filters, and by adding a black matrix layer.

LOW POWER CONSUMPTION

In order to realize low power consumption, improvements must be made in transmittance ratio, efficiency of the backlight, and driving circuits power requirements.



FED TECHNOLOGY

FEDs are similar to CRTs in that electrons are emitted from a cathode and accelerated towards the phosphor through a vacuum cell. However, rather than using thermionic emission, electrons are emitted by a field emission process.

OVERVIEW

- In a field emission display (FED), each pixel has its own electron source that typically consists of a large array of low work function emitter microtips. Electrons are accelerated through a vacuum cell to impinge on a cathodoluminescent phosphor. Instead of using a diode arrangement with proximity focusing, a focus electrode can be incorporated to decrease beam spot size and increase resolution (see cross-section in this page). While most FEDs use metal microtips, amorphous diamond has shown good current - voltage characteristics, however, the emission mechanism is not well understood.

- Most FED designs must be evacuated to low pressures (10^{-7} torr) to prevent contamination and deterioration of the electron emitters. Large display sizes thus need spacers to prevent bending of the faceplate. In low voltage approaches, small spherical spacers can be used. For high voltage operation with large gaps, high aspect ratio spacers are being developed.¹

- An FED faceplate usually consists of a thin glass panel, a conductive layer, and a phosphor (i.e., $Y_2O_3:Eu$, $SrGaS_4:Eu$, $ZnS:Cu,Al$, $Gd_2O_2S:Tb$)². For low voltage designs, transparent conductive oxides (e.g., ITO) are used instead of Al.

ATTRIBUTES

FED advantages include:

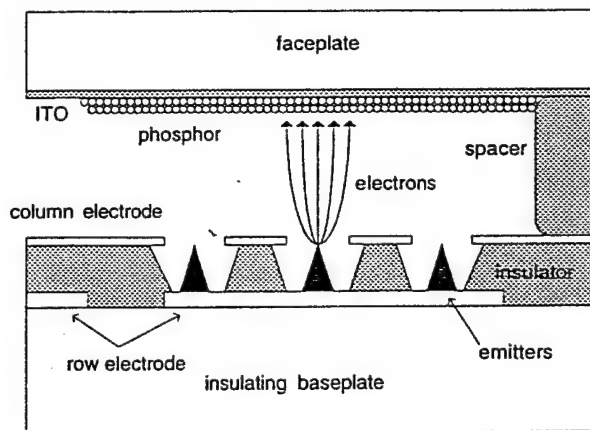
- wide temperature/humidity range
- wide viewing angle
- lambertian emission (CRT-like)
- potential for high brightness and contrast

GENERAL PROBLEMS

- Pixel brightness variations due to electron emission non-uniformities and low reliability of the cathode have been reported for prototype designs.

- Low voltage phosphors consume less power but have low efficiency and rapid saturation due to high current density (~ 0.1 mA/cm²).¹ High voltage designs look more promising.

- Longer lifetime and low driver costs of a high voltage phosphor is challenged by an increase in flashover risk, more stringent surface degasification requirements, wider vacuum gaps and high aspect ratio spacers.



STATUS

Numerous companies³ will fabricate FED devices in 1998. However, all companies are interested in color rather than monochrome (black and white) displays.

[1] J. Browning, C. Watkins, J. Alwan, and J. Hoffman, International Display Research Conference, 1997.

[2] B.K. Wagner, J. Penczek, S. Yang, F. Zhang, C. Stoffers, C.J. Summers, P. N. Yocom and D. Zaremba, International Display Research Conference, 1997.

[3] Pixtech, Micron, Canon, Raytheon, Candescent, FED Corp., Futaba and Motorola.

ELECTROLUMINESCENT TECHNOLOGY

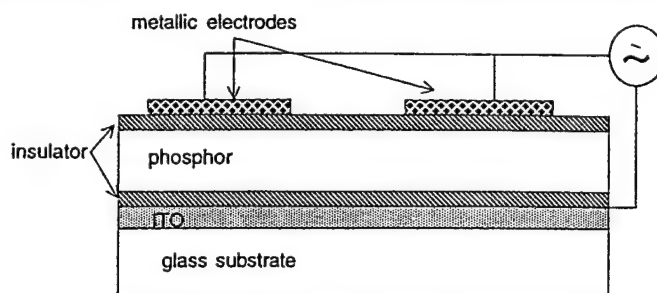
Among display technologies, electroluminescence represents an all solid state approach which provides the most direct conversion of electrical energy into light. Efficiency and performance characteristics depend strongly on materials and fabrication processes used.

OVERVIEW

- Electroluminescent displays (EL) use a phosphor under the influence of an electric field to generate light. Electroluminescence occurs in two forms: injection EL (light release upon recombination of minority and majority carriers), and high field EL (emission is due to impact excitation by accelerated charge carriers).

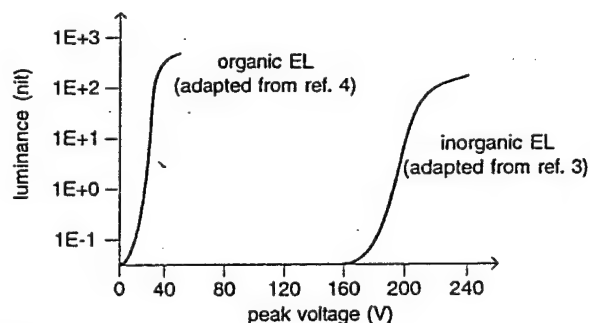
- Thin film EL devices are made up of a stack of conductors and dielectrics with a phosphor in the center (see figure on the right). The thin films are deposited onto a glass substrate. A black thin film layer may be incorporated at the bottom of the structure to provide contrast enhancement. Thin film transistors can be used to address EL for high resolution, low cost devices.

- Different doping elements have been used with a ZnS host, providing a wide range of emission spectra with typical efficiencies up to 5 lm/W (ZnS:Mn, ZnS:TbF₃, ZnS:Mn,TbF₃, SrS and CeF₃). White monochrome emission can be obtained by mixing red-green and blue-green phosphors with high efficiencies. A "color by white" approach for full color has been described in which a white phosphor operates through RGB patterned filters.¹ Another promising design concept consisting of a multilayer stacked structure with organic EL materials with increased efficiency and full color capabilities was recently reported.²



LUMINANCE / VOLTAGE CHARACTERISTICS

One attractive feature of thin film inorganic EL is a very steep luminance vs. voltage slope above threshold (see figure below).³ This along with a fast phosphor time response, allows for a direct addressing of large arrays. Low voltage threshold and similar steep curve characteristics have been reported for organic EL.^{4,5} However, monochrome (black and white) displays may be difficult to produce.



ORGANIC EL DEVICES

Recently, organic materials with high luminous efficiency (up to 12 lm/W), low driving voltage requirements, and fast response times have been described. Needs for improved performance relate to chemical structure of organic thin films, organic - metal contacts, organic-organic layers interface, device structure, non-radiative recombination losses and electrical degradation. Materials include complex metallic compounds with aromatic rings such as anthracene. In early stages of developments, organic EL presents electrical reliability issues such as electrochemical instabilities with formation of radical species, contacts degradation, encapsulation (needed due to air and humidity sensitivity), and low thermal tolerance.

[1] R. O. Tomqvist, International Display Research Conference 1997.

[2] P. E. Burrows, Z. Shen, S. R. Forrest, International Display Research Conference 1997.

[3] M. R. Miller, Seminar Lecture at the SID 1997 Annual Meeting.

[4] P. F. Seidler, E. I. Haskal, A. Curioni, and W. Andreoni, International Display Research Conference 1997.

[5] J. C. Sturm and C. C. Wu, International Display Research Conference 1997.

RESOLUTION

We define resolution in this work to be the maximum spatial frequency of the display. This is about equal to $.5/P$ where P is the pixel size.

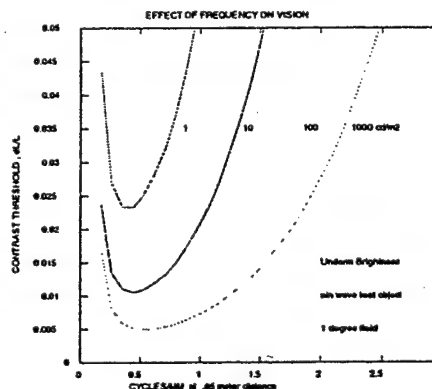
	spatial frequency (cycles/mm)							
peak-to-peak contrast ($\delta L/L$)	.05	.1	.2	.4	.8	1.6	3.2	6.4
2.9								
1.2								
.60								
.30								
.148								
.074								
.037								
.0184								
.0092								
.0046								

In the illustration at the left, sin wave signals of various frequency are shown. Spatial frequencies of over 6 cycles per mm are created from an 80 micron pixel size for the laser printer.

Note: The sin wave pattern is not shown in this copy.

CONTRAST SENSITIVITY VS FREQUENCY

The contrast sensitivity described earlier in this exhibit is a strong function of spatial frequency. For typical viewing distances the response is best at a frequency of about .5 to 1.0 cycles/mm. A display with a maximum spatial frequency of 3 cycles per mm will present all of the information that a human observer can recognize. This can be provided, even in a diagonal direction, with a pixel size of .120 mm.



Interestingly, sensitivity is reduced at low frequency which is why many radiologists will back away from an image to observe large features.

DISPLAY SIZE

Increasingly, digital radiographs are being recorded with success on regions smaller than the conventional 35cm x 43cm (14 x 17 inch) size. A display size of 30cm x 36 cm corresponds to a 2500 x 3000 array of .120 mm pixels. A display of this size will provide high fidelity when combined with a workstation having regional image zoom function.

SURFACE REFLECTIONS

The reflection of environmental light from the surface of a display can severely degrade an otherwise high fidelity image. Approaches to reduce these reflections include absorbent faceplates, black matrix absorbers, rough surfaces, and antireflective coatings. While we have not addressed this problem in this exhibit, it is extremely important for both electronic and film display.

DISPLAY REQUIREMENTS FOR MEDICAL IMAGING

Film Quality Display: We define here a film quality display as one having all of the attributes of transilluminated medical radiography film.

High Fidelity Display: A high fidelity display will provide all of the image quality that can be perceived by the human visual system. It is expected that magnification and contrast/brightness adjustments are done with a computer.

Good Quality Display: We have additionally defined a good quality device suitable for use for certain clinical functions. This quality is typical of the specialized CRT devices now used in medicine.

Specification	Film Quality Display	High Fidelity Display	Good Display
Size	35 x 43 cm ¹	30 x 36 cm	24 x 30 cm
Pixels	4000 x 5000	2500 x 3000	1200 x 1500
Pixel size	.08 mm	.12 mm	.20 mm
Refresh rate	static	static / 80 Hz	static / 80 Hz
Max. luminance	2000 nit	1000 nit	300 nit
Min. luminance	1 nit	5 nit	1.5 nit
Greyscale levels	> 1000	700 ²	700
Emission	lambertian	lambertian	lambertian
Color	monochrome ³	monochrome	monochrome
Contrast ratio ⁴	> 1000	200	150
Large area distortion	< 0.1 %	2 %	2 %
Reflectance	diffuse	diffuse + AR	AR
Viewing angle ⁵ (vert.)	full	± 45°	± 30°
Viewing angle ⁵ (hor.)	full	± 60°	± 45°

[1] 43 x 35 cm is a standard size for radiographic detectors. Displays should have an horizontal/vertical aspect ratio of about 0.8.

[2] The log-luminance versus pixel value relationships should follow a perceptually linear profile based on the DICOM standard.

[3] General preference in the field has been for displays with a white to slightly blue color. Most film bases are tinted blue.

[4] Contrast ratio defined with test pattern images consisting of an inner dark circular spot, surrounded by a bright outer circle with a ratio of radii of 10. The rest of the scene is kept at the same dark level of the inner spot.

[5] Full stated contrast ratio and luminance performance is to be maintained within the required viewing angle. No contrast inversion is allowed.

SUMMARY

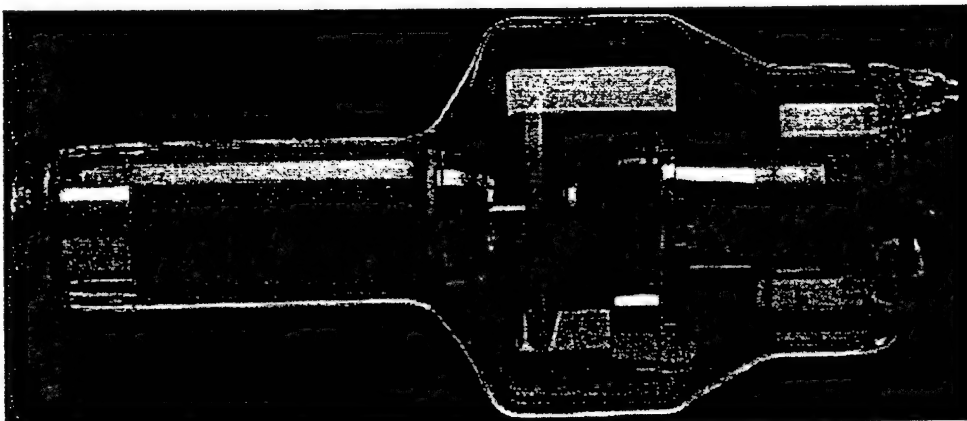
SID: The meetings and publications of the Society for Information Display are useful sources of information on display technology.

Successful integration of digital radiography in medicine will require high fidelity electronic display. Current CRT system do not meet the desired display performance and have excessive size, weight and power consumption. Recent developments in flat panel display technology suggest that high fidelity, light weight displays will be available in the near future:

AMLCD devices will be shortly available in large sizes. High brightness is easily achieved with bright back illumination. Further developments in optical design for monochrome displays should provide high fidelity. Lifetime and temperature sensitivity problems need to be resolved.

FED devices have very attractive emission distribution and potential for very low glare. The technology is considered expensive to manufacture and problems with cathode aging and nonuniformity have to be resolved.

EL devices represent a simple and potentially inexpensive display technology with the ability to achieve very high image quality. However, these devices are more natural for color displays and much materials research is required to achieve methods suitable for large area manufacturing.



ACKNOWLEDGEMENTS:

This exhibit was prepared using digital images printed on a Kodak XLP laser film printer. Graphic composition was done with Visio (Win95) and translated for printing with laboratory software.

The authors wish to acknowledge Ed Muka at the Mallinckrodt Inst. of Radiology for input on CRT quality and glare.

The authors wish to thank Wayne Pitchford for assistance in obtaining SEM images of CRT phosphors.

NOTE FOR THIS PAPER PRINT

The quality of the images shown in this paper copy may not appropriately reflect the illustrated principle, since they were designed to be displayed with radiographic film in a bright viewbox.

Film prints of the patterns and illustrations are available from the authors.

The veiling glare point-spread function of medical imaging monitors

Aldo Badano^{†*}, Michael J. Flynn[†], Ed Muka[‡], Ken Compton[×], Tom Monsees^{*}

[†] X-Ray Imaging Research Laboratory, Henry Ford Health System, Detroit, MI.

[‡] Electronic Radiology Lab, Mallinckrodt Institute of Radiology, St. Louis, MO.

[×] Clinton Electronics Corporation, Rockford, IL.

^{*} True Image, LLC.

ABSTRACT

When radiographic images are displayed using cathode-ray tubes (CRTs), the perception of low-contrast, clinically relevant details can be hindered by veiling glare. To reduce the effect of glare, high performance CRTs typically have an absorptive faceplate. Other approaches that have been implemented in color tubes include filtered and pigmented phosphor grains, and the use of a black absorptive matrix between phosphor dots. In this work, we present results on experimental measurements and computational predictions of the veiling glare for a medical imaging CRT of recent design (Clinton Electronics Corp., DS2000). Experimental measurements were performed using a collimated conic probe with a high gain detector, and test patterns having a dark circular spot of varying diameter in a bright circular field. Computational and experimental results were obtained before and after application of an AR coating to the surface of the monitor. The glare ratio for a 1 cm diameter dark spot was measured to be 138 without AR coating, and 241 with coating. The results establish a bright ring in the PSF at about 45 mm distance. The predictions from the computational model agree well with the measured ring response functions for radii less than 50 mm. We speculate that the veiling glare response for large radii is greatly influenced by electron backscattering processes. While primarily designed to decrease specular reflections, the AR structure also affects the glare characteristics of an emissive display by increasing the probability that a light photon will exit the structure through the outer surface.

Keyword List: CRT, veiling glare, contrast reduction, contrast measurements.

1. INTRODUCTION

When radiographic images are displayed using cathode-ray tubes (CRTs), the perception of low-contrast clinically relevant details can be hindered by veiling glare. The multiple light scattering processes that take place in the emissive structures cause low-frequency degradation that can be significant in a low luminance region surrounded by bright areas. The effect of veiling glare is therefore determined by the luminance distribution of each image scene.

In this paper, we present results on experimental measurements of veiling glare for a medical imaging monochrome cathode-ray tube (CRT) of recent design. Experimental data were obtained before and after application of an anti-reflective coating (AR) to the surface of the monitor. We report results using both direct and indirect measurements. Direct measurements of the veiling glare point-spread function made with a bright spot are difficult to perform due to the luminance difference between the central spot and the tails. On the other hand, we report in this paper that indirect measurements using a dark spot of

^{*} Present affiliation: Center for Integrated Microsystems, University of Michigan, 118C DTM, 2360 Bonisteel Blvd., Ann Arbor, MI 48109-2108, badano@umich.edu.

increasing diameter can be performed if light from the bright regions does not contaminate the low level signals. Computational predictions of an optical Monte Carlo model are then compared to the experimental results. Finally, a discussion on the effect of the AR coating on the luminance spread functions based on the comparison of the results for the veiling glare with and without the AR plate is presented.

2. COMPONENTS OF VEILING GLARE

Veiling glare is commonly associated with the multiple light scattering processes that take place in the emissive structures of CRT that cause contrast degradation in low luminance regions surrounded by bright areas. We have described the optical component of veiling glare (light transport) in previous work.¹⁻³ Two other sources of veiling glare (light leakage and electron backscattering) are less well known, and are considered in more detail in the following sections.

2.1. Light transport

A significant component of veiling glare comes from the light generated in a region of the display that scatters within the emissive structure to emerge as if it was generated in a different region.

To reduce veiling glare, high performance monochrome and color CRTs typically have an absorptive faceplate that reduces the brightness. Other approaches that have been implemented in color designs include filtered and pigmented phosphor grains.⁴ All color tubes presently have a black absorptive matrix between phosphor dots that leads to improved color purity. The absorption of light by this layer greatly contributes to reduce the magnitude of the tails of the luminance spread functions, as we will show later in Section 5.

The contribution to veiling glare due to light transport processes within the emissive structure depends proportionally on the relative location of dark and bright regions in an image. Therefore, its effect is determined by the luminance distribution patterns of each image scene. Conversely, the other two components to glare that will be analyzed in this Section, cause a background signal that is approximately uniform throughout the entire display surface.

2.2. Light leakage

Another component of veiling glare comes from light that leaks through the reflective coating at the inside surface of the phosphor layer and re-enters the emissive structure at another position. The thin aluminum coating covering the phosphor layer has microscopic holes that allow light generated in the phosphor to escape into the bulb volume.

The reflectivity of Al backing films is typically 90% or greater. The transmitted light will scatter off the walls of the bulb, and may eventually come back and exit through the faceplate adding a relatively uniform background to the image signal. This light leakage has been recognized and used as part of an experimental method to determine the Al layer thickness,⁵ and as a method for measuring the display performance according to luminance measurements made from the back of the CRT bulb funnel (implemented by True Image, LLC, Webster Groves, MO).

When the transmitted light intensity through the Al film amounts to 10%, a uniform bright field will be contaminated by an additional constant luminance of 1×10^{-3} of the bright field intensity[†]. If a small dark spot is placed in the center of an image at a luminance level of 1% of the bright field, the image contrast in the dark region will be reduced by 10%.

[†]This figure assumes an absorption of 90% after all scattering events at the walls of the tube. Typically, coatings for the inside surfaces of color CRT bulbs are carbon-based absorptive materials, although metallic coatings having Cu and Ag are also used in certain applications. Monochrome tubes have an Al film deposited on the interior of the glass bulb, which results in increased degradation.

2.3. Electron backscattering

In addition to the optical components associated with light diffusion and light leakage, there is a significant component of glare caused by electron backscattering. The reduction in contrast due to backscattered electrons has been studied for fluorescent screens,⁶ and for scanning electron microscopes.⁷

Color CRT devices are particularly prone to glare from electron backscattering. To obtain good color purity, a shadow mask[†] is located in front of the screen to allow each electron beam to selectively pass through the mask holes and excite the corresponding color phosphor. Although the beams are focused and aligned with the holes, a fraction of the electron beam will directly hit the mask. As some energetic electrons impinge into the shadow mask or the screen, a fraction is backscattered and may eventually hit the phosphor layer at a different location. Short-range contrast degradation is associated with electron scattering in the vacuum space between the mask and the phosphor screen, while long-range effects come from backscattering at the mask and at the walls and funnel of the glass bulb.⁸

The backscattered fraction from a surface depends on the effective atomic number of the material, and can be reduced by using low-Z materials such as graphite,⁹ or Al_2O_3 .¹⁰ The amount of contrast reduction from backscattering is directly proportional to the primary beam intensity. It has been reported that the fraction of contrast loss due to electronic backscattering in color tubes can be as much as 98% of the total glare degradation.⁸ An increase by a factor of about 10 in the contrast ratio of 10×10 cm black squares was achieved by careful selection of coating material and thickness (G. C. de Vries, Philips Display Components Lab, Eindhoven, oral communication, 1998). The absence of a shadow mask in monochrome tubes results in a lower backscattered fraction since all the electrons hit the Al conductive coating and phosphor layer.

2.4. Monte Carlo analysis of electron backscattering in monochrome CRTs

To evaluate the magnitude of the backscatter component for monochrome tubes, calculations were performed with a Monte Carlo radiation transport code, SKEPTIC,¹¹ that specifically models each electron interaction rather than using continuous slowing down approximations. The geometry of the monitor was described in three dimensions by a 40 cm cube representing the vacuum tube. The internal walls of the box were coated with a material commonly encountered inside CRT bulbs with an average elemental composition obtained from CRT coating manufacturers.

To determine the variability between the different coatings used by CRT manufacturers, we computed the backscattering fraction using SKEPTIC for 7 coatings having different elemental compositions (Cl-001, Cl-002, Cl-004 from Acheson Colloids Company, Port Huron, MI, and g972, g984, g985, g9001 from Thompson Consumer Electronics, Lancaster, PA). All conductive coatings were composed of graphite, metallic oxides, and sodium silicates in different proportions. The materials used in this study are representative of coatings employed in color tubes. In monochrome displays, an Al film is used to coat the glass from the yoke assembly to the screen, resulting in a backscattered fraction of about 0.15 for energies between 10 to 100 keV.¹² The results showed that the backscattered fraction was always within 0.15 and 0.18 in the energy range between 5 to 35 keV. The degradation in contrast associated with this amount of backscattering is discussed later.

The emissive structure was described as a 5 μm ZnO phosphor layer over-coated with an Al backing. The phosphor layer was partitioned in 11 elements of full length, 10 of which had a constant width of 3.999 cm, and a central element having a width of 0.005 cm, to accommodate the incoming electron beam. A normally incident electron beam was used entering the box through a small hole in the back face, and impinging into the emissive structure at the center of the front face.

[†]The aperture grille used with in-line electron guns, introduced in 1988, represents another approach employed for color selection. The transmissivity of the beam is 15 to 50% greater compared to shadow mask designs.

The distribution of deposited energy accumulated in each element of the phosphor layer was then related to the primary incident energy deposited in the central element accumulated from all histories. The results of this energy deposition scheme are directly related to the point-spread function of the input electron beam. The energy deposited in the phosphor layer by the back-scattered electrons is related to the energy deposited in the thin central strip by the primary beam. In this case, we assume that the luminance generated is proportional to the deposited energy in the phosphor⁵.

Using a 30 keV mono-energetic beam, we found that the response tail is approximately constant upon the entire phosphor layer, with a magnitude of about 4×10^{-2} cd/m²/cd for a 0.5 μ m Al film. Since the energy of multiply backscattered electrons is significantly lower than the primary energy, we confirmed that the glare component is sensitive to the Al thickness. The magnitude of the spread function decreased to 1×10^{-2} cd/m²/cd for a 1 μ m Al thickness, and to 4×10^{-3} cd/m²/cd for a 2 μ m Al thickness. For a 0.1 m² display area at 100 nit having a 0.5 μ m Al film, a small black spot will have a luminance of 0.4 nit produced by backscattered electrons, which results in a glare ratio G of 250.

3. METHODS

In this work, we experimentally measured the veiling glare for two model DS 2000 HB monochrome monitors at 1600 \times 1280 resolvable pixels manufactured by Clinton Electronics Corporation, Rockford, IL. This twenty inch diagonal CRT has a display area of 362 \times 272 mm and a flat 60 inch radius profile with 110° deflection angle. A nominal brightness of 80 ftL is obtained with a P104 phosphor. A drawing showing the key elements of the emissive structure is presented in Figure 1. A glass faceplate 13 mm thick with 34% transmission and index of refraction equal to 1.525 constitutes the support for a 10-20 μ m thick phosphor layer coated with a thin reflective Al film (90% reflection). After the measurements were carried out without the AR coating, an AR panel consisting of a 3.2 mm thick sheet of glass having 92% transmittance was bonded onto the faceplate with a polyester laminating resin. The resin layer has a thickness of about 2.0-2.5 mm with no significant light absorption. The index of refraction of the resin and AR glass panel were considered similar to the index for the faceplate. The AR panel is coated with a multi-layer (5 - 7 layers) thin film structure with MgF₂ and ITO as the conductive layer. According to the manufacturer (OCLI, Santa Rosa, CA), the absorption of the coating is less than 1% for 550 nm light, and the reflectivity is below 0.1% in the visible range.

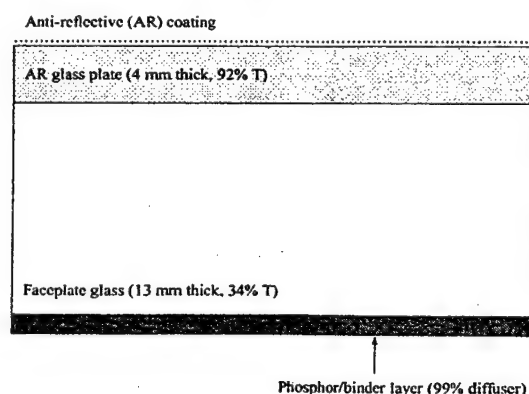


Figure 1. Model of the emissive structure for the CRT monitor simulated in this work.

⁵This assumption is reasonable for cathodoluminescent phosphors under typical electron bombardment regimes, but may not be acceptable for other processes that rely on ionizing radiation to produce luminescence.^{13,14}

3.1. Optical Monte Carlo simulations

Computational predictions of the veiling glare spread functions for the monochrome medical imaging CRT were obtained using DETECT-II, a computational tool for the simulation of light transport processes in emissive structures using Monte Carlo techniques.^{15,16} This program computes the response function of emissive display devices by modeling light scattering through 3-dimensional objects. Rough surfaces and anti-reflection coatings can be described using DETECT-II, for a complete model of the emissive structures considered in this work.

3.1.1. Model of the emissive structure

The geometric model employed for the simulation is based on the technical data provided by the manufacturer. A cross-section of the emissive structure is shown in Figure 1. The linear absorption coefficients were computed according to the information on light transmission, as 0.536 cm^{-1} for the faceplate, and 0.263 cm^{-1} for the AR glass panel. The thin film is modeled as a single-layer coating with optimized thickness (169 nm for 550 nm photon wavelength), and index of refraction equal to 1.23.

All simulations for the CRT monitors described in this Chapter were performed using a mono-energetic light source with a wavelength of 550 nm. This photon energy located in the center of the visible range corresponds to the maximum photopic response of the human eye. For monochrome display devices, this approximation is considered good. Experimentally, the observation of glare effects in such devices does not demonstrate any color shifts.

3.1.2. The discrete ring response function

An important aspect of the simulation is the manner in which the results from the Monte Carlo binning are associated with the experimentally measured values. In this section, we review aspects of the veiling glare model to relate the experimental ring response function $R(r)$ to the discrete Monte Carlo estimate \mathcal{R}_i .¹⁵ For a point source of unit strength (1 cd of light), the N_i photon histories that emerge within a given solid angle Ω are binned into radial bins i of constant thickness Δr . We can express the normalized discrete point-spread function \mathcal{P} as

$$\mathcal{P}_i = \frac{N_i}{N_t 2\pi r_i \Delta r}, \quad (1)$$

where N_t is the total number of histories. The units of \mathcal{P}_i are photons/sr/m² per photons, which is interpreted as proportional to cd/m² per cd, or, 1/m².

The point-spread function \mathcal{P}_i is converted to a ring response function by summing over all angles (which is already done because of the radial bins) and accounting for the ring thickness Δr , as follows

$$\mathcal{R}_i = \frac{N_i}{N_t \Delta r} = 2\pi r_i \mathcal{P}_i. \quad (2)$$

The units of \mathcal{R}_i are the units of $\frac{1}{\Delta r}$, usually 1/mm. Equation 2 represents the Monte Carlo estimate of the ring response function and can be related to the measurements of veiling glare using dark spot test patterns.

3.2. Experimental measurements

Measurements of veiling glare were performed using direct and indirect methods. The measurements were performed on both monitors before an AR was bonded to the faceplate. After the first set of measurements (without the AR), the monitors were sent to the manufacturer, and were return to the lab with AR coated panels. This particular model is commercially available only with the AR panel.

3.2.1. Bright spot measurements with CCD

Direct measurements of a bright spot were also performed using a 1024×1024 CCD.¹⁷ The bright spot was realized by disabling the electron beam sweep and directing the static beam to the center of the display area. In order to reduce the contamination of the low luminance regions by the bright spot, a black patch was placed between the spot and the camera lens. The patch was made with black paper and positioned with a thin black wire at about 10 mm from the display surface.

The images recorded with and without the AR panel were analyzed to extract information on the profile of the point-spread functions. Image values were projected into radial 1-dimensional profiles, by adding the pixel number at each radial location, and then dividing by the numbers of pixels that contributed to each radial bin. The data were then corrected for dark current by subtracting 320 counts to each radial bin average.

3.2.2. Dark spot measurements

Luminance measurements of dark spots of varying size were carried out using a specially designed luminance probe and test patterns that are described elsewhere.^{1,15} Data corresponding to each dark spot diameter was recorded and corrected for the instrument dark current. The baseline luminance correction was obtained by measuring the luminance at the center of the display device with a full field dark image. For these measurements, the brightness and contrast settings of the two units were adjusted to generate about the same maximum and minimum luminance with the minimum luminance set to zero (CRT cut-off). The results were then corrected using the correction factor $\zeta(r_d, d)$ for the appropriate radius of the dark spot (r_d), and the distance d between the probe tip and the display surface. Finally, the difference between the values for 2 consecutive dark spot radius was divided by the difference in radius to yield the ring response function $\mathcal{R}(r)$.

4. RESULTS

Figure 2 shows the Monte Carlo computed ring response functions for one of the CRT devices tested. Without an AR panel, the veiling glare spread function presents a single peak at about 23 mm radius at a magnitude of about 0.001 mm^{-1} . In the case of the AR coated panel, the prediction indicates the presence of several peaks with decreasing amplitude at larger radii.

The images of the bright spot recorded with the CCD camera are shown in Figure 3. In spite of being thin and black, the support wire can be clearly seen in both images. The textured background observed is associated mostly with the roughness of the glass faceplate, and with the nature of the phosphor layer. The attempt to extract the information on the spread function profiles yielded the data plotted in Figure 4. Although much noise is present, the peaks at 22 and 33 mm are still noticeable.

The ring response functions from the dark spot measurements performed before and after the addition of the AR panel are presented in Figure 5. The profiles for both monitor units without the AR panel show a marked peak at about 20 mm with an amplitude of $3 \times 10^{-3} \text{ 1/mm}$, while the results for the AR case present a significant peak at 32 mm with a magnitude of about $1 \times 10^{-4} \text{ 1/mm}$. For each unit and both cases, the magnitude of the tails of the dark spot ring response function slightly increase for larger radii. Without an AR coating, the glare ratio for a 1 cm diameter dark spot was measured to be 138. With an AR coating, the glare ratio for a 1 cm dark spot was 241 due in part to additional glass absorption. While primarily designed to decrease specular reflections, AR coatings also reduce the veiling glare of an emissive display by reducing the amount of light internally reflected at the front surface.

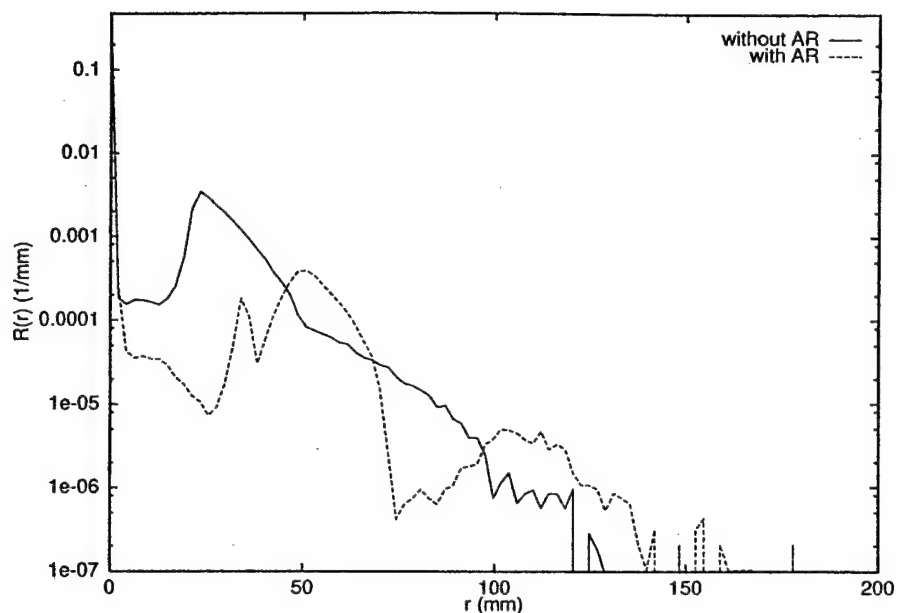
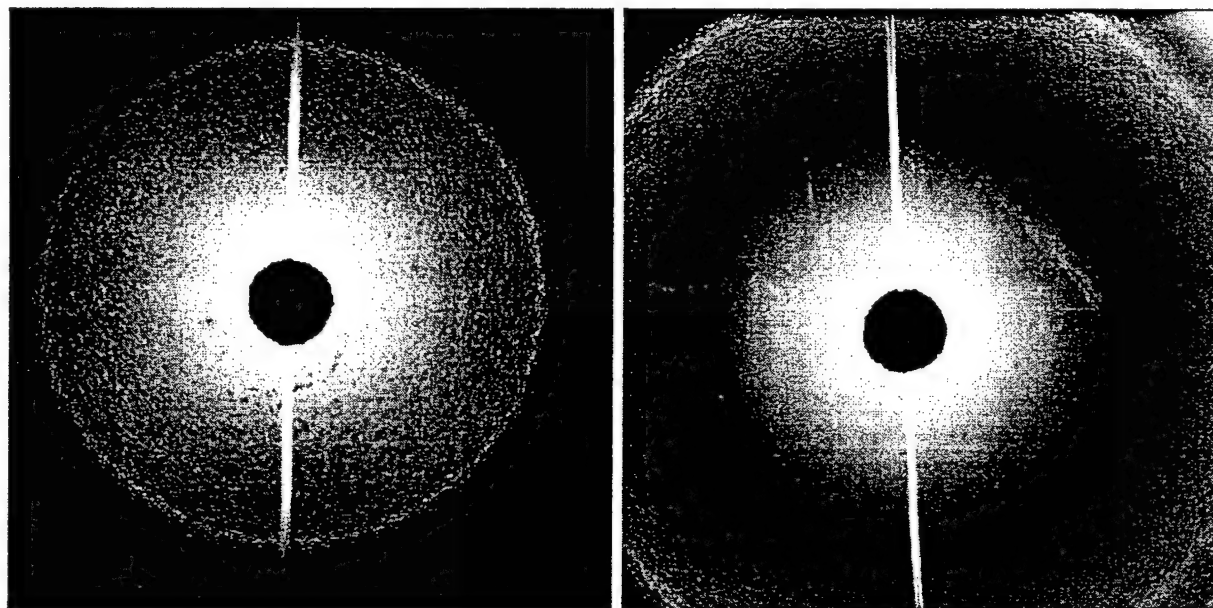


Figure 2. Monte Carlo predictions of the ring response functions for the monochrome CRT with and without the AR panel and AR coating.



(a) Without the AR plate.

(b) With the AR plate.

Figure 3. Bright spot CCD images for the monochrome CRT monitor used in this work. The first peak (seen in both images) is associated with the first total internal reflection scattering events. The increase in the radius of the first peak circle from about 23 to 33 mm can be related to the increase in the front glass thickness.

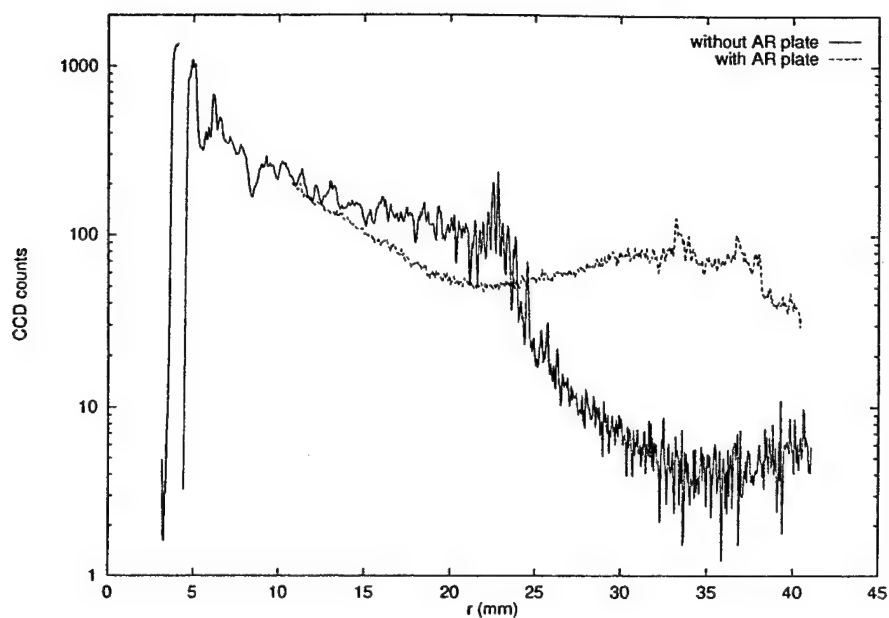


Figure 4. Radial profiles for the CCD camera images of the bright spot. In spite of the noise, peaks are noticeable at 23 and 33 mm radius. The grainy appearance of the surface is related to the glass roughness and to the phosphor layer structure.

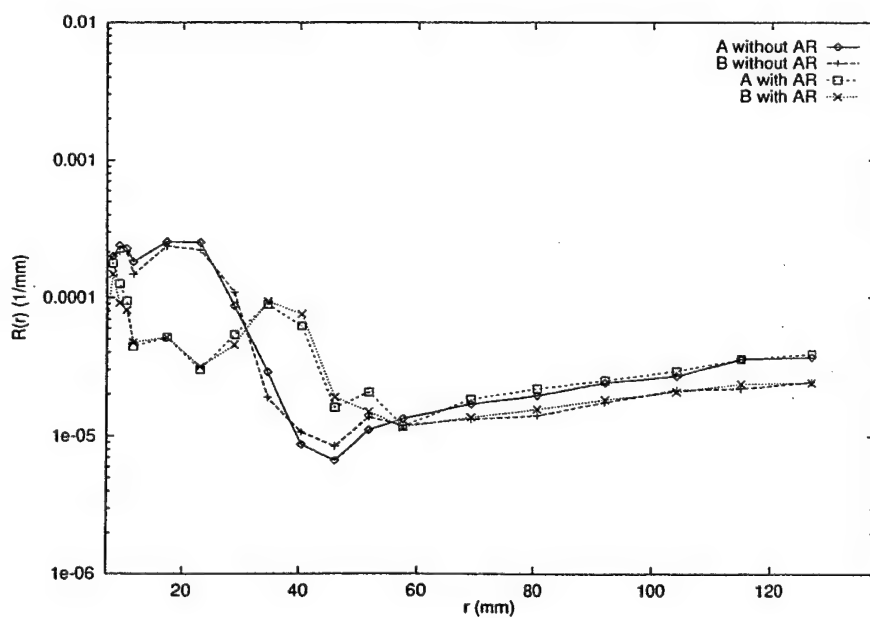


Figure 5. Experimental ring response functions. Two monitors (A and B) were measured with and without the AR panel.

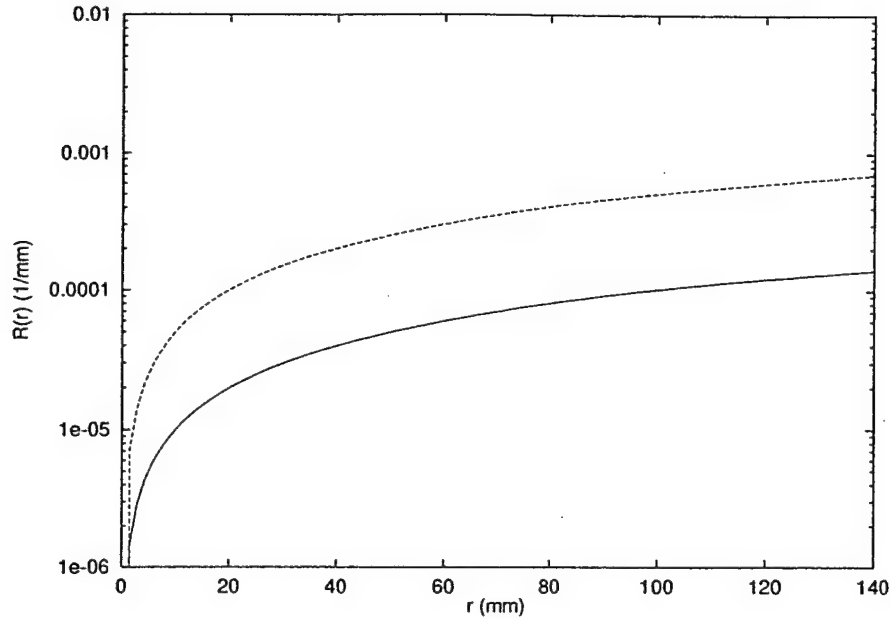


Figure 6. Expected profile of the ring response function associated with electron backscattering or light leakage through the Al coating. The two curves depict different proportionality constants between $R(r)$ and r .

5. DISCUSSION

Both experimental techniques used in this work have confirmed the general profile of the ring response function associated with veiling glare. However, results from the direct measurements do not provide information on the relative magnitude of the response function tails. The position and shape of the functions appear more clearly delineated in the results presented with the indirect measurement method.

The profiles shown in Figure 5 from the indirect method agree reasonably well with the predictions of the Monte Carlo model. For the monitor without an AR panel, both the position and magnitude of the peak are consistent. This peak is associated with photons that are reflected once at the front surface with an incident angle close to the total internal reflection angle, and emerge after reflecting at the phosphor or Al layer. The shape of the peak is directly related to the dispersion in angles that occur at the phosphor layer, where photons are reflected with a Lambertian angular distribution and transmitted through a rough surface into the glass. We infer that the more rounded tip of the peak seen in the experimental data is caused by a broader angular distribution function at the phosphor-glass boundary. This can be due either to a rougher surface between the phosphor and the faceplate, or to a more broad angular output from the phosphor layer than defined by the Lambertian distribution function.

In the case of the monitor with an AR panel, the location of the main peak is displaced to a larger radius due to the increase in faceplate thickness from the bonded AR coated panel. Although the location and magnitude of the peak is consistent with the Monte Carlo predictions, the presence of markedly defined multiple peaks in the simulation results does not agree with the measured data. The simplistic description of the AR coating as a single-layer structure could be responsible for the multiple peaks and valleys that would be associated with the periodic response characteristics of a single dielectric thin layer. A more accurate description for the AR coating may be needed to provide complete agreement between the predictions of the model and the measurement results. Improvements should reflect the structure of current AR coatings including the multiple thin film stack and protective layers. The pattern observed for the structures with thin film coating could be related to the fact that all Monte Carlo simulations

were performed with a mono-energetic source of light. Instead, sampling photons having a distribution in wavelengths representative of the emission spectra of CRT phosphors with corrections for photopic response might lead to better agreement between the Monte Carlo predictions and the experimental results.

A significant difference between the predictions of the Monte Carlo model and the experimental data observed with and without the AR panel is the response at large radii. The simulation results, which considers only the light transport component of veiling glare, show the magnitude of the tails decreasing to negligible values at radii of 140 mm or larger. However, the experimental data in Figure 5 show the magnitude of the veiling glare increasing gradually at large radii. This observation can be explained by the other sources of veiling glare. The magnitude of the ring response function associated with either light leakage through the Al layer or with electron backscatter is proportional to the radius of the bright ring. This relationship between $R(r)$ and r is consistent with the experimental data (see Figure 6).

Such interpretation might explain why the experimentally determined ring response function has a slightly increasing long tail, not seen in the optical Monte Carlo results that account only for the light diffusion component.

REFERENCES

1. A. Badano and M. J. Flynn. Experimental measurements of glare in cathode-ray tubes. *Proceedings of the SPIE*, 3335:188-196, 1998.
2. A. Badano and M. J. Flynn. Monte Carlo modeling of glare in cathode-ray tubes for medical imaging. *Proceedings of the Society for Information Display*, pages 495-498, 1998.
3. M. J. Flynn and A. Badano. Image quality degradation by light scattering in display devices. *Journal of Digital Imaging*, 12(2):50-59, may 1999.
4. M. Kawasaki, N. Tani, and R. Onishi. Improvement of contrast and brightness by using crystal pigment phosphor screens. *Proceedings of the Society for Information Display*, pages 266-269, 1998.
5. G. M. Ehemann, R. LaPeruta, and E. R. Garrity. US5640019: Method of determining the quality of an aluminized, luminescent screen for a CRT, 1997.
6. J. R. Mansell and A. W. Woodhead. Contrast loss in image devices due to electron back-scattered from the fluorescent screen. *Journal of Physics D: Applied Physics*, 16:2269-2278, 1983.
7. F. Hasselbach and H.-R. Krauss. Backscattered electrons and their influence on contrast in the scanning electron microscope. *Scanning Microscopy*, 2(2):1947-1956, 1988.
8. G. C. de Vries. Contrast-enhancement under low ambient illumination. *Proceedings of the Society for Information Display*, pages 32-35, 1995.
9. J. J. van Oekel. Improving the contrast of CRTs under low ambient illumination with a graphite coating. *Proceedings of the Society for Information Display*, pages 427-430, 1995.
10. J. J. van Oekel, M. J. Severens, G. M. H. Timmermans, et al. Improving contrast and color saturation of CRTs by Al_2O_3 shadow mask coating. *Proceedings of the Society for Information Display*, pages 436-439, 1997.
11. S. J. Wilderman. *Vectorized algorithms for Monte Carlo simulation of kilovolt electron and photon transport*. PhD thesis, University of Michigan, 1990.
12. D. C. Joy. A database on electron-solid interactions. *Scanning*, 17:270-275, 1995.
13. T. D. Taulbee, B. D. Rooney, W. Mengesha, and J. D. Valentine. *IEEE Transactions on Nuclear Science*, pages 326-330, 1996.
14. B. D. Rooney and J. D. Valentine. *IEEE Transactions on Nuclear Science*, pages 734-738, 1996.
15. A. Badano. *Image quality degradation by light scattering processes in high performance display devices for medical imaging*. PhD thesis, University of Michigan, 1999.
16. A. Badano and M. J. Flynn. Image degradation by glare in radiologic display devices. *Proceedings of the SPIE*, 3031:222-231, 1997.
17. E. Senol and E. Muka. Spatial frequency characteristics of cathode ray tubes (CRT) soft-copy displays. *Proceedings of the SPIE*, 2431:302-315, 1995.

Small Spot Contrast Measurements in High Performance Displays

Aldo Badano, Michael J. Flynn and Jerzy Kanicki

ABSTRACT

It has been reported recently that conventional methods for measuring the contrast ratio of display devices using small dark spots provide inaccurate data. In this paper, we describe an experimental method for reliable measurements of the small spot contrast ratio, based on a collimated probe that minimizes the signal contamination to less than 10^{-4} of the bright field. Applications to veiling glare measurements and electronic crosstalk characterization are presented.

I. INTRODUCTION

Typically, uniform bright and dark fields are used to determine the full field contrast. However, several standards define contrast as the ratio of the luminance in a bright field to the luminance of a dark small spot. It has been reported recently that conventional methods for measuring the small spot contrast ratio of display devices can provide inaccurate data [1,2].

For measuring small spot contrast ratios, a luminance probe and detector capable of measuring very low luminance values in a small dark region surrounded by a large bright field are required. Often, multiple light reflections in detector optics can substantially alter the measured low luminance value in the dark spot. The measurement error amounts to 1-3% of the bright field intensity [3] for low-flare lenses with anti-reflective coatings. When measuring a test pattern for which the bright field luminance is 500 times the dark spot luminance (i.e. a contrast ratio of 500), the measured contrast ratio will only be 83 if the detector records 1% of the bright field in the dark region.

In this paper, we describe a collimated probe that

AB (badano@umich.edu) and JK (kanicki@eecs.umich.edu) are from the Center for Integrated Microsystems, University of Michigan, Ann Arbor, MI. MJF (mikef@rad.hfh.edu) is from the Dept. of Diagnostic Radiology, Henry Ford Health System, Detroit, MI.

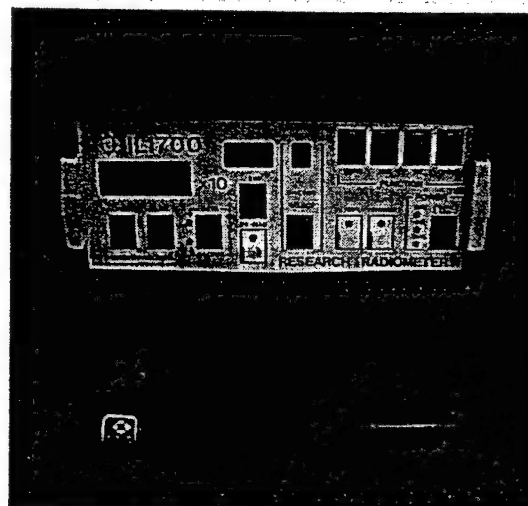


Fig. 1. Photopic probe and IL 1700 research radiometer for measurements of veiling glare ratio.

minimizes contamination from very bright neighboring regions. The probe has been specifically designed to measure small spot contrast ratios in high performance display devices for medical imaging applications. Details pertaining to the optical design and construction of the probe are reported. The application of this probe to measure veiling glare in medical imaging CRTs is demonstrated. Finally, applications of this probe to small spot contrast ratio measurements for AM-LCDs are discussed.

II. COLLIMATED DETECTOR

To develop a luminance probe with minimal response from surrounding bright regions, a collimated design with multiple baffles was employed. The device, shown in Figure 1, is based on a high-gain Si photo-diode sensor with an active area of about 5.7×5.7 mm, a photopic filter, and a research radiometer (SHD 033 sensor, IL 1700 radiometer, International Light Inc.). A standard barrel into which baffles can be positioned using threaded parts is attached to the sensor. A conic probe fabricated on a lathe from aluminum rod is placed at the end of this barrel. The probe tip is designed to minimize the amount of light scattered from the probe back

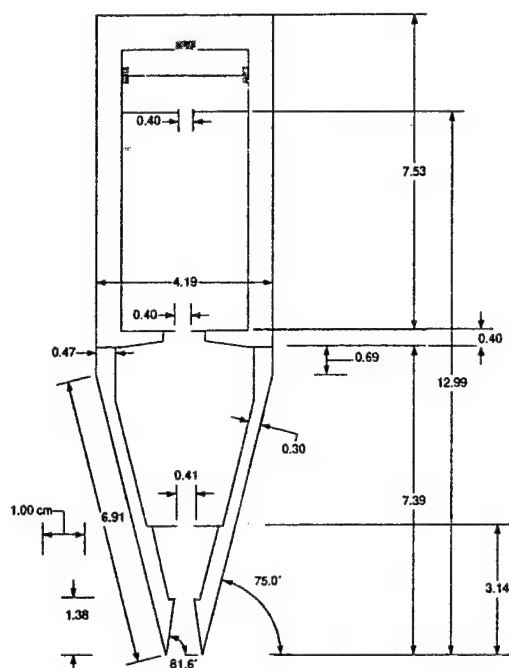


Fig. 2. Schematic drawing of photopic probe showing dimensions in cm and the relative position of apertures and baffles.

to the emissive structure. As shown in Figure 2, the probe entrance aperture has a diameter of 9 mm. The external conic shape of the probe reflects light coming from bright regions away from the display surface. An angle between the walls of the cone and the display surface normal of 15° allows central measurements in 38 cm diagonal displays.

Light entering the probe at oblique angles is trapped by a series of interior baffles and probe chambers. A series of four apertures of about 4 mm diameter creates a highly collimated response. Baffle positions and aperture diameters were determined using manual design methods. Significant signal contamination is prevented by the large number of scattering events from absorptive surfaces required to reach the detector through the multiple apertures.

The response characteristics of the probe were determined by measuring the luminous signal from test patterns having a perfectly black spot. For dark spot diameters smaller than the field of view of the probe, the measured luminance is associated with direct light striking the detector. For larger diameters,

the luminance is caused by scattered light originating in the bright regions that enters the probe after multiple reflections. It is this contamination in the signal that limits the performance of the method. The amount of signal contamination for this probe is a function of both the dark spot radius (r_d) and the distance between the probe and the emissive surface (d). The methods used to characterize the performance of the detector assembly are described in detail elsewhere [4].

III. APPLICATIONS

In this Section, we describe two display performance characterization techniques that rely on small spot contrast ratio measurements based upon the detector assembly described in this work. Both applications (veiling glare measurements on CRTs and crosstalk artifact characterization in AM-LCDs) involve test patterns with small dark regions in an otherwise very bright image.

A. Veiling glare measurements in CRTs

To illustrate the application of the method for devices having veiling glare, measurements were performed for a monochrome medical imaging CRT (Image Systems, 24 inches diagonal, model M24L). We define the veiling glare ratio (G) as the ratio between the luminance of the bright full field L_b , and the luminance in the dark small spot. Test patterns with varying spot diameter were displayed as images with 1000×1000 pixels. With the contrast control set to the maximum level, the monitor brightness control was increased from the minimum level until the full dark field luminance was greater than the value observed with the unit disconnected (CRT cut-off). The luminance was then slightly reduced from this point, and the luminance of a full black field recorded (L_d).

The veiling glare measurements were made with the entrance of the photopic probe at about 1 mm from the surface of the display. The distance d was determined by adding the distance between the probe tip to an estimate of the faceplate thickness based on laser reflection measurements. The thickness was measured to be 13 mm resulting in a to-

tal distance d of 14 mm. Measurements were performed with test patterns of many radii varying from 4 to 160 mm. Figure 3 shows the veiling glare ratio

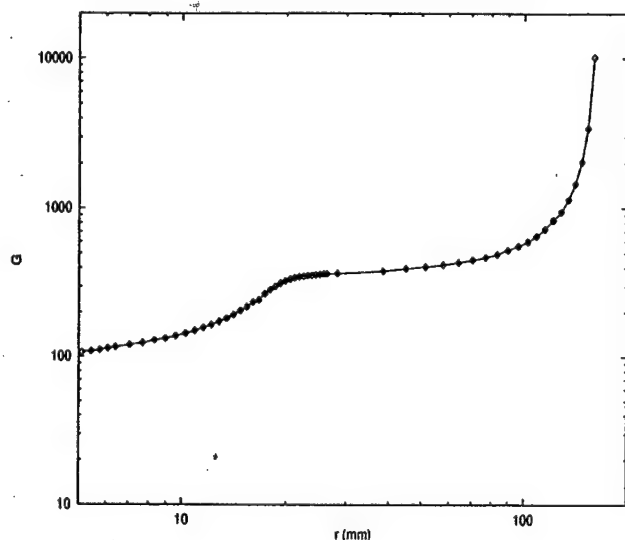


Fig. 3. Veiling glare ratio for a medical imaging CRT measured at a distance of 1 mm from the faceplate surface. Values for the veiling glare ratio can differ significantly (up to a factor of 10) when using different spot size.

tios for the medical imaging CRT. For a radius of 5 mm, G is equal to 130. This experimental method was used in other work to compare the predictions from simulation experiments with veiling glare characteristics of a DS 2000 HB monochrome monitor at 1600×1280 resolvable pixels manufactured for medical imaging applications by Clinton Electronics Corporation, Rockford, IL [5].

B. Crosstalk characterization in AM-LCDs

Small spot contrast ratio measurements are also relevant for flat panel displays [6]. Of particular importance to high-resolution display devices with large number of gray levels is the scene-dependent undesired artifact caused by crosstalk in the active matrix array. In AM-LCDs, crosstalk is associated with the modification of the intended voltage across the liquid crystal cell. The artifact is caused by incomplete pixel charging, by leakage currents through the thin-film transistor, and by displacement currents determined by parasitic capacitive coupling. Display crosstalk is more important for large size

panels having higher resolution and gray-scale [7,8]. Although having different origins, crosstalk artifacts have been also studied for passive matrix polymer light-emitting displays [9].

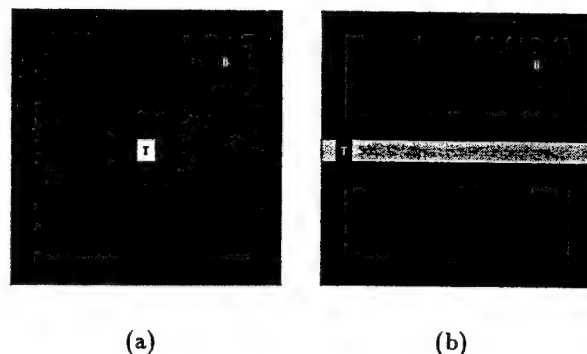


Fig. 4. Crosstalk test patterns with uniform background (a) and with horizontal bar (b). The image values for T (target) and B (background) were assigned 0, 50, 100, 150, 200, and 250 for the three colors of the 256 available levels, resulting in 6 gray levels.

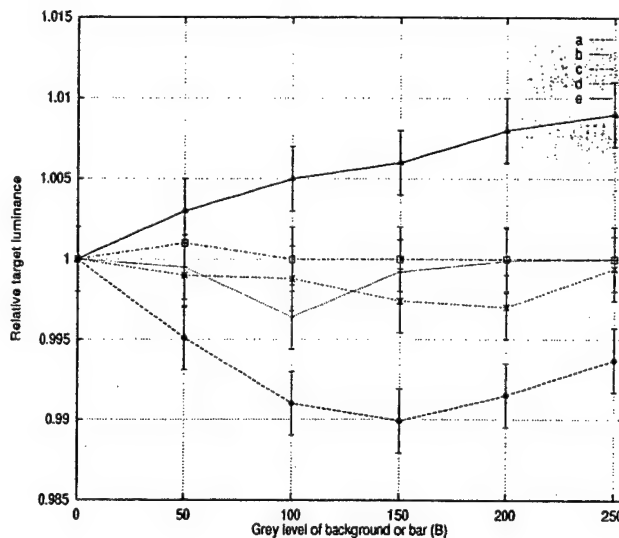


Fig. 5. Relative measured target luminance (T) as a function of the background or bar luminance (B) for: (a) centered white target, (b) horizontal bar with black target, (c) horizontal bar with white target, (d) vertical bar with black target, and (e) vertical bar with white target.

Measurements of display crosstalk were made on a 1024×768 color AM-LCD AKIA AT145X (Hosi-

den Corporation, Japan). We used patterns having a small rectangular target of about 1 cm surrounded by a uniform lighter or darker luminance field. Vertical and horizontal crosstalk was studied by using bar patterns instead of uniform backgrounds, as shown in Figure 4. The tip of the probe was placed at 1 mm of the display surface. Figure 5 shows the change in target luminance (T) associated with the change in luminance levels of the background or bar patterns (B) for a white target. A maximum change of 1% was observed for a centered white target in a uniform field at a grey level of 150.

IV. DISCUSSION

The human visual system is very effective at observing the luminance of dark regions surrounded by bright fields due primarily to the reduced retinal sensitivity to obliquely incident light associated with scattering events in the lens [10–12]. A high quality display device therefore requires a small spot contrast ratio of 400 or more [13]. We described an experimental method capable of measuring the small spot contrast ratio characteristic of high performance display devices. A luminance probe with very low light leakage has been developed for use with this method. Using this probe, we have demonstrated that measurements of very low luminance in small dark spots can be performed even when the surrounding field is 1000 times brighter. Minimum dark spot size have radii from 3 to 6 mm for measurement distances from 2 to 20 mm. The method can be used for measuring small spot contrast ratios up to 10^3 with an error of less than 10%.

V. ACKNOWLEDGMENTS

This work was partially supported by a U.S. Army Breast Cancer research grant (DAMD17-96-1-6283).

REFERENCES

- [1] Boynton PA, Kelley EF. Measuring the contrast ratio of displays. *Information Display* 1996; 11:24–27.
- [2] Boynton PA, Kelley EF. Accurate contrast-ratio measurements using a cone mask. *Proceedings of the Society for Information Display* 1997; 823–826.
- [3] Matsuda S, Nitoh T. Flare as applied to photographic lenses. *Applied Optics* 1972; 11:1850–1856.
- [4] Badano A, Flynn MJ, Muka E, et al. The veiling glare point-spread function of medical imaging monitors. *Proceedings of the SPIE* 1999; 3658.
- [5] Badano A. Image quality degradation by light scattering processes in high performance display devices for medical imaging. Ph.D. thesis, University of Michigan, 1999.
- [6] Boynton PA, Kelley EF. Small-area black luminance measurements on a white screen using replica masks. *Proceedings of the Society for Information Display* 1998; 941–944.
- [7] Libsch FR, Lien A. A compensation driving method for reducing crosstalk in XGA and higher-resolution TFT-LCDs. *Proceedings of the Society for Information Display* 1995; 253–256.
- [8] Libsch FR, Lien A. Understanding crosstalk in high-resolution color thin-film-transistor liquid crystal displays. *IBM Journal of Research and Development* 1998; 42:467–479.
- [9] Braun D. Crosstalk in passive matrix polymer LED displays. *Synthetic Metals* 1998; 92:107–113.
- [10] Spencer G, Shirley P, Zimmerman K, et al. Physically-based glare effects for digital images. *Computer Graphics Proceedings Annual Conference Series SIGGRAPH 95* 1995; 325–334.
- [11] Beckman C, Nilsson O, Paulsson LE. Intraocular light scattering in vision, artistic painting, and photography. *Applied Optics* 1994; 33:4749–4753.
- [12] Stiles WS, Crawford BH. The luminous efficiency of rays entering the eye pupil at different points. *Proceedings of the Royal Society of London* 1937; 122:428–450.
- [13] Flynn MJ, McDonald T, DiBello E, et al. Flat panel display technology for high performance radiographic imaging. *Proceedings of the SPIE* 1995; 2431:360–371.

EXPERIMENTAL MEASUREMENTS OF GLARE IN CATHODE-RAY TUBES

Aldo Badano and Michael J. Flynn

X-Ray Imaging Research Laboratory
Henry Ford Health System, Detroit, MI

Department of Nuclear Engineering and Radiological Sciences
The University of Michigan, Ann Arbor, MI

ABSTRACT

Multiple light reflections in the emissive structure and electron backscattering processes in the vacuum of cathode-ray tubes (CRT) are sources of luminance spread and loss of image quality. To perform glare measurements in CRTs, a detector that can record low intensity signals from small dark fields in the presence of a bright surrounding field is required. We have designed and constructed a luminance probe consisting of a cone-shaped nose and an internally baffled barrel that measures light generated in a spot of about 4 mm diameter. The probe minimizes light scattering from the probe back into the faceplate, and minimizes contributions from bright surrounding regions. In this paper, we report results on the performance of the probe and demonstrate its application for characterizing CRT devices. The probe is shown to be capable of measuring contrast ratios of at least 800 for dark fields with a radius of 2 cm. Measurements on a medical imaging CRTs illustrate how significant veiling glare in the device can result in contrast ratios of about 100 and how the reflection of ambient light can reduce the contrast ratio to below 25.

Keyword List: CRT, glare, luminance measurement, contrast.

SPIE Vol. 3335 Medical Imaging: Image Display (1998)

1 INTRODUCTION

Under optimized viewing conditions, observer performance is limited only by the human visual system. We have previously estimated that the minimum display performance required to achieve these optimized conditions requires a wide luminance range (5 - 1000 cd/m²), a perceptually linear greyscale levels (700), a high contrast ratio (200), and low surface reflection.¹ Displays systems which meet or exceed this requirement can be considered to be high fidelity devices. In general, transilluminated film exceeds the requirements for high fidelity radiographic display. However, currently available medical imaging CRTs have yet to achieve high fidelity performance.

To achieve good display quality in CRT and other emissive devices, degradation by glare and surface reflection has to be minimized. Glare is primarily caused by multiple light reflections in the emissive structure. Electron backscattering processes in the vacuum bulb of CRTs can cause additional glare, particularly with color devices.^{2,3} Another potential contribution to glare can come from holes in the Al conductive layer of monochrome CRTs that results in light emitted into the vacuum bulb. To reduce this problem, the Al film is evaporated on a thin

sheet deposited on top of the rough surface formed by phosphor grains. Since the emissive structure is designed to efficiently transport light out of display, CRT devices typically have excessive glare and surface reflection. This causes significant reduction in contrast, particularly for dark regions surrounded by bright regions.

Several approaches have been employed to reduce the adverse effects of glare in CRT devices. Light diffusion in the emissive structure is controlled by using absorptive faceplate glass and a rough glass surface at the phosphor interface. Since the glass thickness is significant (10 to 20 mm), the front of the display must be flat which promotes specular reflection. This is reduced in some systems by thin film anti-reflective (AR) coatings. Electron backscattering may be reduced by using low-Z material coatings^{4,2} in shadow masks. In addition to contrast reduction, glare in color CRTs degrades color purity and most color tubes use a black matrix to prevent color contamination. Using Monte Carlo simulations^{3,5} we have predicted that black matrix designs and thinner emissive structures might be used to decrease the loss of contrast associated with glare for monochrome devices. While these approaches have improved display performance, CRT display monitors continue to exhibit problems associated with glare and with scatter from environmental light.

The effect of optical and electronic glare in CRTs can be measured by recording the luminance for a small black region surrounded by a uniform bright scene. Investigators from the National Institute of Standards and Technology (NIST) have recently reported results using black squares of varying size on a white background.^{6,7} However, the symmetry of typical CRT point-spread functions (PSFs) suggests that a circular dark region surrounded by a larger bright pattern is more appropriate. In this work, we report on measurements made with test patterns having circular black regions of varying diameter. The luminance in the center of the black region is then related to the integral of the PSF tail beyond the radius of the black pattern.

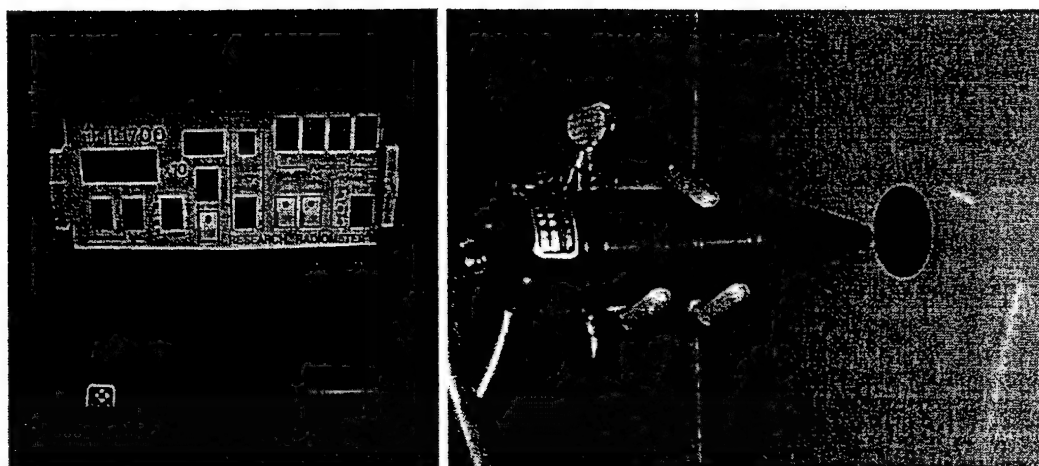
Measurement of the very low luminance in the dark region of a test pattern is difficult because light from the surrounding bright region can alter the response of the measurement system. In general, measurement systems using lens cannot be used because light scattering in the lens optics, referred to as flare, causes significant contamination of the dark field regions.^{6,7} For typical lens this is several percent of the bright field signal and for specially designed lens optics will still cause significant measurement error. NIST has reported a method to improve measurement results by placing a cone constructed of black material in front of the display with the small aperture at the cone tip located over the dark field.⁷ In this work, we report the design and performance of a special purpose luminance probe designed to measure the dark field luminance with minimal contamination from very bright surrounding regions. A series of baffles and a conic probe end prevent light from the surrounding regions from striking the silicon photodetector in the probe.

No detailed experimental reports have been made which document the glare and reflective characteristics of radiographic displays. In this work we have focused on the measurement methods necessary to perform these tests and on the performance of a novel luminance probe. The measurements are applied to laser printed films to demonstrate the applicability of the methods to a system with negligible glare and low reflection of ambient light. The application of the method in a monochrome CRT unit designed for radiologic applications is otherwise demonstrated.

2 METHODS

2.1 Luminance Probe Design

The luminance probe used in this work is based on an SEL 033 luminance sensor, photopic filter, and IL 1700 research radiometer made by International Light Inc. as shown in figure 1a. The sensor is a silicon photodiode with an active area of about 5.7 mm by 5.7 mm. Attached to the sensor is a standard barrel (approximately 4 cm diameter and 7 cm long) into which baffles can be positioned using threaded parts. At the end of this



(a) Photopic probe and IL 1700 research radiometer.

(b) Experimental arrangement for measuring luminance with test patterns on radiographic film.

Figure 1: Photopic probe and experimental setup for measurements on film.

barrel, a conic probe end is placed which was fabricated on a lathe from aluminum bar stock. Interior baffles were assembled by bonding small thin perforated disks of black anodized aluminum on small machined ledges or aperture holders. The entire probe was polished and black anodized to provide a specular absorptive surface. Figure 1b shows the detector assembly positioned to record the luminance of a dark field in a test pattern.

The probe tip is designed to minimize the amount of light that is scattered from the probe back to the emissive structure. As shown in figure 2, the probe entrance aperture has a diameter of 9 mm. The interior of the tip is shaped with a reverse cone geometry creating a sharp circular end to the probe. The inclination of the interior walls of the inner tip minimizes the amount of light that reflects back to the display faceplate. Light entering the probe at oblique angles is otherwise trapped by interior baffles. The outer cone shape of the probe reflects light coming from bright regions in a direction away from the display. A specular surface at 15° from the normal allows central measurements in 38 cm diagonal displays to be made with minimum signal contamination from reflections off the body of the probe.

A series of four baffles create a highly collimated response with a diameter of about 4 mm. Baffle positions and desired aperture diameters were determined using manual design methods. Figure 3 shows drawings that illustrate 4 different aspects of the optical design. The principal rays that define the responsive spot in the detector plane are depicted in figure 3(a). The detector is otherwise in a direct line with only a portion of the back side of each aperture as shown in figure 3(b). Each aperture is very thin to reduce light scattering from the edges of aperture holes. Light entering the probe at oblique angles, figure 3(c), is reflected off the interior side walls of the probe which are not viewed by the detector. The large number of scatterings from black surfaces that would be require to reach the detector through the multiple apertures prevent any significant signal from reaching the detector. In figure 3(d), light rays coming from a region outside the dark spot are shown. Only light rays coming form a very small region in the bright field is able to directly penetrate the first baffle.

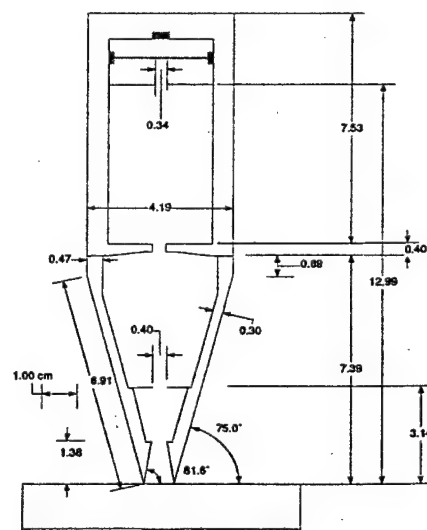


Figure 2: Probe dimensions.

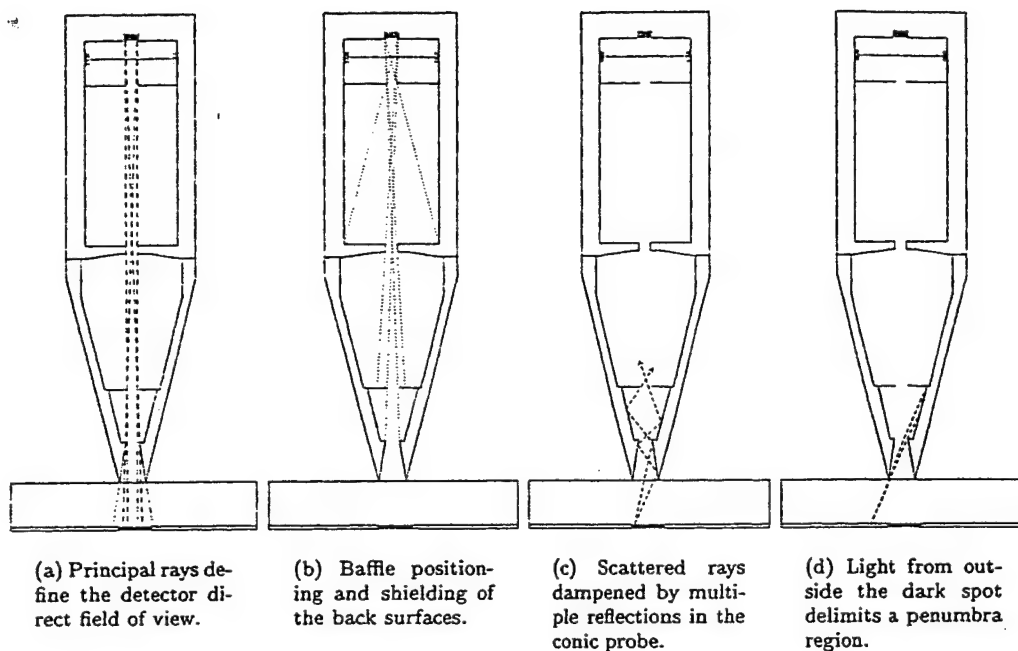


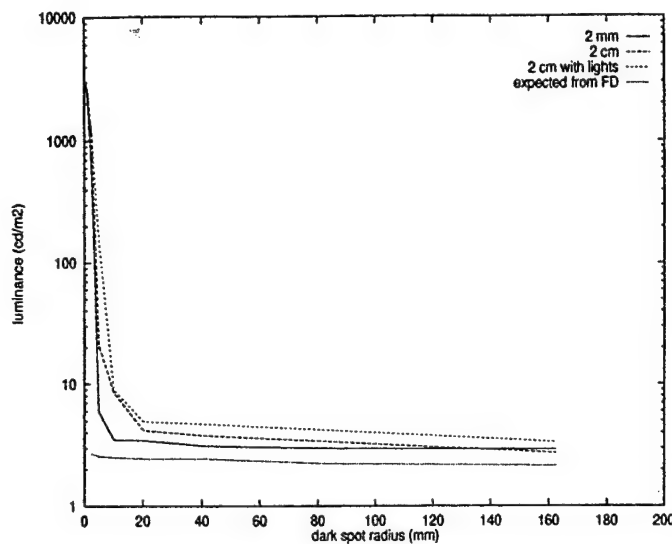
Figure 3: Design drawings for the photopic probe showing aspects of the optical design.

2.2 Detector response to a point source

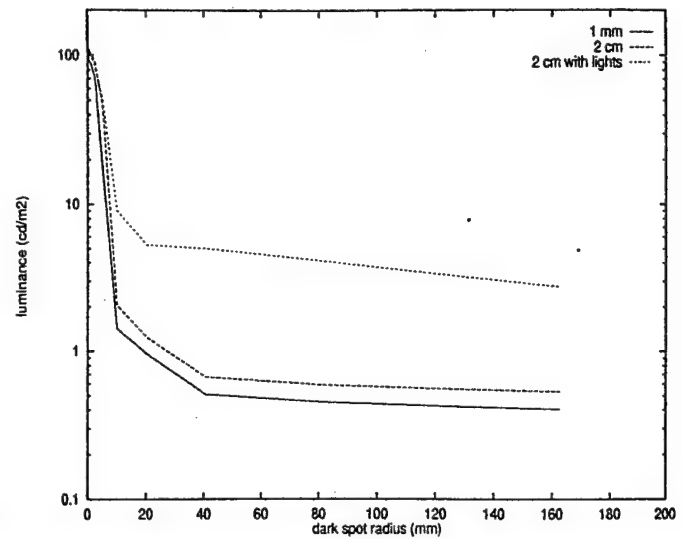
To determine the response of the probe to a point source, a 0.2 mm diameter aperture centered on a .025 mm thick stainless steel disk (Edmund Scientific) was mounted onto a sliding plate and placed on top of an integrating sphere port. The point source of light thus had a broad angular distribution from a small spot. The sliding plate was moved by a mechanical micrometer and measurements were taken at 0.250 mm steps.

Figure 4 shows the point response recorded at distances of 0.1, 1 and 2 cm from the aperture to the probe tip. After a relatively flat response region out to 2 mm from the central axis of the probe, a sharp reduction in response is observed. The recorded luminance decreases to negligible values after 3 mm. Similar response profiles were obtained for the 3 different distances between the probe tip and the point source. The FWHM (full-width-at-half-maximum) values computed for each measurement distance indicate only a slight change as a function of distance as expected from the highly collimated design (see table 1).

The point response results suggest that the probe can measure clearly defined circular dark field regions larger than 10 mm diameter while being successfully shielded from light originating from regions outside its field of view. Furthermore, the probe can be used at distances of at least 2 cm from the display surface. Thus, the glass faceplate thickness which separates the emissive layer from the probe does not hinder measurements of CRT devices.



(a) Measurements on radiographic film. The expected luminance was calculated from the film density (FD) values.



(b) Measurements on a monochrome CRT. The arrows demark a range of dark spot radius that can be used to characterize glare.

Figure 5: Response of the probe to glare test patterns.

3.2 CRT measurements

A similar set of measurements were performed on a monochrome CRT which had previously been supplied as a part of a medical imaging workstation (Image Systems model M24L). Test patterns with the same dimension as was used with the film tests were displayed on the CRT using an Xterminal controller and graphic display software. The graphic tonescale as well as the monitor contrast and brightness were set at extreme positions to present a pattern for which the bright and dark regions were at the limits of the available range. Figure 5(b) shows the results of the CRT measurements. Distances between the glass faceplate and the probe tip of 1 and 20 mm were used and the effect of modest ambient lighting was investigated. The environmental light used for the CRT measurements was not necessarily the same as that for the film measurements. For this display, ambient illumination has a significant impact on the glare characteristics of the device. It should be noted that the monitor tested was made in about 1993 and does not necessarily have the performance of CRTs manufactured more recently.

3.3 Glare ratio results

We define the glare ratio as the ratio of the bright field luminance measured without any dark field pattern to the luminance of the dark field. Table 2 shows the contrast ratios for the experiments reported in this paper for dark fields with radii of 5 mm or larger. The performance of transilluminated film is notably superior in all conditions. While the point response data indicates that light beyond a 5 mm radius does not directly strike the detector, this data clearly suggest that a radius of 10 mm is required to make measurements of very high contrast ratio. At 1 mm from the film, the contrast ratio is 862 which is likely near the true value. However, at a 2 cm distance and for a 10 mm radius the contrast ratio is 355 and is likely contaminated in a small amount from bright field light which enters the probe aperture and is able to reach the photodiode. At this distance good results are obtained for radii larger than 20 mm. The significant glare associated with the CRT device is clearly seen for dark fields between 1 and 2 cm where the contrast ratio is 85 and 127.

Spot radius (mm)	Film			CRT		
	2 mm	2 cm	2 cm with light	1 mm	2 cm	2 cm with light
5.08	511	143	20.0	6.74	2.60	2.39
10.16	862	355	337	85.3	59.5	13.5
20.32	873	723	614	127	98.4	23.2
40.64	963	798	641	240	183	24.6
81.28	1010	886	715	270	207	29.83
162.56	1035	1107	905	300	228	44.36

Table 2: Contrast ratios for the film and CRT measurements. For distances associated with features encountered in diagnostic images (1 to 2 cm), the difference in contrast ratios for film and CRTs is notable.

4 Discussion

For the multi-baffle probe design that we have used, there is a decrease in the total amount of recorded light, or recorded luminance value, when the source-to-probe distance is increased. This is different than for single aperture luminance probes where the inverse square reduction in response for each point source viewed is compensated by the increase in the area of response that the probe records as the distance to the light source is increased. Thus conventional luminance probes with a barrel and a single aperture will record the same luminance value at different distances from the surface of a uniform brightness. Because of the tightly collimated design of this probe, the luminance calibration varies as a function of distance from the surface. The reduction in recorded luminance with distance to the source can be seen in figures 4, and 5. This luminance probe is thus best used for relative measurements such as contrast ratio and not absolute measurements. For figure 5, the luminance was calibrated by making a measurement of the bright field luminance with a standard luminance probe having a photometric calibration performed by International Light Inc. .

In this work we have used film as a surrogate for a test pattern with a true black dark field and a very bright surrounding region. Measurements made with a laboratory diffuse densitometry indicate that the contrast ratio for the film patterns is between 909 and 1144. The film densities for the small dark patterns are slightly less than for the large patterns which is understood to be due to a variation associated with the chemical development process. The contrast ratios measured with the luminance probe demonstrate the same slight variation with dark field radius. However, the dark field luminance measured with the probe is about 1 to 2 cd/m² larger than predicted by the film density. We believe this difference is either due to geometric differences in acceptance angle between the probe and the densitometer or due to a systematic error in establishing the zero value of the photometric probe.

Since the glass faceplate of CRT devices forces the probe to be at some distance from the emissive layer, it is important that a luminance probe be capable of recording reliable contrast ratios at distances of about 2 cm. The results from measurements with the film patterns indicates that very reliable results can be obtained for dark field patterns of 2 cm radius for distances up to 2 cm from the surface. The shape of the CRT point spread function that we have reported in our previous work^{3,5} indicate significant glare at distance from 2 to 5 cm. Test patterns of 2 cm size thus have merit for characterizing CRT systems.

Dark radiographic features of 1 to 2 cm dimension surrounded by bright fields are commonly found in diagnostic images. Our CRT results indicate notable additional degradation in contrast ratio for dark fields of 1 cm radius. Our film results indicate some contamination of the measurement (contrast ratio of 355) for a 1 cm radius dark field observed at 2 cm distance. Nonetheless, the comparable contrast ratio of 85 at the faceplate surface is likely associated with a real difference in CRT performance. We estimate that for the 1 cm radius pattern these CRT measurements at the faceplate may be in error by 10 percent. It would be desirable to further improve the design of this probe to obtain film contrast ratio results at 2 cm distances that have little measurement error.

We have illustrated how a probe of this design can be used to examine the image quality degradation associated with ambient room lighting. However, no attempt was made to establish a standardized environment for illuminating the surface of the display. The approximate illuminance of the surfaces was 100 lux, however both rooms used for this measurement had significant angular dependence for the illumination of the surface. Regardless, the results for the film test patterns demonstrate how effective the black material of the film is at absorbing the illuminating light. Similarly, the very high reflectance of the CRT associated with the non-absorbing properties of the phosphor emissive structure is demonstrated by the severe reduction in contrast ratio. A more controlled illuminating environment is required to quantify the effects of ambient lighting. Furthermore, the influence of ambient light reflection is large enough that measurements of the contrast ratio associated with the device only should be made with black absorbant material positioned to absorb the light emitted from the test pattern.

Previously, we described a method for computing the luminance spread function of emissive displays from the results of the Monte Carlo simulations.³ The results of the Monte Carlo calculation yield the fraction of photons that emerge from the display surface from positions between a radius of r and $r + \delta r$ and are within a specified solid angle. In principle, this differential point spread function, $P(r)\delta r$, can be experimentally measured, however the very low values of $P(r)\delta r$ relative to intensity of a point source make this a difficult measurement.

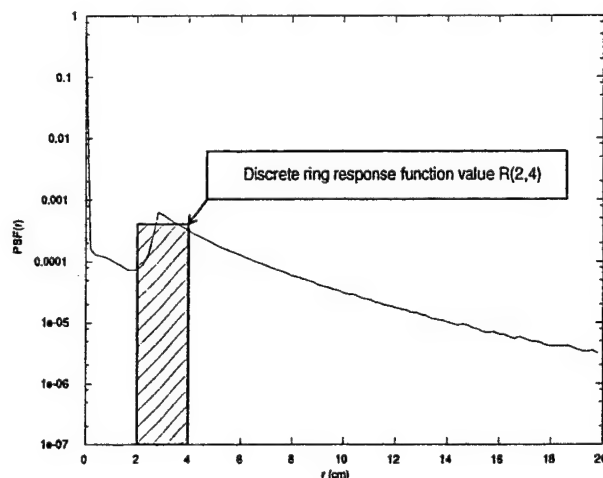


Figure 6: Relationship between the point-spread function predictions from the Monte Carlo calculations and the discrete ring response function obtained from the experimental results.

In this work, the luminance spread function characteristics are determined indirectly by measuring the dark spot luminance for test patterns with increasing dark spot diameter. A ring response function which reflects the diffuse signal contributed by a bright ring to the central dark spot can be obtained by subtracting consecutive values. The ring response function is simply the difference in luminance values for dark field patterns of two different radii, $R(r_i, r_j) = l_{r_j} - l_{r_i}$. This response function $R(r_i, r_j)$ is directly related to the integral of the point spread function from r_i to r_j as illustrated in fig. 6 when appropriately normalized for the units of the point response function. Thus, measurements made with circular dark field patterns of varying diameter can thus be compared to experimental or theoretical descriptions of the point response function.

5 SUMMARY

A cone-shaped luminance probe that allows measurements of the glare characteristics of emissive displays has been designed and constructed. The performance of the detection system was tested using a point source and measurements of test patterns were made with transilluminated film. The response characteristics show that this probe permits the measurements of very low signals without contamination from bright surroundings. The measurement system and the reported test patterns provide a useful method to characterize glare in display devices. The results from measurements made with circular test patterns can be related to the luminance point spread function associated with glare.

6 ACKNOWLEDGMENTS

This work was partially supported by a U.S. Army Breast Cancer research grant (DAMD17-96-1-6283). Fabrication of the cone shaped adapter was expertly done by Richard Drumb in the Breech Research Laboratory of Henry Ford Health System.

7 REFERENCES

- [1] M. J. Flynn, J. Kanicki, A. Badano, and W. R. Eyler. High fidelity electronic display of digital radiographs. 1997. Scientific exhibit presented at the 83rd Scientific Assembly and Annual Meeting of the Radiological Society of North America, november 1997, invited for publication in Radiographics.
- [2] G. C. de Vries. Contrast-enhancement under low ambient illumination. *SID'95 Digest*, pages 32-35, 1995.
- [3] A. Badano and M. J. Flynn. Image degradation by glare in radiologic display devices. In *SPIE Medical Imaging 1997: Image Display*, volume 3031, pages 222-231, 1997.
- [4] J. J. van Oekel. Improving the contrast of CRTs under low ambient illumination with a graphite coating. *SID'95 Digest*, pages 427-430, 1995.
- [5] A. Badano and M. J. Flynn. Monte Carlo modeling of the luminance spread function in flat panel displays. In *International Display Research Conference 1997*, pages 382-385. SID, 1997.
- [6] P. A. Boynton and E. F. Kelley. Measuring the contrast ratio of displays. *Information Display*, 11:24-27, November 1996.
- [7] P. A. Boynton and E. F. Kelley. Accurate contrast-ratio measurements using a cone mask. In *International Display Research Conference*, pages 823-826, 1997.

Monte Carlo Modeling of Glare in Cathode-Ray Tubes for Medical Imaging

Aldo Badano and Michael J. Flynn

ABSTRACT

The luminance range of cathode-ray tube (CRT) systems is limited by glare associated with light diffusion in the thick glass faceplate. This is of particular concern in medical imaging applications, where images with wide luminance range and low contrast detail are displayed. To achieve the required display quality, careful control of the light transport processes in the faceplate of CRTs is needed. In this paper, an optical Monte Carlo simulation code (DETECT-II) for modeling the luminance spread in the CRT emissive structures is described. Using this approach, the effect of rough surfaces and anti-reflective thin-film coatings on luminance spread functions is examined.

Keywords—Glare, CRT, anti-reflective coatings, Monte Carlo, computational modeling.

I. INTRODUCTION

Cathode-ray tube (CRT) systems used for medical imaging applications should have very high brightness (up to $1,000 \text{ cd/m}^2$) while minimizing the degradation of image quality caused by light diffusion in the faceplate. Reduction of luminance spread is usually achieved by increasing glass absorption. However, this solution also severely reduces the display brightness (up to a factor of 0.37).¹ Previous calculations have showed that the luminance spread characteristics of very thin emissive structures permit a better image quality with less degradation by glare and increased brightness.² However, large screen sizes required in radiologic applications* can only be achieved with large bulbs and correspondingly thick faceplates.

Increasingly, ambient light reflection off the device faceplate is becoming a critical consideration when displaying medical radiographic images. Ambient illumination levels vary greatly depending on the medical application and can be difficult to control. Proper modeling and characterization of the effect of anti-reflective (AR) coatings on light spreading in the emissive structures is needed to understand their importance in medical imaging CRTs.

From the Dept. of Diagnostic Radiology, Henry Ford Hospital, Detroit, MI and the Dept. of Nuclear Engineering and Radiological Sciences, University of Michigan, Ann Arbor, MI.

*35 x 43 cm is a standard size for radiographic detectors.

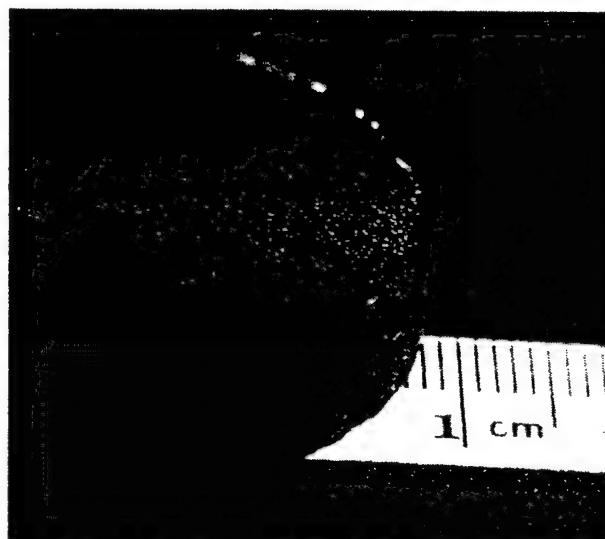


Fig. 1. CRT faceplate core showing the inner surface after removal of the phosphor and Al layers.

To understand the trade-offs in emissive structure design, we developed a simulation code (DETECT-II) that can be used to predict the glare characteristics of an electronic display.^{1,2} In this paper, the application of this code for the simulation of light transport in CRT emissive structures is described. Emphasis is given to the techniques used to computationally describe rough surfaces and AR coatings. This code is used to analyze the glare characteristics of a monochrome CRT. The geometric model for the simulations is based on information obtained from faceplate sample cores of a medical imaging CRT (Clinton Electronics Corp.). The diameter of the cores is about 37 mm. Fig. 1 shows the rough surface typical of wet etching treatment, seen at the inner glass surface in contact with the phosphor grains. As seen in fig. 2, several layers of phosphor grains with broad particle size distribution are overcoated with a very thin Al layer.

II. METHODS

The modeling of light transport processes that occur in emissive structures can be done using either ray tracing or Monte Carlo methods. Ray tracing techniques rely upon a priori knowledge of the system response to determine the principal ray paths that will contribute to the output. On the other hand, Monte Carlo methods track the trajectories of a large number of optical pho-



Fig. 2. Scanning electron microscope image of a CRT faceplate sample. The phosphor layers were exposed using a scalpel scratch. The image dimension is about $50\text{ }\mu\text{m}$. Debris from the sample preparation can be seen on top of the Al layer.

tons to describe the statistically averaged output. Absorption and scattering processes are modeled with the Monte Carlo method by randomly sampling the distance to each event from probability distribution functions. Monte Carlo methods can handle a wide variety of physical cases and are computationally practical when using high speed computers.

To model the luminance spread functions in emissive displays, we developed a Monte Carlo optical transport code written in Fortran 90 (DETECT-II). The geometry is described in 3D Cartesian coordinates using slabs with orthogonal division into cells. The surface definitions include rough surface, mirror, perfect absorber, partial diffuse absorber with lambertian emission and thin film. Photon histories are started as point or planar sources with lambertian or isotropic angular distribution. Individual photons are allowed to be absorbed or scattered in the medium. Required computing time per track ranges from 15 to 100 μs , depending on the complexity of the algorithms involved. To avoid correlations in multidimensional space when a large number of histories are needed, a portable, fast, and very-long period (2^{144}) lagged Fibonacci random number generator is used.^{3,4} In addition, a parallel implementation of this random number generator is easily achievable.

A. Photon polarization

A unique feature of DETECT-II is the tracking of photon polarization. Polarization tracking using Monte Carlo techniques has been used in astrophysical applications.^{5,6} The variation of intensity of each polarization component is described by using the Stokes parameters. These prior

Monte Carlo techniques follow ray paths and not individual photons. We have implemented a different algorithm that tracks polarization states for single optical photons. Neglecting the effect of finite wavelength, the light transport is simulated by tracking individual photons using a physical optics description. When boundary crossings occur, polarization dependencies in the Fresnel coefficients are evaluated. Reflection and transmission coefficients are interpreted as probabilities.⁷

B. Display simulation

An important aspect of our Monte Carlo code is a method for binning results which is designed for display modeling. To simulate display performance, the viewer is assumed to observe the image from a direction normal to the surface. Photons are tracked from the source to the front surface of the display and those within a finite solid angle about the normal are binned into discrete regions on the surface. A solid angle corresponding to a 6° cone is used rather than the typical solid angle of a human observer in order to make efficient use of the photon histories. The binning of the emerging position is done by back-projecting the light path to a virtual plane of emission. This accounts for the difference in index of refraction between air and glass, and allows binning from a large solid angle to a common virtual focal plane inside the emissive structure.

C. Emissive structure models

Our previously reported calculations were made with a very approximate model of a CRT emissive structure with a glass faceplate thickness of 1.6 cm. CRT emissive structures were modeled as single slabs (i.e., the glass faceplate) with surface conditions reflecting different design approaches including black matrix, and reflective metallic coatings (see fig. 3).^{1,2} The phosphor layer was modeled by a 90% diffuse reflectance that includes the reflection from the Al film. However, careful examination of the phosphor-glass interface confirms the presence of regions with glass-to-vacuum, and glass-to-binder contacts. A single uniform vacuum layer between the phosphor and the faceplate is not appropriate since it results in excessive light channeling.

In this paper, we introduce a phosphor-binder layer to understand the effect of the surface roughness on the luminance spread function. The roughness of the inner surface of the faceplate is described using the rough surface scattering description presented in section II-D. Roughness profiles are defined by the maximum angle that the sampling procedure accepts[†]. A two-slab representation

[†]A maximum angle of 0° is equivalent to a smooth surface.

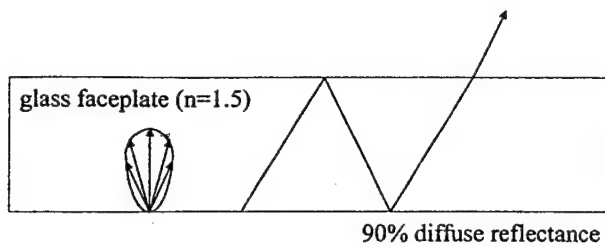


Fig. 3. Cross-section of the geometric model used in previous calculations.

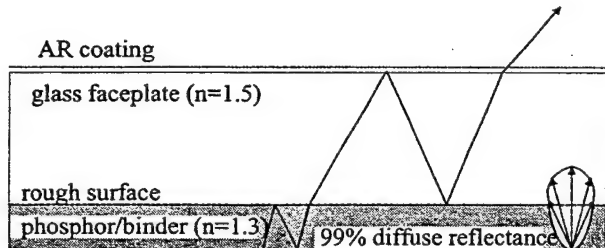


Fig. 4. Cross-section of the geometric model used in this work.

of the emissive structure that depicts the change in index of refraction from the glass (1.523) to a material with an intermediate index (1.3) to accommodate for the interfaces with binder and phosphor grains is used. The phosphor layer is 100 μm thick with a 99% diffuse reflectance at the Al film, as shown in fig. 4. Using this geometry model, the effect of the surface roughness at the interface between the glass and the phosphor layer can be investigated.

D. Rough surface scattering

To describe Fresnel interactions at rough surfaces such as shown in fig. 1, the surface normal is randomly perturbed. This is appropriate for surfaces having sinusoidal profiles with low aspect ratio. The roughness is specified by defining a maximum cone for surface normal variations. A Fresnel analysis is then performed using angles ϕ_1 and ϕ_2 . The diagram in fig. 5 shows a 2D representation of the model, where α is the rotation angle used to simulate a surface slope.

The Fresnel's equations are solved with the incident photon vector expressed in a rotated coordinate system. The out-coming vector is then rotated back to the initial coordinate system. Additionally, a test is performed: $\phi_1 + \alpha < \frac{\pi}{2}$, which prevents a reflection directed into the surface. For a reflection occurring in a valley, the reflected photon may strike a neighboring hill. This is not accounted in the model and thus, surface normal distributions should be limited to modest cone angles.

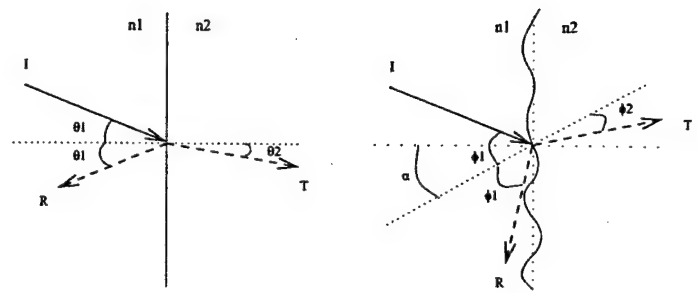


Fig. 5. 2D representation of the rough surface model. θ_1 and θ_2 are given by Snell's law. On the left, the flat surface case is depicted. The surface normal is rotated an angle α on the right. After the boundary analysis is performed in the rotated system, T or R are expressed in the original coordinate system.

E. Transmission of anti-reflective coatings

In general, AR coatings have been directed at reducing the specular reflections from the faceplate of a CRT. While silica-coating or chemically etched rough surfaces have been used for this purpose, the degradation of display resolution is unacceptable for most applications. Recently, thin-film coatings are employed in high-definition CRT systems for medical applications. Materials include organic layers⁸ and metal oxides.^{11,9,10} Multiple layers are used in recent AR coating designs to further decrease the reflectivity, with transparent conductive layers to dissipate static charge and reduce dust build-up, and to provide electromagnetic shielding.¹¹

In addition to a reduction in the reflectance of the display, AR coatings affect the transport of light inside the faceplate by favoring transmission at the glass-air interface. The optical properties of such structures can be described as a function of the wavelength and the incident angle.⁷ By using modified Fresnel coefficients, thin-films can be incorporated as surface types into the simulation code.

III. RESULTS AND DISCUSSION

In this work, we report results using a more accurate model of the emissive structure of CRTs. Figure 6 shows the results for the 3 added components. First, the effect of a second layer (phosphor-binder) is depicted in curve a. All surfaces are smooth and no AR coating is used in this case. The first peak in this curve is associated with reflections off the glass-air interface that are scattered at the phosphor diffuse surface. Additional oscillations are caused by multiple internal reflections occurring in the binder layer and determined by the critical angle of the binder-glass interface.

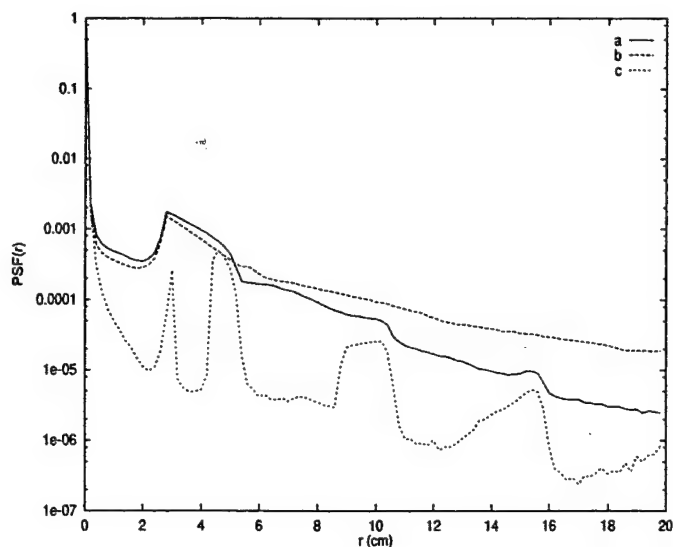


Fig. 6. Point-spread functions CRT emissive structures shown in fig. 4. Curve (a) corresponds to smooth surfaces without AR coating. The effects of rough surface (b) and AR coating (c) are shown separately.

The second case (curve b) reflects a model with a rough surface with a maximum angle of 30° at the binder-glass boundary. The roughness results in a more diffuse response, with a slight reduction of the first peak intensity, and an increase in the magnitude of the tails. The oscillations seen in the case of smooth surfaces become less noticeable. The results predict a reduction of the central peak intensity¹ of 4.6%.

Finally, curve (c) corresponds to a 2-slab structure with no rough surface and an AR coating with optimal index match ($n = 1.234$). For this model, the thickness of the film is $0.169 \mu\text{m}$ for a 550 nm monoenergetic light source. The results confirm the expected reduction in the magnitude of the tails. At the same time, the peak intensity is increased by 2.6% due to the improved index matching at the glass-air interface. Additional peaks appear more clearly due to a reduction of the diffuse contributions.

IV. SUMMARY

The computational modeling of light transport in the emissive structures of CRTs provides a unique tool for the design of high-definition systems. In this paper, we described a new simulation code (DETECT-II) that uses Monte Carlo techniques to predict the optical performance of display devices. Descriptions of rough surfaces and AR thin-film structures were implemented to provide a more detailed model of the optical properties of emissive structures of the type found in high-performance CRT units used in medical imaging applications. Predictions

of the model show agreement with preliminary measurements performed with a unique experimental probe designed for measuring the glare characteristics of CRTs.¹²

V. ACKNOWLEDGMENTS

The authors thanks Ed Muka (Mallinckrodt Institute of Radiology) for discussions on CRT quality and glare, and Wayne Pitchford for assistance with the SEM images of CRT phosphors. This work was partially supported by a U.S. Army Breast Cancer research grant (DAMD17-96-1-6283).

REFERENCES

- [1] A. Badano and M. J. Flynn. Image degradation by glare in radiologic display devices. In *SPIE Medical Imaging 1997: Image Display*, volume 3031, pages 222-231, 1997.
- [2] A. Badano and M. J. Flynn. Monte Carlo modeling of the luminance spread function in flat panel displays. In *International Display Research Conference 1997*, pages 382-385. SID, 1997.
- [3] G. Marsaglia, A. Zaman, and W.W. Tsang. Toward a universal random number generator. *Statistics and Probability Letters*, 8:35-39, 1990.
- [4] F. James. A review of pseudorandom number generators. *Computer Physics Communications*, 60:329-344, 1990.
- [5] S. Bianchi, A. Ferrara, and C. Giovanardi. Monte Carlo simulations of dusty spiral galaxies: extinction and polarization properties. *The Astrophysical Journal*, 465:127-144, July 1996.
- [6] N. V. Voshchinnikov, V. P. Grinin, and V. V. Karjukin. Monte Carlo simulation of light scattering in the envelopes of young stars. *Astronomy and Astrophysics*, 294:547-554, 1995.
- [7] M. Born and E. Wolf. *Principles of optics*. Pergamon Press, 3rd. revised edition, 1965.
- [8] H. S. Tong and G. Prando. Hygroscopic ion-induced antiglare/antistatic coating for CRT applications. *SID'92 Digest*, 1992.
- [9] Y. Ono, Y. Ohtani, K. Hiratsuka, and T. Morimoto. A new antireflective and antistatic double-layered coating for CRTs. *SID'92 Digest*, 1992.
- [10] J. Haisma, J. H. Pasman, J. M. Pasmans, and P. van der Werf. Wide-spectrum tint-free reflection reduction of viewing screens. *Applied Optics*, 24:2679-2686, August 1985.
- [11] Viratec Thin Films. Anti-reflection coatings. Product information, 1997.
- [12] A. Badano and M. J. Flynn. Experimental measurements of glare in cathode-ray tubes. In *SPIE Medical Imaging 1998: Image Display*, volume 3335, 1998.

Image Degradation by Glare in Radiologic Display Devices

Aldo Badano and Michael J. Flynn

X-Ray Imaging Research Laboratory
Henry Ford Health System, Detroit, Michigan

Department of Nuclear Engineering and Radiological Sciences
University of Michigan, Ann Arbor, Michigan

ABSTRACT

No electronic devices are currently available that can display digital radiographs without loss of visual information compared to traditional transilluminated film. Light scattering within the glass faceplate of cathode-ray tube (CRT) devices causes excessive glare that reduces image contrast. This glare, along with ambient light reflection, has been recognized as a significant limitation for radiologic applications. Efforts to control the effect of glare and ambient light reflection in CRTs include the use of absorptive glass and thin film coatings. In the near future, flat panel displays (FPD) with thin emissive structures should provide very low glare, high performance devices. We have used an optical Monte Carlo simulation to evaluate the effect of glare on image quality for typical CRT and flat panel display devices. The trade-off between display brightness and image contrast is described. For CRT systems, achieving good glare ratio requires a reduction of brightness to 30-40 % of the maximum potential brightness. For FPD systems, similar glare performance can be achieved while maintaining 80 % of the maximum potential brightness.

Keyword List: flat panel display, emissive display, digital radiography, CRT, glare.

1 INTRODUCTION

The radiologic information acquired by current digital radiographic systems is often interpreted using film from a laser printer. The electronic display of digital radiographs will require devices with the performance of transilluminated film.¹ High luminance, low noise and wide dynamic range are required, as summarized in Table I. Computer workstations designed for displaying and interpreting digital radiographs all use cathode-ray tube monitors (CRT). However, the limitations of current CRT display devices as compared to transilluminated film have been recognized and include issues such as brightness, resolution, dynamic range, uniformity, and noise.²⁻⁶

Typical CRTs require a thick glass panel between the light emission sites and the viewer. Depending on the curvature ratio of the tube, the faceplate thickness may range between 1.3 and 2.5 cm.⁷ Multipath light scattering in the faceplate adds a diffuse background (glare) to the primary signal that reduces contrast. The degradation

Total dimensions	35 cm x 43 cm
Pixel dimensions	160 μm max. / 80 μm nominal
Array size	2000 x 2500 min. / 4000 x 5000 nominal
Peak luminance	2000 cd/m^2
Minimum luminance	5 cd/m^2
Color	white
Emission distribution	lambertian
Noise power spectrum	white
S/N for each pixel	> 100
S/N for .5 mm region	> 400
Intrascene dynamic range	400
Greyscale	1024 (log or perceptually linear)
Refresh rate	static or 70 Hz
Large area distortion	1 %
Color inversion	none

Table 1: High fidelity display requirements

in image quality is significantly more severe for subtle lesions in dark regions with bright surroundings. To reduce the contrast reduction by glare, dark tinted glass is used for the faceplate. Transmission can be as low as 13 % for a thickness of 1.78 cm (equivalent to an absorption coefficient of 1.15 cm^{-1}).⁸ On the other hand, flat panel field-emission displays⁹⁻¹³ have the potential for a thin faceplate due to a large number of spacers between the electron emitting layer and the phosphor. In this paper, the low frequency degradation of image quality by glare from light scattering in the faceplate of emissive display devices is addressed. The effect of glare for both CRT and flat panel display emissive structures is computationally modeled for test pattern images. Finally, the influence of glare-reducing glass absorbers on both glare and display brightness is reported.

2 GLARE IN EMISSIVE DISPLAYS

Computational models have been used to simulate the effect of device characteristics on display performance including the frequency response of electronics, electron beam spot size, and phosphor granularity.^{14,15} Computational modeling can also be used to simulate glare. This requires accurate knowledge of all processes that propagate light from bright spots in an image to points at substantial distance, i.e. the tails of the device point spread function (PSF). This work has been motivated by a desire to obtain accurate PSFs to model glare. While the tails of these PSFs can have very low values, they can contribute significant signal because of their spatial extent.

Glare measurements on actual CRT emissive structures have been recently reported.¹⁶ These glare measurements and glare measurement results are strongly dependent on the nature of the test image. However, no standard metric has been adopted for reporting the glare characteristics of actual display devices. In this study, a test pattern that we previously described was used.¹⁷ The pattern consists of an inner dark circular spot, surrounded by a bright outer circle with a ratio of radii of 10. The rest of the scene is kept at the same dark level of the inner spot (see Fig. 1). The glare ratio is defined as the difference in display luminance between the central pixel in the pattern and the brightest pixel in the bright region.

The impact of electron backscattering on display performance has not been considered in previous studies. For an Al layer, the backscattering fraction for an electron beam energy of 10 keV is about 12.5-15 % and 14-15 % for 30 keV.^{18,19} The backscattered electrons are subjected to the electromagnetic fields present in the

vacuum region. The backscattered electrons will eventually impinge on the phosphor at a distance from its initial interaction position which is a function of the backscattering angle and energy. The backscattering energy, which is a function of the backscattering angle, will eventually result in the backscattered electron impinging into the phosphor at a certain distance from its initial interaction position. This results in an electronic contribution to glare that is not considered in this work.

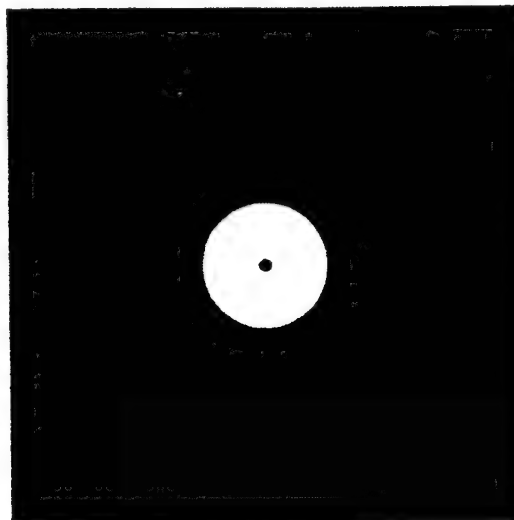


Figure 1: Test pattern for glare measurements.

3 MODELING GLARE IN DISPLAY DEVICES

3.1 Monte Carlo calculation of the point spread function

In a cathodoluminescent display device, the emissive structure includes all components that convert energetic electrons to visible light. Typical emissive structures components include: cathodoluminescent phosphors, conductive layers, reflective or absorptive films, transparent support (faceplate), and anti-reflective and anti-glare materials. In this work, we have modeled the glare characteristics of 2 types of emissive structures. All surfaces are modeled as perfectly flat. The angular distribution emerging from the phosphor layer was assumed to be lambertian.

Structures CRT-A and CRT-B are typical CRT display devices. Both have a faceplate thickness of 1.6 cm. CRT-A has an Al conductive and reflective layer on the back of the phosphor layer producing a reflection of 90 %. CRT-B has a perfectly absorbing black matrix coated in between the phosphor dots, with an aperture ratio of 50 %. For each CRT structure, 5 levels of absorption coefficient were considered (0.0, 0.2, 0.4, 0.6, and 1.0 cm^{-1}). Emissive structures FPD-A and FPD-B are typical of flat-panel emissive displays. The thicknesses are 0.3 and 0.1 cm respectively. For each FPD structure, 8 levels of absorption coefficient were considered (0.0, 0.2, 0.4, 0.6, 1.0, 3.0, 5.0 and 9.0 cm^{-1}). Cross-sections of the emissive structures are presented in figures 2 and 3.

In previous work, we described Detect-II, an optical Monte Carlo code, capable of simulating the optical transport processes in emissive structures. Unique features of the code include special binning for simulating display performance characteristics, and photon polarization tracking.¹⁷ Detect-II was used to obtain the PSFs of different emissive structures. The results of the Monte Carlo calculation yield the number of photons, P_0 , that originate from the source point and are observed within the solid angle of the observer. Secondly, the number

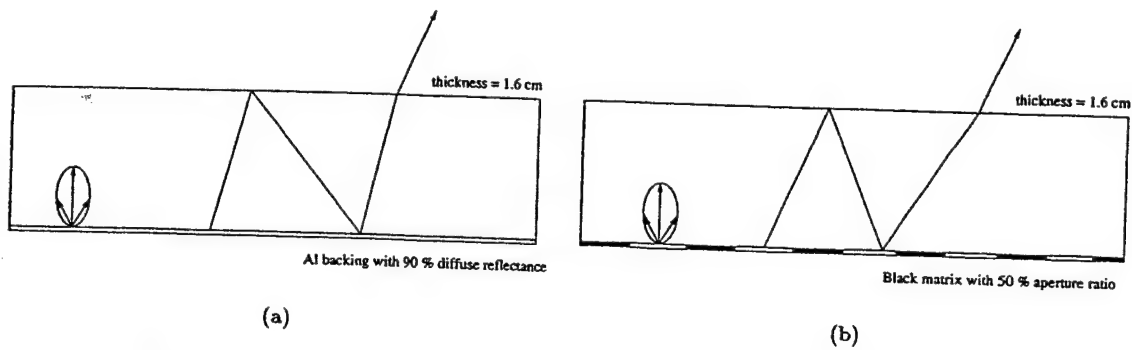


Figure 2: Cross-sections of emissive structures (a) CRT-A, and (b) CRT-B.

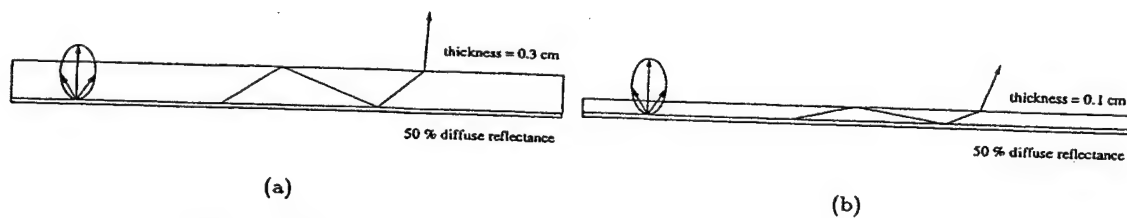


Figure 3: Cross-sections of emissive structures (a) FPD-A, and (b) FPD-B.

of photons observed within the solid angle of the observer but last associated with a point on the emission layer which is located at a radius from r to Δr from the source point are binned within N bins out to a distance $N\Delta r(P_i$ for $i = 1..N$). This is then converted to the differential probability of light emission per unit area,

$$L(i) = \frac{dL}{dA}$$

$$L(i) = \frac{P_i/P_0}{\pi[(i+1)\Delta r]^2 - (i\Delta r)^2}$$

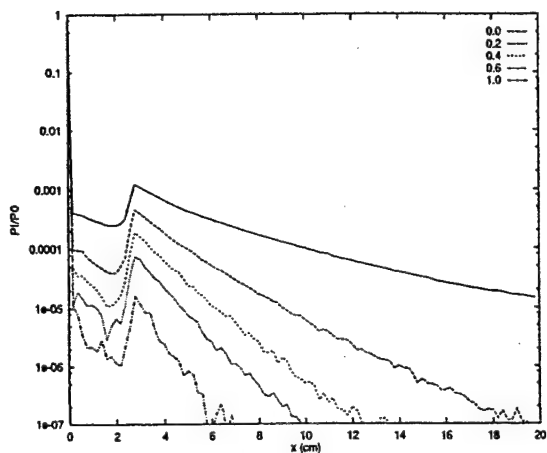
for,

$$r = i\Delta r$$

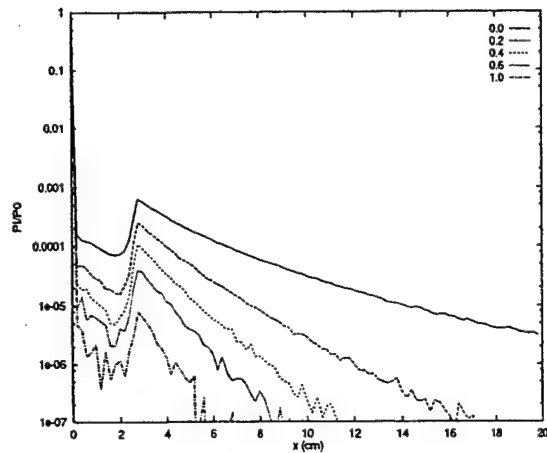
$$i = 1..N$$

where $L(i)$ is a discrete representation of the continuous luminance point spread function $L(r)$. $L(r)$ can be interpreted as the observed luminance in cd/m^2 resulting from a point source located at the origin of the emissive surface with a luminous intensity of 1 cd.

Because $L(0)$ is associated with a point source and goes to a very large number when small Δr are used for the binning of the Monte Carlo code, we define $L(i)$ only for values of i ranging from 1 to N . Instead, the luminous intensity of the central peak, $I(0)$, was defined as the fraction of unscattered light that reaches the viewer from a point source producing a luminous intensity of 1 cd. $I(0)$ describes the brightness of images not degraded by glare. For a digital display, the luminance associated with an emissive structure having an apparent luminous intensity of $I(0)$ per pixel is $I(0)/\rho_p$, where ρ_p is the number of pixels per m^2 . $I(0)$ can be deduced from P_0 and the lumens of light associated with the number of histories started at the phosphor layer. For the emissive structures studied in this work, P_0 is the same in the absence of absorbers. We therefore have normalized $I(0)$ to 1000. The relative reduction of $I(0)$ with absorption is used as a measure of brightness.

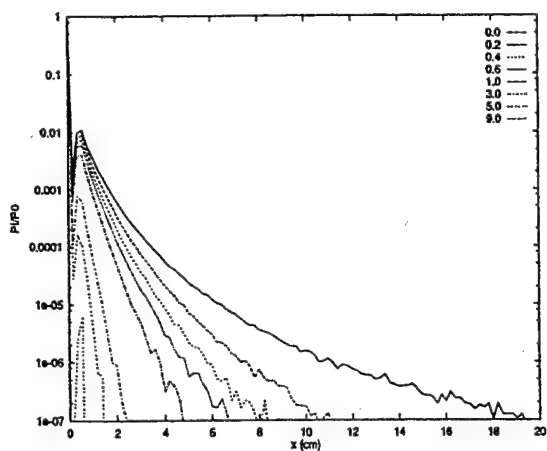


(a)

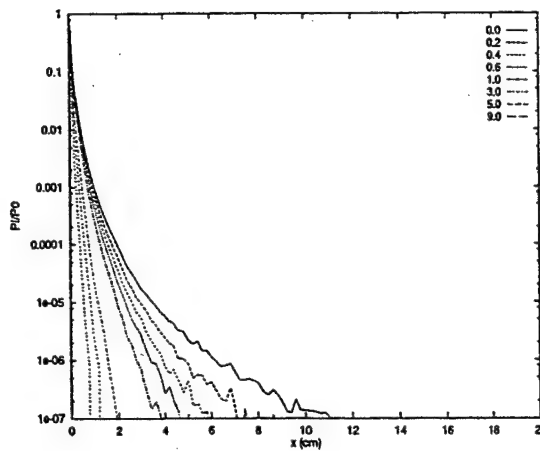


(b)

Figure 4: P_i/P_0 for CRT-A (a), and CRT-B (b) computed for different absorption coefficients in cm^{-1} with $\Delta r = 0.2$ cm.



(a)



(b)

Figure 5: P_i/P_0 for FPD-A (a), and FPD-B (b) computed for different absorption coefficients in cm^{-1} with $\Delta r = 0.2$ cm.

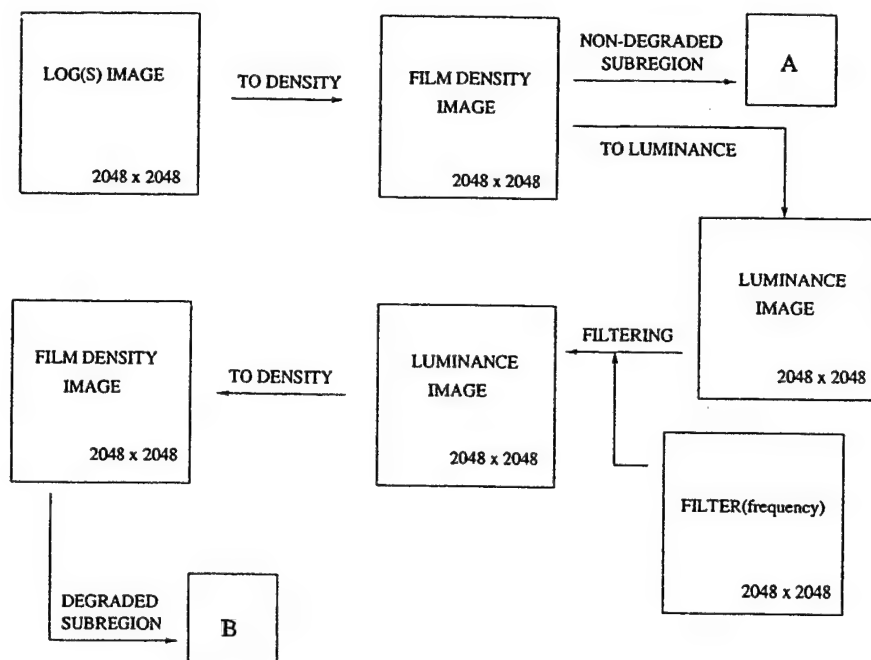


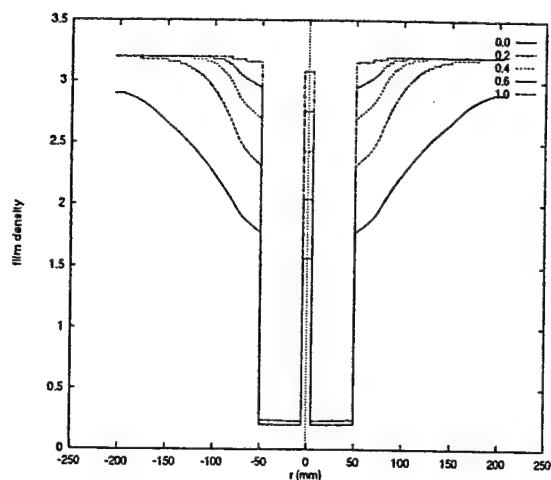
Figure 6: Processing steps for convolution of radiographic images with glare PSF.

Monte Carlo data was computed out to a distance of 20 cm for 100 bins with a spacing of 2 mm. A two dimensional point spread function ($L(x, y)$) was interpolated from this for a 20 x 20 cm area with 2048 x 2048 pixels having dimensions of 0.2 x 0.2 mm. All points out to a radius of 2 mm were set equal to $L(1)$. The remaining points at larger radius were linearly interpolated from $L(i)$. All points other than the center point were then converted from cd/m^2 to cd/pixel by multiplying each value by an area per pixel of 0.04 mm^2 to correspond with digital images having a 0.2 mm pixel size. Finally, the point spread function was normalized so that the sum of all points in the 2-dimensional discrete array was 1.0. This insures that the convolution with the PSF preserves the average brightness of a displayed scene. Implicitly, the display of an image with high glare is thus assumed to be adjusted to preserve the same average brightness.

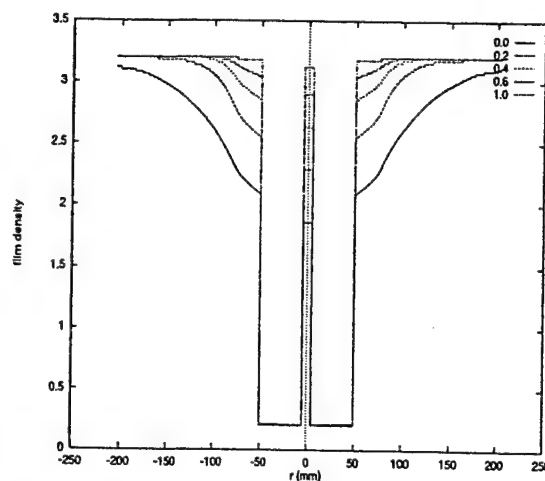
Figures 4 and 5 show the P_i/P_0 of the 4 emissive structures computed in this work. The amplitude of the tails of these functions decreases with the absorption level. For CRT-A, the tail extends up to a distance of 20 cm, with a large amplitude for low absorption levels. For CRT-B, the overall same profile is observed, although the tail amplitudes are lower and decrease more rapidly with distance as compared to the PSFs of CRT-A. For the flat-panel emissive structures, tails have a greater amplitude close to the origin and a rapid fall-off. For the thinner structure (FPD-B), the amplitudes of the tails are still significant close to the origin but rapidly decay to very low numbers with distance.

3.2 Computational simulation of glare for displayed radiographs

In this study, we assumed that the display of radiographs in electronic devices can be modeled by convolving radiographic images in luminance units with the 2-dimensional PSF, $L(x, y)$. The convolution process is performed on images in luminance units, since the degrading effect of glare is linear after the visible light has been generated in the phosphor layer. For simulation purposes, images in film density units are first obtained by (a) computationally generating a test pattern image of film density, (b) digitizing available radiographic films, or (c) converting CR

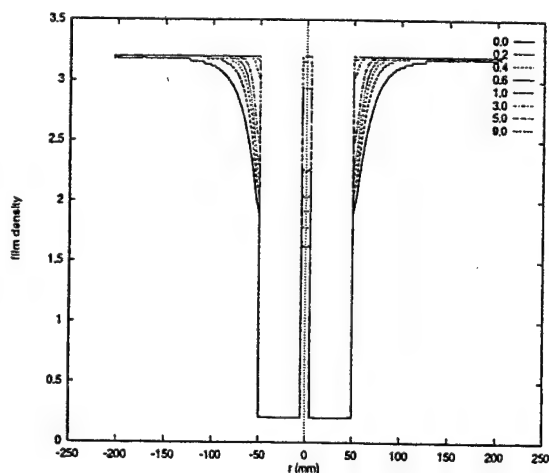


(a)

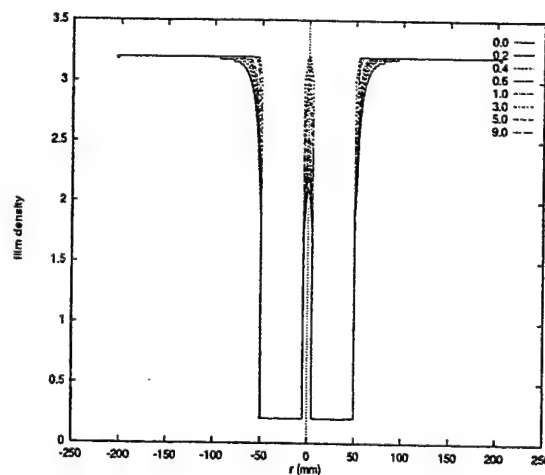


(b)

Figure 7: Test pattern image center data row for different absorption coefficients in cm^{-1} after convolution with PSFs of (a) CRT-A, and (b) CRT-B.



(a)



(b)

Figure 8: Test pattern image center data row for different absorption coefficients in cm^{-1} after convolution with PSFs of (a) FPD-A, and (b) FPD-B.

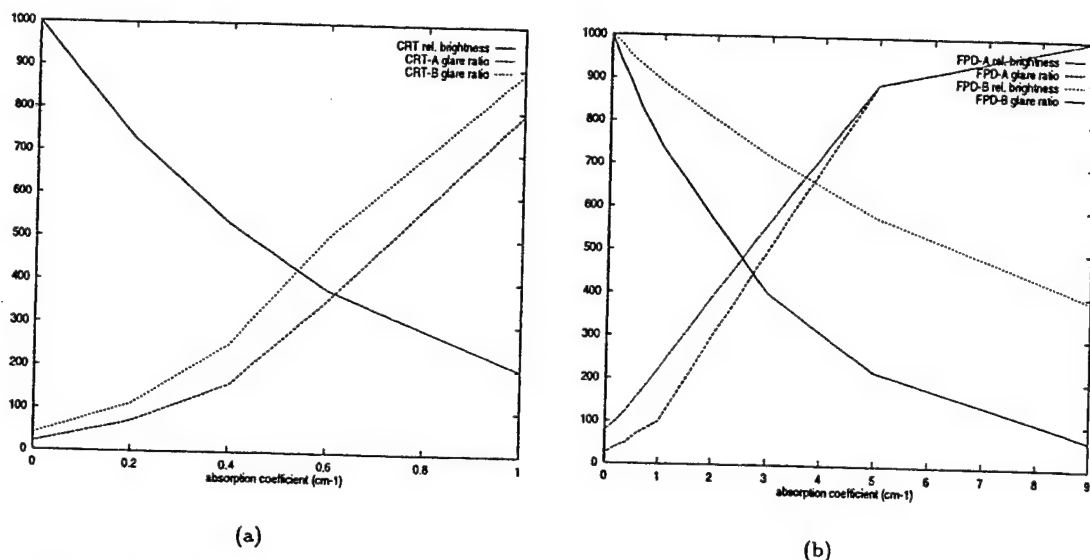


Figure 9: Glare ratios and central pixel relative brightness as a function of absorption coefficient for (a) CRT, and (b) flat-panel emissive structures.

data in units of $\log(\text{signal})$ to film density units using parameterized HD curves. These images were then converted from density to luminance units using the following relationship: $L = L_{max} * 10^{-FD}$, where L_{max} is the viewbox luminance (assumed at 3000 cd/m^2), and FD is the film density.

To simulate the degradation of image quality by glare, $2K \times 2K$ images were convolved in the frequency domain with $2K \times 2K$ filters generated from $L(x, y)$. Because $L(x, y)$ has extended tails, $L(x, y)$ arrays of $4K \times 4K$ are needed for exact solutions. Our use of $2K \times 2K$ kernels may introduce aliasing artifacts, although none were observed in the images studied to date.

$L(x, y)$ was first transformed using a 2-dimensional fast Fourier transform (FFT). Since this function is symmetric, we stored the magnitude of the Fourier coefficients in real arrays that were then used as filter functions. The $2K$ luminance images were read, Fourier transformed and filtered by multiplying the complex transformed image by the filter value. The complex array resulting from this multiplication was then converted back to luminance space by an inverse FFT procedure. After the convolution process was performed, images were converted back to film density units. All computations were performed on a DEC Alphastem 2000. The convolution process for the $2K$ images including reading and writing operations, conversion to luminance units, FFT, filtering, inverse FFT and conversion to film density units was coded in fortran90 and required about 60 s per image. The processing steps are summarized in Fig. 6. Provision was made to extract a subregion in film density units from the undegraded and glare degraded image, i.e. A and B in Fig. 6. This was done to permit observer studies where A and B are printed on film using a laser printer.

Using this method, circular test patterns of the type shown in Fig. 1 were convolved with the filters computed for the 4 emissive structures. Figures 7 and 8 show the results of computed film density along a row through the center of a test pattern with a 10 cm diameter bright circle with a 1 cm diameter dark center. A diffuse glare component can be seen surrounding the bright circle with the amount of glare being inversely related to the amount of absorber. The glare ratio was computed as the ratio of the luminance in the bright area to the luminance in the dark spot. Figure 9 shows the reduction in glare and improvement in glare ratio that can be achieved by increasing the amount of absorbers. Also shown is the decrease in overall brightness caused by absorption.

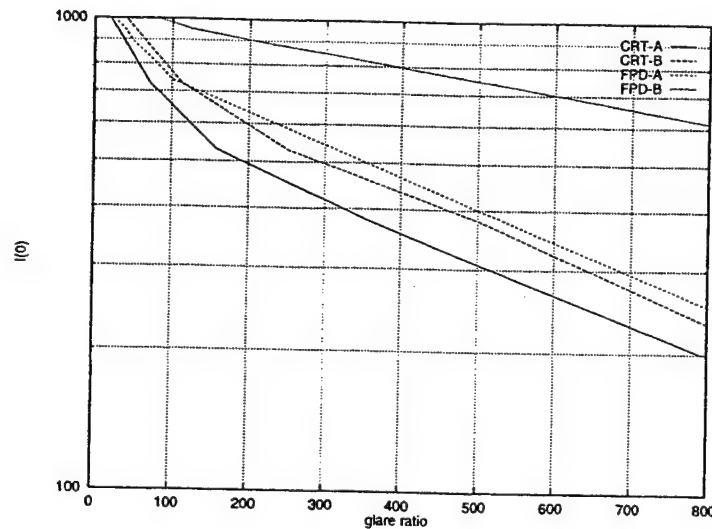


Figure 10: Relative brightness as a function of glare ratio for emissive structures CRT-A, CRT-B, FPD-A, and FPD-B.

4 DISCUSSION

In this study we computed results for circular test patterns of 4 cm diameter and 20 cm diameter in addition to the reported results for 10 cm diameter. The glare ratios measured for the different patterns are different because the component in the dark center is integrated over a larger radius. Further work should be done to identify which test pattern is best with respect to predicting adverse glare degradation in clinical radiographs.

We have conducted preliminary studies using clinical radiographs obtained from a digital radiography system. For both chest and skeletal radiographs, small lesions were added to the $\log(\text{signal})$ data in regions where glare degradation was anticipated. Subjective observation of this data indicates that a glare ratio of 250 measured with a 10 cm diameter test pattern does not create appreciable degradation in the clinical image. Further work will be necessary to understand how differing amounts of glare impact radiologic observation.

From our results it is apparent that emissive structures which are designed to minimize glare will have reduced brightness. This is illustrated in Fig. 10 where we have plotted the relative brightness, $I(0)$, as a function of the glare ratio for all cases considered. For the same glare ratio, the black matrix structure is seen to perform better than a conventional monochrome CRT although in this simulation we have not accounted in differences of phosphor luminous efficiency. Notably, a significant improvement is seen in very thin flat panel displays for which the high frequency of multipath reflections allow the phosphor to damp the tail of the PSF.

5 ACKNOWLEDGMENTS

This work was partially supported by an U.S. Army Breast Cancer research grant.

6 REFERENCES

- [1] M. J. Flynn, T. McDonald, E. DiBello, E. Jorgensen, and W. Worobey. Flat panel display technology for high performance radiographic imaging. In *SPIE Medical Imaging 1995*, volume 2431-33, 1995.
- [2] D. Gur. Experience with CRT displays in the Radiology Department. *SID'91 Digest*, pages 353-354, 1991.
- [3] E. Muka and H. Blume. Display of medical images on CRT displays. In *SPIE Medical Imaging 1995*, 1995.
- [4] H. Roehrig, H. Blume, T. L. Ji, and M. Browne. Noise of CRT display systmes. In *SPIE Medical Imaging 1993: Image Capture, Formatting and Display*, volume 1897, pages 232-245, 1993.
- [5] H. Blume, H. Roehrig, T. Lan Ji, and M. Browne. Very-high-resolution monochrome CRT displays. *SID'91 Digest*, pages 355-358, 1991.
- [6] H. Blume. Very-high-resolution CRT display systems. *SID'92 Digest*, pages 699-702, 1992.
- [7] A. Imamura, T. Ikoma, H. Makio, and K. Kikuchi. Very-high-resolution CRT display systems. *SID'92 Digest*, pages 501-504, 1992.
- [8] Clinton Electronics Corporation. *CRT design guide*.
- [9] C. Ajluni. FED technology takes display industry by storm. *Electronics design*, pages 56-66, October 1994.
- [10] K. Derbyshire. Beyond AMLCDs: field emission displays? *Solid State Technology*, pages 55-65, November 1994.
- [11] C. Ajluni. Can FED "Davids" vanquish the AMLCD "Goliaths"? *Thin-film Technology*, pages S3-S8, December 1996.
- [12] Francis Courreges. Parameters in FED product design. *Journal of the Society of Information Display*, pages 10-12, November 1996.
- [13] Henry F. Gray. The field-emitter display. *Journal of the Society of Information Display*, pages 9-14, March 1993.
- [14] E. Muka, T. Mertelmeier, R. Slone, and E. Senol. Impact of image noise and phosphor granularity on the specification of high-resolution medical image CRT displays. In *SPIE Medical Imaging 1997*, 1997.
- [15] T. Mertelmeier and T. E. Kocher. Monitor simulations for the optimization of medical soft-copies. In *SPIE Medical Imaging 1996: Image Display*, volume 2707, pages 322-333, 1996.
- [16] G. Spekowius, M. Weibrecht, C. D'adda, A. Antonini, C. Casale, and H. Blume. A new high brightness monochrome monitor based on color CRT technology. *SPIE: Medical Imaging 1997*, 1997.
- [17] A. Badano, M. J. Flynn, E. Samei, and K. G. Kearfott. Performance of low-voltage phosphors in emissive flat panel displays for radiologic applications. In *SPIE Medical Imaging 1996: Image Display*, volume 2707, pages 312-321, 1996.
- [18] P. Hovington, D. Drouin, and R. Gauvin. CASINO: A new Monte Carlo code in C language for electron beam interaction - Part I: Description of the program. *Scanning*, 19:1-14, 1997.
- [19] D. C. Joy. A database on electron-solid interactions. *Scanning*, 17:270-275, 1995.

Monte Carlo Modeling of the Luminance Spread Function in Flat Emissive Displays

Aldo Badano and Michael J. Flynn

X-Ray Imaging Research Laboratory, Henry Ford Health System
2799 W. Grand Blvd., Detroit, MI 48202
Voice: (313)876-1192, Fax: (313)876-9143
badano@rad.hfh.edu, mikef@rad.hfh.edu

Department of Nuclear Engineering and Radiological Sciences
The University of Michigan, Ann Arbor, MI

For inclusion in the IDRC Main Conference
Presentation preference: ORAL

ABSTRACT

The luminance spread functions of thin emissive displays have been computationally modeled. Thin emissive structures are found to have high quality due to frequent absorption in the phosphor layer.

1 Introduction

For demanding applications like graphic arts and medical imaging, display devices with very good image quality are required. High brightness, low noise, wide luminance range and low glare are specifically required for digital radiographic display devices.¹ To depict good contrast over the wide range of signals in a digital radiograph requires a dynamic range of 100. To minimize the degradation of contrast in regions of minimum luminance, the glare from surrounding bright regions should be less than 0.25 of the minimum luminance (i.e. 1/400 of the maximum luminance). This work examines the design requirements for achieving this low glare in thin emissive display devices.

Currently, workstations designed for displaying and interpreting digital radiographs all use cathode ray tube devices (CRTs). Multipath light scattering in CRT faceplates causes extended tails in the luminance spread function.^{2,3} Black matrix coatings and glass absorption are approaches that have been used to control glare from optical scattering at the expense of display brightness. In addition to the optical transport processes, electron backscattering in the vacuum tube has been reported to contribute to glare.^{4,5} In general, the image quality of CRT devices has been inadequate for displaying digital radiographs in medical diagnostic applications.

On the other hand, flat emissive displays have the potential for better image quality than is possible with a CRT. For these devices a thin faceplate can be employed due to the large number of spacers between the electron

emitting layer and the phosphor. Extended electron backscattering is not present and lateral transport of optical photons can be controlled more effectively. For thin emissive structures, no results have been reported on the optical transfer characteristics of and its effect on glare, brightness, and resolution. In this paper, we examine the optical transport processes in the faceplate of thin emissive display devices and its effect on low frequency image signals. The effect of glare for flat panel emissive structures is computationally modeled and the characteristics of the luminance spread functions are reported. In addition, the influence of glass absorption on glare and display brightness is analyzed.

The point spread function and modulation transfer function (MTF) are commonly used to describe the resolution of imaging devices. The glare in a display device may also be described by the point spread function if care is taken to document the low signals in the tail of the function which can extend for considerable distances. These tails are associated with a low frequency drop in the MTF which can be used to describe contrast reduction due to glare. We have used numeric Monte Carlo methods in this work to deduce the 2-dimensional point spread function of specific systems over distances equal to the full display size. This is then used to evaluate measures of image quality.

2 Computational methods

The modeling of the light transport processes that occur in emissive structures can be done using either ray tracing or Monte Carlo methods. Ray tracing techniques rely upon a priori knowledge of the system response to determine the principal ray paths that will contribute to the output. On the other hand, Monte Carlo methods track the trajectories of a large number of optical photons to describe the statistically averaged output. Absorption and scattering processes can easily be modeled with the Monte Carlo method, by sampling distances to each collision from probability distribution functions. Absorption is then expressed as a linear coefficient (cm^{-1}). Monte Carlo methods can handle a wide variety of physical cases, and are computationally practical when using high speed computers.

To model the luminance spread functions in emissive displays, we have developed a Monte Carlo optical transport code written in fortran 90 (Detect-II). The geometry is described in 3-dimensional cartesian coordinates using slabs with orthogonal dicing into cells. The surface definitions include rough surfaces, mirrors, perfect absorbers, partial diffuse absorbers with lambertian emission and thin films. Photon histories are started in point or planar sources with lambertian or isotropic angular distribution. In addition, photons are allowed to be absorbed or scattered in the medium. A unique feature of Detect-II is the tracking of photon polarization. In very thin structures, multiple light reflections occur, and polarization dependencies in the Fresnel coefficients have to be considered.

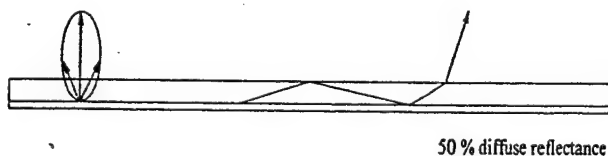


Figure 1: Cross-section of thin emissive structure model.

solid angle of a human observer in order to make efficient use of the photon histories. The binning of the emerging position is done by backprojecting the light path to the emission site, to account for the difference in index of refractions between air and glass. In effect, this bins from a large solid angle to a common virtual focal plane inside the emissive structure.

An important aspect of the code is the special binning designed for display modeling. To simulate display performance, the viewer is assumed to observe the image from a direction normal to the surface. Photons are tracked from the source to the front surface of the display and those within a finite solid angle about the normal are binned into discrete regions on the surface. A solid angle corresponding to a 6° cone is used rather than the typical

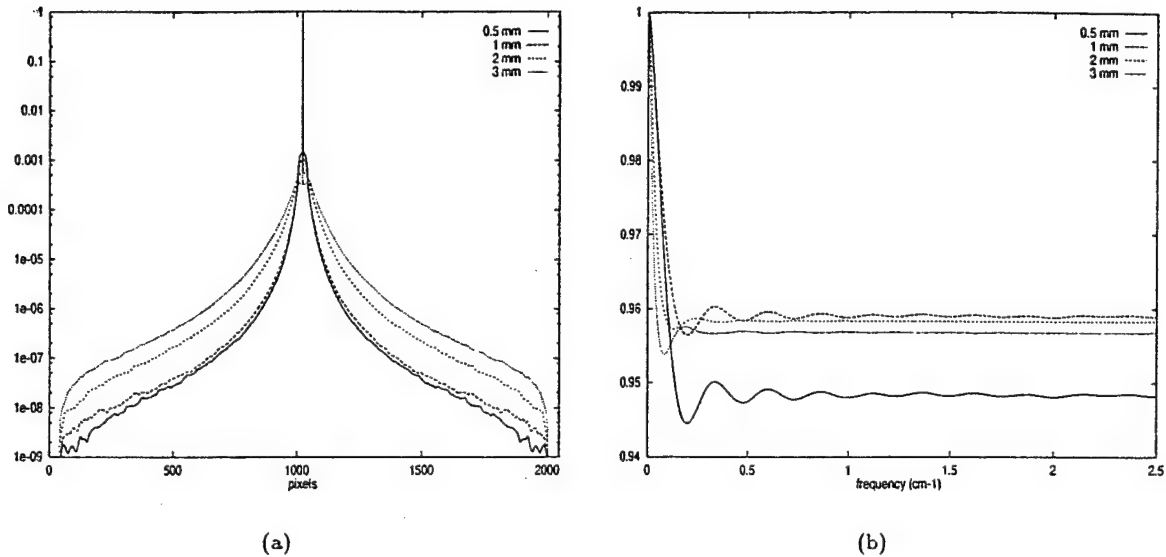


Figure 2: Line-spread functions (a) and modulation transfer functions (b) for different faceplate thicknesses with no glass absorption (for a pixel size of 0.2 mm).

In a thin cathodoluminescent display device, the emissive structure includes all components that convert energetic electrons to visible light. Typical emissive structures components include: cathodoluminescent phosphors, conductive layers, reflective or absorptive films, transparent support (faceplate), and antireflective and antiglare coatings. In this work, we have modeled the glare characteristics of thin emissive structures with different faceplate thicknesses (0.5, 1.0, 2.0, and 3.0 mm) and for absorption levels of 0.0, 1.0, 3.0, 5.0, 9.0, and 12.0 cm⁻¹. All surfaces are modeled as perfectly flat. Light entering the phosphor layer is assumed to return into the faceplate with a probability of 0.5 with a lambertian angular distribution. A cross-section of the emissive structure is presented in figure 1.

In previous work, we described methods to obtain the 2-dimensional (2D) luminance spread function from the Monte Carlo results.³ A brief summary is given in this paragraph to facilitate the interpretation of the results presented in this paper. The Monte Carlo calculation yields the number of photons, P_0 , that originate from the source point and are observed within the solid angle of the observer associated with a point on the emission layer which is located at a radius from r to Δr from the source point. This is then converted to the discrete differential probability of light emission per unit area $L(i)$, which is a discrete representation of the continuous luminance spread function $L(r)$. $L(r)$ can be interpreted as the observed luminance in cd/m² resulting from a point source located at the origin of the emissive surface with a luminous intensity of 1 cd. For the central peak, $I(0)$, is defined as the fraction of unscattered light that reaches the viewer from a point source producing a luminous intensity of 1 cd. $I(0)$ describes the brightness of images not degraded by glare.

We have used the 2D luminance spread function to simulate image degradation by convolving this function with values for an image scene. These convolutions are done in the frequency domain using a 2D Fourier transform. To describe the degradation both the line-spread function (LSF) and the modulation transfer function (MTF) are deduced. The 1-dimensional (1D) luminance LSF is computed by projecting the 2D luminance spread function and normalizing the 1D vector to unity. A 1D Fourier transform is then performed on the LSF to obtain the MTF.

Glare measurements on CRT emissive structures typically are performed with a large bright region and a small black spot.^{6,4,5} The results of these glare measurements are strongly dependent on the nature of the test

image. However, no standard metric has been adopted for reporting the glare characteristics of actual display devices. In this study, we use a circular test pattern that we have previously described.⁷ The pattern consists of an inner dark circular spot, surrounded by a bright outer circle with a ratio of radii of 10. The rest of the scene is kept at the same dark level of the inner spot. The glare ratio is defined as the difference in display luminance between the central pixel in the pattern and the brightest pixel in the bright region.

3 Results

Figure 2 (a) shows the LSF of emissive structures considered in this work with no glass absorption. For thin emissive structures with faceplate thickness less than 3 mm, the LSFs show high amplitudes close to the origin with tails that decay rapidly to very low numbers. Moreover, the LSF for 0.5 and 1 mm have similar features, differing only at large distances and very close to the origin. At 3 mm, a peak is observed that defines a halo around the center spot. The amplitudes at short distances are lower than for thinner faceplates by a factor of at least 0.25. In figure 2 (b), the MTFs of the same emissive structures are plotted. The drop in amplitude is approximate constant for all frequencies, up to the Nyquist limit.

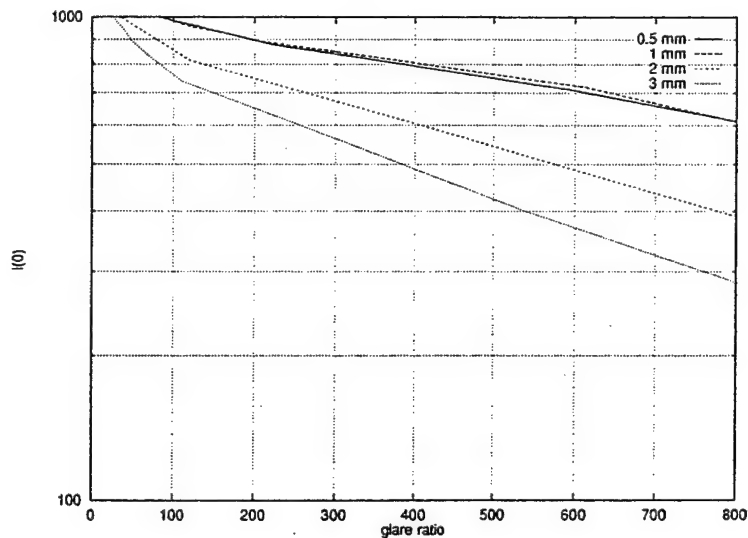


Figure 3: Relative brightness as a function of the glare ratio for different faceplate thicknesses. For each curve, glass absorption is varied to decrease $I(0)$ and increase the glare ratio.

To determine if an emissive structure is capable of achieving the high glare ratio needed for radiologic interpretation (i.e., about 400), we have computed test pattern glare ratios for emissive structures of different thicknesses and with different absorption levels. Figure 3 illustrates the relative brightness $I(0)$ as a function of the glare ratio for the emissive structures considered. Higher glare ratios are possible to achieve by increasing the absorption level, although decreasing brightness. To obtain a given glare ratio, an increase in faceplate thickness results in a reduction of the display brightness. For a glare ratio of 400, the brightness has to be reduced by 37.5 % if the thickness of the emissive structure is increased from 1 to 3 mm. Again, similar characteristics are observed for faceplate thicknesses of 0.5 and 1 mm. As seen in figure 2 (a), the similar features in the LSFs may be responsible for the similarities in the achievable brightness for a given glare ratio.

4 Summary

The luminance spread functions of thin emissive structures typical of flat cathodoluminescent displays have been modeled with an optical Monte Carlo code. The tails of the spread functions show that even for thin structures, the light scattering within these structures has to be controlled in order to achieve glare ratios suitable for high-performance applications. The use of absorption in the faceplate has been shown to be a possible solution, although affecting the display brightness. Other solutions may include the use of a black matrix coating in between the phosphor dots.

5 Acknowledgements

This work was partially supported by an U.S. Army Breast Cancer research grant.

6 REFERENCES

- [1] M. J. Flynn, T. McDonald, E. DiBello, E. Jorgensen, and W. Worobey. Flat panel display technology for high performance radiographic imaging. In *SPIE Medical Imaging 1995*, volume 2431-33, 1995.
- [2] E. B. Gindele and S. L. Shaffer. A physical optics CRT faceplate halation model. *SID'91 Digest*, pages 446-450, 1991.
- [3] A. Badano and M. J. Flynn. Image degradation by glare in radiologic display devices. In *SPIE Medical Imaging 1997: Image Display*, 1997. .
- [4] G. C. de Vries. Contrast-enhancement under low ambient illumination. *SID'95 Digest*, pages 32-35, 1995.
- [5] J. J. van Oekel. Improving the contrast of CRTs under low ambient illumination with a graphite coating. *SID'95 Digest*, pages 427-430, 1995.
- [6] G. Spekowius, M. Weibrecht, C. D'adda, A. Antonini, C. Casale, and H. Blume. A new high brightness monochrome monitor based on color CRT technology. *SPIE: Medical Imaging 1997*, 1997.
- [7] A. Badano, M. J. Flynn, E. Samei, and K. J. Kearfott. Performance of low-voltage phosphors in emissive flat panel displays for radiologic applications. In *SPIE Medical Imaging 1996: Image Display*, volume 2707, pages 312-321, 1996.

Performance of Low-Voltage Phosphors in Emissive Flat Panel Displays for Radiologic Applications

Aldo Badano^{1,2}, Michael J. Flynn^{1,2}, Ehsan Samei^{1,2}, Kimberlee G. Kearfott²

¹ X-Ray Imaging Research Laboratory
Henry Ford Health System, Detroit, Michigan

² Department of Nuclear Engineering and Radiological Sciences
University of Michigan, Ann Arbor, Michigan

ABSTRACT

To date, the lack of adequate electronic display devices has been the primary factor limiting the use of digital radiographic images. Flat panel display technology using field emissive cathodes in microvacuum cells has emerged as a potential solution. However, the performance characteristics of low-voltage cathodoluminescence in the range below 1 kV is not well understood. In this paper, we discuss issues concerning the prediction of phosphor efficiency, and describe the processes of light generation and transport which influence the performance of phosphor screens.

Keyword List: flat panel display, emissive display, digital radiography, field emission, low-voltage phosphor.

1 INTRODUCTION

The low noise, wide dynamic range information recorded in a radiograph is normally displayed on transilluminated film with image detail and contrast at the limits of detection for the human visual system.¹ The electronic display of medical radiographs requires devices with similar image quality. Pixel sizes of 80 μm are ideally needed, although visible individually only with high contrast. Maximum luminance of more than 2000 cd/m^2 assures that the human visual system is able to achieve good contrast sensitivity over the range from 5 to 2000 cd/m^2 .

Additionally, high fidelity systems must limit lateral light transport from the intended position of light emission which might otherwise reduce contrast. Image degradation from lateral light transport is often referred to as glare and is associated with extended, low amplitude tails on the display systems point spread function. Transilluminated film has minimal lateral light transport since the display brightness is modulated by the thin film of dark grains near the surface. An added benefit of the superficial emission of light is the ability to use rough coatings which limit the specular reflection of environmental light. The problem of lateral light diffusion occurring in electronic display systems is considered in this paper.

Most medical electronic display systems in use today use cathode ray tubes (CRT) as the light producing component. The numerous problems in the performance of these devices are now well recognized. In particular,

the thick glass separating the phosphor and the viewer* cause considerable lateral light transport and limit the ability to control surface reflections. Several new methods for electronic display, commonly referred to as flat panel display (FPD) devices, offer potential for improved quality.¹ Of particular interest in our research is the field emitter display (FED) which is now under development by several companies.^{3,4}

Both CRT and FED devices generate and emit light from a cathodoluminescent emissive structure. Electrons traveling in a vacuum first strike a phosphor to produce light. After multiple internal reflections, the light escapes the surface to produce the visible image. Components of the emissive structure may include the phosphor material, phosphor binder material, conductive layers, glass support layers, reflective layers, transparent conductive layers, or thin film filters. In this paper, we specifically focus on the performance of emissive structures of the type appropriate for use in FED devices.

2 THE EMISSIVE STRUCTURE

The element of the emissive structure responsible for the generation of light (cathodoluminescent phosphor) can be of granular or thin film type. Granular phosphors are made with different grain size, grain density and binder characteristics. They can exhibit good light production and are commonly used in CRT systems. Typical materials include ZnO:Zn , ZnCdS:Al,Cu , $\text{ZnGa}_2\text{O}_4\text{:Mn}$, $\text{ZnGa}_2\text{O}_4\text{:Mn}$, $\text{Y}_2\text{O}_3\text{:Eu}$, $\text{Y}_2\text{O}_2\text{S:Eu}$, $\text{Y}_2\text{O}_2\text{S:Eu}$, ZnS:Ag , $\text{Y}_3(\text{Ga/Al})_5\text{O}_{12}\text{:Tb}$, $\text{Y}_2\text{SiO}_5\text{:Ce}$.⁵⁻⁹ Very thin, or monolayer, phosphor layers with grains about $3\text{ }\mu\text{m}$ in size are now employed for high resolution monochrome CRT applications.¹⁰

Thin films can be grown as a single crystal film, as a polycrystalline layer, or as a layer with oriented crystal fibers. Thin film phosphors have been grown on a variety of substrates, although substrate-film boundary effects on efficiency have been reported.¹¹ Several authors have investigated thin film phosphors including ZnO:Zn , $\text{ZnGa}_2\text{O}_4\text{:Mn}$, $\text{Y}_2\text{O}_3\text{:Eu}$, $\text{Y}_3\text{Al}_5\text{O}_{12}\text{:Tb}$.⁶ The physical form of the phosphors affects the optical performance by altering the light paths a photon follows before exiting the structure.^{12,10} In general, thin films are low cost and easy to fabricate, but have low luminous efficiency. Color has been a major aim of low-voltage phosphor research; however, for a radiologic application, a broad white spectrum is required. This can be obtained with a mixture of emitters with line spectra or with a binary phosphor having a broad emission spectrum. Figure 1 presents the spectra of some monochrome phosphors being considered. One of the oldest phosphors, ZnO , has a broad greenish spectra and maintains particularly good efficiency when excited by low-energy electrons.

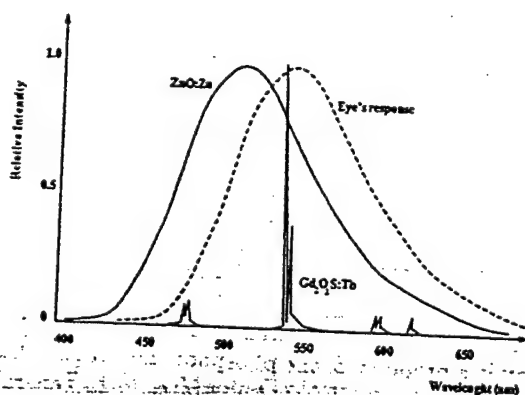


Figure 1: Phosphor spectra.

that improves the optical performance of the structure. Low-voltage applications as FEDs require the use of very thin metallic conductive films, or the positioning of the conductor out of the electron paths. Transparent ITO

*For glass supported by spacers, approximately 0.4 mm of glass thickness are required per cm^2 of surface area between the posts to prevent the surface from imploding into the vacuum.² For large CRTs, the glass on the front surface will have thicknesses of about 15 mm .

layers with thicknesses between 100 and 350 nm have been used in demonstrated devices,¹⁶ but novel solutions as mixing conductive metallic particles with the phosphor grains, or altering the conductivity of the phosphor layer have also been reported.¹⁷

For both CRT and FED devices, a glass faceplate is needed to provide support and vacuum integrity. The thickness required is defined by the required support ability given the mechanical strength and critical cracking threshold of the glass. Large vacuum tubes (CRTs) have thick glass faceplates, while FEDs have the potential for use of a thinner glass given the distribution of the vacuum pressure over a large number of spacers. Internal reflections in this glass layer are a major problem which leads to poor image quality associated with glare. The viewing side of the glass may have antireflection coatings or antiglare structures that minimize ambient light reflection.

3 EMISSIVE PERFORMANCE

For lambertian angular emission, the display brightness can be computed as $L = \epsilon_l p_e / \pi a$, where p_e and a are the power and area of the element considered and L is the luminance in cd/m^2 . The luminous efficiency ϵ_l needs to be about 6.2 lm/W to achieve a luminance of 2,000 cd/m^2 with a power density of 0.1 W/ cm^2 . At this power density, a 35 cm by 43 cm display device will dissipate 150 W on the display surface if the total field of the display is at full luminance. To regulate this luminance with static current regulation, the peak current per pixel needs to be 10 nA for a device with 100 μm pixels and an accelerating voltage of 1000 V. Flat panel display devices commonly scan a full row of the display with time modulation in the column direction. For a system with 3500 rows, the peak current would thus increase to 35 μA per pixel. In contrast, a full raster scan of 3500 by 4300 pixels would require a peak current of 150 mA in addition to the very high frequency needed to drive the rows and columns.

To predict the effect on ϵ_l of the system parameters, we model the process in three independent stages. First, the incident electron beam will deposit energy into the phosphor with an efficiency ϵ_e , which relates the energy of the incoming electrons to the deposited energy in the phosphor. Electrons also deposit energy in other materials such as the binder, and in other layers, which will not contribute to the luminescent process. For electron accelerating voltages in the range from 20 to 30 kV, electrons will penetrate from 1 to 2 μm into the phosphor.¹⁸ For voltages of 1 kV, the penetration of electrons is only to a maximum depth of 20 nm.¹⁹ This very small electron penetration can reduce ϵ_e in FED emissive structures where low-voltage operation is desired for other reasons.

Secondly, the energy deposited by the electrons into the phosphor is converted to light photons in the luminescence sites with a quantum efficiency ϵ_p . This intrinsic efficiency is a property of the phosphor, although it has been reported that it may differ up to a factor of 2 for phosphors deposited on different substrates.¹¹ In general, ϵ_p is well known for solid crystal scintillators, and it is recognized that CsI:TI has one of the highest values (11.9% energy conversion, and 52 light photons/keV).²⁰ However, ϵ_p is not well documented for powdered phosphors.

Once the light is generated, it diffuses and eventually reaches the viewer by escaping the structure with an efficiency ϵ_g , which is dependent on light emission characteristics, spatial distribution of emitted photons, and

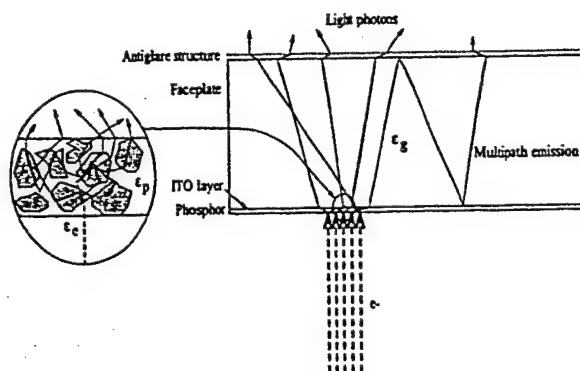


Figure 2: The emissive structure.

relative dimensions of the emissive structure components. The complex light transport that takes place may consist in several possible processes which include reflection and refraction at the surfaces, and scattering and absorption in the medium (see Fig. 2). The relative importance of these processes depends strongly on the physical form of the phosphor. Granular phosphors will force light photons to have many internal reflections at the grain boundaries before escaping. Then a multitude of interaction boundaries are presented to photons that escape from a granule into the binder. On the other hand, thin film phosphors provide an homogeneous medium for the photons to reach the film surface. Due to multiple scattering, powdered phosphors have a lambertian emission, while thin film phosphors emit with a more forward peaked angular distribution. The glass and other films (ITO conductive layer) will provide further opportunities for deflection until the photon successfully exits the emissive structure.

The total luminous efficiency is computed as the linear combination of efficiencies, $\epsilon_l = K_\lambda \epsilon_e \epsilon_p \epsilon_g$, where K_λ is the luminosity in lm/W, accounting for the photopic eye's response. Experimental values of about 13 lumens/Watt for 1 kV voltages have been recently reported for both ZnO:Zn and Gd₂O₂S:Tb granular phosphors.⁹ This model for computing total luminous efficiency is useful for the study of the performance and design of emissive structures, as it allows the prediction of the glare and resolution characteristics of an emissive system. However, other considerations are relevant for emissive structures in radiologic applications including the angular dependence of emissions and the spatial response.

4 COMPUTATIONAL MODELING OF EMISSIVE STRUCTURES

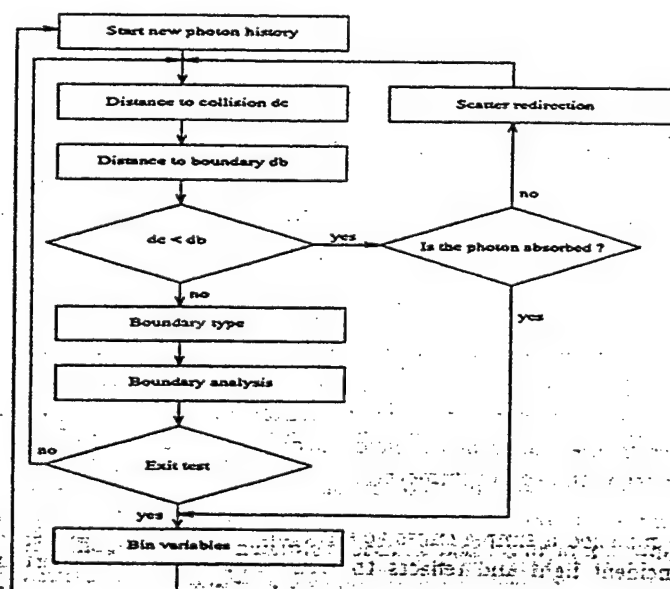


Figure 3: Monte Carlo code simplified flow chart.

the source to the front surface of the display and those within a finite solid angle about the normal are binned into discrete regions on the surface (Fig. 4b). A solid angle corresponding to a 6 degree cone is used rather than

To model the performance of the emissive structure, we used a Monte Carlo code written in fortran90 and run using a DEC Alphaserber 2000 (see Fig. 3).[†] The geometry is described in 3 dimensional cartesian coordinates using slabs with orthogonal dicing into cells as shown in Fig. 4a. Each cell is initially assigned a default surface type (smooth) for each of its facets. The user then changes the definition of any surface to any other types including rough surfaces, perfect mirrors, perfect absorbers, partial absorbers with lambertian distribution in the reflected emission and thin films. Photons are created in point or planar sources with lambertian or isotropic angular distribution. In addition, photons are allowed to be absorbed or scattered in the medium. Photon characteristics as direction, energy and polarization are tracked in the analysis.²² To simulate display performance, the viewer is assumed to observe the image from a direction normal to the surface. Photons are tracked from the

[†] The Monte Carlo code used, DETECT II, is based on an earlier optic Monte Carlo code, DETECT, which has been used to model optical transport in radiation detectors.²¹

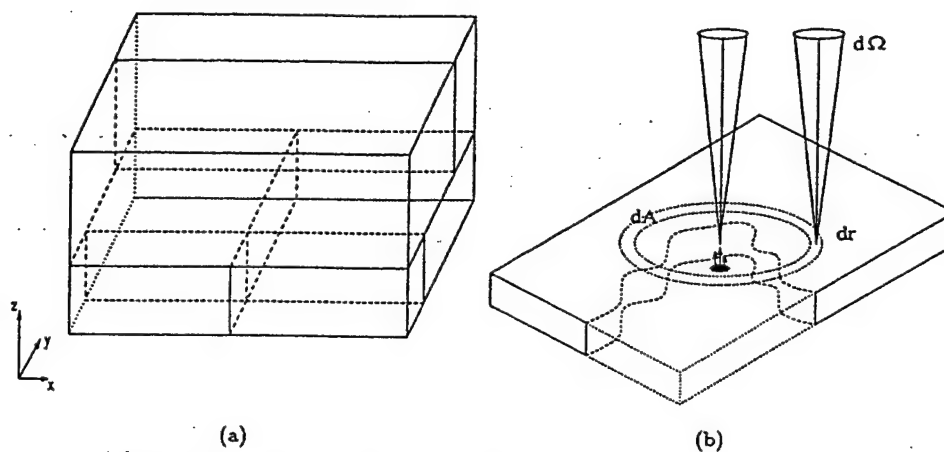


Figure 4: (a) Binning for the Monte Carlo code. (b) Monte Carlo code geometry.

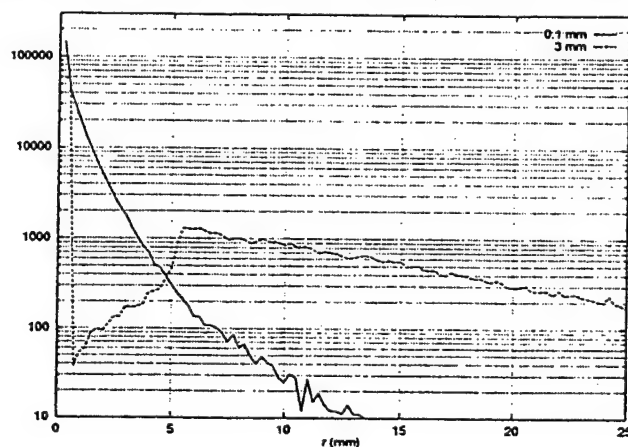


Figure 5: $p(r)drd\Omega$.

the typical solid angle of a human observer in order to make efficient use of the photon histories. The results are then expressed in terms of the number of photons that exit the front surface within the defined solid angle per unit radius, $p(r)drd\Omega$, or per unit area, $p(r)dAd\Omega$. Typically the emission probability is computed as a one dimensional function of radius from the center of the display surface. $p(r)drd\Omega$ is computed when determining the point spread function (PSF) from a point source in the center of the field. $p(r)dAd\Omega$ is computed when evaluating the emission pattern from distributed sources with radial symmetry.

In order to benchmark our calculations, we have modeled a simple emissive structure consisting of flat glass having a back surface which absorbs 40% of the incident light and reflects the remainder with a lambertian distribution.²⁷ The absorption was estimated by transmission measurements made with a diffuse densitometer. Glass absorption of 0.3 cm^{-1} was used. Results were computed for both a point source and a distributed source emitting light in a lambertian distribution into the glass from the diffusive back layer.

The distributed source was assumed to emit light uniformly over the back surface except for a 4 mm diameter dark region in the center. No light photons were generated in the dark spot, however incident photons from the glass region were treated the same as for the rest of the back surface. Only front surfaces were considered smooth. Fig. 5 shows the corresponding PSF, $p(r)drd\Omega$ in the case of the distributed source where the glass thickness is

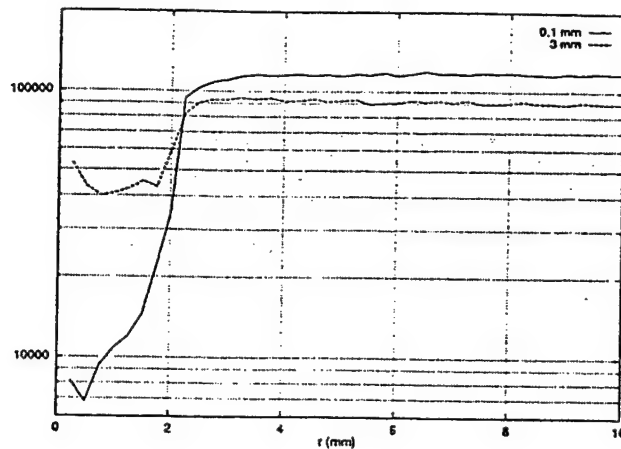


Figure 6: $p(r)dAd\Omega$ for the test pattern for 0.1 and 3 mm glass thickness.

either 3 mm or 0.1 mm. Fig. 6 shows the results for $p(r)dAd\Omega$, for these two situations. For the purpose of this study, we can define a glare ratio, given as the ratio of the luminance outside the dark spot of the test pattern divided by the luminance in the center of the dark spot.

5 MEASUREMENTS OF GLARE

The emissive structure used for benchmark computations was selected because of our ability to experimentally simulate this structure. The diffusive surface was simulated by using 3 mm flat optical glass with a 0.3 mm diffusing layer of uniform thickness. The flashed opal glass used (Rolyn Optics, see Fig. 8b) is typically made by fusing particulate material into the glass. The particulate piece used absorbs very little light, transmits 40% in a diffuse distribution, and reflects an estimate 58% in a diffuse distribution. The diffuse transmission was measured with an optical densitometer. The glass is otherwise opaque allowing no direct pattern to be viewed in transmission. To simulate the light source, the back side of the opal surface was illuminated with a patterned light source.

The experiment was conducted with a uniform light source generated by a 50 mm exit port of an integrating sphere and a scientific cooled CCD camera (Princeton Instruments) with a 105 mm micro Nikkor lens and a macro adapter (see Fig. 7). A 40 mm circular bright field with a 4 mm diameter dark spot located at the center was created by placing a film over the exit port of the integrating sphere. The pattern (see Fig. 8a) was printed on single emulsion film with a film with a laser film printer. The film density in the bright region was 0.14 and in the dark region 3.2. We then placed a flashed opal glass (Rolyn Optics) over the patterned film and recorded the image with the camera. The test pattern was recorded with 1:1 magnification onto the sensor such that the sensor field was inscribed in the circular bright field of the pattern. The diffuse surface of the opal glass provides a useful model for the multiple processes that occur in a powdered phosphor layer which produces diffuse internal scattering.

The results of our experimental measurements of the emission distribution from the film pattern alone and from the flashed opal glass illuminated by the film pattern are shown in Fig. 9. To obtain these results, the center of the dark region was first identified and then sensor values extracted along multiple lines through the center. The data from several segments beginning at the center of the pattern was then averaged. The results for the film show clearly demarked edges for the dark spot with a glare ratio of 25. The result with the flashed opal glass show a blur at the edge of the dark spot, a gradual reduction in luminance at large radius, and a glare

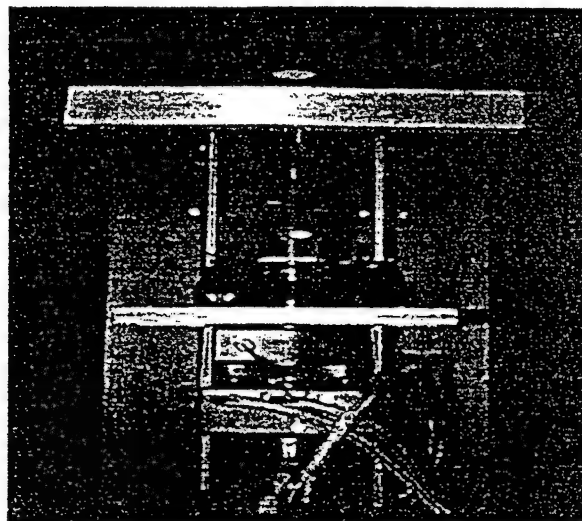


Figure 7: Experimental set up.

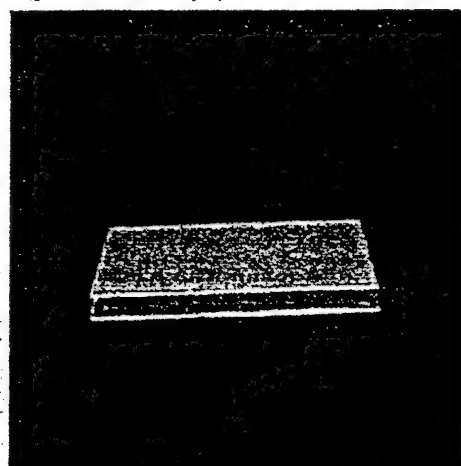
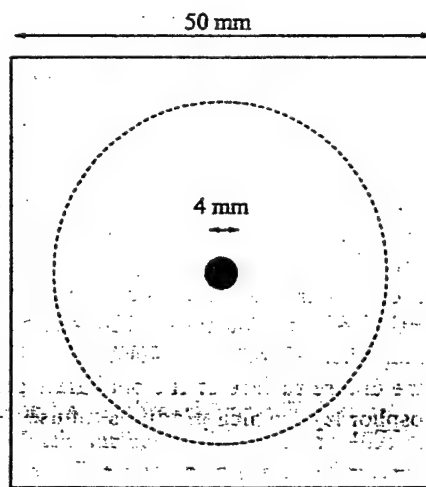


Figure 8: (a) Test pattern for glare measurements. (b) Flashed opal glass.

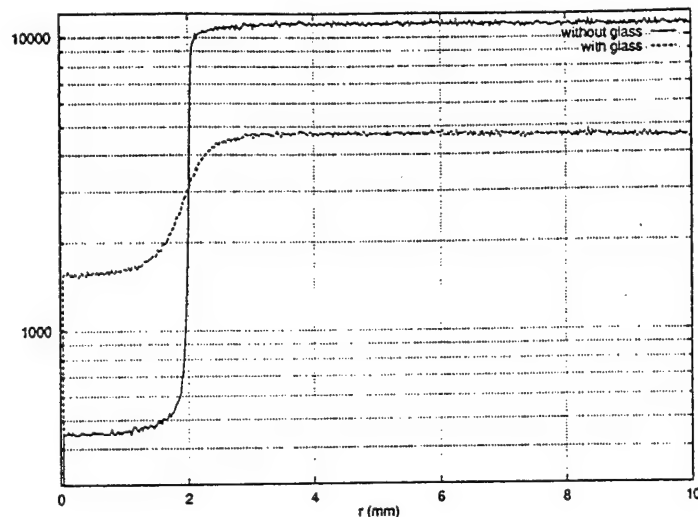


Figure 9: Measured point response function with and without a 3 mm glass.

ratio of 3.3. The results are in very good agreement with the Monte Carlo calculations.

6 Discussion

Our preliminary results demonstrate that optical Monte Carlo calculations can be used to model the multiple internal reflections occurring in an emissive structure and accurately predict the emissive performance seen by an observer. While the geometry used for the results presented in this paper is relatively simple, it is quite similar to the geometry of CRT systems. Moreover, the determination of glare for the type of light source studied is a demanding problem to model since it is dependent on the many multiple reflections occurring inside the glass layer as the optical photon migrates laterally.

It is notable that the glare ratio predicted by our computational model is very close to the experimental result, 2.3 versus 3.3. Additionally, the model predicts the blur at the boundary of the black spot as well as the gradual falloff in luminance as the outside border of the test pattern is approached. The difference observed may be due to the approximate handling of polarization and treatment of the side boundaries in the calculations. Secondly, the size of the source for the computed results was not exactly the same as for the experimental results.

We have used this model to demonstrate how reduction in the thickness of the glass layer to a distance similar to the pixel size can significantly improve the glare performance. This result is obtained because of the absorption that occurs in the diffusive back layer. As the glass layer is reduced in thickness, the lateral distance that a photon travels before striking the back layer is reduced. Thus the photon will strike the back layer much more frequently for a given lateral distance with significantly increased probability of absorption. The increase in overall brightness predicted by the model is associated with increased light loss from the edge of the pattern for the 3 mm glass layer compared with the 0.1 mm glass layer.

The optical Monte Carlo code we have developed has the capability to model very complex geometries. We intend to explore methods for designing FED emissive structures which have good luminous efficiency while controlling glare. The use of very thin emissive structures has the additional benefit that the outer surface can be made very rough. All modern radiologic films use a rough overcoat layer to control the surface reflections from

ambient light and we believe that electronic devices can be built with similar characteristics. A significant design issue that must be addressed is the mechanical support and durability of emissive structures with such thin outer layers.

The test pattern we have used to study the glare performance of the simple model for an emissive structure should have general use for evaluating radiologic display devices. We have selected a black spot which is 4 mm in diameter since that is significantly larger than the resolution response of most systems intended for displaying digital radiographs but still small enough to capture the full impact of the broad portion of the point response function. We have otherwise chosen to limit the area of the pattern to 40 mm. The dark spot thus represents 10% of the diameter of the bright circular field. The glare value at the center of the dark spot is thus the integration of the broad tail of the PSF from a radius of 2 mm to 20 mm. However, we do not have any understanding as to what value of glare ratio is required to achieve high fidelity in the display of digital radiographs.

7 SUMMARY

We have modeled the optical transport processes that take place in an emissive structure using Monte Carlo techniques. We have observed good agreement between experimental measurements and the predictions of the model for a simple benchmark problem. It is shown how thin emissive structures improve image glare in the presence of absorption in the back layer. Computer modeling will be used to evaluate more complex emissive structures and their optical performance.

8 ACKNOWLEDGMENT

The authors gratefully acknowledge the support of the Organization of the American States.

9 REFERENCES

- [1] M. J. Flynn, T. McDonald, E. DiBello, E. Jorgensen, and W. Worobey. Flat panel display technology for high performance radiographic imaging. In *SPIE Medical Imaging 1995*, volume 2431-33, 1995.
- [2] P. Holloway, J. Sebastian, T. Trottier, H. Swart, and R. Peterson. Production and control of vacuum in field emission flat panel displays. *Solid State Technology*, pages 47-54, August 1995.
- [3] K. Derbyshire. Beyond AMLCDs: field emission displays? *Solid State Technology*, pages 55-65, November 1994.
- [4] C. Ajluni. FED technology takes display industry by storm. *Electronics design*, pages 56-66, October 1994.
- [5] S. Itoh, H. Toki, Y. Sato, K. Morimoto, and T. Kishino. The ZnGa₂O₄ phosphor for low voltage cathodoluminescence. *Journal of the Electrochemical Society*, 138(5):1509-1512, May 1991.
- [6] D. W. Smith, A. Vecht, C. S. Gibbons, D. Morton, and C. Waldin. Thin-film phosphors for FED application. In *SID'95*, volume XXVI, 1995.
- [7] H. Tanner, A. Vecht, C. S. Gibbons, and D. Charlesworth. High-resolution phosphors: characterization and assessment. In *SID'95*, volume XXVI, 1995.

- [8] T. E. Felter, A. A. Talin, M. E. Malinowski, L. Shea, B. E. Russ, A. G. Chakhovskoi, J. McKittick, and J. Talbot. Characterization of ZnGa₂O₄ and YAG:Cr phosphors for field-emission displays. In *SID'95*, volume XXVI, pages 466-469, 1995.
- [9] S. Yang, C. Stoffers, S. M. Jacobsen, C. J. Summers, P. N. Yocom, and S. McClelland. Characterization of potential low-voltage phosphors for field emission devices. *SPIE*, 2408:194-199, 1995.
- [10] L. Ozawa and K. Oki. A phosphor screens for high-resolution CRTs. *Journal of the Society for Information Display*, 3(2):51-57, 1995.
- [11] J. Almeida, F. Barbo, M. Bertolo, A. Bianco, A. Braem, S. Cerasari, C. Coluzza, T. Dell'orto, S. Fontana, G. Margaritondo, Nappi E, G. Paic, F. Piuze, R. Sanjines, T. Scognetti, and S. Sgobba. Morphological effects in the quantum yield of cesium iodide. *Nuclear Instruments and Methods in Physics Research A*, 361:524-538, 1995.
- [12] L. Ozawa. *Cathodoluminescence. Theory and applications*. Kodansha, 1990.
- [13] J. Sebastian, S. Jones, T. Trotter, H. Swart, and Holloway P. Electron-stimulated surface reactions between residual vacuum gas and ZnS field-emission-display phosphors. *Journal of the Society of Information Display*, 3(4):147-149, December 1995.
- [14] S. Itoh, T. Kimizuka, and T. Tonegawa. Degradation mechanism for low voltage cathodoluminescence of sulfide phosphors. *Journal of the Electrochemical Society*, 136(6):1819-1823, June 1989.
- [15] S. M. Jacobsen, S. Yang, F. L. Zhang, C. J. Summers, C. Bojko, N. Kumar, L. Fredin, and H. Schmidt. Improved performance of low-voltage phosphors for field emission displays. In *SID'95*, volume XXVI, pages 631-633, 1995.
- [16] N. Kumar, C. Xie, N. Potter, A. Krishnan, D. Eichm, E. Schlam, H. Schmidt, and S. Wagal. Field-emission displays based in diamond thin films. *SID 93 Digest*, 1993.
- [17] Yamaura et al. US patent number 4,680,231, July 1987.
- [18] W. Ehrenberg and D King. The penetration of electrons into luminescent materials. *Proc. Phys. Soc.*, 81:751-766, 1963.
- [19] M. J. Flynn. The transport and energy loss effects of charged particles in emulsion radiation detectors. *PhD dissertation, University of Michigan*, 1974.
- [20] G. F. Knoll. *Radiation detection and measurements*. Wiley, 2nd. edition, 1989.
- [21] G. F. Knoll and T. F. Knoll. Light collection in scintillation detector composites for neutron detection. *IEEE Transactions on Nuclear Science*, 35(1):872-875, July 1988.
- [22] M. Born and E. Wolf. *Principles of optics*. 3rd. revised edition, 1965.



The University of Michigan
Ann Arbor, Michigan



Henry Ford Health System
Detroit, Michigan

**IMAGE QUALITY DEGRADATION
BY LIGHT SCATTERING PROCESSES
IN HIGH PERFORMANCE DISPLAY DEVICES
FOR MEDICAL IMAGING**

by
Aldo Badano

A dissertation submitted in partial fulfillment of the requirements
for the degree of Doctor of Philosophy (Nuclear Engineering)
in the University of Michigan.

IMAGE QUALITY DEGRADATION BY LIGHT SCATTERING PROCESSES IN HIGH PERFORMANCE DISPLAY DEVICES FOR MEDICAL IMAGING

by
Aldo Badano

A dissertation submitted in partial fulfillment
of the requirements for the degree of
Doctor of Philosophy
(Nuclear Engineering)
in The University of Michigan
1999

Doctoral Committee:

Professor Michael J. Flynn, Co-Chairperson
Professor Kimberlee J. Kearfott, Co-Chairperson
Professor Jerzy Kanicki
Professor David K. Wehe

© Aldo Badano 1999
All Rights Reserved

To my parents, for their encouragement has beaten the distance.

To Maricel, for the sacrifices and for our future.

To Gina and her clear eyes, for brightening my days.

A mis padres, cuyo empuje a vencido la distancia.

A Maricel, por los sacrificios y por nuestro futuro.

A Gina y sus ojos claros, por iluminar mis días.

ABSTRACT

IMAGE QUALITY DEGRADATION BY LIGHT SCATTERING PROCESSES IN HIGH PERFORMANCE DISPLAY DEVICES FOR MEDICAL IMAGING

by

Aldo Badano

Co-Chairperson: Michael J. Flynn

Co-Chairperson: Kimberlee J. Kearfott

This thesis addresses the characterization of light scattering processes that degrade image quality in high performance electronic display devices for digital radiography. Using novel experimental and computational tools, we study the lateral diffusion of light in emissive display devices that causes extensive veiling glare and significant reduction of the physical contrast. In addition, we examine the deleterious effects of ambient light reflections that affect the contrast of low luminance regions, and superimpose unwanted structured signal.

The analysis begins by introducing the performance limitations of the human visual system to define high fidelity requirements. It is noted that current devices severely suffer from image quality degradation due to optical transport processes. To model the veiling glare and reflectance characteristics of display devices, we introduce a Monte Carlo light transport simulation code, DETECT-II, that tracks individual

photons through multiple scattering events. The simulation accounts for the photon polarization state at each scattering event, and provides descriptions for rough surfaces and thin film coatings. A new experimental method to measure veiling glare is described next, based on a conic collimated probe that minimizes contamination from bright areas. The measured veiling glare ratio is taken to be the luminance in the surrounding bright field divided by the luminance in the dark circle. We show that veiling glare ratios in the order of a few hundreds can be measured with an uncertainty of a few percent. The veiling glare response function is obtained by measuring the small spot contrast ratio of test patterns having varying dark spot radius. Using DETECT-II, we then estimate the ring response functions for a high performance medical imaging monitor of current design, and compare the predictions of the model with the experimentally measured response function.

The data presented in this thesis demonstrate that although absorption in the faceplate of high performance monochrome cathode-ray tube monitors have reduced glare, a black matrix design is needed for high fidelity applications. For a high performance medical imaging monitor with anti-reflective coating, the glare ratio for a 1 cm diameter dark spot was measured to be 240.

Finally, we introduce experimental techniques for measurements of specular and diffuse display reflectance, and we compare measured reflection coefficients with Monte Carlo estimates. A specular reflection coefficient of 0.0012, and a diffuse coefficient of 0.005 nits/lux are required to minimize degradation from ambient light in rooms with 100 lux illumination. In spite of having comparable reflection coefficients, the low maximum luminance of current devices worsens the effect of ambient light reflections when compared to radiographic film. Flat panel technologies with optimized designs can perform even better than film due to a thin faceplate, increased

light absorption, and high brightness.

ACKNOWLEDGEMENTS

This work has been greatly enhanced by the active guidance of my advisor Michael J. Flynn. I want to thank him for introducing me to a exciting research project, and for countless intellectual exchanges and critical reviews that have been most helpful in ensuring the quality of this work.

I want to express my sincere thanks to Kim Kearfott, who guided me through the first stages of my program at the University of Michigan. I wish to express my respect and recognition to Jerzy Kanicky for providing professional guidance and a different perspective on academic work. In addition, I want to thank Ed Muka for his collaboration in CRT measurements.

My appreciation also goes to fellow students and staff at the X-ray Imaging Research Lab – specially to David Reimann, Sean Hames, Ehsan Samei and Allen Seifert –, and at the Department of Nuclear Engineering and Radiological Sciences, all of whom contributed in many ways to make this period of my life more enjoyable.

PREFACE

This thesis deals with the loss of image quality associated with light scattering in electronic displays for medical imaging applications. The degradation is most important in radiologic images with wide signal range and low noise. However, up to the present time, the deleterious effects of optical transport processes have been poorly described and often disregarded. This work demonstrates that high fidelity can be achieved only in designs that limit the numerous opportunities for multiple scattering of light photons traveling through the layers of emissive structures.

Each Chapter of this thesis is organized in a format consistent with manuscript submission to peer-reviewed journals, and therefore can be read more or less independently. Useful pointers to where related information can be found in other parts of the thesis have been added.

Chapter I gives an introduction to those aspects of human visual system performance that affect display requirements for high fidelity, and establishes the aim of the research. A broad review of current display technology is provided. Chapter II describes in detail a Monte Carlo code for light transport simulation (DETECT-II) that can be used to predict the optical performance of display devices. In Chapter III, a novel experimental method for measuring veiling glare characteristics of display devices using a collimated detector is described.

Monte Carlo predictions and experimental results for veiling glare in a high performance medical imaging CRT are compared in Chapter IV. The experimental

methods developed for display reflectance evaluation are then presented in Chapter V. Monte Carlo estimates of diffuse reflectance are reported for various emissive structure designs. Finally, Chapter VI provides an analysis of the significance associated with each Chapter, and looks at areas where unanswered questions still remain.

TABLE OF CONTENTS

DEDICATION	ii
ACKNOWLEDGEMENTS	iii
PREFACE	iv
LIST OF FIGURES	x
LIST OF TABLES	xiii

CHAPTER

I. HIGH FIDELITY DISPLAY OF RADIOGRAPHS	1
1.1 Introduction	1
1.2 Display performance	2
1.2.1 Luminance range	2
1.2.2 Gray-scale and contrast	3
1.2.3 Resolution	4
1.2.4 Ambient light reflections	5
1.2.5 Display specifications	6
1.3 Cathode-ray tubes	7
1.3.1 Design characteristics	7
1.3.2 Veiling glare	8
1.3.3 Phosphors	9
1.4 Active matrix liquid crystal displays	10
1.4.1 Liquid crystal displays	10
1.4.2 AMLCD technological trend	11
1.5 Thin emissive technologies	12
1.5.1 Field emission display	12
1.5.2 Organic light-emitting devices	14
1.6 Summary	15
1.7 Aim of this work	15
1.8 Figures	18
1.9 Tables	31
1.10 References	33

II. COMPUTATIONAL MODELING OF LIGHT TRANSPORT PROCESSES	36
2.1 Introduction	36
2.1.1 Ray tracing	36
2.1.2 Numerical solutions to Maxwell's equations	37
2.1.3 Monte Carlo techniques	37
2.2 DETECT-II: A Monte Carlo light transport code	38
2.2.1 Polarization	38
2.2.2 Geometry model	41
2.2.3 Light sources	41
2.3 Optical scattering processes	42
2.3.1 Smooth boundaries	42
2.3.2 Rough surface scattering	44
2.3.3 Anti-reflective coating	44
2.3.4 Bulk absorption	46
2.3.5 Mie scattering	46
2.4 Random number generation	48
2.4.1 Properties of random number generators	48
2.4.2 Algorithms for random number generation	49
2.4.3 DETECT-II random number generator	50
2.5 Modeling of display devices	50
2.5.1 Emissive structure models	50
2.5.2 Binning for display simulation	51
2.5.3 The discrete spread function	52
2.5.4 Display reflectance modeling	53
2.6 Figures	54
2.7 References	60
 III. A METHOD FOR MEASURING VEILING GLARE IN HIGH PERFORMANCE DISPLAY DEVICES	 64
3.1 Introduction	64
3.2 Analytic model for veiling glare	66
3.3 A collimated probe and luminance detector	67
3.4 Experimental methods	69
3.4.1 Probe response versus spot diameter	70
3.4.2 Measurements for a display with no veiling glare . .	71
3.4.3 Measurements for a monochrome CRT	72
3.5 Results	73
3.5.1 Probe response versus spot diameter	73
3.5.2 Measurements for a display with no veiling glare . .	74
3.5.3 Measurements for a monochrome CRT	75

3.6	Discussion	75
3.7	Figures	78
3.8	References	84

IV. VEILING GLARE IN HIGH PERFORMANCE CRT MON-ITORS 86

4.1	Introduction	86
4.2	Components of veiling glare	87
4.2.1	Light diffusion	87
4.2.2	Light leakage	88
4.2.3	Electron backscattering	88
4.2.4	Monte Carlo analysis of electron backscattering in monochrome CRTs	90
4.3	Methods	91
4.3.1	Optical Monte Carlo simulations	92
4.3.1.1	Model of the emissive structure	93
4.3.1.2	The discrete ring response function	93
4.3.2	Experimental measurements	94
4.3.2.1	Bright spot measurements with CCD	94
4.3.2.2	Dark spot measurements	95
4.4	Results	96
4.5	Discussion	97
4.6	Figures	100
4.7	References	104

V. AMBIENT LIGHT REFLECTION IN DISPLAY DEVICES 105

5.1	Introduction	105
5.2	Characterization of display reflections	107
5.2.1	Specular reflection	107
5.2.2	Diffuse reflection	108
5.3	Experimental methods	109
5.3.1	Specular reflection	109
5.3.2	Diffuse reflection	110
5.4	Experimental results	112
5.5	Monte Carlo simulation of ambient reflections in CRTs	112
5.6	Requirements for ambient light reflections	114
5.6.1	Specular reflection requirements for high fidelity	115
5.6.2	Diffuse reflection requirements for high fidelity	116
5.7	Conclusions	117
5.8	Figures	119
5.9	Tables	123
5.10	References	125

VI. CONCLUSIONS	126
---------------------------	-----

LIST OF FIGURES

Figure

1.1	Stimulus response relationship and light adaptation.	18
1.2	Contrast response of the human visual system.	19
1.3	Contrast threshold as a function of luminance.	20
1.4	Standard display curve shown as luminance versus display value. . .	21
1.5	Cross-section of a typical cathode-ray tube bulb.	22
1.6	Scanning electron microscope image of a CRT faceplate sample. . .	22
1.7	CRT faceplate core after removal of the phosphor and Al layers. . .	23
1.8	Effect of contrast degradation in glare test patterns.	23
1.9	Photos of CRT phosphors.	24
1.10	Cross-section of typical CRT emissive structure.	25
1.11	Cross-section illustration of an active-matrix liquid crystal display. .	26
1.12	In a liquid crystal display, light is transmitted through several layers.	27
1.13	Improvement in viewing angle for a multi-domain liquid crystal display.	28
1.14	Pixel structure of a thin-film transistor design for AMLCD.	28
1.15	Thin-film transistor design having a larger aperture ratio in an AMLCD.	29
1.16	Typical field emission display (FED) cross-section.	29
1.17	A typical electro-luminescent (EL) display cross-section.	30

1.18	Luminance versus driving voltage for electro-luminescent devices. . .	30
2.1	Cartesian geometry for the Monte Carlo code DETECT-II.	54
2.2	DETECT-II pseudo-code depicting the tracking of single photons. .	55
2.3	Two-dimensional representation of the rough surface model.	56
2.4	Two-dimensional spectral test for a congruential generator.	56
2.5	Two-dimensional spectral test for L'Ecuyer generator.	57
2.6	Two-dimensional correlations in DETECT-II.	57
2.7	Cross-section of the geometric models used in this work.	58
2.8	Binning of Monte Carlo results for display applications.	58
2.9	Angular dependency in Mie scattering.	59
3.1	Computer graphic patterns for veiling glare.	78
3.2	Photopic probe and radiometer for measurements of veiling glare. .	79
3.3	Schematic drawing of photopic probe showing dimensions in cm. . .	80
3.4	Design drawings for the photopic probe.	81
3.5	Experimentally measured probe response values.	81
3.6	Experimental data points with corrections.	82
3.7	Inverse veiling glare ratios measured on radiographic film.	82
3.8	Veiling glare ratio for a medical imaging CRT.	83
3.9	Ring response function for the medical imaging CRT.	83
4.1	Model of the emissive structure for the CRT monitor.	100
4.2	Monte Carlo predictions of the ring response functions.	101
4.3	Monte Carlo predictions: effect of light absorption.	101

4.4	Monte Carlo predictions: effect of AR coating.	102
4.5	Bright spot CCD images for the monochrome CRT monitor.	102
4.6	Radial profiles for the CCD camera images of the bright spot.	103
4.7	Experimental ring response functions.	103
5.1	Small spot light source for specular reflections.	119
5.2	Portable white room viewed through a hole.	119
5.3	White reflective box for diffuse reflection measurements.	120
5.4	Model of the emissive structure for the CRT monitor.	121
5.5	Binning of photon histories for simulations of diffuse reflections.	121
5.6	Standard display transformation of image value to log-luminance.	122

LIST OF TABLES

Table

1.1	Just noticeable differences for different display brightness.	31
1.2	Display requirements for medical imaging.	32
5.1	Specular and diffuse reflection coefficients for high performance. . .	123
5.2	Monte Carlo estimates of diffuse reflectance.	124
5.3	High fidelity specular reflection coefficients.	124
5.4	High fidelity diffuse reflection coefficients.	124

CHAPTER I

HIGH FIDELITY DISPLAY OF RADIOGRAPHS

1.1 Introduction

The display of radiographic images using electronic devices is now common within diagnostic radiology and within referring medical services. However, the quality of digital images displayed on electronic devices is typically less than the quality observed with printed films. For electronic displays to fully replace radiographic film, their diagnostic performance needs to be similar or superior to film. In this Chapter, an overview of the current state of display technology is presented to declare the motivation for this research study. The analysis begins in Section 1.2, where the limitations of the observer (the human visual system) are considered in order to define those aspects of display quality that are important for interpreting diagnostic radiographs. Display device performance requirements for parameters such as luminance range, contrast, resolution and surface reflections are defined and minimum device requirements for radiologic applications are suggested. Display devices including cathode-ray tubes (CRTs) and flat panel technologies (Sections 1.3 to 1.5) are then considered with respect to their potential for meeting these requirements. Finally, Section 1.7 establishes the goal and specific aims of the research, and introduces the

structure of this document.

1.2 Display performance

For a display device with ideal performance, both image quality and observer performance are constrained by human visual system limitations. Data from psycho-visual experiments can be used to establish the performance of a high fidelity device which can stimulate the human visual system over its full range of response. These visual performance requirements are then used along with radiologic application requirements to specify device parameters such as luminance range, gray-scale mapping functions, contrast, resolution and display size. In this Section, well-known characteristics of the human visual system are reviewed and used to define high fidelity display device performance.

1.2.1 Luminance range

The neural response of photo-receptors in the eye is known to be linear at low light levels and to saturate at higher levels [3, 24]. In addition, psycho-visual experiments have been used to describe the adaptation of the human visual system to the average luminance of the scene observed [18, 23]*. Using electro-physiological observations and computer simulations, Normann [25] and Baxter [2] have reported on the relationship between photo-receptor sensitivity and image processing at neural centers for visual tools involving the detection of low-contrast radiological features in non-uniform backgrounds. The sensitivity response function for the complete visual system can be approximately described by an expression of the form $R = I/(I + S)$ [16], where R is the photo-receptor response, I is the retinal intensity, and S represents

*Luminance is a photometric measurement unit reflecting the brightness of a small region on a display surface. The SI unit of brightness is the nit, which is a candela per square meter (cd/m^2). 1 cd/m^2 is equal to 0.2919 foot-lambert (fL).

a constant that conforms with the state of adaptation. This relationship was first introduced as part of Hecht's photochemical theory of photo-receptor response [17], and confirmed experimentally by several authors (e.g., [3]). Figure 1.1 depicts the measured rate of neuronal signals for different adaptation states using the above general expression with illustrative numerical values.

When the observer is adapted to a particular average luminance, the change in neuronal response associated with a small change in luminance is a biologic indication of contrast. This perceived contrast is maximal near the average luminance and is markedly reduced for regions in the scene with higher or lower luminance, as shown in Figure 1.2. The display of intensity information over a wide luminance range produces images with high physical contrast (large $\Delta L/L$ for a specific image intensity change)[†]. However, the perceived contrast is modified by the observer's biological contrast response. To maintain satisfactory biologic contrast response over the full luminance range, the ratio of the maximum luminance to the minimum luminance in a radiologic display, L_{max}/L_{min} , should be limited to about 100. This corresponds to the luminance range produced by two regions of film with a film density change of 2.0. For general radiography, film densities are commonly in the range from 0.2 to 2.2. At higher density, a "bright light" is needed for viewing.

1.2.2 Gray-scale and contrast

The physical contrast required to detect a test pattern having a sinusoidal variation in luminance over a uniform background can be described by a visual contrast sensitivity function that depends on luminance and spatial frequency as well as other parameters of secondary influence [19]. In psychophysics, sensitivity is related to de-

[†]In this work, contrast is defined using the Michelson definition: $C = (L_{max} - L_{mean})/L_{mean}$ [21].

tection and usually defined as the reciprocal of the contrast threshold. At a spatial frequency of 1 cycle per mm where the observer has good response, the contrast threshold is nearly constant at high luminance and is higher below 10 cd/m² (see Figure 1.3 on page 20) [1].

When digital images are displayed in electronic devices, the image display value (DV) is mapped into display luminance using a gray-scale function. At high luminance where the threshold contrast ($\Delta L/L$) is constant, a gray-scale mapping for which $\log(\text{luminance})$ is proportional to DV will produce uniform contrast. However, for many display systems, the dim regions occur at a luminance where the contrast threshold is poor [28]. A gray-scale map can be defined such that each increment in DV causes a just noticeable difference increment (JND) in luminance [5, 45]. This relationship is shown in Figure 1.4. Devices with a maximum luminance of 1000 cd/m² and a minimum luminance of 5 cd/m² have about 600 JNDs, as seen in Table 1.1 on page 31. Such a display system provides good contrast performance.

Quantum noise in digital radiographs can often exceed the contrast threshold and be visually apparent. For typical noise power spectra associated with computed radiography systems, the standard error of the quantum noise exceeds the visual threshold (0.007 at 100 cd/m²) for a noise equivalent quanta equal to about 75,000 using a transformation curve with a gamma of 2.0. This occurs for an exposure of about 1.5 mR to a computed radiography plate (115 kVp filtered beam).

1.2.3 Resolution

The visual contrast sensitivity is a strong function of spatial frequency. For typical viewing distances, the response is best at a frequency of about 0.5 to 1.0 cycles

per mm [26]. A display with a maximum spatial frequency of 3 cycles per mm[†] will present all the information that a human observer can perceive. This can be provided, even in a diagonal direction, with a pixel size of 120 μm . Interestingly, sensitivity is reduced at low frequency causing radiologists to back away from an image to observe large features.

Increasingly, digital radiographs are being recorded successfully on regions smaller than the conventional 35 \times 43 cm size. A display size of 30 \times 36 cm corresponds to a 2500 \times 3000 array of 0.120 μm pixels. This display size, combined with a regional image zoom function will provide a high fidelity workstation.

1.2.4 Ambient light reflections

The luminous intensity and the spatial distribution of light sources in rooms where electronic devices are utilized to display radiographic images can vary significantly. The observed image quality is always affected by the scattering of ambient light in the direction of the viewer. With radiographic film, these reflections are highly dampened and diffused due to a thin emulsive layer with absorbent dark grains coated on the front surface.

When using electronic display devices, the display reflectance can be generally described as a superposition of specular and diffuse components. The diffuse component adds a uniform background luminance that reduces substantially the observed contrast in dim regions. Diffuse reflectance can be dampened with absorptive faceplate and black matrix designs. The image quality degradation introduced by the specular component is associated with the overlay of structured luminous patterns onto the radiologic image that affects the detection of diagnostic features. Moreover,

[†]Display resolution is defined as the maximum spatial frequency of the device. This is equal to $0.5/P$ where P is the pixel size.

the addition of reflected patterns can cause visual fatigue. To reduce specular reflections, anti-reflective coatings can be used. Approaches to reduce these reflections include absorbent faceplate, black matrix absorber, rough surfaces, and anti-reflective coatings. In a room producing an illuminance of 100 lux, a display device having 0.01 1/sr diffuse reflection coefficient will noticeably decrease the contrast for regions with a luminance less than 5 cd/m². High fidelity electronic displays should have Lambertian angular emission while minimizing ambient light reflections.

1.2.5 Display specifications

The foundations of the above discussion rely on simple models of perception of detail by the human visual system. When considering the complex nature of the visual system and the perception processes, limitations of the presented approach arise. For instance, when subtle details are displayed in radiographic images, structured luminance levels outside the foveal field are likely to impact the observer performance. Recent research efforts utilizing complex backgrounds suggest that human performance is markedly degraded by the presence of surrounding patterns [10, 15, 34]. In spite of this, the above discussion results in a useful guide for defining device requirements for radiologic displays.

In Table 1.2, the image quality specifications for three radiographic display qualities are summarized. Film quality display is defined as one having all the attributes of transilluminated medical radiography film. A high fidelity display is one that has all of the image quality that can be perceived by the human visual system. It is expected that magnification, and contrast and brightness adjustments are done using computer software. We have additionally defined a good quality device suitable for certain clinical functions. This quality is typical of the specialized CRTs now used

in medicine.

1.3 Cathode-ray tubes

To date, CRTs are the only choice for an electronic display device in the radiology practice. Improved designs have only recently allowed higher brightness, increased resolution and better contrast. In this Section, a review of CRT technology is presented, focusing on design aspects that affect display quality.

1.3.1 Design characteristics

In a CRT, electrons are accelerated within the large vacuum bulb with a high voltage of up to 30 kV. The beam scans the plate in a raster fashion, exciting the cathodoluminescent phosphor with a small beam spot (see Figure 1.5 on page 22). To reduce mechanical stress, thick glass is used for the funnel and plate. For 74 cm diagonal bulbs with relatively flat faceplate, 13.7 mm thick glass is normally used.

Typical CRT emissive structures consist of a cathodoluminescent material (phosphor) deposited onto a glass faceplate panel as a powder layer. In color tubes, a light absorbent, carbon based black matrix separates the RBG phosphor dots for color purity. A sub-micron reflective layer of Al is overlaid on top of the phosphor to conduct the incoming electron current and maximize light output towards the viewer. For that purpose, a filming material is used to assure a smooth, continuous and highly reflective film.

Figure 1.6 shows a scanning electron microscope image of the emissive structure of a monochrome CRT, where multiple layers of phosphor grains can be observed under the thin Al coating. The glass faceplate can absorb up to 70% of the direct light, thus improving contrast, and may have a rough surface on the vacuum side to reduce specular reflections. A photograph of the interior surface of a CRT faceplate

sample after the Al and phosphor layers were removed is shown in Figure 1.7.

To obtain adequate brightness, a high-current beam is deflected, while maintaining a small focal spot that is related to the display resolution. The thick faceplate causes image quality degradation by glare, and contributes to the weight of the device.

1.3.2 Veiling glare

Glare is the diffuse spreading of light caused by multiple scattering processes in emissive display devices resulting in low frequency degradation of image quality (perceived as contrast reduction). This phenomenon is present in all imaging systems and has been studied for detectors [7,12,29,38,48], and for the human eye [4,27,35,36].

Light rays generated in the phosphor grains must undergo multiple scattering events before escaping the emissive structure and eventually being detected by the observer. Light diffusion in the emissive structure multiple layers causes luminance spread functions with tails that extend up to a distance of 20 cm. When displaying images with wide luminance range, this diffuse component over large areas degrades the maximum contrast capabilities of the device.

In Figure 1.8, the effect of glare degradation has been simulated. The circular test pattern used to measure veiling glare characteristics in electronic devices has been convolved with a point-spread function typical of conventional CRTs. The pattern on the right depicts the expected reduction in contrast. The diffuse component is clearly observed in the image data profiles shown below.

Another source of image quality degradation in CRTs comes from light leakage through Al layer non-uniformities (cracks, holes). Particularly for color tubes, electron backscattering in the emissive structure and in components such as aperture

grille and shadow masks has been identified as additional source of veiling glare, responsible for reduction in contrast and poor color saturation [14, 42, 43].

It is useful to define the veiling glare ratio as the luminance in a full bright field to the luminance in a central dark spot of a given diameter. Although the quantitative relationship between this ratio and image quality degradation has not been fully described, good performance display devices require ratios greater than 150 for a black spot diameter of 1 cm. For high fidelity display, the veiling glare ratio should approach 400.

1.3.3 Phosphors

Cathodoluminescent phosphors convert energy deposited by energetic electrons to light (see Figure 1.10). Electrons penetrate a cover layer and travel into individual phosphor grains. Light then scatters within the emissive structure until escaping from the display surface. The total luminous efficiency is computed as a linear combination of efficiencies and a photopic correction K_λ : $\epsilon = K_\lambda \epsilon_e \epsilon_p \epsilon_g$, where ϵ_e is the energy deposition efficiency, ϵ_p is the energy quantum efficiency, and ϵ_g is the escape efficiency. For typical devices, ϵ is 20.8 lm/W for P104 phosphors and 13.5 lm/W for P45.

Total display brightness is a function of the electron beam power (p_l , W), the display area (a_l , m²), and the luminous efficiency (ϵ , lm/W),

$$L = \frac{\epsilon p_l}{\pi a_l}. \quad (1.1)$$

For example, a CRT with a display area of 0.3×0.4 m, a 1 mA electron beam accelerated to 20,000 V (20 W), and a phosphor emissive layer with an efficiency of 10 lm/W will have a display brightness of 530 cd/m².

Current models of eye-brain function indicate that humans depend on display

brightness for interpreting contrast and detail in a scene. Color is evaluated from separate eye receptors and interpreted as a low resolution difference signal (R-G and Y-B). It is commonly believed that inspection of detailed scene as found in medical radiography is best done with a display having a broad light spectrum perceived as white and various shades of gray. Figure 1.9 shows highly magnified recordings of a uniform gray region (5 mm in diameter) from three CRT devices depicting differences in color formation and noise characteristics.

1.4 Active matrix liquid crystal displays

Recent improvements in size, contrast ratio, and viewing angle have established active matrix liquid crystal displays (AMLCD[§]) as candidates for radiologic applications. In this Section, the fundamentals of such devices are presented, and current engineering challenges are outlined.

1.4.1 Liquid crystal displays

When the molecule orientation within a liquid crystal (LC) is altered by the application of an electric field, the optical characteristics of the LC cell change. This electro-optical effect is used in liquid crystal displays (LCD) to modulate light transmission. Light is emitted from the back-light and directed to the front through the LC cell. The transmission is associated with the state of polarization of the light as it passes through the polarizer films and LC layer. In an AMLCD, the switch between ON and OFF states is controlled by a thin-film transistor (TFT) deposited onto the glass substrate (see Figure 1.11 on page 26).

As shown in Figure 1.12, multiple layers are needed to effectively modulate display luminance. Overall transmission is poor (3-5%) for full color TFT-LCDs, and

[§]AMLCD is an industry term for active-matrix liquid crystal display.

up to 15% for monochrome designs, thus requiring high efficiency back-lights. Full ON and OFF states (“black” and “white”) have typically good angle of view. Yet, for intermediate gray levels the emission distribution is severely affected due to the optical anisotropy of the LC cell. Other problems include gate signal distortion for large area displays, lifetime, and temperature sensitivity. Amorphous Si:H TFT-LCDs are now larger with higher resolution and improved gray-scale. Different companies have produced full color AMLCDs up to 1 m in diagonal having SXGA resolution (1280×1024), and brightness up to 250 cd/m^2 .

1.4.2 AMLCD technological trend

To use AMLCD in medical applications, the viewing angle, brightness, contrast ratio, and number of gray levels must be improved. Since light transmitted through the LC cell can follow paths with different lengths and directions, the overall transmission depends on its emission angle. Solutions that provide a more uniform response include: in-plane switching, optically negative birefringent compensation plates, and multi-domain designs. Figure 1.13 illustrates typical improvements in viewing angle characteristics for a multi-domain design.

Transmitted light intensity is limited by polarizers, color filters, and other layers, as well as by the geometric aperture ratio of the pixel cell (see Figure 1.14 on page 28). One method to improve aperture ratio is to reduce the indium tin oxide (ITO) pixel electrode to bus line separation. Figure 1.15 shows a TFT design with overlap between ITO and bus lines. As the gate signal reaches the other end of the gate line conducting path, it suffers a time constant of about $\tau = RC$. This delay limits display size and resolution. For large area high resolution displays, Cu or Al metalization must be used. Monochrome displays 33 cm in diagonal, with 3072×2048 array having

pixel pitch of 90 μm have been developed.

By improving the polarizers, reducing the dispersion of pigments in color filters, and by adding a black matrix layer, current twisted-nematic mode LCDs have realized high pixel contrast ratio of 100, viewed from normal incidence. For low power consumption, improvements in transmission, efficiency of the back-light, and driving circuit power requirements must be demonstrated. These devices can effectively absorb ambient light and reduce reflections, as has been demonstrated for military applications [6].

1.5 Thin emissive technologies

Among the developing flat panel technologies, field emission displays (FEDs) and organic light-emitting devices (OLEDs) have confirmed auspicious attributes. In this Section, a discussion of the current state-of-the-art is given, and notable aspects of these technologies are summarized.

1.5.1 Field emission display

In an FED device, each pixel has its electron source that typically consists of a large array of low work function emitter micro-tips [13]. Electrons are accelerated through a vacuum cell to impinge on a cathodoluminescent phosphor[¶]. A schematic cross-section of a typical FED is depicted in Figure 1.16. Instead of using a diode arrangement with proximity focusing, a focus electrode can be incorporated to decrease beam spot size and increase resolution [40]. While most FEDs use metallic micro-tips, amorphous diamond has shown good current-voltage characteristic, however, the emission mechanism is not well understood.

[¶]FEDs are similar to CRTs in that electrons are emitted from a cathode and accelerated towards the phosphor through a vacuum cell. Instead of using thermionic emission, electrons are emitted by a cold field emission process.

Most FED designs must be evacuated to low pressures (10^{-7} torr) to prevent contamination and deterioration of the electron emitters. Large display sizes thus need spacers to prevent bending of the faceplate. In low voltage designs, small spherical spacers can be used. For high voltage operation with large gaps, high aspect ratio spacers are being developed [8].

FED faceplate usually consists of a thin glass panel, a conductive layer, and a cathodoluminescent phosphor (e.g., $\text{Y}_2\text{O}_3\text{:Eu}$, $\text{SrGaS}_4\text{:Eu}$, ZnS:Cu,Al , $\text{Gd}_2\text{O}_2\text{S:Tb}$). For low voltage approaches, transparent conductive oxides (e.g., ITO) are used instead of Al. In general, phosphor efficiency is greater at high voltages. Devices with high voltage designs will have large spacers and focused electron beams.

Currently, several engineering aspects are being investigated to improve FED overall efficiency. Pixel brightness variations due to electron emission non-uniformities and low reliability of the cathode have been reported for prototype designs. Recently, active elements such as metal-oxide semiconductor field effect transistor (MOSFET) have been employed to control and stabilize the emission current of field emission arrays [46]. Low voltage phosphors consume less power but are less efficient and saturate rapidly due to high current density (0.1 mA/cm^2), making high voltage designs look more promising. Devices with long lifetime and low driver cost are challenged by an increase in flash-over risk, more stringent surface de-gasification requirements, wider vacuum gaps and uniformity of spacers arrays.

FED advantages include wide temperature and humidity range, wide viewing angle, Lambertian emission (CRT-like), and potential for high brightness and contrast. Numerous companies have announced FED products for 1999, but are all interested in color rather than monochrome (black and white) displays.

1.5.2 Organic light-emitting devices

Among display technologies, electro-luminescence (EL) represents an all solid state approach that provides the most direct conversion of electrical energy into light [20, 32]. Their efficiency and performance characteristics depend strongly on the materials and fabrication processes used. EL devices use a phosphor under the influence of an electric field to generate light.

As shown in Figure 1.17, thin film EL devices are made up of a stack of conductors and dielectrics deposited onto a substrate [41]. A black thin film layer may be incorporated at the bottom of the structure to provide contrast enhancement, and thin film transistors can be used for addressing of high resolution, low cost devices. One attractive feature of thin film inorganic EL is a very steep luminance versus voltage slope above threshold, as seen in Figure 1.18. This, along with a fast phosphor time response, allows for direct addressing of large arrays.

Recently, good light emission, fast response and extended lifetime have been reported for amorphous and crystalline organic thin film stacks that can be deposited on flexible substrates [32, 33, 39, 44]. With vertically stacked pixel architecture, these devices allow for color, gray-scale and intensity tuning [11, 31]. Different organic compounds have been used, providing a wide range of emission spectra with typical efficiencies up to 15 lm/W. Using transparent organic layers, devices with high transmission in the visible spectral region have been developed [9]. A “color by white” approach for full color has been described in which a white phosphor operates through RGB patterned filters. Organic light-emitting devices (OLEDs) made with organic semiconductors with the processability of conventional polymers are currently being investigated [22].

Improvements are still needed in the chemical structure of the organic thin films,

organic-metallic contacts, organic-organic layers interface, and in the understanding of non-radiative recombination losses and electrical degradation. In early stage of development, OLEDs present reliability issues such as electro-chemical instabilities with formation of radical species, contact degradation, encapsulation (needed due to air and humidity sensitivity), and low thermal tolerance [32].

1.6 Summary

Successful integration of digital radiography in medicine will require high fidelity electronic displays. Current CRT systems do not meet the desired performance and have excessive volume, weight and power consumption. Recent developments in flat panel display technology suggest that high fidelity, light weight displays will be available in the near future. Large size AMLCD devices have been demonstrated. High brightness can be easily achieved with bright back illumination. Further developments in optical design for monochrome displays should provide high fidelity and improve the angular dependencies of the gray-scale. FED devices have attractive emission distribution and potential for low veiling glare. The technology is considered expensive to manufacture and problems with cathode aging and non-uniformity have to be contemplated. OLEDs represent a simple and potentially inexpensive display technology with the ability to achieve high image quality. However, extensive research and development is required to achieve suitable large area manufacturing methods.

1.7 Aim of this work

As discussed in this introductory Chapter, no electronic device is currently available that can display digital radiographs without loss of visual information compared

to transilluminated film. Among the limitations of current display devices, the characteristics of light transport in the faceplate of CRT monitors that causes excessive veiling glare, and unwanted ambient light reflections have not yet been fully described in the literature.

This dissertation considers in detail the effects of light scattering processes on the degradation of image quality in electronic display devices by developing appropriate experimental methods and computational modeling tools. This work does not study other aspects related to display quality such as spatial resolution, overall grey-scale, and driving techniques. As we will show, the light scattering processes in display devices can severely affect optical performance. Nonetheless, they are often disregarded. Knowledge about the effect of veiling glare and ambient light reflections on display image quality will permit the investigation of the relationships between display performance and medical diagnostic efficacy. Moreover, the experimental and computational methods introduced in this thesis represent valuable tools for evaluating and designing optimized display devices for high fidelity applications.

This document is organized as follows:

- In Chapter II, an optical Monte Carlo code for light transport simulation that predicts both veiling glare ratios and display reflections (DETECT-II) is detailed.
- A novel experimental method that permits the characterization of veiling glare and luminance spread functions in display devices by measuring small spot contrast ratios is presented in Chapter III.
- Simulation results from DETECT-II are benchmarked in Chapter IV against data taken with the experimental veiling glare method using a medical imaging

CRT with and without anti-reflective panel.

- Chapter V presents a discussion on the effect of ambient light reflections on display image quality with a description of experimental methods and results. Diffuse reflectance data obtained with DETECT-II are related to experimental results for the same CRT studied as part of Chapter IV.
- Finally, Chapter VI summarizes the findings and conclusions of this work, and suggests promising future research directions.

1.8 Figures

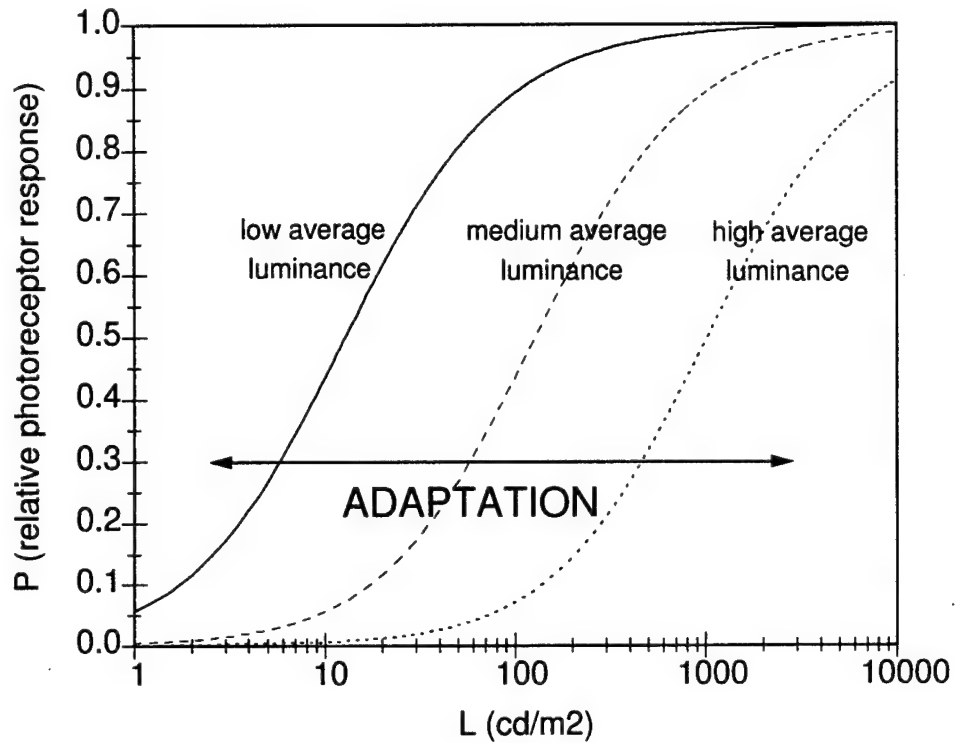


Figure 1.1: Stimulus response relationship and light adaptation. The profile of the response function was approximated using an expression of the form $R = I/(I + S)$ [2], where R is the photo-receptor response, I is the retinal intensity, and S is a parameter that represents the state of adaptation. Same incremental changes in stimulus cause different response according to the adaptation state.

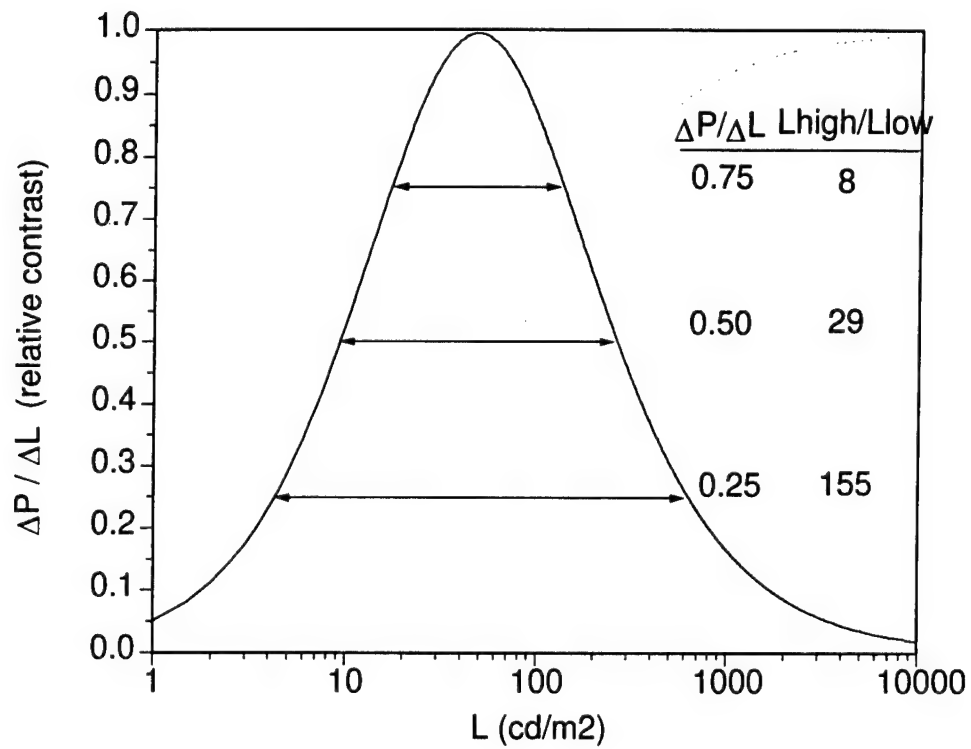


Figure 1.2: Contrast response of the human visual system. The curve was obtained by differentiating the photo-receptor response. The perception of contrast deteriorates rapidly as the intensity of the stimulus is increased or decreased with respect to the optimum response coordinate.

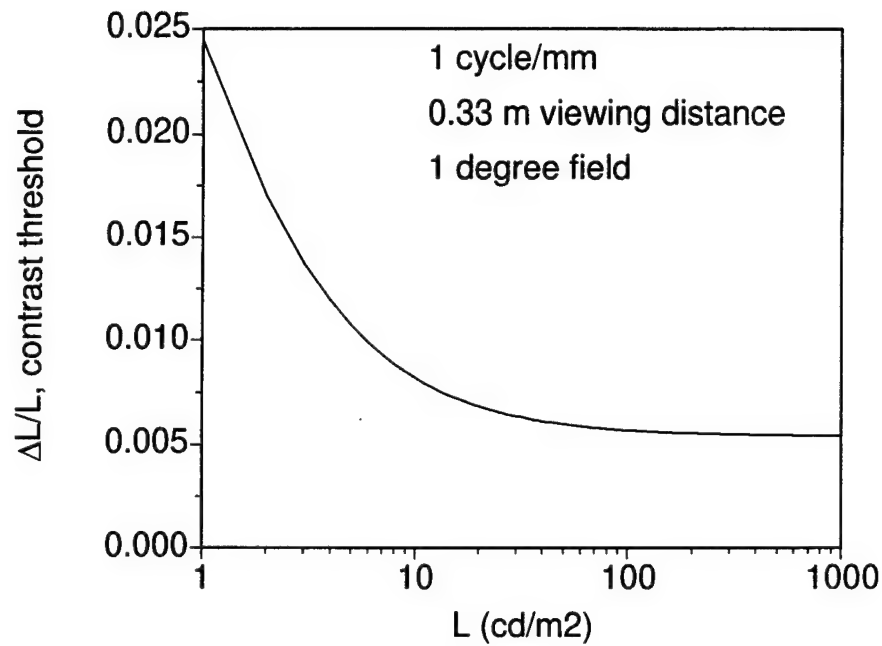


Figure 1.3: For a particular spatial frequency in the signal, the contrast threshold of the human visual system can be plotted as a function of luminance. While constant at higher luminance values, the threshold deteriorates at low luminance, which is known as the Weber-Fechner law [30].

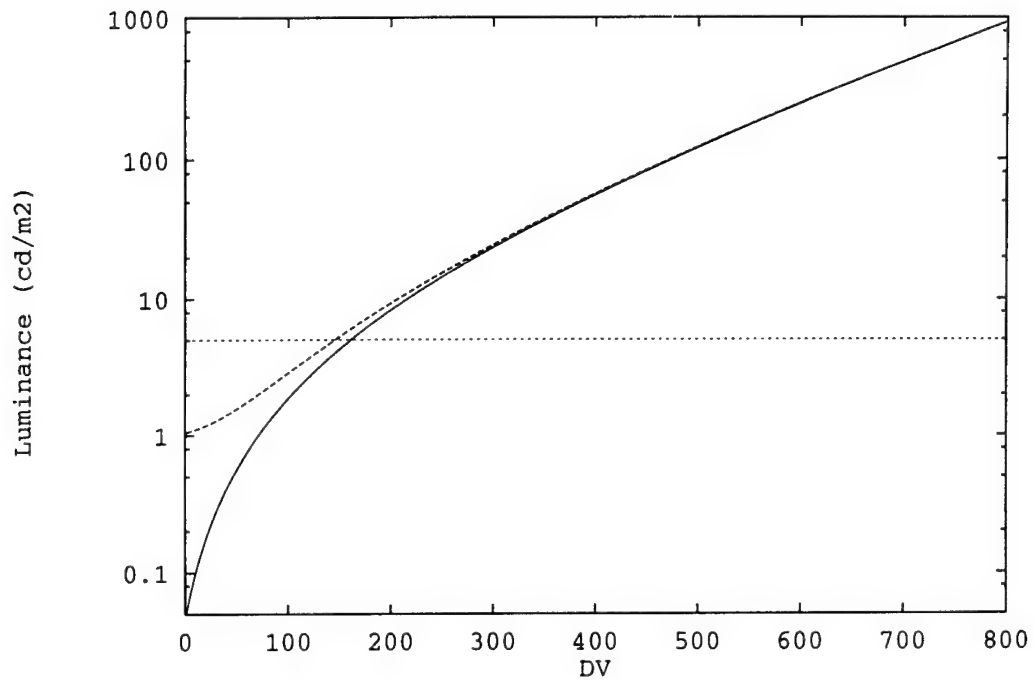


Figure 1.4: Standard display function curve shown as luminance versus display value (DV) [5, 45]. A unit change in DV causes a luminance change equal to the contrast threshold at the indicated luminance level. The upper curve depicts the effect of diffuse ambient light reflection for a display device having a 0.01 1/sr diffuse reflection coefficient in a room producing 100 lux. The difference between the standard curve and the modified curve becomes small for regions where the luminance is greater than 5 cd/m².

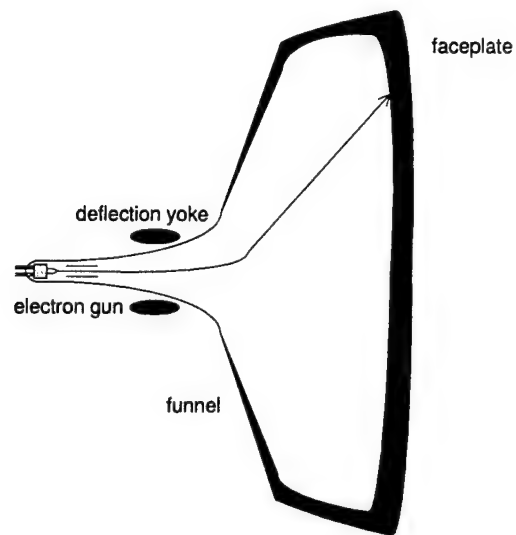


Figure 1.5: Cross-section illustrating the relative dimensions of a typical cathode-ray tube bulb.

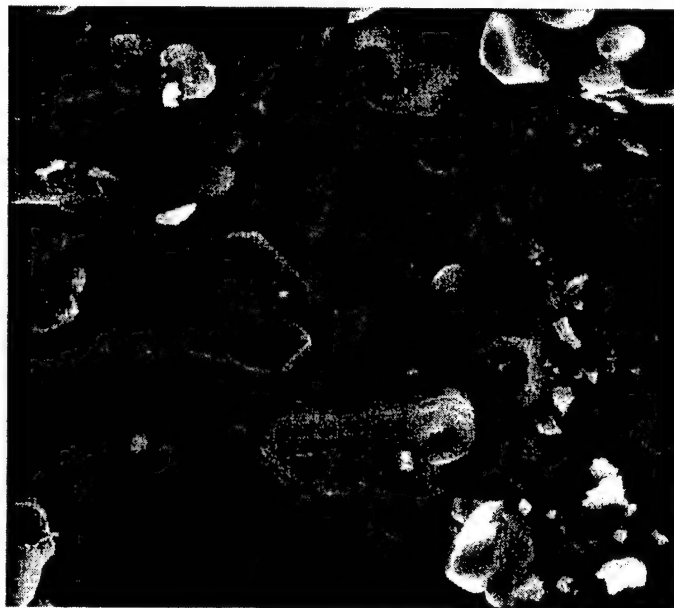


Figure 1.6: Scanning electron microscope image of a CRT faceplate sample. The phosphor layers were exposed using a scalpel scratch. The width of the image corresponds to $50\text{ }\mu\text{m}$. Debris from the sample preparation process can be seen on top of the Al layer.

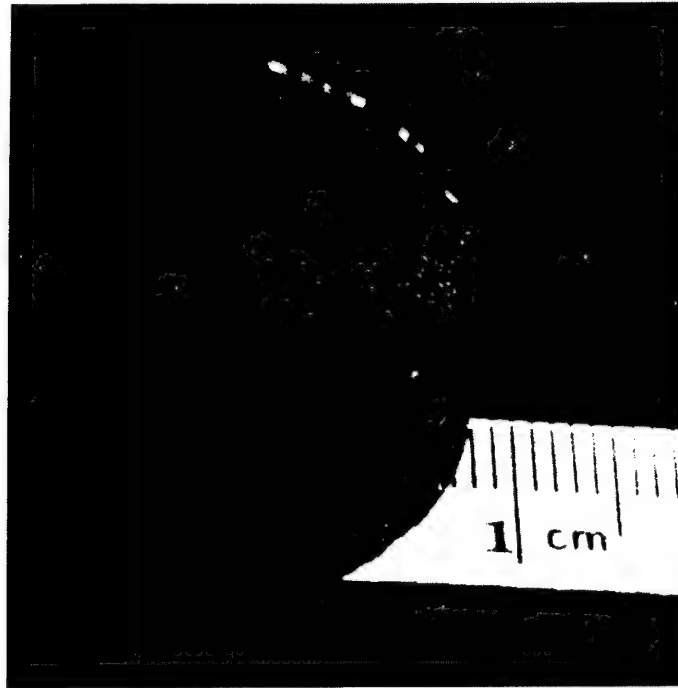


Figure 1.7: CRT faceplate core showing the inner surface after removal of the phosphor and Al layers. The roughness in the interior surface contributes to diffusively scatter internal reflections.

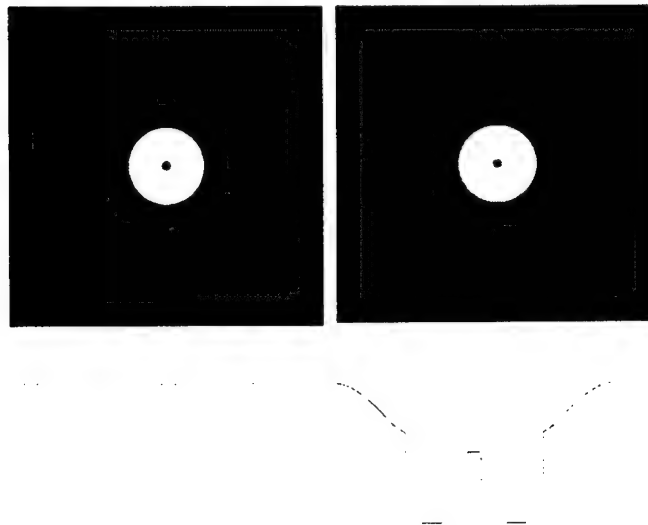


Figure 1.8: Effect of contrast degradation in glare test patterns. The curves depict a center data row from the above images, showing the diffuse background component that reduces the glare ratio (defined as L_{max}/L_{min}).



Figure 1.9: Photos of CRT phosphors: (a) Some high brightness phosphors (notably P104) contain a mixture of phosphors with different color and often produce a noisy image. (b) Phosphors which naturally emit a broad spectrum (such as P45) typically have reduced luminous efficiency. (c) Color monitors rely on simultaneous stimulation of red, green, and blue phosphors to simulate a white or gray emission. To date, the color matrix technology has not been exploited by loading each cell with a high luminosity white phosphor.

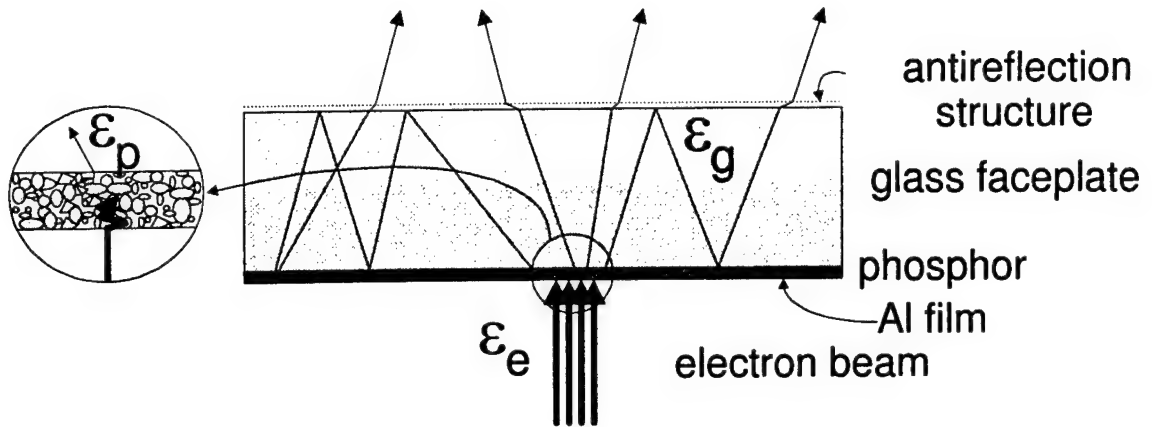


Figure 1.10: Cross-section of typical CRT emissive structure. Light generated in the phosphor layer by electron impact scatters in the different components until its fate is determined. The processes can be described by three efficiencies. First, the incident electron beam will deposit energy into the phosphor with an efficiency ϵ_e , which relates the energy of the incoming electrons to the deposited energy in the phosphor. Secondly, the energy deposited by the electrons into the phosphor is converted to light photons in the luminescence sites with a quantum efficiency ϵ_p . Once the light is generated, it diffuses and eventually reaches the viewer by escaping the structure with an efficiency ϵ_g , which is dependent on light emission characteristics, spatial distribution of emitted photons, and relative dimensions of the emissive structure components. The complex light transport that takes place may consist in several possible processes which include reflection and refraction at the surfaces, and scattering and absorption in the medium.

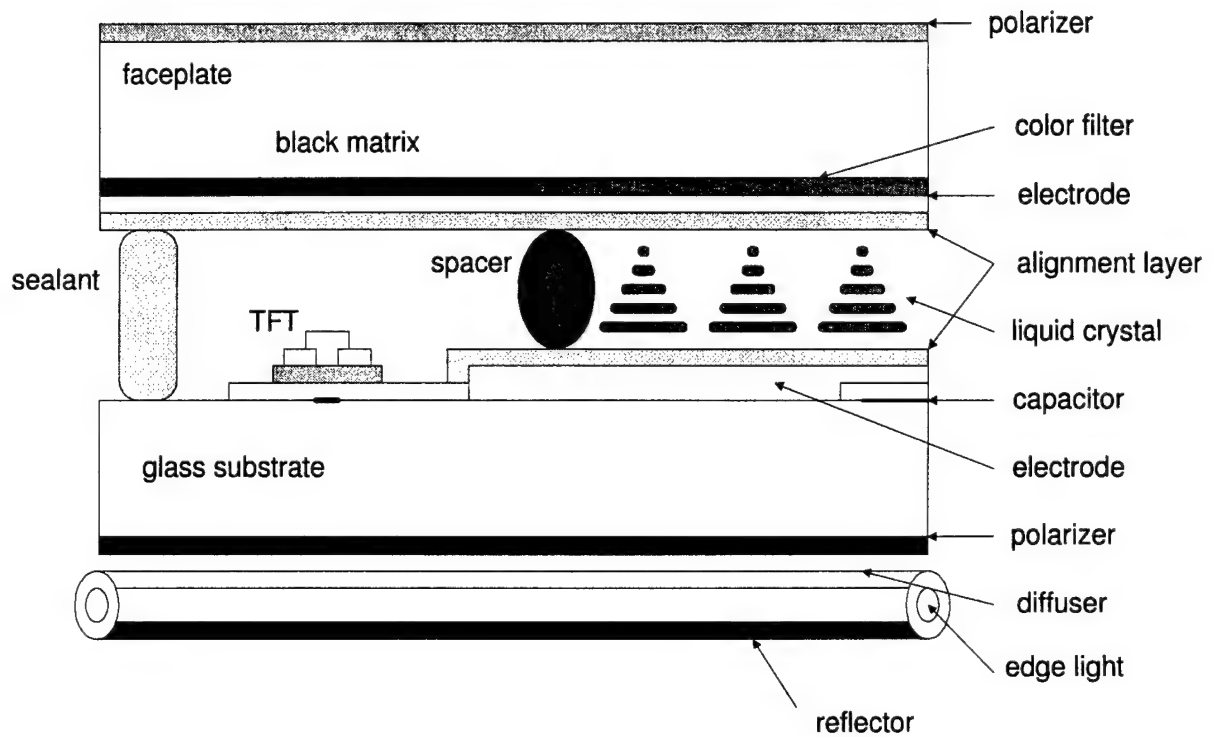


Figure 1.11: Cross-section illustration of an active-matrix liquid crystal display. The liquid crystal cell that modulates light intensity according to the driving voltages, is confined by multi-layer structures.

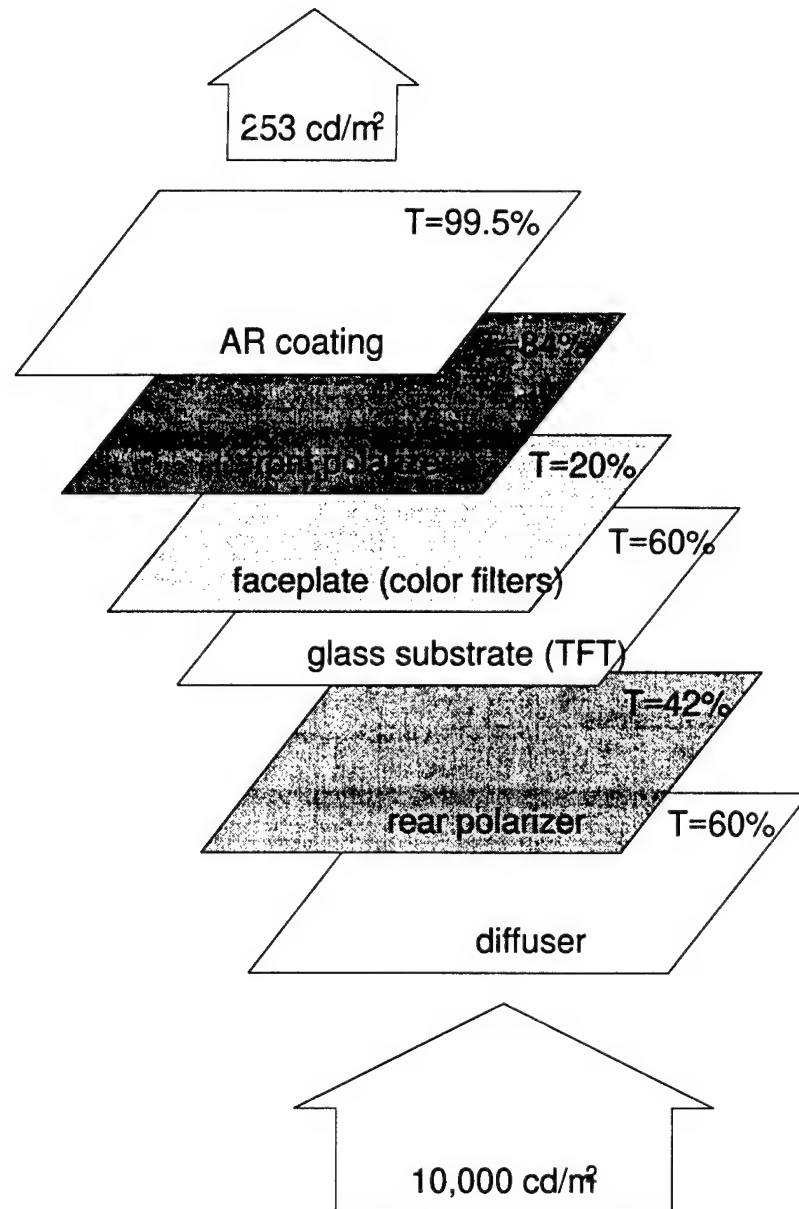


Figure 1.12: In a liquid crystal display, light is transmitted through several layers. Overall transmission is only 3-5% for color designs. The absence of color filters in monochrome designs can elevate this up to 15%.

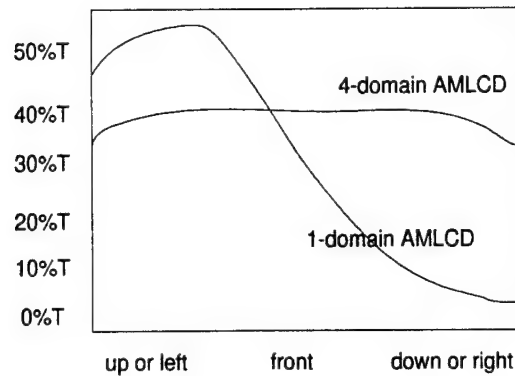


Figure 1.13: Improvement in viewing angle for a multi-domain liquid crystal display. Because anisotropies in the liquid crystal configuration are averaged over all domains, the emission angular distribution is enhanced. Ideally, emitted light should approach a Lambertian distribution.

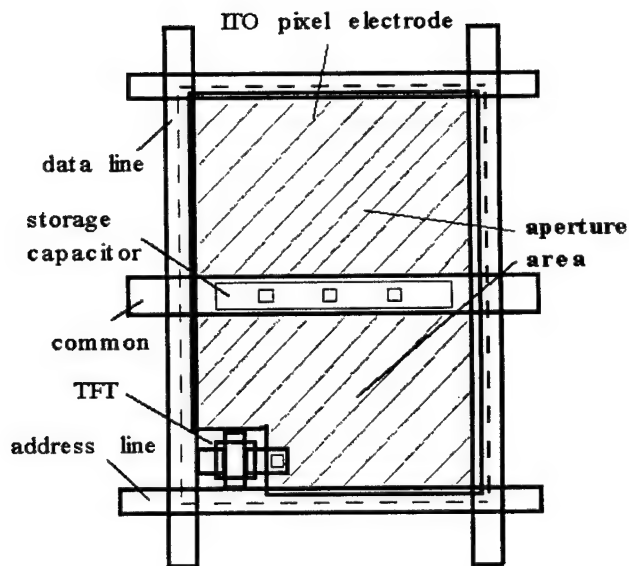


Figure 1.14: Pixel structure showing the aperture area of a thin-film transistor design for active-matrix liquid crystal display (AMLCD). In this design, the ITO pixel electrode overlaps the bus line separation.

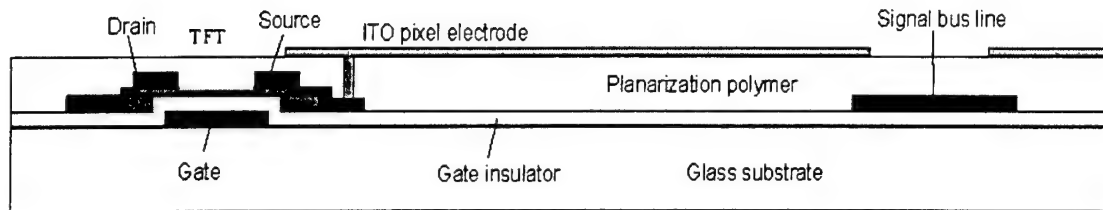


Figure 1.15: Thin film transistor design with overlap between ITO and bus line having a larger pixel aperture ratio in an active-matrix liquid crystal display (AMLCD) design.

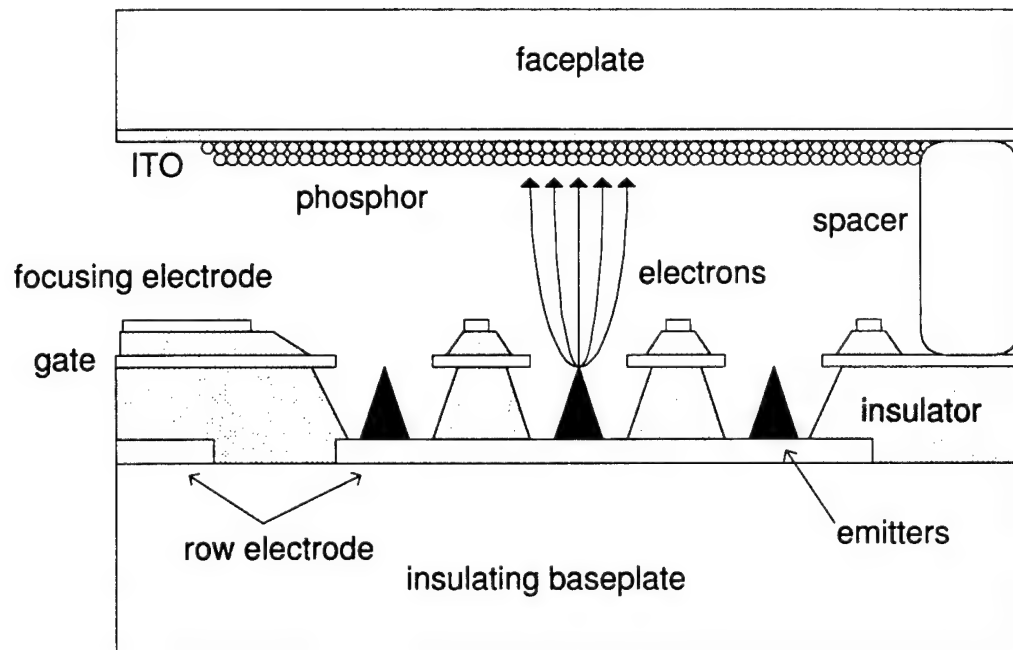


Figure 1.16: Typical field emission display (FED) cross-section illustrating the sharp emitters and the structures that confine the micro-vacuum cell.

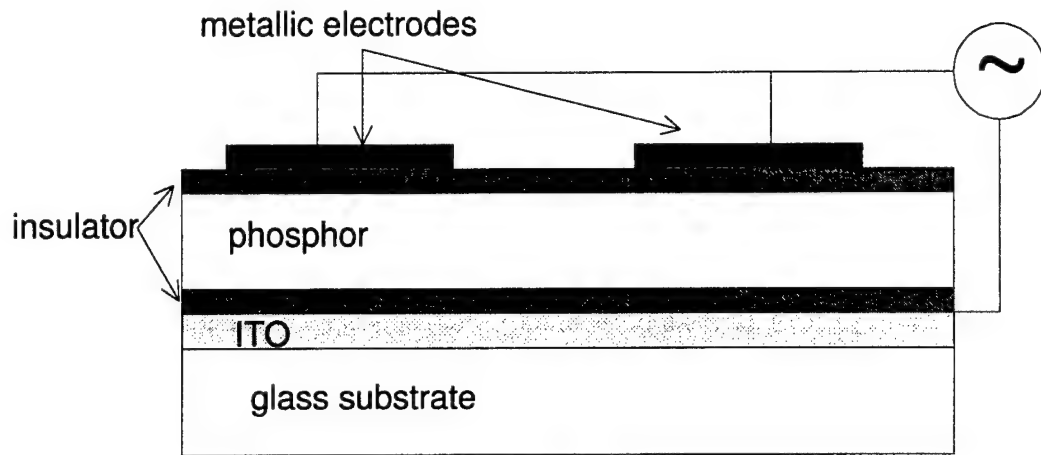


Figure 1.17: A typical electro-luminescent (EL) display cross-section showing the film arrangement needed for a display device, although layers for specific designs may differ.

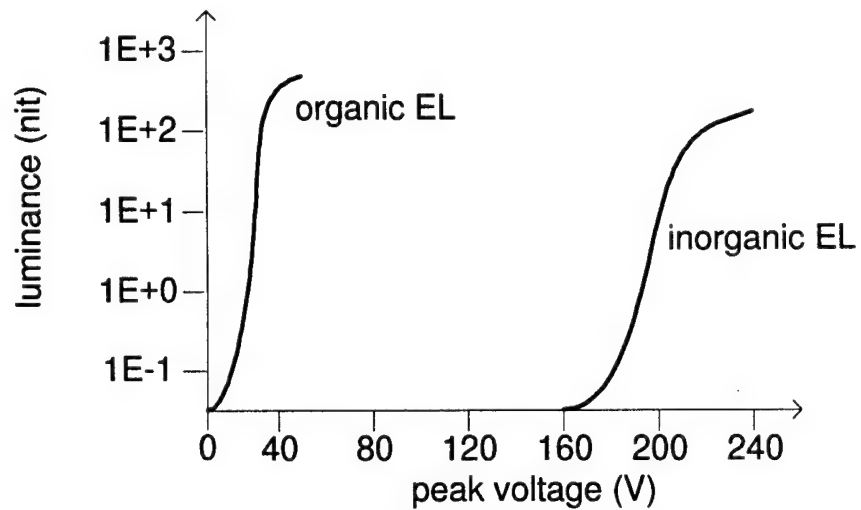


Figure 1.18: Attained luminance versus driving voltage for organic and inorganic electro-luminescent devices (adapted from [37,47]).

1.9 Tables

Table 1.1: Just noticeable differences for different display brightness.

L_{low} (cd/m ²)	L_{high} (cd/m ²)	JNDs
0.5	100	430
1	200	500
2	400	567
5	1000	630
10	2000	700
20	4000	740

Table 1.2: Display requirements for medical imaging.

Specification	Film Quality	High Fidelity	Good
<i>Spatial</i>			
Size (cm) ^a	35×43	30×36	24×30
Pixels	4000×5000	2500×3000	1200×1500
Pixel size (mm)	0.08	0.12	0.20
Refresh rate (Hz)	static	static - 80	static - 80
Area distortion (%)	< 0.1	2	2
<i>Grey-scale</i>			
Maximum luminance (cd/m ²)	2000	1000	300
Minimum luminance (cd/m ²)	1	5	1.5
Gray-scale levels ^b	> 1000	700	700
Emission	Lambertian	Lambertian	Lambertian
Color ^c	monochrome	monochrome	monochrome
<i>Optical</i>			
Veiling glare ratio ^d	> 1000	200	100
Specular reflectance ^e	0.02	0.002	0.004
Diffuse reflectance (nit/lux) ^e	0.02	0.01	0.02
Viewing angle (V) ^f	full	± 45°	± 30°
Viewing angle (H)	full	± 60°	± 45°

^a 43×35 cm is a standard size for radiographic detectors. Displays should have a horizontal/vertical aspect ratio of about 0.8.

^b The log-luminance versus pixel value relationships should follow a perceptually linear profile based on the DICOM standard.

^c General preference in the field has been for displays with a white to slightly blue color. Most film bases are tinted blue.

^d Contrast ratio defined with test pattern images consisting of a 1 cm centered dark circular spot, surrounded by a bright field.

^e A discussion on the requirements for specular and diffuse reflection coefficients is given in Chapter V.

^f Full stated contrast ratio and luminance performance is to be maintained within the required viewing angle. No contrast inversion is allowed.

1.10 References

1. P. G. J. Barten. Physical model for the contrast sensitivity of the human eye. *Proceedings of the SPIE*, 1666:57–72, 1992.
2. B. Baxter, H. Ravindra, and R. A. Normann. Changes in lesion detectability caused by light adaptation in retinal photoreceptors. *Investigative Radiology*, 17:394–401, 1982.
3. D. A. Baylor and M. G. F. Fuortes. Electrical responses of single cones in the retina of the turtle. *Journal of Physiology*, 207:77–92, 1970.
4. C. Beckman, O. Nilsson, and L.-E. Paulsson. Intraocular light scattering in vision, artistic painting, and photography. *Applied Optics*, 33(21):4749–4753, July 1994.
5. H. Blume and B. M. Hemminger. Image presentation in digital radiology: perspectives on the emerging DICOM display function standard and its application. *Radiographics*, 17:769–777, 1997.
6. R. Brinkley, G. Xu, A. Abileah, et al. Wide-viewing-angle AMLCD optimized for gray-scale operation. *Proceedings of the Society for Information Display*, pages 471–474, 1998.
7. N. Bromberg and J. Bickford. Veiling glare in the imaging chain. *Proceedings of the SPIE*, 454:387–391, 1984.
8. J. Browning, C. Watkins, J. Alwan, et al. Scaling of FED technology. *International Display Research Conference*, pages F–42, 1997.
9. V. Bulovic, G. Gu, P. E. Burrows, M. E. Thompson, and S. R. Forrest. Transparent light emitting devices. *Nature*, 380(29), 1996.
10. A. E. Burgess, X. Li, and Craig K. Abbey. Visual signal detectability with two noise components: anomalous masking effects. *Journal of the Optical Society of America A*, 14(9):2420, 1997.
11. P. E. Burrows, Z. Shen, and S. R. Forrest. Saturated full color stacked organic light emitting devices. *International Display Research Conference*, pages 318–321, 1997.
12. Ed Caruthers. Monte Carlo studies of image spread by X-ray image intensifiers. *Proceedings of the SPIE*, 535:140–147, 1985.
13. B. R. Chalamala, Y. Wei, and B. E. Gnade. FED up with fat tubes. *IEEE Spectrum*, pages 42–51, April 1998.
14. G. C. de Vries. Contrast-enhancement under low ambient illumination. *Proceedings of the Society for Information Display*, pages 32–35, 1995.
15. M. P. Eckstein, A. J. Ahumada, and A. B. Watson. Visual signal detection in structured backgrounds. II. Effects of contrast gain control, background variations, and white noise. *Journal of the Optical Society of America A*, 14(9):2406–2421, 1997.
16. R. M. Giantz. Visual adaptation: a case of nonlinear summation. *Vision Research*, 12:103–109, 1972.

17. S. Hecht and Y. Hsia. Relation between visual acuity and illumination. *Journal of General Physiology*, 11:255–281, 1928.
18. S. Hecht and Y. Hsia. Dark adaptation following light adaptation to red and white lights. *Journal of the Optical Society of America*, 35(4):261–267, April 1945.
19. D. H. Kelly. Visual contrast sensitivity. *Optica Acta*, 24(2):107–129, 1997.
20. R. Khormaei, S. Thayer, K. Ping, et al. High-resolution active-matrix electroluminescent display. *Proceedings of the Society for Information Display*, pages 137–139, 1994.
21. A. A. Michelson. *Studies in Optics*. The University of Chicago Press, 1962.
22. W. E. Moerner. Polymer luminescence: those blinking single molecules. *Science*, 277(5329):1059–1060, August 1997.
23. R. A. Norman and I. Perlman. The effects of background illumination on the photoreponses of red and green cones. *Journal of General Physiology*, 286:491–507, 1979.
24. R. A. Norman and F. S. Werblin. Control of retinal sensitivity: light and dark adaptation of vertebrate rods and cones. *Journal of General Physiology*, 63:37–61, 1974.
25. R. A. Normann, B. S. Baxter, H. Ravindra, et al. Photoreceptor contributions to contrast sensitivity: Applications in radiological diagnosis. *IEEE Transactions on Systems, Man, and Cybernetics*, SMC-13(5):944–953, 1983.
26. C. Owsley, R. Sekuler, and D. Siemsen. Contrast sensitivity throughout adulthood. *Vision Research*, 23(7):689–699, 1983.
27. L.-E. Paulsson and J. Sjostrand. Contrast sensitivity in the presence of a glare light. *Investigative Ophthalmology*, 19(4):401–406, April 1980.
28. E. Peli, J. Yang, R. Goldstein, et al. Effect of luminance on suprathreshold contrast perception. *Journal of the Optical Society of America A*, 8:1352–1359, August 1991.
29. J. A. Seibert, O. Nalciglu, and W. Roeck. Characterization of the veiling glare PSF in X-ray image intensified fluoroscopy. *Medical Physics*, 11(2):172–179, March 1984.
30. M. I. Sezan, K. L. Yip, and S. J. Daly. Uniform perceptual quantization: applications to digital radiology. *IEEE Transactions on Systems, Man, and Cybernetics*, SMC-17(4):622–634, 1987.
31. J. R. Sheats. Stacked organic light-emitting diodes in full color. *Science*, 277(5323):191–2, July 1997.
32. J. R. Sheats, H. Antoniadis, M. Hueschen, et al. Organic electroluminescent devices. *Science*, 273(5277):884–8, August 1996.
33. Z. Shen, P. E. Burrows, V. Bulovic, et al. Three-color, tunable, organic light-emitting devices. *Science*, 276:2009–2011, June 1997.

34. R. J. Snowden and S. T. Hammett. The effects of surround contrast on contrast thresholds, perceived contrast and contrast discrimination. *Vision Research*, 38:1935–1945, 1998.
35. G. Spencer, P. Shirley, K. Zimmerman, et al. Physically-based glare effects for digital images. *Computer Graphics Proceedings, Annual Conference Series SIGGRAPH 95*, pages 325–334, 1995.
36. W. S. Stiles. The effect of glare on the brightness difference threshold. *Proceedings of the Royal Society of London*, B104:322–351, 1929.
37. J. C. Sturm and C. C. Wu. Integrated organic light emitting diode structures using doped polymers. *International Display Research Conference*, pages F11–F18, 1997.
38. R. K. Swank. Calculation of modulation transfer functions of X-ray fluorescent screens. *Applied Optics*, 12(8):1865–1870, August 1973.
39. N. Takada, T. Tsutsui, and S. Saito. Strongly directed emission from controlled-spontaneous- emission electroluminescent diodes with europium complex as an emitter. *Japanese Journal of Applied Physics*, 33(6B):L863–6, June 1994.
40. C.-M. Tang and T. A. Swyden. Beam collimation from field-emitter arrays with linear planar lenses. *International Display Research Conference*, pages 115–118, 1997.
41. C. W. Tang and S. A. VanSlyke. Organic electroluminescent diodes. *Applied Physics Letters*, 51(12):913–915, September 1987.
42. J. J. van Oekel. Improving the contrast of CRTs under low ambient illumination with a graphite coating. *Proceedings of the Society for Information Display*, pages 427–430, 1995.
43. J. J. van Oekel, M. J. Severens, G. M. H. Timmermans, et al. Improving contrast and color saturation of CRTs by Al_2O_3 shadow mask coating. *Proceedings of the Society for Information Display*, pages 436–439, 1997.
44. T. Wakimoto, Y. Yonemoto, J. Funaki, et al. Stability characteristics of quinacridone and coumarin molecules as guest dopants in the organic LEDs. *Synthetic Metals*, 91:15, 1997.
45. ACR/NEMA Working Group XI. Greyscale display function standard, draft version 1.2. Technical report, ACR/NEMA, March 1997.
46. K. Yokoo, M. Arai, M. Kawakami, H. Kayama, N. Kitano, and H. Mimura. Emission characteristics of JFET-based field emitter arrays. In *1997 55th Annual Device Research Conference Digest*, pages 152–153. IEEE Electron Devices Society, June 1997.
47. M. Yoshimi. *Current topics in amorphous materials: Physics and Technology*, chapter Light-emitting device, pages 415–420. Elsevier Science, 1993.
48. H. D. Zeman, E. B. Hughes, J. N. Otis, et al. Veiling glare of a linear multichannel Si(Li) detector. *Proceedings of the SPIE*, 535:214–221, 1985.

CHAPTER II

COMPUTATIONAL MODELING OF LIGHT TRANSPORT PROCESSES

2.1 Introduction

The simulation of light scattering processes in emissive structures for display performance prediction has usually been performed using two different methods: ray tracing and numerical solutions to Maxwell's electro-magnetic equations. Computational tools that use these methods are very useful for solving particular design problems. However, situations arise where these tools have limited applicability due to lack of a priori knowledge of the system response, to extensive computational times, or to complex geometries.

2.1.1 Ray tracing

The most widely used technique for the simulation of light diffusion is ray tracing [16]. Following bundles of optical rays through multiple interactions, ray tracing techniques rely on previous knowledge about the system response to efficiently determine the initial position, direction, and other attributes of the principal paths that will contribute to the output. Ray tracing methods that originate the source photons with discrete pre-determined position coordinates and directions are known as deterministic ray tracing. Implementations that use sampling procedures to define

initial photon characteristics are often called stochastic ray tracing [17].

A commercial software package, ARGUS, is available for the modeling of display performance of high resolution CRTs [14, 35, 36]. In this model, the digital signal is traced from the digital-to-analog converter to the video amplifier, and to the electron gun impinging on a phosphor to generate the luminance image. Most of its applicability relates to the modeling of the electronic signals and of the electron beam characteristics. Light scattering processes are modeled using simplistic filter functions associated with a generic CRT design [15]. This approach does not allow for the modeling of light transport in particular devices with improved designs.

2.1.2 Numerical solutions to Maxwell's equations

The second approach involves the numerical solution of the differential equations that govern light propagation in layered structures. In these methods, the full electromagnetic Maxwell's equations are solved using numerical approximations (i.e., finite-difference) to describe the light propagation through multiple layers with appropriate boundary conditions. These techniques have been developed and applied mostly in LCD optical modeling. The predictions have been compared to experimental results yielding good agreement for 1-dimensional problems [5–7]. However, such approach does not describe internal multiple reflections, and exact modeling of 3-dimensional structures requires long computational times [51].

2.1.3 Monte Carlo techniques

In this work, light transport processes that occur in 3-dimensional emissive structures are simulated using Monte Carlo methods. Monte Carlo methods track the trajectories of a large number of optical photons to describe the statistically averaged output. A major advantage with respect to the stochastic ray tracing techniques is

the way that absorption and scattering processes are modeled. In the Monte Carlo method, the distance to each event is randomly sampled from probability distribution functions, and the minimum distance event is chosen to occur. Monte Carlo methods can handle a wide variety of physical cases and are computationally practical when using high speed computers.

The transport of optical photons through emissive materials using Monte Carlo techniques has been previously used to predict light collection properties of scintillating detectors [3,4,23,24,42] and phosphor screens [41]. Monte Carlo approaches have also been used in radiative transfer modeling for atmospheric applications [17], and in lighting [44] and thermal design applications [30]. In this Chapter, a light transport Monte Carlo simulation code, DETECT-II, is described. Emphasis is given to the description of its unique features, including photon polarization tracking, special binning techniques for display simulation, and random number generation with very long period.

2.2 DETECT-II: A Monte Carlo light transport code

In DETECT-II, individual photons are followed from the light source until they exit the structure. Photon paths are determined by the interaction of the light quanta with optical boundaries, and by events that may result in absorption or re-direction. At each point in the trajectory, the direction of propagation (given by the directional cosines) and the polarization state of the photon are known.

2.2.1 Polarization

If we consider the xy -plane perpendicular to the direction of propagation of the wave, where the electric field E (and also the magnetic field) vibrates harmonically, we can define the polarization ellipse by projecting the magnitude of the amplitudes

of E into the xy -plane, and by considering the phase difference. In addition to the relative projection of the field maxima, left-handed and right-handed states can be associated with the rotation direction [2, 22]. Three special cases are of particular interest. Completely unpolarized light (or natural light) has the property that the ensemble average intensity of the field components along any direction perpendicular to the direction of propagation is the same, and not affected by retardation of one of its components. Linearly polarized light occurs when the projection reduces to a straight line. When the ratio of the amplitudes and the phase difference are time independent, the axis of the ellipse are equal, and circularly polarized light is observed.

A unique feature of DETECT-II is the technique for photon polarization tracking. Several attempts to incorporate the effect of photon polarization in photon transport simulation tools have been reported. In γ -ray spectroscopy, McMaster [34] theoretically described polarization phenomena associated with the interactions between photons and electrons. In this approach, the polarization state of a radiation beam is represented in a matrix notation using the Stokes parameters associated with physically measurable properties of the beam [11]. In such a treatment, after the photon beam undergoes an interaction, the matrix characteristics of the interaction are used to calculate the scattered intensity. Although this approach facilitates numerical calculations [33], it implies that the tracking of polarization states is done for a beam of particles by evolving the polarization vector through multiple scattering events.

Similar treatments of polarization have been described for ray tracing methods [9, 10, 48], including applications in lighting models [52] and biaxial optical elements [46]. The evaluation of the polarization within these programs is done,

similarly to the method proposed by McMaster, using Jones and Mueller matrices by averaging polarization states computed for a given number of rays [21].

Polarization has also been incorporated in Monte Carlo light transport simulations [1, 28, 47]. The same matrix approach describing variations in the energy associated with each polarization component is described using the Stokes parameters. These prior Monte Carlo codes follow ray paths and not individual photons.

A different approach that tracks polarization states for single optical photons has been implemented in DETECT-II. When using Monte Carlo methods to simulate light transport processes by tracking photons (individual quanta), the intensity of each photon has to be conserved*, and the polarization vector normalized to unity [49]. Details on the polarization tracking algorithm are presented next.

It is possible to associate a polarization state with each ray, and describe its change along a photon history. Photon histories are started with random linear polarization (i.e., the angle of the polarization vector normal to the path is arbitrarily selected in $[0, \pi/2]$)[†].

Relative to the plane of incidence defined at the first surface, the polarization state is computed in terms of the polarization components along the parallel and perpendicular directions (ω_{\parallel} and ω_{\perp}). If the incident polarization is random, then, both ω_{\parallel} and ω_{\perp} will be distributed isotropically. For the first surface encounter, the reflection probabilities are computed using Equations 2.1-2.4.

The tracking of polarization is carried out along the photon history using the same procedures to obtain the polarization components after each interaction. At

*This is valid for scattering phenomena that do not involve change in photon energy, as it is done with wavelength-shifters in scintillation detectors [24].

[†]Light emission at luminescent centers can be anisotropic [38] which may result in preference for a certain polarization direction. However, the light emission from phosphor crystals is de-polarized at room temperature. An example of an anisotropic center is the Tl^+ defect in CsI:Tl , whose emission becomes de-polarized at $T > 230 \text{ K}$ [37].

an optical boundary, the polarization components are projected into the parallel and perpendicular directions defined by the surface normal and the incident vector direction. The polarization of a photon after reflection is given by $\omega'_{\parallel} = r_{\parallel}\omega_{\parallel}$, and $\omega'_{\perp} = r_{\perp}\omega_{\perp}$. Similarly, after refraction, $\omega'_{\parallel} = t_{\parallel}\omega_{\parallel}$, and $\omega'_{\perp} = t_{\perp}\omega_{\perp}$. After the surface scattering is completed, the photon polarization components are normalized to $\omega'^2_{\parallel} + \omega'^2_{\perp} = 1$.

2.2.2 Geometry model

In DETECT-II, the geometry is described in 3-dimensional Cartesian coordinates using slabs with orthogonal division into cells, as shown in Figure 2.1. The geometry descriptor and related code routines were adapted from a Monte Carlo code for electron transport simulation, SKEPTIC [50]. The 3-dimensional objects are defined as a stack of slabs along the z axis, with division of each slab into cells in the x and y direction. The dividing surfaces defined for one slab do not have to be continued into the neighboring slabs. The same file that contains the parameters that define the geometric objects can be used for radiation and light transport simulations, simplifying the calculation of problems that involve both processes. The surface characteristics at the sides of each cell are assigned different surface types, which include smooth, rough, absorptive, diffuse and thin films.

2.2.3 Light sources

Photons can originate from a point source or from a planar distributed source with isotropic, Lambertian angular emission, or oriented along particular directions. Sources that are distributed in 3-dimensional objects can also be used. The current version of DETECT-II allows to sample from a 3-dimensional distributed source with constant intensity over the entire volume. Sampling from arbitrary distribution func-

tions can be easily implemented for problems such as the generation of luminescence based on the interaction of soft radiation with crystalline materials, where light is generated with an intensity that varies as a function of position.

For each photon, the wavelength is defined and tracked with the history. In the current version of DETECT-II, models for anti-reflective coating and Mie scattering include dependencies with photon wavelength. No provision is present to model wavelength shifting or wavelength dependent absorption. Each photon wavelength is randomly determined from a spectra having multiple lines by specifying the number of lines and the relative line weight. An extensions for sampling the photon energy from arbitrary distributions would require a different sampling scheme to assign a wavelength for each history.

2.3 Optical scattering processes

The current version of DETECT-II models optically isotropic material (i.e., optical properties are identical along different spatial directions). This allows the modeling of most materials found in emissive displays, but is not applicable to liquid crystal displays where the modulation of light intensity is done by highly anisotropic materials as the liquid crystal and the polarizers.

2.3.1 Smooth boundaries

At the optical boundaries, an analysis is performed depending on the surface type and material properties, using Fresnel's equations considering the polarization of the incoming photon. The tracking algorithm is based on 2 fundamental assumptions. First, a geometrical optics approach is used that neglects the effect of finite wavelengths, and utilizes macroscopic Maxwell's equations (see Section 2.3.3 on page 44 for the treatment of thin films). Second, light paths are assumed to apply to one sin-

gle quanta (light photon). The reflection and transmission coefficients are therefore interpreted as probabilities. Details concerning the implementation of the assumptions are given in Section 2.2.1. Figure 2.2 presents a pseudo-code overall description of DETECT-II.

The laws of refraction and reflection established for plane waves incident upon plane boundaries remain valid for individual photons when interpreted as probabilities. If a light ray of intensity I falls on a boundary, it is split into a reflected (R) and a transmitted (T) wave, and the change of polarization state is predicted by the corresponding Fresnel's formulas (for plane waves), which are presented below. When considering a single photon quanta, the transmission and reflection coefficients associated with the corresponding probabilities for parallel and perpendicular components, are expressed as:

$$P_{\parallel,trans} = t_{\parallel}^2 = T_{\parallel}/I_{\parallel}$$

$$P_{\perp,trans} = t_{\perp}^2 = T_{\perp}/I_{\perp}$$

$$P_{\parallel,refl} = r_{\parallel}^2 = R_{\parallel}/I_{\parallel}$$

$$P_{\perp,refl} = r_{\perp}^2 = R_{\perp}/I_{\perp} ,$$

where t_{\perp}^2 , t_{\parallel}^2 , r_{\perp}^2 and r_{\parallel}^2 are the reflectivity and transmissivity for both components,

$$t_{\parallel}^2 = \frac{\sin(2\theta_1) \sin(2\theta_2)}{\sin^2(\theta_1 + \theta_2) \cos^2(\theta_1 - \theta_2)} \quad (2.1)$$

$$t_{\perp}^2 = \frac{\sin(2\theta_1) \sin(2\theta_2)}{\sin^2(\theta_1 + \theta_2)} \quad (2.2)$$

$$r_{\parallel}^2 = \frac{\tan^2(\theta_1 - \theta_2)}{\tan^2(\theta_1 + \theta_2)} \quad (2.3)$$

$$r_{\perp}^2 = \frac{\sin^2(\theta_1 - \theta_2)}{\sin^2(\theta_1 + \theta_2)} . \quad (2.4)$$

2.3.2 Rough surface scattering

To describe Fresnel interactions at rough surfaces of the type found in emissive display devices (see Figure 1.7 on page 23), an algorithm that randomly perturbs the surface normal was developed. This description is appropriate for surfaces having undulating profiles with low aspect ratio. The roughness is specified by defining a maximum cone within which surface normal tilting can occur. The tilting angle α is sampled uniformly from a cosine distribution within the allowed range. The diagram in Figure 2.3 shows a 2-dimensional representation of the model, where α is the tilting angle used to simulate a surface slope. A Fresnel analysis is then performed using angles ϕ_1 and ϕ_2 .

The Fresnel equations are solved with the incident photon vector expressed in a rotated coordinate system. The out-coming vector is then rotated back to the initial coordinate system. Additionally, a test is performed: $\phi_1 + \alpha < \frac{\pi}{2}$, which prevents a reflection directed into the surface. For a reflection occurring in a valley, the reflected photon may strike a neighboring hill. This is not accounted in the model, and therefore, surface normal distributions should be limited to modest cone angles ($\alpha < 30^\circ$).

2.3.3 Anti-reflective coating

In general, AR coatings are used to reduce specular reflections from the surface of a display device. While silica-coating or chemically etched rough surfaces have been used for this purpose, the degradation of display resolution is unacceptable for most applications. Recently, thin-film coatings have been introduced in high-definition CRT systems for medical applications. Materials include organic layers [45] and metal oxides [18, 39, 40]. Multiple layers are used in recent AR coating designs to

further decrease the reflectivity, with transparent conductive layers to dissipate static charge and reduce dust build-up, and to provide electro-magnetic shielding[†].

In addition to a reduction in the reflectance of the display, AR coatings affect the transport of light inside the faceplate by favoring transmission at the glass-air interface. The optical properties of such structures can be described as a function of the wavelength and the incident angle [2]. By using modified Fresnel coefficients, thin-films are incorporated as a specific surface type into the simulation code. The current version of DETECT-II describes AR coatings using a 1-layer simplification. The equations for multi-layer stacks [2] can be incorporated to provide a more accurate model of current AR designs.

For an homogeneous dielectric film between two homogeneous media, it is useful to define the effective index p_i as

$$p_i = n_i \cos \theta_i \quad (i = 1, 2, 3) , \quad (2.5)$$

where n_i is the index of refraction of media 1, 2, and 3[§], and θ_i is the angle of incidence in medium i . In addition, a wavelength-dependent parameter β can be defined as

$$\beta = \frac{2\pi}{\lambda_0} n_2 h \cos \theta_2 , \quad (2.6)$$

where λ_0 is the photon wavelength, n_2 is the index of refraction of the thin film material, and h is the thin film thickness.

The reflection and transmission coefficients are now expressed in terms of p_i as

$$r_{12} = \frac{p_1 - p_2}{p_1 + p_2} \quad (2.7)$$

$$t_{12} = \frac{2p_1}{p_1 + p_2} \quad (2.8)$$

[†]As described in product literature by OCLI, Santa Rosa, CA, and Viratec Thin Films, Faribault, MN.

[§]Medium 2 corresponds to the thin film layer.

with analogous expressions for r_{23} and t_{23} .

The reflectivity and transmissivity can be computed using the following expressions:

$$t^2 = \frac{n_3 \cos \theta_3}{n_1 \cos \theta_1} \frac{t_{12}^2 t_{23}^2}{1 + r_{12}^2 r_{23}^2 + 2r_{12} r_{23} \cos 2\beta} \quad (2.9)$$

$$r^2 = \frac{r_{12}^2 + r_{23}^2 + 2r_{12} r_{23} \cos 2\beta}{1 + r_{12}^2 r_{23}^2 + 2r_{12} r_{23} \cos 2\beta}. \quad (2.10)$$

A straightforward calculation reveals that Equation 2.10 remains unchanged if β is replaced by $\beta + \pi$, or, when the thickness of the thin dielectric film is increased by Δh , where

$$\Delta h = \frac{\lambda_0}{2n_2 \cos \theta_2}. \quad (2.11)$$

For normal incidence and optimal thin film thickness, r^2 becomes

$$r^2 = \left(\frac{n_1 n_3 - n_2^2}{n_1 n_3 + n_2^2} \right)^2. \quad (2.12)$$

2.3.4 Bulk absorption

Naturally to Monte Carlo methods, bulk absorption in the structure materials is modeled with a linear coefficient. To determine if such an event occurs, the distance to next boundary is compared to the sampled distance to collision. To determine the distance to collision, we use direct sampling techniques from the cumulative distribution function associated with the exponential density function.

2.3.5 Mie scattering

Mie theory describes the scattering of light by spheres of finite size [2]. DETECT-II currently uses the Rayleigh approximation, corresponding to the limiting case of Mie theory for small spheres. The ratio of the scattering cross-section to the geometric area of the sphere depends on the parameter x , $x = 2\pi R/\lambda$. When $x \ll 1$,

using first expansions in the general expression of the scattering cross-section, we obtain the Rayleigh limiting case, where,

$$\sigma_{sca} \propto x^4 \pi R^2 \propto \frac{1}{\lambda^4} . \quad (2.13)$$

If N is the number density of scatterers associated with crystal imperfections or defects, the scattering coefficient is given by

$$\mu_{sca}(E) = \frac{1}{N\sigma_{sca}(E)} . \quad (2.14)$$

This dependency of the scattering coefficient with the photon energy is implemented in the current version of DETECT-II.

The angular scattering probability has in some cases been assumed isotropic [13]. However, in average, the intensity of Rayleigh scattering for unpolarized light is proportional to $1 + \cos^2\theta_s$. In Monte Carlo simulations with randomly linear polarization vectors, the intensity of the scattered light is a function of the angle between the polarization vector and the scattered direction (χ), according to $I_{sca} \propto \sin^2\chi$ [22]. This expression is used in DETECT-II.

The description of point scatterers can be applied to model scattering events caused by local imperfections in crystalline structures. Descriptions applicable to larger spheres and polarized light are available and could be used [22]. As the size of the particle causing the scattering event increases, and this approximation breaks down, the distribution function becomes forward-peaked, as can be seen in the example shown in Figure 2.9. However, events in granular films such as the phosphor layer will require a model that considers material inhomogeneities and provides an improved geometric descriptor.

2.4 Random number generation

Specialized random number generation deficiencies is required due to possible systematic errors in Monte Carlo calculations caused by multi-dimensional correlations [12]. Although many random number generators will pass standard tests and have very long periods, calculations exist where correlations result in up to a 20% difference in the expected results [43]. The interplay between the algorithm structure and material properties of a modeled system, and the correlations in the sequence leads to the observation that a generator is only "good" in conjunction with a specific application for which it has to be tested.

2.4.1 Properties of random number generators

For the typical computations required to simulate display optical performance using DETECT-II, a random number generator with long period, good efficiency, and with no multi-dimensional correlations is required. In addition, generators with simple procedures for parallel execution are useful [29]. Many commonly used generators don't meet all of these conditions [20]. Random number generators defined as intrinsic functions implemented in different compilers have been proved to have dubious quality [19], and are not portable[¶]. When doing Monte Carlo calculations on different computers, exact agreement with previous and trusted calculations is essential. The portability requirement is often confused in the literature with reproducibility. A portable random number generator is always reproducible, but not the opposite. Moreover, for parallel execution, reproducibility in a "strong" sense is required both on the same processor with different partitioning scheme of the

[¶]In this work, a portable random number generator is defined as such that yields the same random number sequence when compiled and run in different platforms and systems, and is therefore, reproducible.

processing resources, and between processors [32].

The n -dimensional spectral test is often used as an empirical technique which examines the lattice structure of all the points formed by taking n successive values in the sequence, and tries to find statistical evidence of correlations [8, 26, 27]. Figure 2.4 shows 2-dimensional correlation patterns observed for a commonly used random number generator. The data were obtained by assigning consecutive pairs as (x, y) coordinates. The generator employed for this figure is a linear congruential multiplicative generator used in the radiation transport computer code EGS4. In this work, 2-dimensional spectral tests were used to uncover possible sequence correlations.

2.4.2 Algorithms for random number generation

Random number generators provided as intrinsic functions in compilers are attractive because they are potentially portable and often, highly efficient. However, in most languages, the actual generator used is not defined by the standard and is therefore, compiler-dependent. For example, current versions of Digital Fortran 90 use a random number generator proposed by L'Ecuyer [25], based on the combination of two multiplicative congruential generators with total period of 10^{18} (see Figure 2.5 on page 57).

Current versions of IBM xlf90 use a single multiplicative congruential generator known to have good quality but with a period of only 10^9 . Other compilers (i.e., Silicon Graphics) use a lagged-Fibonacci generator with long period and good quality. Some generators depend on existing routines from previous versions of Fortran or C compilers, which vary in quality, some of them known as bad [19].

2.4.3 DETECT-II random number generator

DETECT-II uses a very-long period (10^{43}) generator based on the lagged-Fibonacci series method, proposed by Marsaglia and Zaman [31]. The implementation is a modification by James [20] that returns a vector of random numbers per call. Figure 2.6 shows that no 2-dimensional correlations are apparent for this generator. Compiling and generating up to 500 random numbers yields the same sequence in 32 and 64-bit architectures. In addition, this generator employs a trivial technique for computing non-overlapping subsequences, although lack of correlation between these has not yet been proved (James F., oral communication, 1996).

2.5 Modeling of display devices

DETECT-II has been specially adapted to model optical transport processes in display devices. In this Section, we focus on the description of the emissive structures, and the special binning of photon histories for display simulation. Another important aspect of the code is the interpretation of the Monte Carlo results in terms of display performance. Lastly, we concentrate on the analysis of the luminance spread function that is later related in Chapter IV to experimental results.

2.5.1 Emissive structure models

Basic emissive structures are modeled with DETECT-II as slabs with surface conditions reflecting different design approaches. Of particular importance is the description of the cathodoluminescent phosphor. Initially, the phosphor layer was modeled by a 90% Lambertian reflective surface that included the reflection from the Al film (as depicted in Figure 2.7). However, careful examination of the phosphor-glass interface confirms the presence of regions with glass-to-vacuum, and glass-to-

binder physical contact. A single uniform vacuum layer between the phosphor and the faceplate is not appropriate since it may result in excessive light channeling.

We therefore introduced a phosphor-binder layer with surface roughness, that depicts the change in index of refraction from the glass (1.523) to a material with an intermediate index (1.3) to accommodate for the interfaces with binder and phosphor grains. The roughness of the inner surface of the faceplate is described using the rough surface scattering description presented in Section 2.3.2. Roughness profiles are defined by the maximum angle that the sampling procedure accepts^{||}. A phosphor layer with a 99% diffuse reflectance at the Al film is shown in Figure 2.7. Using partial absorption at the phosphor emissive surface, black matrix designs are easily described.

2.5.2 Binning for display simulation

An important aspect of DETECT-II is a method for binning results which is designed specifically for display simulations that make efficient use of the photon histories. In DETECT-II, the Monte Carlo results are binned within a given solid angle Ω into radial bins (see Figure 2.8 on page 58). To simulate display performance, the viewer is assumed to observe the image from a direction normal to the display surface. Photons are tracked from the source to the front surface of the display and those within a finite solid angle about the normal are binned into discrete regions on the surface. A solid angle corresponding to a 6° cone is used rather than the typical small solid angle of a human observer. The binning of the emerging position is done by back-projecting the light path to a virtual plane of emission. This accounts for the difference in index of refraction between air and glass, and allows binning from a large solid angle to a common virtual focal plane inside the emissive structure. This

^{||}A maximum angle of 0° is equivalent to a smooth surface.

manner of binning photon histories is equivalent to the actual detection of light rays by the human eye, but with a larger solid angle that improves the efficiency of the computations.

2.5.3 The discrete spread function

To specifically describe the performance of display devices with respect to veiling glare, the binning of the Monte Carlo results into a discrete response function N_i is useful**. The resulting vector is then normalized to 1 by dividing by the total number of photons binned.

The Monte Carlo calculation yields the number of photons, \mathcal{P}_0 , that originate from the source point and are observed within the solid angle of the observer. The source is placed at the front of the phosphor layer. The initial directional cosines are sampled randomly from a Lambertian distribution function that is typical of light transmitted through a layer with multiple scattering. Secondly, the number of photons observed within the solid angle of the observer that are associated with a point on the emission layer located at a radius between r and $r + \Delta r$ from the source point are binned within N bins out to a distance $N\Delta r$ (\mathcal{P}_i for $i = 1 \dots N$). This is then converted to the differential probability of light emission per steradian per unit area,

$$\mathcal{L}(i) = \frac{dL}{dA} \quad (2.15)$$

$$\mathcal{L}(i) = \frac{\mathcal{P}_i/\mathcal{P}_0}{\pi[(i+1)\Delta r]^2 - (i\Delta r)^2} \quad (2.16)$$

for

$$r = i\Delta r \quad (2.17)$$

**The construction of specific spread functions and their relationship to experimental methods is discussed in Chapters III and IV.

$$i = 1..N, \quad (2.18)$$

where $\mathcal{L}(i)$ is a discrete representation of the continuous luminance point-spread function $L(r)$. $L(r)$ can be interpreted as the observed luminance in cd/m^2 resulting from a point source located at the origin of the emissive surface with a luminous intensity of 1 cd.

For each run, statistics on angular emission, photon path lengths, photon energy, and scattering events are also reported. In addition, 2-dimensional plots of photon paths can be obtained for detailed analysis of particular emissive structure configurations.

2.5.4 Display reflectance modeling

To simulate display reflections, the same geometric descriptions used for veiling glare calculations are employed, but with the light source placed outside the emissive structure according to arbitrary spatial distribution functions. For simulation of diffuse reflections, we used a distributed uniform planar source with isotropic angular distribution function located in proximity to the display faceplate. Details on the modeling of devices for simulation of ambient light reflections and their relationships with the experimental measurements are given in Chapter V.

2.6 Figures

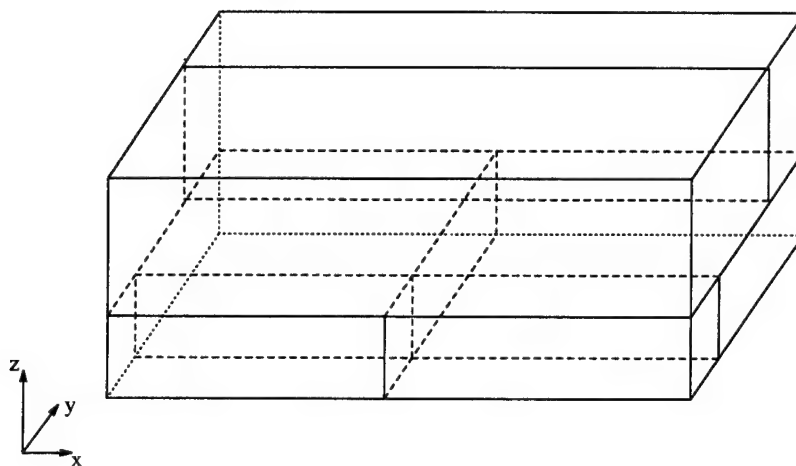


Figure 2.1: Cartesian geometry for the Monte Carlo code DETECT-II.

- Read user-defined data and set up the case
 - geometry (`geometry.in`)
 - material properties (`material.in`)
 - surface types (`surface.in`)
 - run parameters (`input.in`)
 - * number of histories and other MC parameters
 - * source characteristics
 - * surface types parameters
 - * binning and reporting options
- Loop over number of histories
 - start a new photon from the source
 - loop over number of events
 - * locate cell numbers
 - * determine distance to boundary
 - * determine distance to collision
 - * if collision occurred,
 - determine collision type and outcome
 - cycle over events
 - * if collision did not occurred,
 - advance photon position
 - perform boundary analysis
 - kill photons that exit volume
 - tally and bin
 - if not yet successful, update cell numbers
- Report results

Figure 2.2: DETECT-II pseudo-code depicting the tracking of single photons.

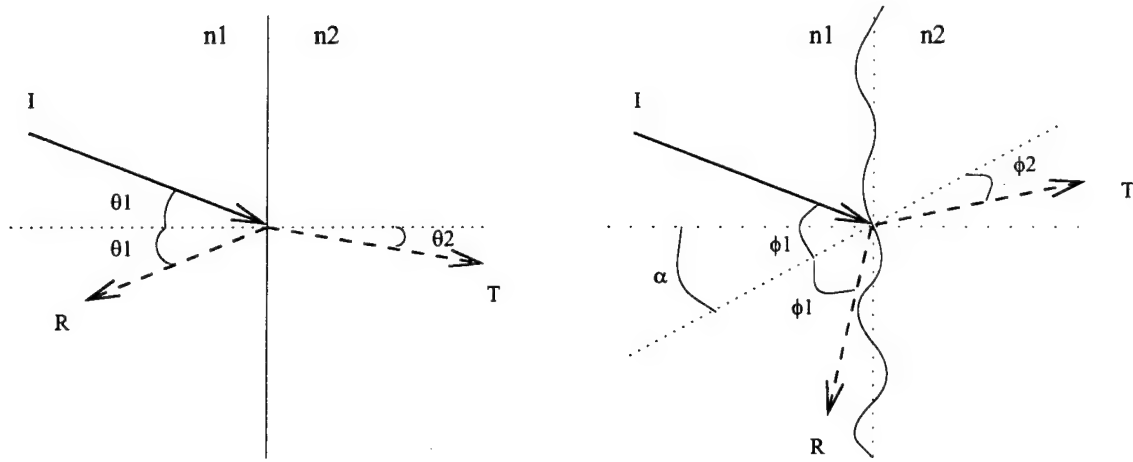
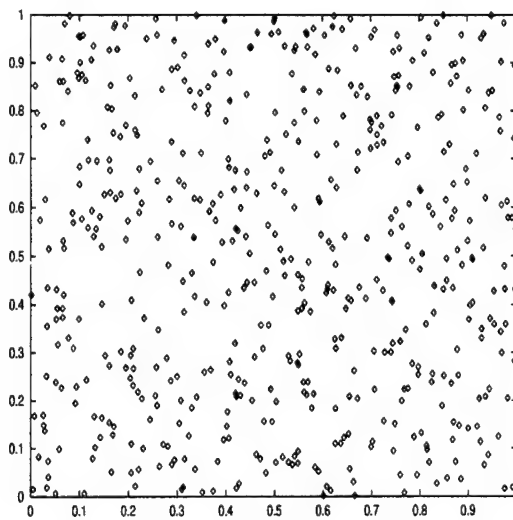
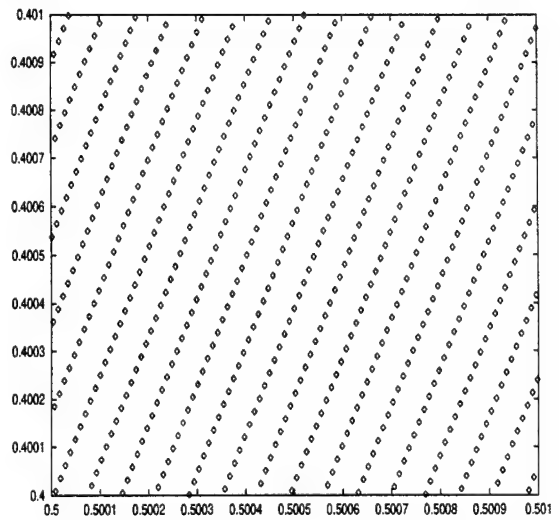


Figure 2.3: Two-dimensional representation of the rough surface model. θ_1 and θ_2 are given by Snell's law. On the left, the flat surface case is depicted. The surface normal is rotated an angle α on the right. After the boundary analysis is performed in the rotated system, T or R are expressed in the original coordinate system.



(a) $0 < x < 1, 0 < y < 1$



(b) $0.500 < x < 0.501, 0.400 < y < 0.401$

Figure 2.4: Two-dimensional spectral test for a linear congruential multiplicative generator (modified EGS4). The correlation patterns have 538 points each.

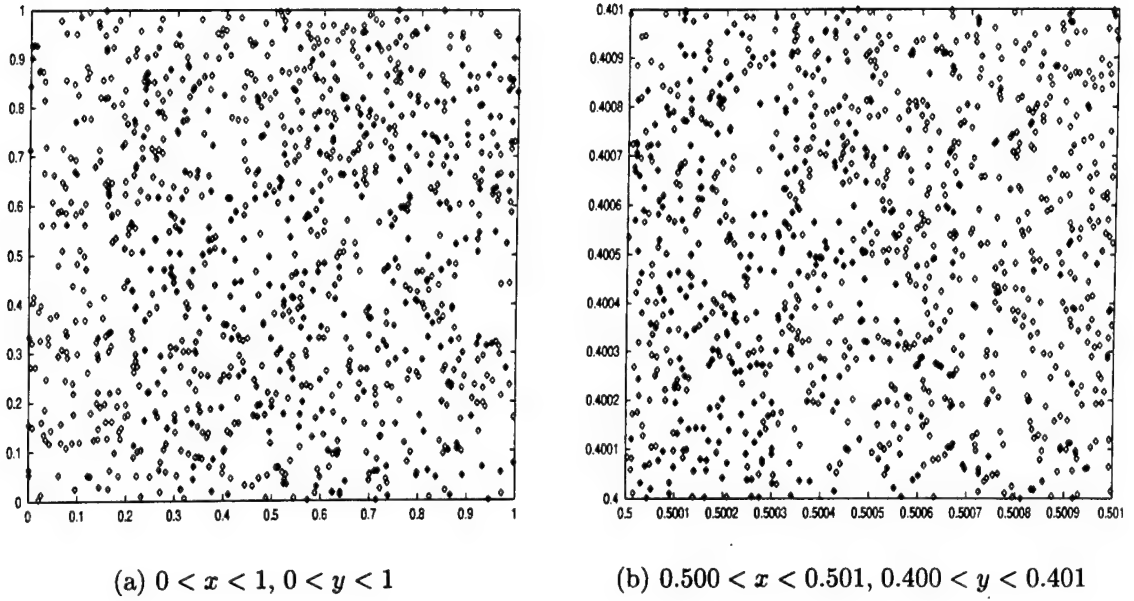


Figure 2.5: Two-dimensional spectral test for L'Ecuyer generator in the Digital Fortran 90. The correlation patterns have 1036 points each.

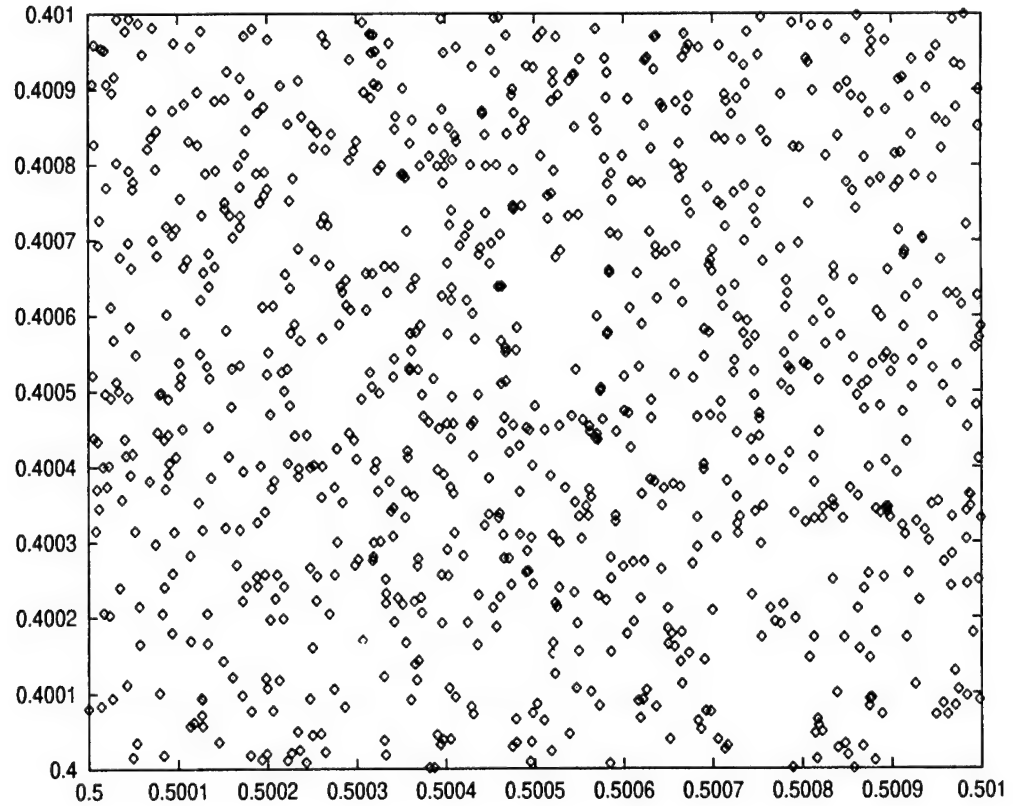


Figure 2.6: Two-dimensional correlations in the random number generator implemented in DETECT-II.

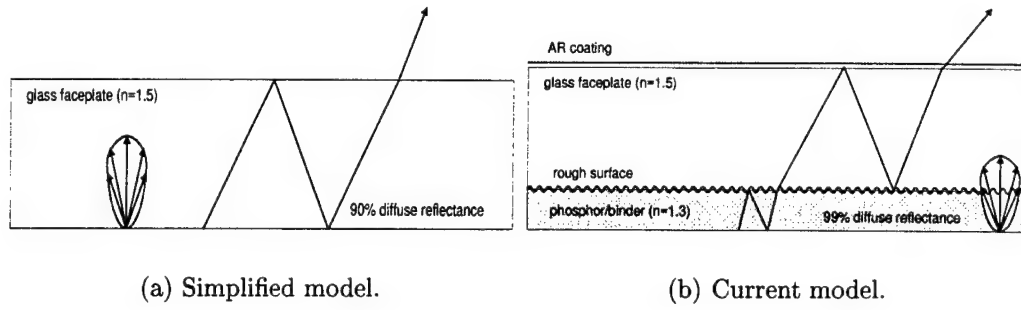


Figure 2.7: Cross-section of the geometric models used in this work.

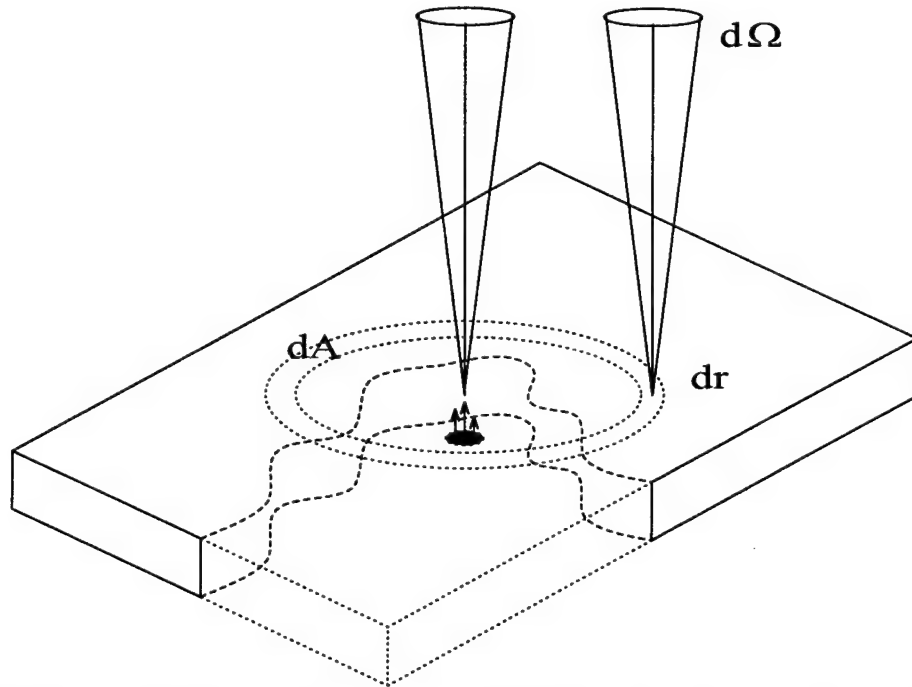


Figure 2.8: Binning of Monte Carlo results for display applications. Light photons exiting within a given solid angle Ω are binned into rings and the results expressed as $p(r)drd\Omega$, or as $p(r)dAd\Omega$.

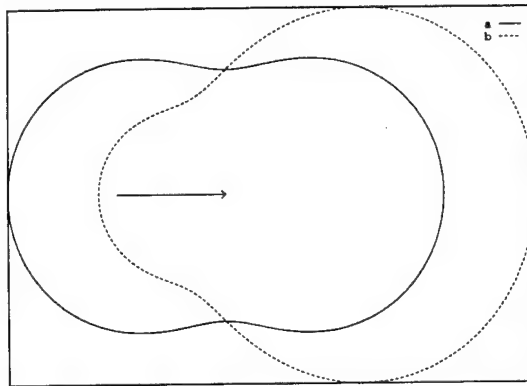


Figure 2.9: Angular dependency in Mie scattering. (a) Rayleigh limit for small spheres. (b) Mie distribution for spherical gold particles of about $0.080\ \mu\text{m}$ for a wavelength of $550\ \text{nm}$, adapted from [2].

2.7 References

1. S. Bianchi, A. Ferrara, and C. Giovanardi. Monte Carlo simulations of dusty spiral galaxies: extinction and polarization properties. *Astrophysical Journal*, 465:127-144, July 1996.
2. M. Born and E. Wolf. *Principles of optics*. Pergamon Press, 3rd. revised edition, 1965.
3. C. Carrier and R. Lecomte. Effect of geometrical modifications and crystal defects on light collection in ideal rectangular parallelepipedic BGO scintillators. *Nuclear Instruments and Methods in Physics Research*, A294:355-364, 1990.
4. R. Chakarova. Monte Carlo study of light transport in scintillating fibers. *Nuclear Instruments and Methods in Physics Research*, A364:90-94, 1995.
5. C.-J. Chen, A. Lien, and M. I. Nathan. 4 x 4 and 2 x 2 matrix formulations for the optics in stratified and biaxial media. *Journal of the Optical Society of America A*, 14(11):3125-3134, November 1997.
6. J. Chen, P. J. Bos, D. R. Bryant, et al. Four-domain TN-LCD fabricated by reverse rubbing or double evaporation. *Proceedings of the Society for Information Display*, pages 868-868, 1995.
7. J. Chen, P. J. Bos, J. R. Kelly, et al. Optical simulation of electro-optical performance of low- δ nd multi-domain TN displays. *Proceedings of the Society for Information Display*, pages 937-940, 1997.
8. Chiang-Kao and J. Y. Wong. Random number generators with long period and sound statistical properties. *Computers & Mathematics with Applications*, 36(3):113-121, 1998.
9. R. A. Chipman. Polarization analysis of optical systems. *Optical Engineering*, 28(2):90-99, 1989.
10. R. A. Chipman. Mechanics of polarization ray tracing. *Optical Engineering*, 34(6):1636-1645, 1995.
11. U. Fano. Description of states in quantum mechanics by density matrix and operator techniques. *Reviews of Modern Physics*, 29(1):74-93, January 1957.
12. A. M. Ferrenberg, D. P. Landau, and Y. J. Wang. Monte carlo simulations: hidden errors from 'good' random number generators. *Physical Review Letters*, 69:3382, 1992.
13. M. Firbank, S. R. Arridge, M. Schweiger, et al. An investigation of light transport through scattering bodies with non-scattering regions. *Physics in Medicine and Biology*, 41:767-783, 1996.
14. E. B. Gindele, B. R. Gandhi, and S. L. Shaffer. A non-linear CRT system simulation model. *Proceedings of the Society for Information Display*, pages 785-788, 1990.
15. E. B. Gindele and S. L. Shaffer. A physical optics CRT faceplate halation model. *Proceedings of the Society for Information Display*, pages 446-450, 1991.

16. A. S. Glassner. *An Introduction to ray tracing*. Academic Press, 1989.
17. Y. Govaerts. Modeling the scattering of light in three-dimensional canopies: contribution of a Monte Carlo ray tracing approach. In *Second Topical Symposium on Combined Optical-Microwave Earth and Atmosphere Sensing*, pages 31–4. IEEE Microwave Theory & Tech. Soc., April 1995.
18. J. Haisma, J. H. Pasman, J. M. Pasmans, et al. Wide-spectrum tint-free reflection reduction of viewing screens. *Applied Optics*, 24:2679–2686, August 1985.
19. K. G. Hamilton. Pseudorandom number generators for personal computers. *Computer Physics Communications*, 75:105–117, 1993.
20. F. James. A review of pseudorandom number generators. *Computer Physics Communications*, 60:329–344, 1990.
21. R. C. Jones. A new calculus for the treatment of optical systems. *Journal of the Optical Society of America*, 46:126–131, 1956.
22. M. Kerker. *The scattering of light*. Academic Press, 1969.
23. G. Kiel. Design principles of fluorescence radiation converters. *Nuclear Instruments and Methods*, 87:111–123, 1970.
24. G. F. Knoll and T. F. Knoll. Light collection in scintillation detector composites for neutron detection. *IEEE Transactions on Nuclear Science*, 35(1):872–875, July 1988.
25. P. L'Ecuyer. Efficient and portable combined random number generators. *Communications of the ACM*, 31, June 1988.
26. P. L'Ecuyer. Testing random number generators. In *1992 Winter Simulation Conference*, pages 305–313. IEEE, December 1992.
27. P. L'Ecuyer. Bad lattice structures for vectors of nonsuccessive values produced by some linear recurrences. *Journal on Computing*, 9(1):57–60, 1997.
28. C. Lo, B. J. Palmer, M. K. Drost, and J. R. Welty. Incorporation of polarization effects in Monte Carlo simulations of radiative heat transfer. *Numerical Heat Transfer, Part A*, 27:129–142, 1995.
29. J. Makino. On the structure of parallelized random number sources. *Computer Physics Communications*, 78:105–112, 1993.
30. J. D. Maltby and P. J. Burns. Performance, accuracy, and convergence in a three-dimensional Monte Carlo radiative heat transfer simulation. *Numerical Heat Transfer, Part B*, 19:191–209, 1991.
31. G. Marsaglia, A. Zaman, and W.W. Tsang. Toward a universal random number generator. *Statistics and Probability Letters*, 8:35–39, 1990.
32. M. Mascagni, S. A. Cuccaro, D. V. Pryor, et al. A fast, high quality, and reproducible parallel lagged-fibonacci pseudorandom number generator. *Journal of Computational Physics*, 119:211–219, 1995.

33. G. J. McCallum and J. Vervier. *Scintillation Spectroscopy*, chapter Detectors sensitive to gamma ray polarization, pages 183–253. Gordon and Beach Science, 1967.
34. W. H. McMaster. Matrix representation of polarization. *Reviews of Modern Physics*, 33(1):9–29, January 1961.
35. T. Mertelmeier and T. E. Kocher. Monitor simulations for the optimization of medical soft-copies. *Proceedings of the SPIE*, 2707:322–333, 1996.
36. E. Muka, T. Mertelmeier, and R. M. Slone. Impact of phosphor luminance noise on the specification of high-resolution CRT displays for medical imaging. *Proceedings of the SPIE*, 3031, 1997.
37. V. Nagirnyi, A. Stolovich, S. Zazubivich, et al. Peculiarities of the triplet relaxed excited-state structure and luminescence of a CsI:Tl crystal. *Journal of Physics: Condensed Matter*, 7:3637–53, May 1995.
38. V. Nagirnyi, S. Zazubivich, V. Zepelin, et al. A new model for the visible emission of the CsI:Tl crystal. *Chemical Physics Letters*, 4-5:533–8, September 1994.
39. Y. Ono, Y. Ohtani, K. Hiratsuka, et al. A new antireflective and antistatic double-layered coating for CRTs. *Proceedings of the Society for Information Display*, 1992.
40. T. Oyama, H. Ohsaki, Y. Hayashi, and Y. Tachibana. A new layer system for wideband anti-reflection coatings designed for CRTs. *Proceedings of the Society for Information Display*, pages 262–265, 1998.
41. T. Radcliffe, G. Barnea, B. Wowk, et al. Monte Carlo optimization of metal/phosphor screens at megavoltage energies. *Medical Physics*, 20(4):1161–9, 1993.
42. P. Schauer and R. Autrata. Light transport in single-crystal scintillation detectors in SEM. *Scanning*, 14:325–333, 1992.
43. F. Schmid and N. B. Wilding. Errors in Monte Carlo simulations using shift register random number generators. *International Journal of Modern Physics*, 6C(6):781–787, 1995.
44. R. Schweitzer, J. McHugh, P. J. Burns, and C. Zeeb. Daylighting design via Monte Carlo with a corresponding scientific visualization. In *SUPERCOMPUTING '93*, pages 250–9. IEEE Comput. Soc. Press, November 1993.
45. H. S. Tong and G. Prando. Hygroscopic ion-induced antiglare/antistatic coating for CRT applications. *Proceedings of the Society for Information Display*, 1992.
46. J. D. Trolinger, R. A. Chipman, and D. K. Wilson. Polarization ray tracing in birefringent media. *Optical Engineering*, 30(4):461–465, 1991.
47. N. V. Voshchinnikov, V. P. Grinin, and V. V. Karjukin. Monte Carlo simulation of light scattering in the envelopes of young stars. *Astronomy and Astrophysics*, 294:547–554, 1995.
48. E. Waluschka. Polarization ray trace. *Optical Engineering*, 28(2):86–89, 1989.
49. A. Wightman. Note on polarization effects in Compton scattering. *Physical Review*, 74(12):1813–1817, December 1948.

50. S. J. Wilderman. *Vectorized algorithms for Monte Carlo simulation of kilovolt electron and photon transport*. PhD thesis, University of Michigan, 1990.
51. B. Witzigmann, P. Regli, and W. Fichtner. Rigorous electromagnetic simulation of liquid crystal displays. *Journal of the Optical Society of America A*, 15(3):753–7, 1998.
52. L. B. Wolff and D. J. Kurlander. Ray tracing with polarization parameters. *IEEE Transactions on Computer Graphics and Applications*, pages 44–55, November 1990.

CHAPTER III

A METHOD FOR MEASURING VEILING GLARE IN HIGH PERFORMANCE DISPLAY DEVICES

3.1 Introduction

There is a significant need to improve the performance of display devices in high fidelity applications such as medical imaging, graphic arts, and industrial inspection. A wide luminance range (5-1,000 cd/m²) with minimal image quality degradation due to luminance spread is required for low contrast details to be visible. However, the image quality of electronic display devices is often limited by extensive veiling glare that causes a low-frequency degradation resulting in contrast reduction. In cathode-ray tubes (CRTs), veiling glare is caused by multiple light scattering in the thick glass faceplate [10], by backscattered electrons in the vacuum tube [8,11,19,20], and by light leakage through non-uniformities in the reflective coatings. New flat panel technologies employing discrete pixel designs generally have less veiling glare than CRT devices. Veiling glare has otherwise been studied in other components of the imaging chain, such as for detectors [6,7,16,21] and lenses [12], and for the human eye [2,17].

Several groups have suggested that the veiling glare characteristics of display

devices be measured using test patterns with rectangular fields of different sizes at low luminance surrounded by bright regions [3,8]. However, the radial symmetry of the veiling glare processes suggests that a test pattern with circular targets is more appropriate. In this work, we define a luminance point spread function with radial dependency and use this function as a basis for performing experimental measurements using circular test patterns.

For measuring veiling glare in high performance display devices, a luminance probe and detector capable of measuring very low luminance values in a small dark region surrounded by a large bright field are required. However, multiple light reflections in detector optics can substantially alter the measured low luminance value in the dark spot. The measurement error amounts to 1-3% of the bright field intensity [12] for low-flare lenses with anti-reflective coatings. When measuring a test pattern for which the bright field luminance is 500 times the dark spot luminance (i.e., a contrast ratio of 500), the measured contrast ratio will only be 83 if the detector records 1% of the bright field in the dark region. For veiling glare measurements this light leakage should be less than 0.01%, which results in a contrast ratio of 476 for the preceding example.

In this work, we describe a collimated probe that minimizes contamination from very bright neighboring regions. The probe has been specifically designed to measure veiling glare using a test pattern with a circular dark spot of varying diameter. Details pertaining to the optical design and construction of the probe are reported. By measuring test patterns digitally printed on radiographic film, the response attributes of the detection assembly have been established. Finally, the method is demonstrated by measuring the veiling glare characteristics of a monochrome medical imaging CRT.

3.2 Analytic model for veiling glare

The contrast degradation caused by veiling glare can be described by a normalized continuous point spread function $P(r, \theta)^\dagger$. This function describes the luminance (cd/m^2) at (r, θ) resulting from a point source of light with unit intensity, 1 cd, located at $r = 0$. The units of the point spread function, $P(r, \theta)$, are thus m^{-2} . It is useful to assume that $P(r, \theta)$ is shift-invariant and radially symmetric, $P(r)$. The veiling glare, $L_g(x, y)$, produced in a display by an image with a primary luminance of $I(x, y)$ can then be estimated using a convolution integral:

$$L_g(x, y) + I(x, y) = \iint I(x', y') P(r') dx' dy' , \quad (3.1)$$

where $r' = \sqrt{(x - x')^2 + (y - y')^2}$, and both $L_g(x, y)$ and $I(x, y)$ have units of cd/m^2 . Our use of the point spread function is equivalent to classical definitions [15], although the function is typically used to describe short range blur associated with resolution and not the long range processes associated with veiling glare [16].

To model test patterns consisting of a black circular region surrounded by a circular region of uniform luminance, I_o , it is useful to define the ring response function, $R(r)$, as:

$$R(r) = \int_0^{2\pi} P(r, \theta) r d\theta = 2\pi r P(r) , \quad (3.2)$$

where $R(r)$ has units of m^{-1} . This function describes the luminance at $(0, 0)$, in cd/m^2 , produced by an infinitely thin ring source of light having a total intensity of 1 cd distributed uniformly over a distance of $2\pi r$. The luminance in the center of the dark spot is then given by:

$$L_g = L_g(0, 0) = I_o \int_{r_d}^{r_l} R(r) dr , \quad (3.3)$$

[†]In principle, $P(r, \theta)$ may also have a wavelength dependence associated with light transport processes. This is particularly true when anti-reflection coatings or tinted optical components are used. In this work, we address only monochromatic devices and ignore any wavelength dependency.

where r_d is the radius of the black circle and r_l is the radius of the luminous surrounding region.

In this work, we define the veiling glare ratio (G) as I_o/L_g , a function that depends on the two radii associated with the test pattern, $G(r_d, r_l)$. In practice, we have considered the dependence of G on r_d when r_l is constant, $G(r_d)$. If experimental measurements are made with a set of test patterns having black disks of varying radius, r_i where $i = 1, 2, \dots, n$, and the same radius r_l for the luminous region (see Figure 3.1 on page 78), the measured set of glare ratios, G_i , provides information describing both the short and long range characteristics of veiling glare. Notably, two measurements with different black circles can easily be related to the integration of the ring response function between the two different radii of the black circles:

$$\frac{1}{G_i} - \frac{1}{G_{i+1}} = \int_{r_i}^{r_{i+1}} R(r) dr. \quad (3.4)$$

If $R(r)$ is slowly varying over this range of radii, we can use this expression to numerically estimate $R(r)$ from a full set of measurements of G_i .

3.3 A collimated probe and luminance detector

To determine the veiling glare ratio of a display device, the luminance from small circular dark spots needs to be accurately measured. To develop a luminance probe with minimal response from surrounding bright regions, a collimated design with multiple baffles was employed. The device is based on a high-gain Si photodiode sensor with an active area of about 5.7×5.7 mm, a photopic filter, and a research radiometer (SHD 033 sensor, IL 1700 radiometer, International Light Inc.). A standard barrel (4 cm diameter and 7 cm long) into which baffles can be positioned using threaded parts is attached to the sensor. A conic probe fabricated on a lathe

from aluminum rod is placed at the end of this barrel. The assembled components are shown in Figure 3.2.

The probe tip is designed to minimize the amount of light scattered from the probe back to the emissive structure. As shown in Figure 3.3, the probe entrance aperture has a diameter of 9 mm. The interior of the tip is shaped with a reverse cone geometry creating a pointed entrance aperture. The inclination of the interior walls of the inner tip minimizes the amount of light reflecting back to the display faceplate. The external conic shape of the probe reflects light coming from bright regions away from the display surface. An angle between the walls of the cone and the display surface normal of 15° allows central measurements in 38 cm diagonal displays.

The surface characteristics of the first few millimeters of internal wall of the probe tip was thought to have a major impact on the reduction of scattered light that contaminate dark spot measurements. For this reason, both highly reflective and diffuse absorptive surface finishings were evaluated. The comparison showed that a highly specular surface at the inside front end resulted in a lower dark spot luminance. The specular surface was realized by polishing about 3 mm of the interior wall of the tip with very fine grit polishing paper.

Light entering the probe at oblique angles is trapped by a series of interior baffles and probe chambers. A series of four apertures of about 4 mm diameter creates a highly collimated response. Baffle positions and aperture diameters were determined using manual design methods. Figure 3.4 shows drawings that illustrate three aspects of the optical design. The principal rays that define the detector active area are depicted in Figure 3.4(a). The detector is directly exposed to only a portion of the back surface of each aperture as shown in Figure 3.4(b). Each aperture is very

thin to reduce light scattering from the edges. Light entering at oblique angles, Figure 3.4(c), is reflected off the interior walls of the probe that are not viewed by the detector. Significant signal contamination is prevented by the large number of scattering events from absorptive surfaces required to reach the detector through the multiple apertures.

The probe assembly was accomplished by a sequential procedure of painting and aperture bonding for each of four chambers. All interior walls except for the reversed conic tip are coated with a black absorptive paint (KRYLON, Ultra Flat Black 1602) to effectively dampen light reflected inside the probe. Interior baffle apertures were fabricated by attaching small, thin perforated disks of black anodized aluminum on either machined ledges in the conical end or on standard aperture holders screwed into the barrel. The bonding of baffles and apertures was performed using a two-part black epoxy. The specially machined conical end was attached to a standard baffle which in turn was attached to the end of the barrel. Finally, the external surface was polished and black anodized to provide a specular absorptive surface.

All apertures were originally made with the same diameter (4 mm). However, when the probe was initially assembled, apparent light diffraction was observed by looking at a small dark spot in a bright field with the eye in the position of the sensor. It was determined that scattering from the edge of the first aperture was responsible for the interference pattern. This effect was successfully eliminated by slightly increasing the diameter of the first aperture to 4.1 mm.

3.4 Experimental methods

In this Section, we describe the experimental methods used to test the performance of the proposed method to measure veiling glare in display devices. Correction

factors are introduced by using opaque dark spots, and spots of known luminance with negligible veiling glare. The novel method introduced in this work is investigated using data taken for a display device with no veiling glare. Finally, the application of this method for a monochrome CRT is described.

3.4.1 Probe response versus spot diameter

The response characteristics of the probe can be determined by measuring the luminous signal from test patterns having an opaque spot which emulated a device with no veiling glare. For dark spot diameters smaller than the field of view of the probe, the measured luminance is associated with direct light striking the detector. For larger diameters, the luminance is caused by scattered light originating in the bright regions that enters the probe after multiple reflections. It is this contamination in the signal that limits the performance of the method. The amount of signal contamination for this probe is a function of both the dark spot radius (r_d) and the distance between the probe and the emissive surface (d).

To characterize the performance of the proposed method, veiling glare test patterns having a 320 mm diameter bright circular field with varying dark spot diameters were printed on 35×43 cm transparent Estar film with a laser printer (KODAK Ektascan, model XLP). The transilluminated patterns do not suffer degradation of image quality by veiling glare. Much light scattering occurs in the film emulsion, but is locally confined to the thin emulsion containing absorptive grains that modulate luminance. The optical density in the dark circles was supplemented with black absorptive paper glued to the film back side to obtain negligible transmittance through the spot.

The test patterns were back-illuminated in a dark room with a fluorescent lamp

illuminator used for viewing radiographic film. The maximum luminance in the bright field of the test patterns was about 2,040 cd/m². Black velvet was used to cover the detector assembly to shield the films from reflections coming from objects in the room. Measurements were performed for values of r_d from 0 to 10 mm, and distances d of 2, 10, and 20 mm. A correction factor was then computed as a bivariate function $\zeta(r_d, d)$, expressed as a fraction of the bright field intensity.

The correction factor ζ represents the dark signal contamination due to scattered light. A corrected veiling glare ratio (G_{corr}) can then be computed from measured values (G_{meas}) as follows,

$$G_{corr}(r_d, d) = G_{meas}(r_d, d) \frac{1}{1 - \zeta(r_d, d)G_{meas}(r_d, d)}. \quad (3.5)$$

Using this expression, a criteria for the application of the correction can be established. For example, for a device capable of a contrast ratio of 300, a maximum correction of 1% due to light leakage is obtained for ζ less than 3.3×10^{-5} .

3.4.2 Measurements for a display with no veiling glare

The same test patterns used in the performance characterization experiment were utilized to understand how the proposed method performs when measuring veiling glare ratios in a test environment similar to a display device with no glare and low luminance. In this case, no additional absorption was employed in the dark target resulting in a film transmission of about 0.003. The transmission of the dark spot was determined by measuring the relative signal using a bright view-box masked with black absorptive paper with a centered hole of about 3 mm in diameter. The transmission $T_d(d)$ was computed as the ratio of the luminous signal when the hole was centered in the dark spot, to the signal for the same test pattern with no dark circular spot (i.e., a full bright circular field). Although the printing parameters

were identical, the transmission values for film patterns with different dark spot diameter varied due to variations in film development conditions. The luminous signal resulting from the transmission through the film was subtracted from the measured luminance to estimate the veiling glare (L_g).

To simulate display devices, the luminance in the bright region of the test patterns was reduced to be similar to the luminance found in high performance monitors. A film with uniform optical density was placed inside the illuminator between the lamps and the diffuser to obtain a bright field luminance of 170 cd/m². Measurements were performed with test patterns having dark spot radii varying from 4 to 80 mm. The measurements were intentionally made at distances different than those used to measure the light leakage correction (i.e., 5 and 15 mm versus 2, 10, and 20 mm).

3.4.3 Measurements for a monochrome CRT

To illustrate the application of the method for devices having veiling glare, measurements were performed for a monochrome medical imaging CRT (Image Systems, 24 inches diagonal, model M24L). Test patterns with varying spot diameter were displayed as images with 1000×1000 pixels (see Figure 3.1 on page 78). With the contrast control set to the maximum level, the monitor brightness control was increased from the minimum level until the full dark field luminance was greater than the value observed with the unit disconnected. The brightness was then slightly reduced from this point, and the luminance of a full black field recorded (L_d). The veiling glare measurements were made with the entrance of the photopic probe at about 1 mm from the surface of the display. The distance d was determined by adding the distance between the probe tip to an estimate of the faceplate thickness based on laser reflection measurements. The thickness was measured to be 13 mm

resulting in a total distance d of 14 mm. Measurements were performed with test patterns of many radii varying from 4 to 160 mm.

3.5 Results

In this Section, we present the results obtained for perfectly dark spots, for spots with known luminance, and finally, for a medical imaging monochrome CRT.

3.5.1 Probe response versus spot diameter

Figure 3.5 depicts the light leakage in test patterns with perfectly black spots measured at distances of 2, 10 and 20 mm. The measured data points are expressed as a fraction of the measured signal for a uniformly bright field. The recorded measurements for small radii define the collimated region of direct path light response with a width of 10% of the maximum equal to 2.5 to 3.5 mm radius. For values of the correction factor ranging from about 3×10^{-5} to 10^{-3} , the correction decreases exponentially with increasing spot radius. For a distance of 2 mm, the data asymptotically approaches a value of about 3×10^{-5} . At relative response values of 3×10^{-5} , the noise of the luminance detector measured with the probe aperture blocked was less than 10% of the signal (i.e., 1 pA).

The relative response at large radii represents a correction factor ζ that can be used to adjust the dark luminance values recorded in actual devices according to Equation 3.5. To provide a practical mechanism for computing corrected glare ratios (G_{corr}), a surface fitting was performed for $\zeta(r_d, d)$ for correction factors ranging from 3×10^{-5} to 10^{-3} . A second degree polynomial expression with cross terms was obtained for the logarithmic values of the correction using a least-square fitting technique (MAPLE V, Waterloo Maple Inc.). The polynomial expression used for computing the correction factor is: $\log \zeta(r_d, d) = -0.435 r_d + 0.00339 d^2 - 0.0778 d -$

$$0.00129 r_d d^2 + 0.0371 r_d d - 1.85.$$

Figure 3.6 shows the experimental data points for the measured signal contamination along with the polynomial function $\zeta(r_d, d)$ for the distances d used in the experiment. Data is presented for the region of radii and distances where the function is defined, namely, $3 \times 10^{-5} < r_d < 10^{-3}$, and $3 \text{ mm} < d < 10 \text{ mm}$. The results predicted using Equation 3.5 agree well with the experimental points.

3.5.2 Measurements for a display with no veiling glare

For measurements performed using veiling glare test patterns with known dark spot transmission, the measured dark signal (L_{meas}) was interpreted as

$$L_{meas}(r_d) = L_g(r_d) + [T_d(r_d) + \zeta(r_d, d)]L_b, \quad (3.6)$$

where L_g is the contribution associated with veiling glare, and L_b is the luminance in the uniform bright field. For an ideal detector ($\zeta = 0$) and perfectly black targets ($T_d = 0$), L_{meas} is identical to L_g . In this case, due to negligible veiling glare contribution for radiographic film, and a priori knowledge of the values for $T_d(r_d)$ and $\zeta(r_d, d)$, L_{meas} is expected to be zero and can thus be related to the uncertainty introduced by the method in the estimation of G .

The same relationship described by Equation 3.6 can be expressed in terms of veiling glare ratios as,

$$\frac{1}{G_{corr}(r_d)} = \frac{1}{G_{meas}(r_d)} - T_d(r_d) - \zeta(r_d, d), \quad (3.7)$$

where G_{meas} is the measured uncorrected veiling glare ratio. Again, for a perfect detector and true black spots, G_{meas} is equal to G_{corr} .

Figure 3.7 shows the inverse of the corrected veiling glare ratio, as defined in Equation 3.7, for radiographic film at 5 and 15 mm distance between the probe and

the film surface. For both distances, $1/G$ is within ± 0.00012 for dark spot radii larger than 5 mm. Since these experimental conditions are not expected to have any veiling glare, these results represent the measurement error for the method.

3.5.3 Measurements for a monochrome CRT

For CRT measurements, an equation similar to Equation 3.7 was used to correct for the black luminance:

$$\frac{1}{G_{corr}(r_d)} = \frac{1}{G_{meas}(r_d)} - \frac{L_d}{L_b} - \zeta(r_d, d). \quad (3.8)$$

Figure 3.8 shows the corrected veiling glare ratios for the medical imaging CRT. For a radius of 5 mm, G_{corr} is equal to 130. The data were numerically differentiated according to Equation 3.4. Figure 3.9 shows the computed ring response function $R(r)$. At short distances, $R(r)$ has a plateau with magnitude equal to $5 \times 10^{-4} \text{ mm}^{-1}$. At about a radius of 20 mm, the magnitude drops to about $2 \times 10^{-5} \text{ mm}^{-1}$. This value remains approximately constant up to the large radius measured for this monitor. A small increase in the magnitude of the tail can be observed as the radius increases which suggests that $P(r)$ decreases with less than a $1/r$ dependency (see Equation 3.2 on page 66). The ring response function may also be influenced by the edges in the CRT faceplate that can act as partial reflectors.

3.6 Discussion

The human visual system is very effective at observing images having a very large luminance range. The perception of brightness is generally understood to be logarithmically proportional to luminance [1] and capable of adapting to different average luminance in the observed scene [13, 14]. Additionally, the human visual system performs well when observing the luminance of dark regions surrounded by

bright fields. The very low intrinsic veiling glare of the eye is primarily determined by the retina which has reduced sensitivity to obliquely incident light associated with scattering events in the lens [2,17,18]. A high quality display device thus requires a veiling glare ratio of 400 or more for relatively small dark spots [9].

We have described an experimental method capable of measuring the large veiling glare ratios characteristic of high performance display devices. A luminance probe with very low light leakage has been developed for use with this method. Using this probe, we have demonstrated that measurements of very low luminance in small dark spots can be performed even when the surrounding field is 1,000 times brighter.

The method described is applicable to very small dark spots. The minimum spot diameter that can be measured using this method depends on the distance between the entrance aperture of the probe and the emissive surface due to the imperfect collimation provided by the design. A good approximation for the minimum spot diameter for a given distance d' can be obtained by computing the value of r_d for which $\zeta(r_d, d')$ is equal to 10^{-3} . Minimum dark spot size thus have radii from 3 to 6 mm for measurement distances from 2 to 20 mm.

Using a display device with negligible veiling glare, we have shown for the distances considered that the uncertainty in the method is below 10^{-4} for $1/G$. The method can thus be used for measuring glare ratios up to 10^3 with an error of less than 10%. Furthermore, when this measurement method is applied to construct the ring response function associated with veiling glare (as described in Equation 3.4), the error introduced by the method is small enough to allow features in $R(r)$ to be clearly observed.

Measurement artifacts caused by multiple scattering in lenses prevents their use for measuring veiling glare. Other investigators have used masking techniques (in-

cluding flat and conic black masks) to shield the lens and camera from the bright regions when performing similar measurements [4, 5]. Flat masks perform better when placed adjacent to the emissive surface. For CRT devices, cone masks have proven useful due to the reflection of light away from the thick faceplate.

While the probe and method described in this work were developed to measure veiling glare from light transport processes, contributions to glare from other sources cannot be discriminated. In CRTs, other significant sources are electron backscattering, and frequency response of the drive amplifier.

3.7 Figures

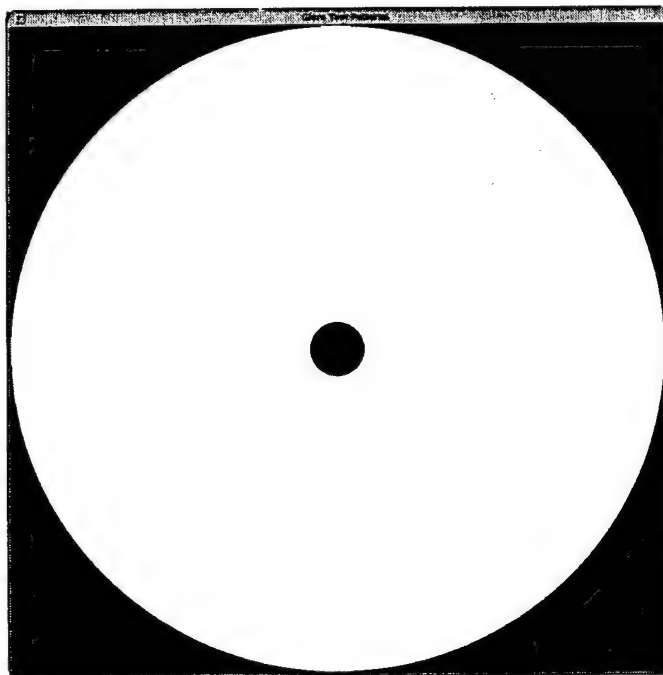


Figure 3.1: Computer graphic patterns for veiling glare. During the measurements, the bright circular field diameter is maintained constant while the dark spot diameter is varying from 0 up to the bright field diameter.

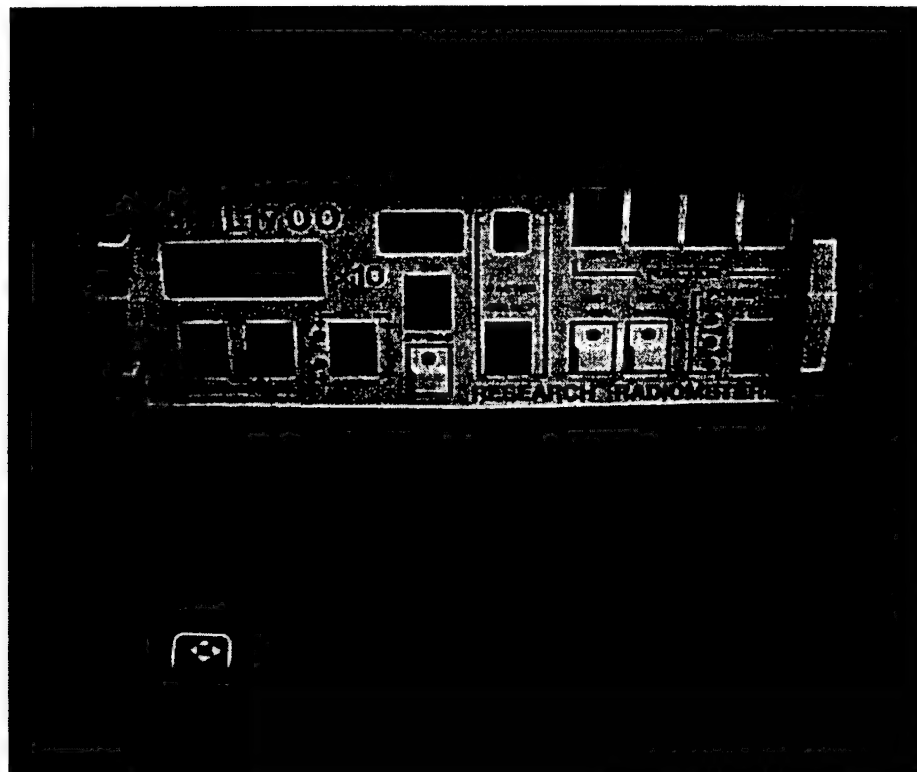


Figure 3.2: Photopic probe and IL 1700 research radiometer for measurements of veiling glare ratio.

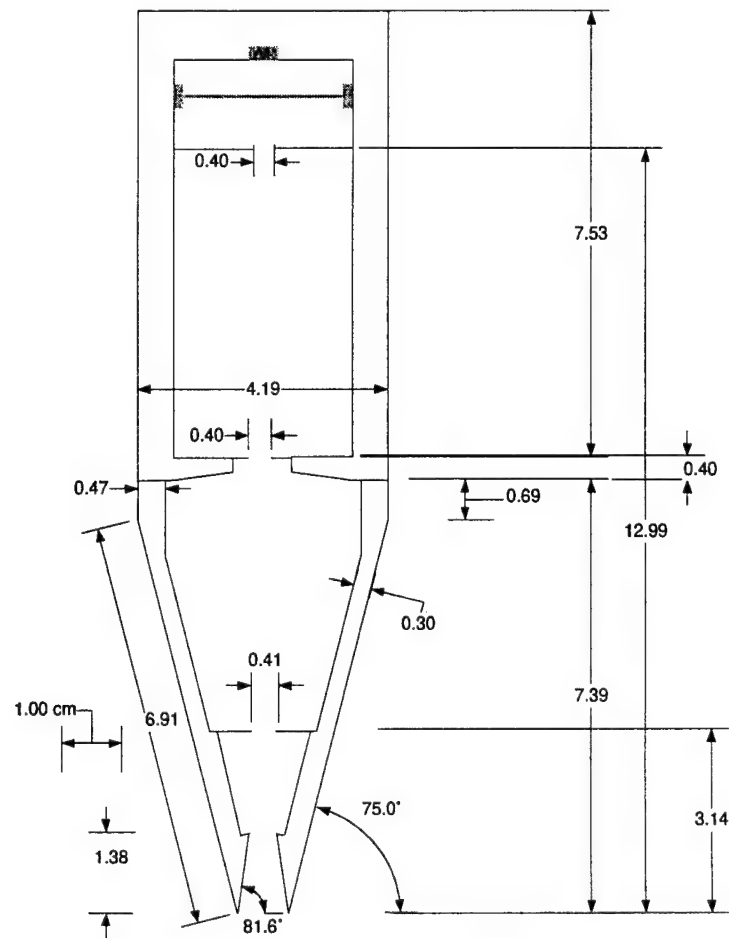


Figure 3.3: Schematic drawing of photopic probe showing dimensions in cm and the relative position of apertures and baffles.

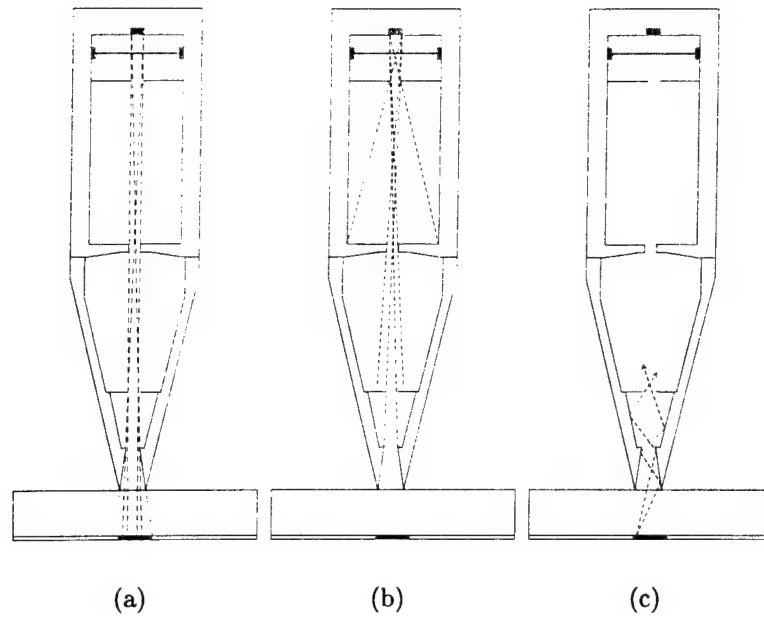


Figure 3.4: Design drawings for the photopic probe showing aspects of the optical design. (a) Principal rays that define the detector direct field of view. (b) Baffle positioning and back surfaces viewed by the detector. (c) Scattered rays absorbed by multiple reflections in the conic probe.

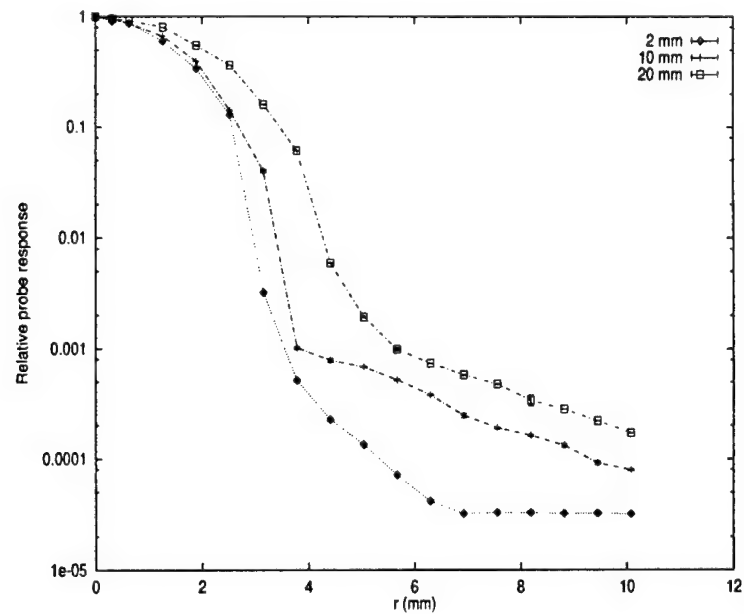


Figure 3.5: Experimentally measured probe response values as a function of the dark spot radius for 2, 10, and 20 mm distance between the tip of the probe and the emissive surface. The factor is expressed as a fraction of the bright region signal. The bright circular region was 320 mm in all cases.

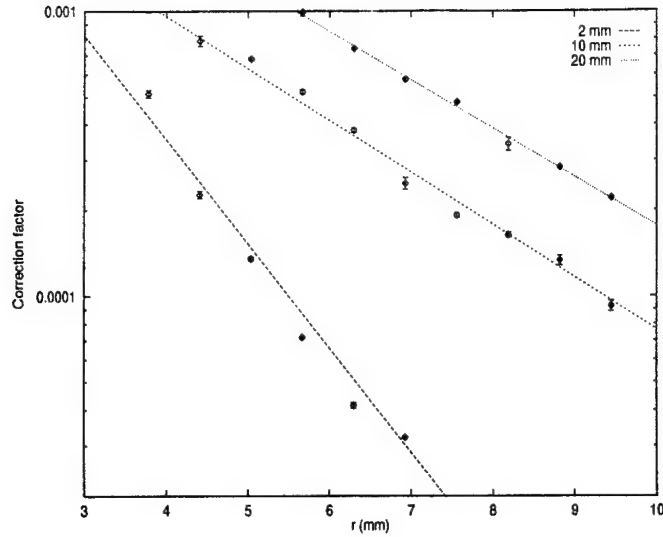


Figure 3.6: Experimental data points plotted along with correction function ζ curves for 2, 10, and 20 mm distance d . The range of values showed represents the area where the function $\zeta(r_d, d)$ is defined, namely, $3 \times 10^{-5} < r_d < 1 \times 10^{-3}$, and $3 \text{ mm} < d < 10 \text{ mm}$. The error bars represent a standard deviation of 20 consecutive measurements recorded at each point with the radiometer.

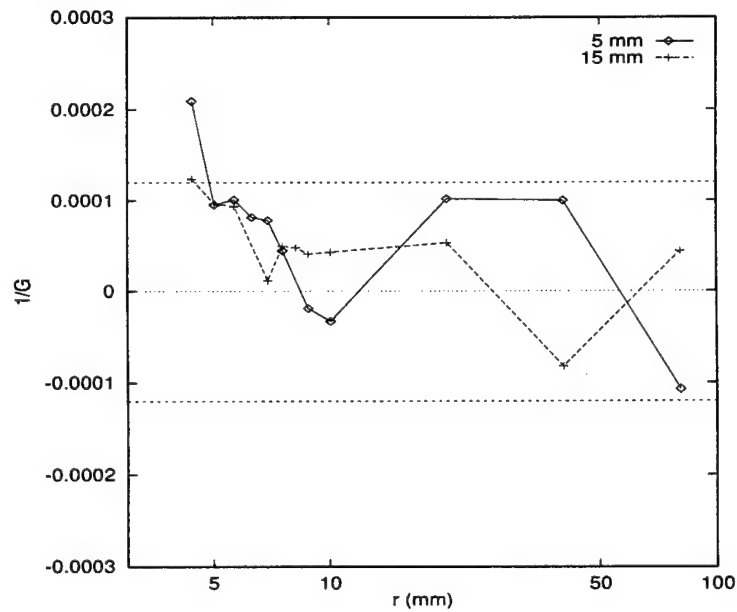


Figure 3.7: Inverse veiling glare ratios measured for test patterns on radiographic film at a distance of 5 and 15 mm distance. The values for $1/G$ were computed by subtracting the known $T_d(r_d)$ and the correction factor ζ (see Equation 3.7) for each dark spot diameter. Due to the negligible veiling glare of radiographic film, the small values of $1/G$ for radii greater than 1 cm relate to the error of the method, i.e., ± 0.00012 for $1/G$.

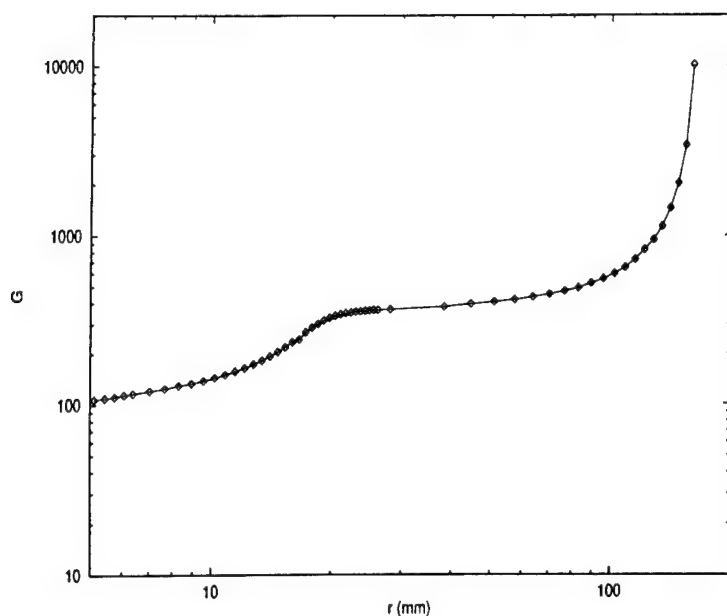


Figure 3.8: Veiling glare ratio for a medical imaging CRT measured at a distance of 1 mm from the faceplate surface.

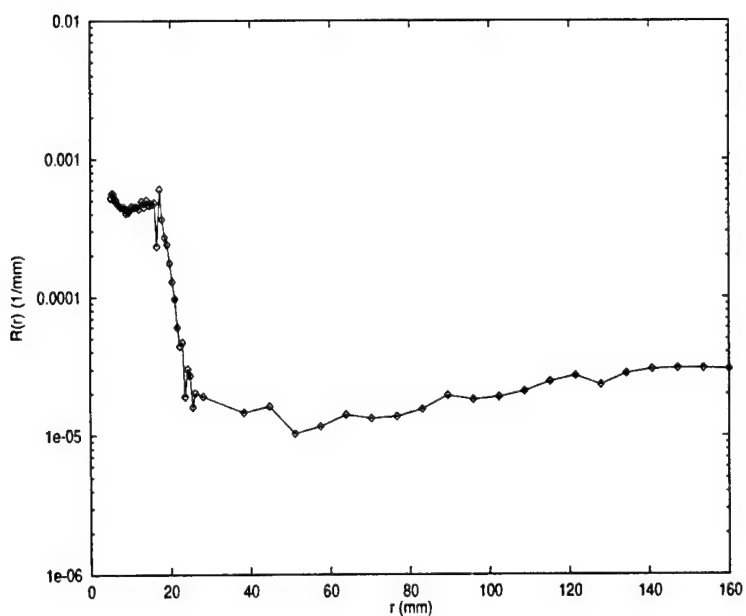


Figure 3.9: Ring response function for the medical imaging CRT. The magnitude of the tails caused by light transport processes that occur in the display emissive structures can be measured using this approach.

3.8 References

1. D. A. Baylor and M. G. F. Fuortes. Electrical responses of single cones in the retina of the turtle. *Journal of Physiology*, 207:77-92, 1970.
2. C. Beckman, O. Nilsson, and L.-E. Paulsson. Intraocular light scattering in vision, artistic painting, and photography. *Applied Optics*, 33(21):4749-4753, July 1994.
3. H. Blume. Very-high-resolution CRT display systems. *Proceedings of the Society for Information Display*, pages 699-702, 1992.
4. P. A. Boynton and E. F. Kelley. Measuring the contrast ratio of displays. *Information Display*, 11:24-27, November 1996.
5. P. A. Boynton and E. F. Kelley. Accurate contrast-ratio measurements using a cone mask. *Proceedings of the Society for Information Display*, pages 823-826, 1997.
6. N. Bromberg and J. Bickford. Veiling glare in the imaging chain. *Proceedings of the SPIE*, 454:387-391, 1984.
7. Ed Caruthers. Monte Carlo studies of image spread by X-ray image intensifiers. *Proceedings of the SPIE*, 535:140-147, 1985.
8. G. C. de Vries. Contrast-enhancement under low ambient illumination. *Proceedings of the Society for Information Display*, pages 32-35, 1995.
9. M. J. Flynn, T. McDonald, E. DiBello, et al. Flat panel display technology for high performance radiographic imaging. *Proceedings of the SPIE*, 2431:360-371, 1995.
10. E. B. Gindele, B. R. Gandhi, and S. L. Shaffer. A non-linear CRT system simulation model. *Proceedings of the Society for Information Display*, pages 785-788, 1990.
11. J. R. Mansell and A. W. Woodhead. Contrast loss in image devices due to electron back-scattered from the fluorescent screen. *Journal of Physics D: Applied Physics*, 16:2269-2278, 1983.
12. S. Matsuda and T. Nitoh. Flare as applied to photographic lenses. *Applied Optics*, 11(8):1850-1856, August 1972.
13. R. A. Norman and I. Perlman. The effects of background illumination on the photore-sponses of red and green cones. *Journal of General Physiology*, 286:491-507, 1979.
14. R. A. Norman and F. S. Werblin. Control of retinal sensitivity: light and dark adaptation of vertebrate rods and cones. *Journal of General Physiology*, 63:37-61, 1974.
15. K. Rossmann. Point-spread function, line-spread function, and modulation transfer function: Tools for the study of imaging systems. *Radiology*, 93:257-272, August 1969.
16. J. A. Seibert, O. Nalcioğlu, and W. Roeck. Characterization of the veiling glare PSF in X-ray image intensified fluoroscopy. *Medical Physics*, 11(2):172-179, March 1984.

17. G. Spencer, P. Shirley, K. Zimmerman, et al. Physically-based glare effects for digital images. *Computer Graphics Proceedings, Annual Conference Series SIGGRAPH 95*, pages 325–334, 1995.
18. W. S. Stiles and B. H. Crawford. The luminous efficiency of rays entering the eye pupil at different points. *Proceedings of the Royal Society of London*, 122:428–450, 1937.
19. J. J. van Oekel. Improving the contrast of CRTs under low ambient illumination with a graphite coating. *Proceedings of the Society for Information Display*, pages 427–430, 1995.
20. J. J. van Oekel, M. J. Severens, G. M. H. Timmermans, et al. Improving contrast and color saturation of CRTs by Al_2O_3 shadow mask coating. *Proceedings of the Society for Information Display*, pages 436–439, 1997.
21. H. D. Zeman, E. B. Hughes, J. N. Otis, et al. Veiling glare of a linear multichannel Si(Li) detector. *Proceedings of the SPIE*, 535:214–221, 1985.

CHAPTER IV

VEILING GLARE IN HIGH PERFORMANCE CRT MONITORS

4.1 Introduction

When radiographic images are displayed using cathode-ray tubes (CRTs), the perception of low-contrast clinically relevant details can be hindered by veiling glare. The multiple light scattering processes that take place in the emissive structures cause low-frequency degradation that can be significant in a low luminance region surrounded by bright areas. The effect of veiling glare is therefore determined by the luminance distribution of each image scene.

In this Chapter, we present results on experimental measurements of veiling glare for a medical imaging monochrome cathode-ray tube (CRT) of recent design. Experimental data were obtained before and after application of an anti-reflective coating (AR) to the surface of the monitor. We report results using both direct and indirect measurements. Direct measurements of the veiling glare point-spread function made with a bright spot are difficult to perform due to the luminance difference between the central spot and the tails. On the other hand, we will show that indirect measurements using dark spot of increasing diameter can be performed if light from the bright regions does not contaminate the low level signals. Computational predictions

of an optical Monte Carlo model are then compared to the experimental results. Finally, a discussion on the effect of the AR coating on the luminance spread functions based on the comparison of the results for the veiling glare with and without the AR plate is presented.

4.2 Components of veiling glare

Veiling glare is commonly associated with the multiple light scattering processes that take place in the emissive structures of CRT that cause low-frequency degradation, most significant in low luminance regions surrounded by bright areas. We have already introduced this optical component of veiling glare in Section 1.3.2 on page 8. However, other sources of veiling glare (light leakage and electron backscattering) are less known, and merit also a detailed description.

4.2.1 Light diffusion

To reduce veiling glare, high performance monochrome and color CRTs typically have an absorptive faceplate that reduces the brightness. Other approaches that have been implemented in color designs include filtered and pigmented phosphor grains [4]. All color tubes presently have a black absorptive matrix between phosphor dots that leads to improved color purity. The absorption of light by this layer greatly contributes to reduce the magnitude of the tails of the luminance spread functions, as we will show later in Section 4.5.

The contribution to veiling glare due to light transport processes within the emissive structure depends proportionally on the relative location of dark and bright regions in an image. Therefore, its effect is determined by the luminance distribution patterns of each image scene. Conversely, the other two components to glare that will be analyzed in this Section, cause a background signal that is approximately

uniform throughout the entire display surface.

4.2.2 Light leakage

The reflectivity of Al backing films is typically in the order of 90% or greater. The transmitted light will scatter off the walls of the bulb, and may eventually come back and exit through the faceplate adding a uniform background to the image signal. This light leakage has been recognized and used as part of an experimental method to determine the Al layer thickness [2], and for adjusting the display curve according to illuminance measurements made inside the CRT bulb (implemented by True Image, LLC, Webster Groves, MO).

When the transmitted light intensity through the Al film amounts to 10%, a uniform bright field will be contaminated by an additional constant luminance of 5×10^{-4} the bright field intensity*. If a small dark spot is placed in the center of an image at a luminance level of 1% of the bright field, its physical contrast will be affected by a background signal, decreasing from 99 to 94.

In addition, the thin aluminum coating that covers the phosphor layer may have small cracks or holes that will allow more light generated in the phosphor to escape towards the vacuum cell, resulting in further decrease in contrast.

4.2.3 Electron backscattering

In addition to an optical component determined primarily by light diffusion and leakage, there is a significant component of glare caused by electron backscattering. The reduction in contrast due to backscattered electrons has been studied for fluorescent screens [5], and for scanning electron microscopes [3].

*This figure assumes an absorption of 90% after all scattering events at the walls of the tube. Typically, coatings for the inside surfaces of CRT bulbs are carbon-based absorptive materials, although metallic coating having Cu and Ag are also used in certain applications.

To obtain good color saturation, a shadow mask[†] is located in front of the screen to allow each electron beam to selectively pass through the mask holes and excite the corresponding color phosphor. Although the beams are focused and aligned with the holes, a fraction of the Gaussian-shaped beam will directly hit the mask. As some energetic electrons impinge into the shadow mask or the screen, a fraction is backscattered and may eventually hit the phosphor layer at a different location. Short-range contrast degradation is originated by electron scattering in the vacuum region between the mask and the phosphor screen, while the long-range effect comes from backscattering at the mask and at the inner magnetic shield and funnel of the glass bulb [1].

The backscattered fraction depends on the effective atomic number of the coating, and therefore can be reduced by using low-Z materials such as graphite [8], or Al_2O_3 [9]. The amount of contrast reduction from backscattering is directly proportional to the primary beam intensity. It has been reported that the fraction of contrast loss due to electronic backscattering in color tubes can be as much as 98% of the total glare degradation [1]. Reduction by a factor of about 10 in the contrast ratio of 10×10 cm black squares was achieved by careful selection of coating material and thickness (G. C. de Vries, Philips Display Components Lab, Eindhoven, oral communication, 1998). The absence of a shadow mask in monochrome tubes results in a lower backscattered fraction since all the electrons hit the Al conductive coating and phosphor layer.

[†]The aperture grille used with in-line electron guns, introduced in 1988, represents another approach employed for color selection. The transmissivity of the beam is 15 to 50% greater compared to shadow mask designs.

4.2.4 Monte Carlo analysis of electron backscattering in monochrome CRTs

To evaluate the magnitude of the backscatter component for monochrome tubes, calculations were performed with a Monte Carlo radiation transport code, SKEPTIC [10], that specifically models each electron interaction rather than using continuous slowing down approximations. The geometry of the monitor was described in three dimensions by a 40 cm cube representing the vacuum tube. The internal walls of the box were coated with a material commonly encountered inside CRT bulbs with an average elemental composition obtained from CRT coating manufacturers. The electrons that are backscattered into the vacuum region are not accelerated because all of the electron energy is gained close to the cathode.

To determine the variability between the different coatings used by CRT manufacturers, we computed the backscattering fraction using SKEPTIC for 7 coatings having different elemental compositions (CI-001, CI-002, CI-004 from Acheson Colloids Company, Port Huron, MI, and g972, g984, g985, g9001 from Thompson Consumer Electronics, Lancaster, PA). All conductive coatings were composed from graphite, metallic oxides, and sodium silicates in different proportions. The results showed that the backscattered fraction was always within 0.15 and 0.18 in the energy range between 5 to 35 keV.

The emissive structure was described as a 5 μm ZnO phosphor layer over-coated with an Al backing. The phosphor layer was partitioned in 11 elements of full length, 10 of which had a constant thickness of 3.999 cm, and a central element having a thickness of 0.005 cm, to accommodate the incoming electron beam. A normally incident electron beam was used entering the box through a small hole in the back face, and impinging into the emissive structure at the center of the front face.

The distribution of deposited energy accumulated in each element of the phosphor layer was then related to the primary incident energy deposited in the central element accumulated from all histories. The results of this energy deposition scheme are directly related to the point-spread function of the input electron beam (equivalent to \mathcal{P}_i , defined in page 52). The energy deposited in the phosphor layer by the back-scattered electrons is related to the energy deposited in the thin central strip by the primary beam. In this case, we assume that the luminance generated is proportional to the deposited energy in the phosphor[†].

Using a 30 keV mono-energetic beam, we found that the response tails is approximately constant upon the entire phosphor layer, with a magnitude of about 4×10^{-2} cd/m²/cd for a 0.5 μ m Al film. Since the energy of a multiply backscattered electron is significantly lower than the primary energy, we confirmed that the glare component is sensitive to the Al thickness. The magnitude of the spread function decreased to 1×10^{-2} cd/m²/cd for a 1 μ m Al thickness, and to 4×10^{-3} cd/m²/cd for a 2 μ m Al thickness. For a 0.1 m² display area at 100 nit having a 0.5 μ m Al film, a small black spot will have a luminance of 0.4 nit, resulting in a glare ratio G of 250.

4.3 Methods

In this work, we experimentally measured the veiling glare for two 1600×1280 resolvable pixels DS2000 monochrome CRT monitors manufactured by Clinton Electronics Corporation, Rockford, IL[§]. All the measurements performed for this CRTs

[†]This assumption is reasonable for cathodoluminescent phosphors under typical electron bombardment regimes, but may not be acceptable for other processes that rely on ionizing radiation to produce luminescence [6, 7].

[§]The monitors were kindly provided by Ken Compton from Clinton Electronics Corporation, Rockford, IL.

were carried out in collaboration with Ed Muka, at the Electronic Radiology Lab, Mallinckrodt Institute of Radiology, St. Louis, MO. Software required for the monitor set up was installed by Tom Monsees, True Image, LLC, Webster Groves, MO. This 20 inches diagonal model has a display area of 362×272 mm and a flat profile with 110° deflection angle. The nominal brightness of 100 ftL is obtained with a P104 phosphor. A drawing showing the key elements of the emissive structure is presented in Figure 4.1. A glass faceplate 13 mm thick with 42% transmission and index of refraction equal to 1.525 constitutes the support for a 10-20 μm thick phosphor layer coated with a thin reflective Al film (90% reflection). After the measurements were carried out without the AR coating, an AR panel consisting of a 3.2 mm thick sheet of glass having 92% transmittance was glued onto the faceplate with a polyester laminating resin. The adhesive layer has a thickness of about 2.0-2.5 mm with no significant light absorption. The index of refraction of the resin and AR glass plate were considered similar to the index for the faceplate. The AR panel is coated with a multi-layer (5 - 7 layers) thin film structure with MgF_2 and ITO as the conductive layer. According to the manufacturer (OCLI, Santa Rosa, CA), the absorption of the coating is less than 1% for 550 nm light, and the reflectivity is below 0.1% in the visible range.

4.3.1 Optical Monte Carlo simulations

Computational predictions of the veiling glare spread functions for the monochrome medical imaging CRT were obtained using DETECT-II, a computational tool for the simulation of light transport processes in emissive structures using Monte Carlo techniques (see Chapter II). This program computes the response function of emissive display devices by modeling light scattering through 3-dimensional objects. Rough

surfaces and anti-reflection (AR) coatings can be described using DETECT-II, for a complete model of the emissive structures considered in this work.

4.3.1.1 Model of the emissive structure

The geometric model employed for the simulation is based on the technical data provided by the manufacturer. A cross-section of the emissive structure is shown in Figure 4.1. The linear absorption coefficients were computed according to the information on light transmission, resulting in 0.536 cm^{-1} for the faceplate, and 0.263 cm^{-1} for the AR glass plate. The thin film is modeled as a single-layer coating with optimized thickness (169 nm for 550 nm photon wavelength), and index of refraction equal to 1.23.

All simulations for the CRT monitors described in this Chapter were performed using a monoenergetic light source with a wavelength of 550 nm. This photon energy located in the center of the visible range corresponds to the maximum photopic response of the human eye. For monochrome display devices, this approximation is considered good. Experimentally, the observation of glare effects in such devices does not demonstrate any color shifts.

4.3.1.2 The discrete ring response function

An important aspect of the simulation is the manner in which the results from the Monte Carlo binning are associated with the experimentally measured values. In this section, we review aspects of the veiling glare model described in Chapter III and to relate the experimental ring response function $R(r)$ to the discrete Monte Carlo estimate \mathcal{R}_i . For a point source of unit strength (1 cd of light), the N_i photon histories that emerge within a given solid angle Ω are binned into radial bins i of constant thickness Δr . We can express the normalized discrete point-spread function

\mathcal{P} as

$$\mathcal{P}_i = \frac{N_i}{N_t 2\pi r_i \Delta r}, \quad (4.1)$$

where N_t is the total number of histories. The units of \mathcal{P}_i are photons/sr/m² per photons, which is interpreted as proportional to cd/m² per cd, or, 1/m².

Similar to Equation 3.2, the point-spread function \mathcal{P}_i is converted to a ring response function by summing over all angles (which is already done because of the radial bins) and accounting for the ring thickness Δr , as follows

$$\mathcal{R}_i = \frac{N_i}{N_t \Delta r} = 2\pi r_i \mathcal{P}_i. \quad (4.2)$$

The units of \mathcal{R}_i are the units of $\frac{1}{\Delta r}$, usually 1/mm. Equation 4.2 represents the Monte Carlo estimate of the ring response function and can be related to the measurements of veiling glare using the test patterns described in Chapter III.

4.3.2 Experimental measurements

Measurements of veiling glare were performed using direct and indirect methods. The measurements were performed in the monitors (two of them) before an AR panel with AR coating was glued to the faceplate. After the first set of measurements (without the AR), the monitors were sent to the manufacturer, and were return to the lab with the AR coatings. This particular model is commercially available with the AR plate.

4.3.2.1 Bright spot measurements with CCD

Direct measurements of a bright spot were performed at the Electronic Radiology Laboratory[¶] using a 1024×1024 CCD. The bright spot was realized by disabling the electron beam sweep and directing the static beam to the center of the display area.

[¶]The bright spot measurements with the CCD were performed by Ed Muka at the Electronic Radiology Lab, Mallinckrodt Institute of Radiology, St. Louis, MO.

In order to reduce the contamination of the low luminance regions by the bright spot, a black patch was placed between the spot and the camera lens. The patch was made with black paper and positioned with a thin black wire at about 10 mm from the display surface.

The images recorded with and without the AR plate were analyzed to extract information on the profile of the point-spread functions. Image values were projected into radial 1-dimensional profiles, by adding the pixel numbers at each radial location, and then dividing by the numbers of pixels that contributed to each radial bin. The data were then corrected for dark current by subtracting 320 counts to each radial bin average.

4.3.2.2 Dark spot measurements

Luminance measurements of dark spots of varying size were carried out using the luminance probe and test patterns described in Chapter III. The data was analyzed to obtain the ring response function $\mathcal{R}(r)$, using the techniques described in Chapter III (see page 66). A summary of the different steps involved in the data analysis is presented next. Data corresponding to each dark spot diameter was recorded and corrected for the instrument dark current. The baseline luminance correction was obtained by measuring the luminance at the center of the display device with a full field dark image. For these measurements, the brightness and contrast settings of the two units were adjusted to generate about the same maximum and minimum brightness. The results were then corrected using the correction factor $\zeta(r_d, d)$ for the appropriate radius of the dark spot (r_d), and the distance d between the probe tip and the display surface^{||}. Finally, the difference between the values for 2 consecutive dark spot radius was divided by the difference in radius to yield the

^{||}see Equation 3.5 on page 71.

ring response function $\mathcal{R}(r)$.

4.4 Results

Figure 4.2 shows the Monte Carlo computed ring response functions for the medical imaging CRT. Without an AR panel, the veiling glare spread function presents a single peak at about 23 mm radius at a magnitude of about 0.001. In the case of the AR coated panel, the prediction indicates the presence of several peaks with decreasing amplitude at larger radii.

The images of the bright spot recorded with the CCD camera are shown in Figure 4.5. In spite of being thin and black, the support wire can be clearly seen in both images. The textured background observed is associated mostly with the roughness of the glass faceplate, and with the nature of the phosphor layer. The attempt to extract the information on the spread function profiles yielded the data plotted in Figure 4.6. Although much noise is present, the peaks at 22 and 33 mm are still noticeable.

The ring response functions from the dark spot measurements performed before and after the addition of the AR panel are presented in Figure 4.7. The profiles for both monitor units without the AR panel show a marked peak at about 20 mm with an amplitude of 3×10^{-3} , while the results for the AR case present a significant peak at 32 mm with a magnitude of about 1×10^{-4} . For each unit and both cases, the magnitude of the tails of the dark spot ring response function slightly increase for larger radii. Without an AR surface, the glare ratio for a 1 cm diameter dark spot was measured to be 138. With an AR surface, the glare ratio for a 1 cm dark spot was 241 due in part to additional glass absorption. While primarily designed to decrease specular reflections, AR coatings also reduce the veiling glare of an emissive

display by reducing the amount of light internally reflected at the faceplate surface.

4.5 Discussion

Both experimental techniques used in this work have confirmed the general profile of the ring response function associated with veiling glare. However, results from the direct measurements do not provide information on the relative magnitude of the response function tails. The position and shape of the functions appear more clearly delineated in the results presented with the indirect measurement method.

The profiles shown in Figure 4.7 from the indirect method agree reasonably well with the predictions of the Monte Carlo model. For the monitor without an AR plate, both the position and magnitude of the peak are consistent. This peak is associated with photons that are reflected once at the front surface with an incident angle close to the total internal reflection angle, and emerge after reflecting at the phosphor or Al layer. The shape of the peak is directly related to the dispersion in angles that occur at the phosphor layer, where photons are reflected with a Lambertian angular distribution and transmitted through a rough surface into the glass. We infer that the more rounded tip of the peak seen in the experimental data is caused by a broader angular distribution function at the phosphor-glass boundary. This can be due either to a rougher surface between the phosphor and the faceplate**, or to a more broad angular output from the phosphor layer than defined by the Lambertian distribution function.

In the case of the monitor with an AR plate, the location of the main peak is displaced to a larger radius due to the increase in faceplate thickness from the glass plate laminated with the AR films. Although the location and magnitude of

**The roughness used for the simulations is defined by the maximum tilting angle in the rough surface description (see page 44). The description does not allow for large tilting angles.

the peak is consistent with the Monte Carlo predictions, the presence of markedly defined multiple peaks in the simulation results does not agree with the measured data. The simplistic description of the AR coating as a single-layer structure could be responsible for the multiple peaks and valleys that would be associated with the periodic response characteristics of a single dielectric thin layer. More accurate description for the AR coating may be needed to provide complete agreement between the predictions of the model and the measurement results. Improvements should reflect the structure of current AR coatings including the multiple thin film stack and protective layers. The pattern observed for the structures with thin film coating could be related to the fact that all Monte Carlo simulations were performed with a monoenergetic source of light. Instead, sampling photons having a distribution in wavelengths representative of the emission spectra of CRT phosphors with corrections for photopic response might lead to better agreement between the Monte Carlo predictions and the experimental results.

Another mismatch between the predictions of the Monte Carlo model and the experimental data observed with and without the AR panel, is the response at large radii. The simulation results show that the magnitude of the tails decrease to small numbers at radius of about 140 mm. However, the experimental data in Figure 4.7 suggest that the magnitude of the veiling glare remains approximately constant at large radii. This observation can be explained if other sources of veiling glare (discussed in Section 4.2 on page 87) are considered. The magnitude of the contributions from light leakage through the Al layer, and from electron backscatter are theoretically proportional to the area of the bright field. At larger radii, the area of a thin ring at high luminance will increase with its radius. Such interpretation might explain why the experimentally determined ring response function has a slightly in-

creasing long tail, even though this is not seen in the optical Monte Carlo results that account for only the light diffusion component.

The Monte Carlo simulation code was used to predict the changes in the veiling glare of modified emissive structures. Figure 4.3 confirms that clear glass faceplate have much worse performance than designs with absorptive glass, with tails that extend at a magnitude of about 0.01 throughout the display area. The addition of a black matrix further reduces the magnitude of the tails.

Figure 4.4 shows the effect of the AR coating. The profile observed for the monitor with AR plate and coating can also be compared with the same model but without the coating. The displacement of the peak to a large radius is seen when the model includes the AR plate without any thin film coating. The results suggest that the AR coating is responsible for a reduction in the amount of light intensity that originates the prominent peak.

4.6 Figures

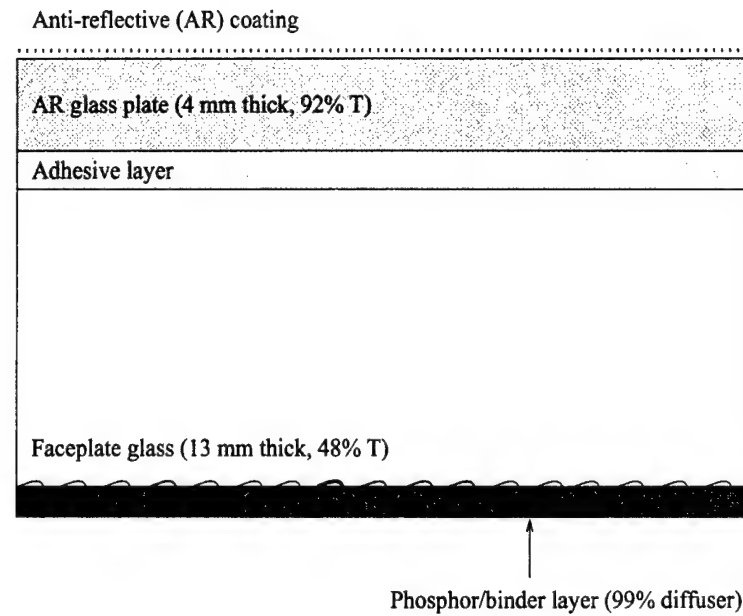


Figure 4.1: Model of the emissive structure for the CRT monitor simulated in this work.

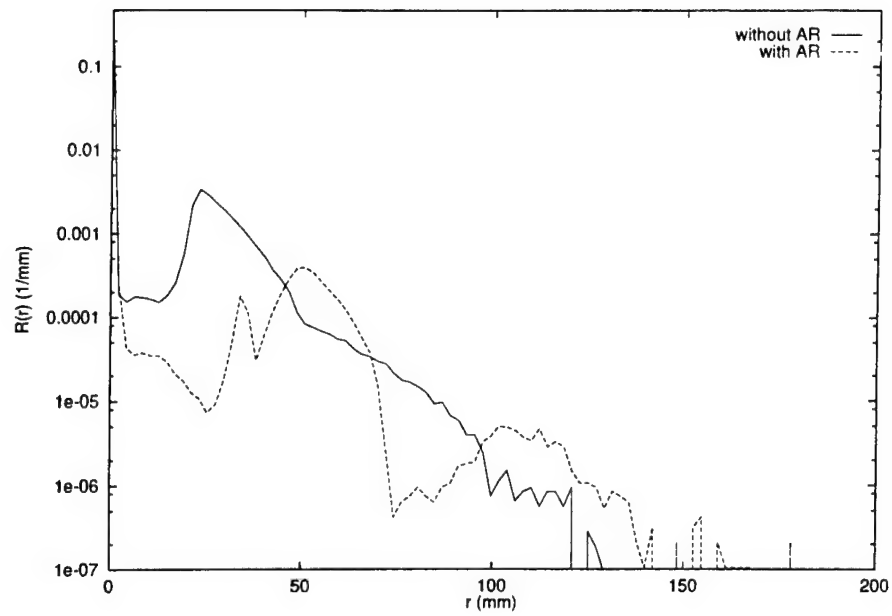


Figure 4.2: Monte Carlo predictions of the ring response functions for the monochrome CRT with and without the AR panel and AR coating.

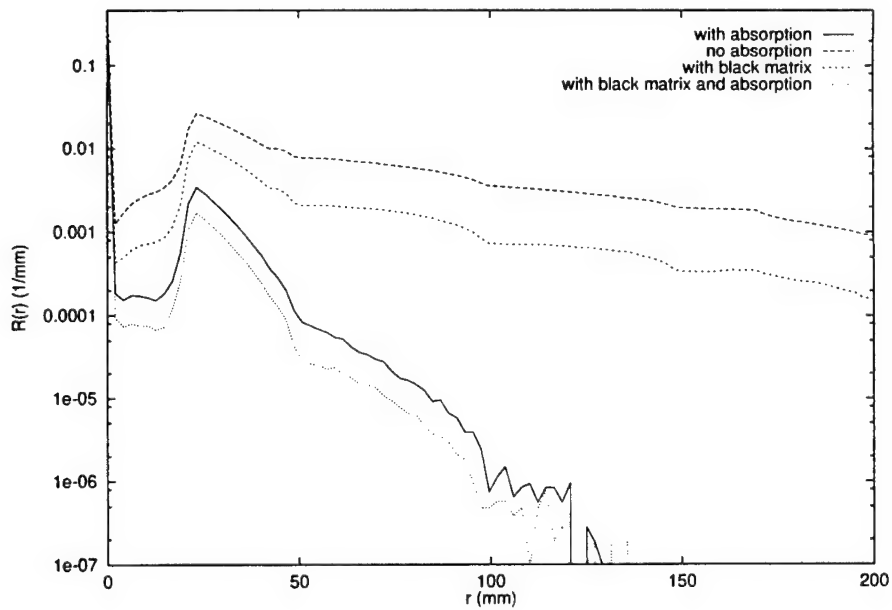


Figure 4.3: Monte Carlo predictions of the ring response functions for the monochrome CRT: effect of light absorption in the faceplate and in the black matrix.

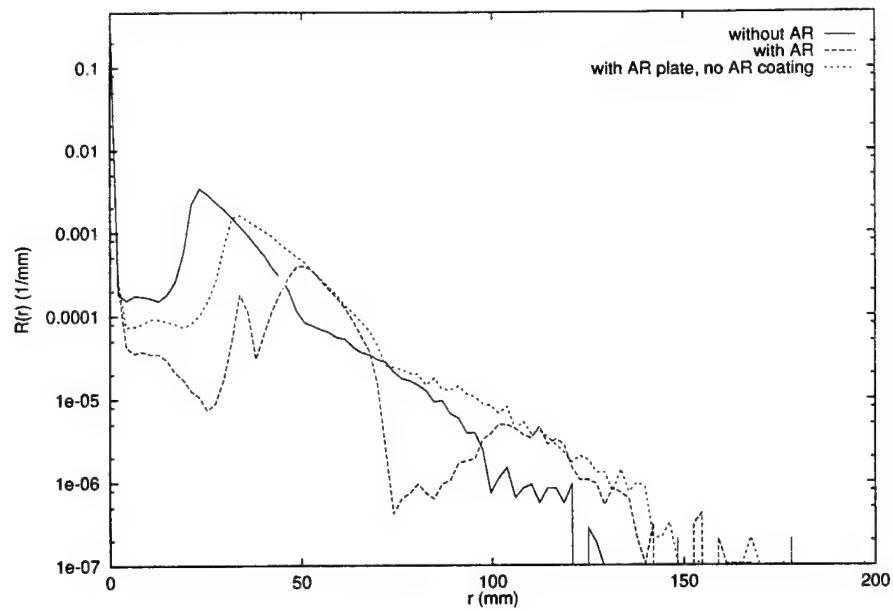
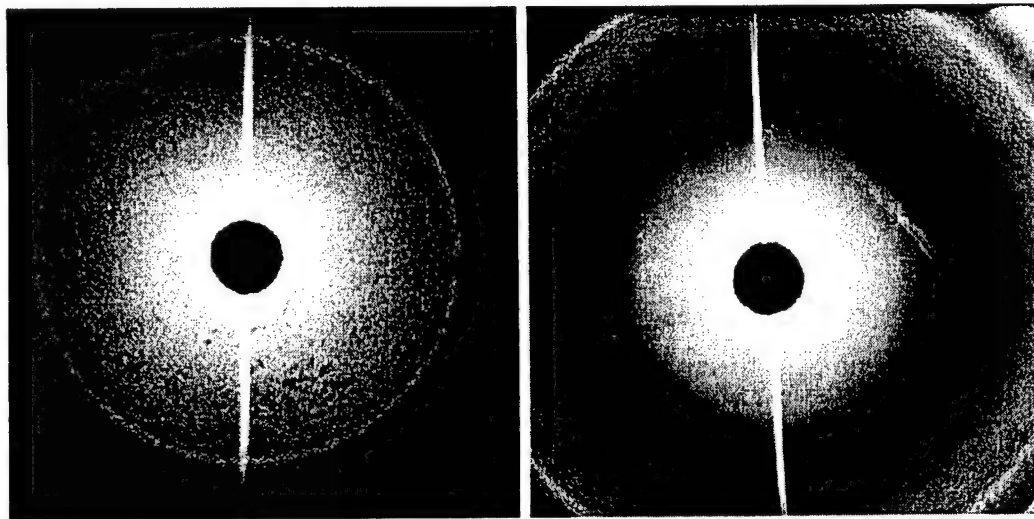


Figure 4.4: Monte Carlo predictions of the ring response functions for the monochrome CRT: effect of AR coating and absorption in the AR plate.



(a) Without the AR plate.

(b) With the AR plate.

Figure 4.5: Bright spot CCD images for the monochrome CRT monitor used in this work. The first peak (seen in both images) is associated with the first total internal reflection scattering events. The increase in the radius of the first peak circle from about 45.6 to 65.4 mm can be related to the increase in the front glass thickness.

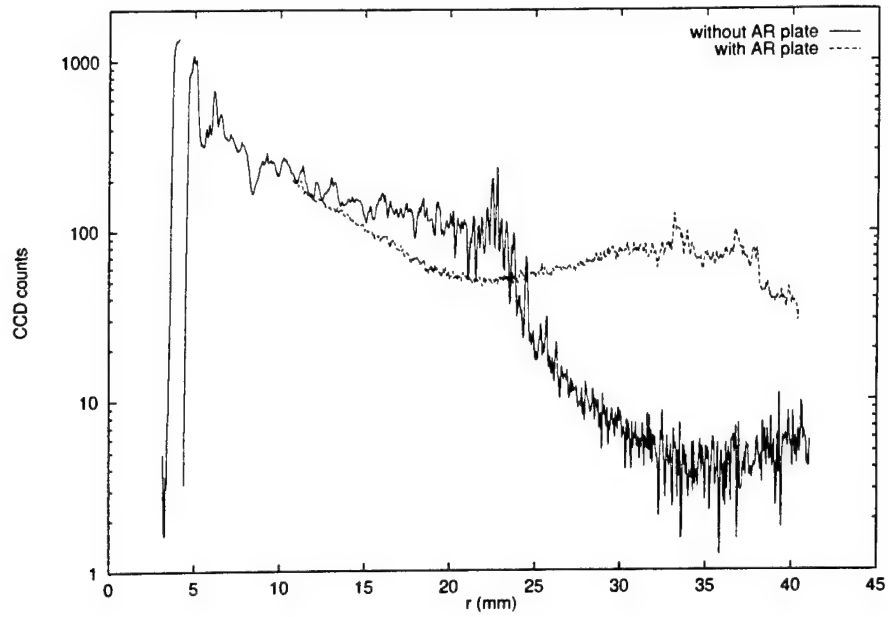


Figure 4.6: Radial profiles for the CCD camera images of the bright spot. In spite of the noise, peaks are noticeable at 46 and 65 mm. The grainy appearance of the surface is related to the glass roughness and to the phosphor layer structure.

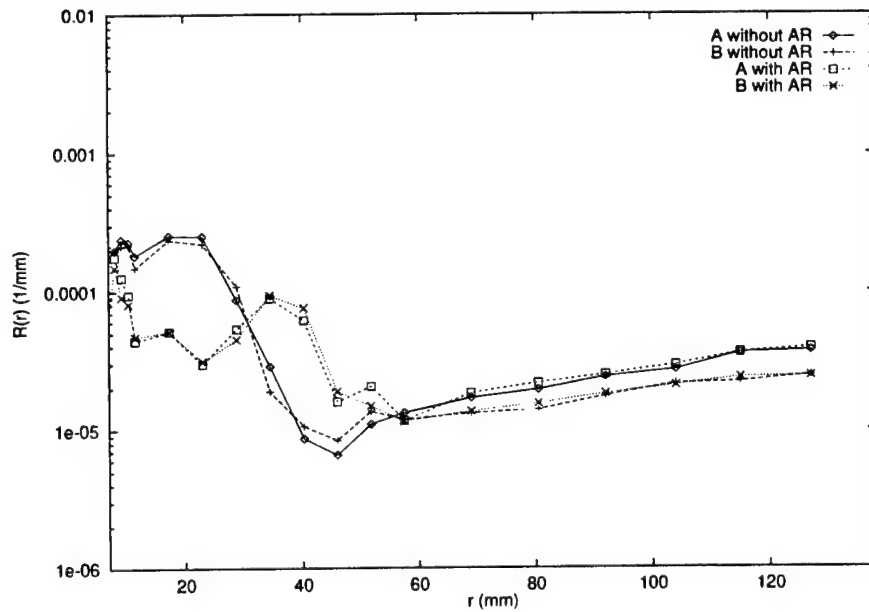


Figure 4.7: Experimental ring response functions measured with the methods described in Chapter III. Two monitors (A and B) were measured with and without the AR panel.

4.7 References

1. G. C. de Vries. Contrast-enhancement under low ambient illumination. *Proceedings of the Society for Information Display*, pages 32–35, 1995.
2. G. M. Ehemann, R. LaPeruta, and E. R. Garrity. US5640019: Method of determining the quality of an aluminized, luminescent screen for a crt, 1997.
3. F. Hasselbach and H.-R. Krauss. Backscattered electrons and their influence on contrast in the scanning electron microscope. *Scanning Microscopy*, 2(2):1947–1956, 1988.
4. M. Kawasaki, N. Tani, and R. Onishi. Improvement of contrast and brightness by using crystal pigment phosphor screens. *Proceedings of the Society for Information Display*, pages 266–269, 1998.
5. J. R. Mansell and A. W. Woodhead. Contrast loss in image devices due to electron back-scattered from the fluorescent screen. *Journal of Physics D: Applied Physics*, 16:2269–2278, 1983.
6. B. D. Rooney and J. D. Valentine. *IEEE Transactions on Nuclear Science*, pages 734–738, 1996.
7. T. D. Taulbee, B. D. Rooney, W. Mengesha, and J. D. Valentine. *IEEE Transactions on Nuclear Science*, pages 326–330, 1996.
8. J. J. van Oekel. Improving the contrast of CRTs under low ambient illumination with a graphite coating. *Proceedings of the Society for Information Display*, pages 427–430, 1995.
9. J. J. van Oekel, M. J. Severens, G. M. H. Timmermans, et al. Improving contrast and color saturation of CRTs by Al_2O_3 shadow mask coating. *Proceedings of the Society for Information Display*, pages 436–439, 1997.
10. S. J. Wilderman. *Vectorized algorithms for Monte Carlo simulation of kilovolt electron and photon transport*. PhD thesis, University of Michigan, 1990.

CHAPTER V

AMBIENT LIGHT REFLECTION IN DISPLAY DEVICES

5.1 Introduction

Due to the nature of CRT emissive structures, a large fraction of the light that illuminates the device is reflected either at the first surface or after multiple internal scattering. A front rough surface cannot be used because it will introduce image blur due to the thick glass faceplate. Light that enters the faceplate and strikes the phosphor layer encounters a structure which by design is highly reflective. The phosphor structure consists of small grains in a binder with a reflective backing. Similar to radiographic screens, this structure is designed for good light emission with little self-absorption. Therefore, monochrome CRT devices used for high resolution radiographic display typically have poor performance with respect to both specular and diffuse reflection of ambient light. This has forced the use of very dark rooms for diagnostic interpretation, and has severely handicapped the deployment of electronic imaging systems in patient care areas.

To dampen specular reflections, anti-reflective (AR) structures are used that consist of several thin film layers designed to reduce the reflectance of the front surface by increasing the light transmission into the faceplate [12]. Normally, AR coatings

will also include a conductive layer that dissipates the static charge generated at the front surface and helps maintain a dust free surface [10]. The reflections from AR coatings can have a color shift when illuminated with a broad spectrum light source because of the wavelength dependency of the thin film response [4]. However, by decreasing the reflection of incident light, AR coatings may increase diffuse reflections since more light enters the faceplate. The effectiveness of AR coatings is then associated with a compromise between the specular and diffuse components of ambient light reflection.

To reduce diffuse reflectance, CRTs may have an absorptive faceplate which attenuates light that scatters several times in the glass. For a faceplate with a transmittance of 50%, the diffuse reflections will be reduced by at least 25%, since the reflected light will travel through the glass twice. More reduction is typically found because of the oblique directions that the reflected light may travel and because of multiple internal scattering. However, this reduction comes at the expense of a decrease in display brightness of 50%. In color monitors, the black matrix material that is between phosphor dots is of considerable benefit in absorbing incident light without reducing brightness. In this sense, the design of color monitors is advantageous from the standpoint of both veiling glare and ambient reflection. However, black matrix phosphor technologies have not been used to date with high brightness monochrome phosphors.

Ideally, a display device will have a design that specifically absorbs ambient light. New flat panel display devices offer opportunities for the absorption of ambient light that are not possible with CRTs. Active-matrix liquid crystal display devices are being built with designs that optimize the absorption of ambient light for use in sunlit environments such as for avionic applications [5]. New devices may be able

to achieve better ambient light reflection performance than now experienced with radiographic films.

In this Chapter, specular and diffuse components of ambient light reflection from display devices are evaluated with respect to their physics and their effect on image quality is examined. Secondly, experimental methods for display reflectance measurements are introduced. Using a light transport simulation code (DETECT-II), computational predictions are then compared with experimental results, and improved design approaches are evaluated for better performance. Finally, the significance and effect of display reflectance on image quality are addressed with emphasis on defining device requirements based on observer performance.

5.2 Characterization of display reflections

The reflectance of display devices can be characterized by separate components involving specular and diffuse light scattering. Both components have markedly distinct effect on image quality, and require different experimental measurement methods.

5.2.1 Specular reflection

Specular reflections produce distinct virtual images at the display surface that mirror luminous objects in the room. The reflected luminance $L_S(\theta)$ can be related to the source luminance $L_s(\theta)$ by

$$R_S(\theta) = L_S(\theta)/L_s(\theta) ,$$

where θ is the incident angle, and R_S is the dimensionless specular reflection coefficient. Specular reflections can severely degrade image quality in specific regions by adding interfering structured signal to the image content and by causing localized

regions of contrast reduction.

5.2.2 Diffuse reflection

Ambient illumination of the display surface will also produce diffuse reflections with no detail and similar intensity over the entire screen. Typically, light photons will strike the display surface and emerge with a broad angular distribution due to surface roughness and multiple scattering processes. Diffuse reflections can be characterized by a coefficient defined as

$$R_D(\theta_i, \phi_i, \theta_o, \phi_o) = L_D(\theta_o, \phi_o) / I(\theta_i, \phi_i) , \quad (5.1)$$

where $L_D(\theta_o, \phi_o)$ is the diffusely reflected luminance measured at an angle (θ_o, ϕ_o) from the surface normal, and $I(\theta_i, \phi_i)$ is the illuminance at the surface from light incident at an angle (θ_i, ϕ_i) . Because of the units associated with measures of luminance (nit) and illuminance (lux), R_D has units of 1/sr. For an ideal Lambertian reflector, L_D is independent of angle and the reflection coefficient is only a function of the illumination angle, $R_D(\theta_i, \phi_i)$. If the illumination of the surface is from many directions, as is the case in a room, the illuminance will have differential contributions from different directions such that

$$I = \int_0^{2\pi} \int_0^{\frac{\pi}{2}} I(\theta_i, \phi_i) d\theta_i d\phi_i , \quad (5.2)$$

where $I(\theta_i, \phi_i) d\theta_i d\phi_i$ is the differential illuminance averaged over all angles. The diffuse reflection coefficient that is specific to a particular lighting condition can be defined as

$$R_D(\theta_o) = L_D(\theta_o) / I ,$$

where $R_D(\theta_o)$ is a weighted average that depends on the angular distribution of illumination.

5.3 Experimental methods

Methods for measuring reflection coefficients have been the focus of recent efforts [2, 6, 8, 9]. While test methods have been proposed as part of an international standard [1], the defined experimental techniques are deficient with respect to repeatability and reliability due to variations in instrumentation response and light source geometry [13]. Moreover, Kelley [7] and Becker [2] have recently suggested that for FPD devices, difficulties can arise when reflections fall in the intermediate regime between specular and diffuse. They propose using the bi-directional reflection distribution function (BRDF) to fully describe the performance in any ambient lighting condition (similar to Equation 5.1). The BRDF is the luminance reflected from a display at all angles for a given illumination condition, and is a function of both source direction and type, and of the observer direction.

We have used an application oriented method to experimentally evaluate diffuse and specular reflection coefficients from devices that are representative of the current state-of-the-art in displays for medical imaging purposes (manufactured by Clinton Electronics Corp., Siemens AG, Image Systems Corp., and Data Ray Corp.), along with a color monitor (manufactured by Hitachi Ltd.). We also included measurements for radiographic film (Eastman Kodak, Ekstascan HNC) and for AMLCDs of current design (manufactured by Hosiden Corp., and Optical Imaging Systems Inc.).

5.3.1 Specular reflection

For measurement of specular reflection, a small uniform source of light can be used to create a specularly reflected image on an otherwise black display surface located in a dark room. To minimize the diffuse component, the area of the light source should be as small as possible. We have used a small spot lamp with a

diffuse white luminous area of about 5.7 cm diameter (see Figure 5.1 on page 119). Using a spot photometer, the luminance of the reflected imaged is then related to the luminance of the light source when directly viewed. We have used a MINOLTA LS110 spot photometer which measures luminance in a $1/3$ degree spot. Typical values for the reflection angles include 15° and 30° , at distances ranging from 50 to 100 cm. Since most displays are viewed from a direction near the surface normal, we have made measurements with the light source and the spot photometer at 75 cm from the center of the display and 15° from the surface normal.

5.3.2 Diffuse reflection

The diffuse reflection from display devices is measured by illuminating the display device in an off condition with a diffuse source*. Others have used various lamps at different positions in a dark room [1,13]. Inconsistent results can be caused in part by variations in illumination that come from the walls, objects, and persons in the room.

To establish consistent illumination conditions, we have used a reproducible, portable device consisting of a 40 x 40 x 40 cm box with white reflective sides and two 9 W fluorescent lamps located at the back corners. Illuminance is measured with a small illuminance probe placed on the surface of the display (International Light, Inc., IL 1400). Luminance in a normal direction with respect to the display surface is then measured through a hole in the back of the box with a spot photometer. The absence of specular reflections is confirmed by the dark circle that appears in the display surface when viewing through the back aperture (see Figure 5.2 on page 119).

The white box, showed in Figure 5.3 on page 120, creates in effect a reproducible

*For devices that rely on changes in transmission to modulate the luminance of the scene (i.e., transilluminated film, liquid crystal displays), measurements of diffuse reflections with fields at different luminance levels are required.

white room that can be taken to different locations for comparison measurements, providing an angular distribution of illumination representative of that found in patient care areas.

The measured luminance per illuminance is then reported as lumens/sr/m² (i.e., cd/m² or nit) per lumens/m² (i.e. lux) which has units of 1/sr. More conveniently, the diffuse reflection coefficient R_D is expressed in units of luminance per illuminance, since these can be directly associated to visual effects.

As discussed previously, the diffuse reflection coefficient is specific to the angular distribution of illumination associated with particular measurement conditions. When using the experimental technique described in this work, the obtained result corresponds to

$$R_D(0) = L_D(0)/I$$

with I being the total illuminance at the display surface. The illuminance probe used records incident light with a broad angular response (International Light Inc., model SCL110).

When measuring reflections from radiographic film, attention must be given to the optical density values in the image since they affect the light diffusion characteristics of the device. For this reason, reflection measurements were taken with 3 films having different optical density values. The difference is associated in part with ambient light which is transmitted to the view box and reflected back. This dependence of the reflection coefficients with the image luminance pattern is not observed in CRTs, where measurements are performed with the display turned off.

5.4 Experimental results

In Section 5.3, practical experimental techniques to measure specular and diffuse reflection coefficients have been delineated. Next, we report experimental results for several high performance display devices including film, monochrome and color CRTs, and AMLCDs. The results are compared with data obtained for transilluminated radiographic film using the same experimental techniques.

Table 5.1 reports the results on diffuse and specular coefficients for all display devices studied in this work. The specular reflection coefficient was measured to vary in a range from 0.0019 to 0.042. The coefficients measured for the monitors without AR coating are consistent with the value computed according to Fresnel equations for a glass-air optical boundary (0.04). Devices with AR coating have a smaller specular reflection coefficient. Among them, the lower R_S was measured for monitors having the most advanced AR coating designs. The specular coefficient for devices with AR coatings are all smaller than for radiographic film.

The measured values for the diffuse reflection coefficients all fall within a smaller range (0.018 - 0.064 nits/lux) with the exception of an AMLCD designed for avionic applications. This measurement proves that low diffuse reflection coefficients can be achieved with advanced optical design. Although the values of R_D for all the other devices (including radiographic film) are comparable, the effects on image quality will be more significant in those devices with low luminance, as we will discuss later in Section 5.6.

5.5 Monte Carlo simulation of ambient reflections in CRTs

Calculation of the specular reflection coefficient can be performed analytically using Fresnel formulations (see Section 2.2.1 on page 38). For a change in index

of refraction change of 1.5 at optical frequencies, the reflection coefficient remains approximately 0.04 for angles of incidence less than 40° [†], and can be very small for a single thin film layer with optimized thickness and index of refraction. In the case of diffuse reflections, the Monte Carlo simulation code DETECT-II can be used to model reflections from devices with different emissive structure designs, as it has been done for predictions of veiling glare calculations in Chapter IV.

For the simulation of diffuse ambient light reflections, we use the same model (DS2000 from Clinton Electronics Corp., Rockford, IL) of CRT emissive structures as described in Chapter IV (see Figure 5.4 on page 121). A planar light source with isotropic emission is located outside the emissive structure. The distributed source causes an illumination into the display surface that has no preferred direction and constant intensity throughout the entire faceplate. Photons that are emitted with normal direction relative to the display surface within a very small solid angle, and from a small region in the center of the display are counted. The ratio between the counted and incident photons divided by the solid angle of acceptance can be associated with the diffuse reflection coefficient expressed as 1/sr.

Table 5.2 shows the computed diffuse reflection coefficients for CRTs having different emissive structure designs using DETECT-II. Results are presented for 6 designs that include a model of an actual display device for which experimental measurements are reported later. The results show that devices with clear faceplates have very high diffuse reflection coefficients (case A against B in Table 5.2). It can be seen that the presence of an AR coating slightly increases R_D by about 10% (case C against B). However, when the coating is applied with a glass plate having 92% transmission, the diffuse reflection coefficient decreases about 38% (case D against

[†]This value for the specular reflection coefficient is typical of display devices with a glass faceplate.

B). The use of a black matrix design with the configuration of case D causes a reduction in R_D of 55% (case F against D).

A notable aspect of the Monte Carlo results is the agreement between the predictions of the model and the experimentally measured diffuse reflection coefficient for the CRT monitor studied as part of Chapter IV. For both cases, R_D was found to be 0.018 nits/lux.

5.6 Requirements for ambient light reflections

At high luminance, a function that maps an image value to brightness such that the logarithm of the luminance is linearly proportional to the image value will produce a uniform perception of contrast at all brightness levels. This occurs because the human vision system perceives contrast as a relative change in luminance ($\Delta L/L$) for sufficiently bright scenes. However, for many display systems, the dark regions of the scene occur at such a low luminance level that the contrast response of the human observer is poor [11]. To compensate for this, the relative contrast ($\Delta L/L$) at low luminance can be increased relative to that at high luminance. An industry standard display curve that maps image values to luminance can be used to obtain a uniform perception of brightness in both dark and bright regions of an image [3, 14]. This relationship is shown in Figure 5.6 where it can be seen that the slope of the curve relating log-luminance to image value is greater at low luminance. This standard display curve is based on psycho-visual models of experiments that measure the threshold contrast of a small test pattern on a uniform background to establish the contrast for which the test pattern can just be detected. The luminance difference associated with this contrast threshold is often referred to as the just noticeable difference (JND) in luminance and the standard display curve is often plotted in

units of JNDs which are taken to be proportional to display values.

Many systems will calibrate the display device luminance response curve such that it follows the display standard curve based on measurements made with or without no ambient illumination. In general, the diffuse reflectance should not significantly change this display curve, and specular reflections of illuminated objects should have contrast below the visual threshold.

5.6.1 Specular reflection requirements for high fidelity

The image quality degradation associated with specular reflections are notably different than those associated with diffuse reflection or veiling glare. While similar contrast reduction occurs where specular reflections contribute to display luminance, the detailed patterns of the specular reflection are more problematic. The specific pattern of a reflection may overlay complex structures in the image scene and reduce the conspicuity of diagnostic features. Additionally, there is a belief that the presence of these added features in the image, and the human observers need to separate reflection artifacts from image information, contributes to visual fatigue.

Assuming that it is possible to eliminate specular reflections from light directly coming from lighting fixtures in the room by correct placement of the monitors, we can define a criteria for determining the maximum permissible specular reflection coefficient for high fidelity displays. By maintaining the specular reflections in a dark region having a luminance L_{min} of the scene below the visual contrast threshold $C_t(L_{min})$, we can compute the required R_S for a given illuminance I , using the following expression:

$$R_S = \frac{\pi L_{min} C_t}{0.9I} . \quad (5.3)$$

Table 5.3 shows the maximum R_S required for specular reflections from white

objects not to be detected, at different illuminations. The results suggest that for a typical illumination of 100 lux, display devices having 400 nit maximum luminance will require a specular reflection coefficient R_S less than 0.002. The data in Table 5.3 also demonstrate that higher R_S can be tolerated in high brightness display devices.

5.6.2 Diffuse reflection requirements for high fidelity

To illustrate the effect of diffuse reflections on image quality, we have plotted the expected curve when a background luminance of 1, 4, or 10 cd/m^2 is added to the normal display luminance (see Figure 5.6 on page 122). For the monochrome monitor tested for this work with a diffuse reflection coefficient of about 0.06, an added luminance of 6 cd/m^2 results from an illuminance of 100 lux which is typical of common office lighting. The significant reduction in the slope of the curves for low image values, which are at a luminance of 1 cd/m^2 for the monochrome monitor, is associated with a significant reduction in the perceived contrast.

Ideally, the added luminance should not be greater than 25% of the minimum luminance of the display device. For example, a display with a luminance range from 3 to 300 cd/m^2 could be used in a room with 100 lux ambient illumination if $R_D \leq 0.006$ nit/lux. For film viewed in a luminance range from 20 to 2,000 cd/m^2 , no significant degradation occurs if $R_D \leq 0.04$ nit/lux. In the case of diffuse reflections, the effect on image quality can be compensated by correcting the display calibration curve with measurements of the ambient illuminance in the faceplate of the device.

For establishing a requirement for diffuse reflectance, it is useful to relate the unstructured background luminance and the reduction in contrast at low luminance with the relative change in contrast resulting from ambient illumination. Setting the maximum allowed relative change to 25%, we can construct a similar table to express

the required R_D for a given room illuminance I , that ensures this condition.

Table 5.4 presents the required R_D for display devices used in ambient illuminations I , computed with the following expression:

$$R_D = \frac{L_{min}}{4I} . \quad (5.4)$$

For a room with a typical office lighting illumination of 100 lux, high performance displays having a luminance range of 4-400 nit will require a diffuse reflection coefficient smaller than 0.01 nit/lux. For very bright devices having this value for the reflection coefficient, an illuminance of 500 lux will not significantly degrade image quality.

5.7 Conclusions

In the previous Section, we have defined the display requirements with respect to specular and diffuse reflectance for high fidelity applications. Before that, we reported in Section 5.4, measured values for the specular and diffuse reflection coefficients of display devices used in diagnostic imaging applications.

As can be seen from the data presented in this work, none of the devices included in this study meet the requirements for high fidelity (see also Table 1.2) due to the low minimum luminance. However, a device with advanced AR coating can achieve good performance with respect to specular reflections of ambient light ($R_S = 0.004$) if its maximum brightness is about 300 cd/m². If the same maximum luminance is obtained for CRT designs with absorptive faceplate and AR coating, acceptable diffuse reflectance ($R_D = 0.02$ nit/lux) can still be achieved.

The reflectance of radiographic films is commonly believed to be modest due to absorption by the blackened grains in the emulsion layer. While diagnostic interpretations are performed in rooms with specially arranged dim lighting, radiographic

film can still be viewed relatively well in bright rooms as is often required in areas of patient care such as the emergency room. However, we have showed that the reflection coefficients R_S and R_D for current electronic display devices can be measured to be lower than the values for radiographic film. As we discussed in this Chapter, the requirements on display reflectance are intimately associated with the maximum and minimum luminance of the device. Therefore, specifications on requirements for display reflectance need to be always related to the brightness of the device. This interplay, present between other display specifications as well, is crucial when defining overall display quality.

5.8 Figures

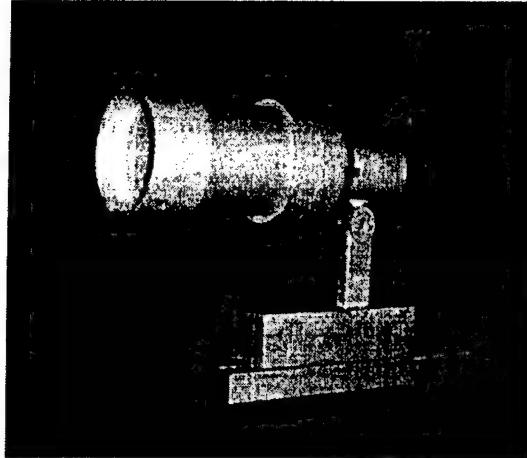


Figure 5.1: Small spot light source for specular reflections. The diameter of the light fixture is about 5 cm.

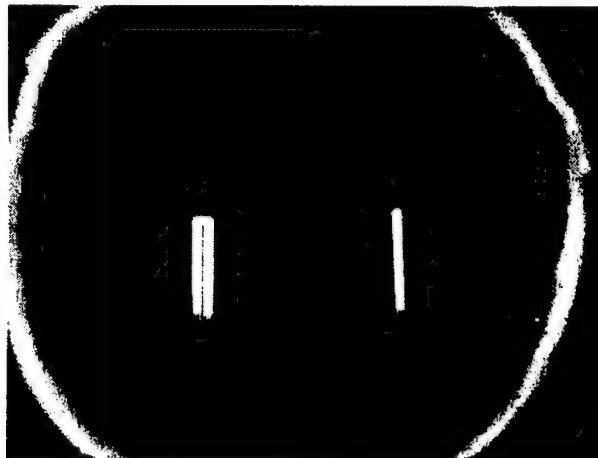


Figure 5.2: Portable white room viewed in a normal direction through a hole in the back of the box.

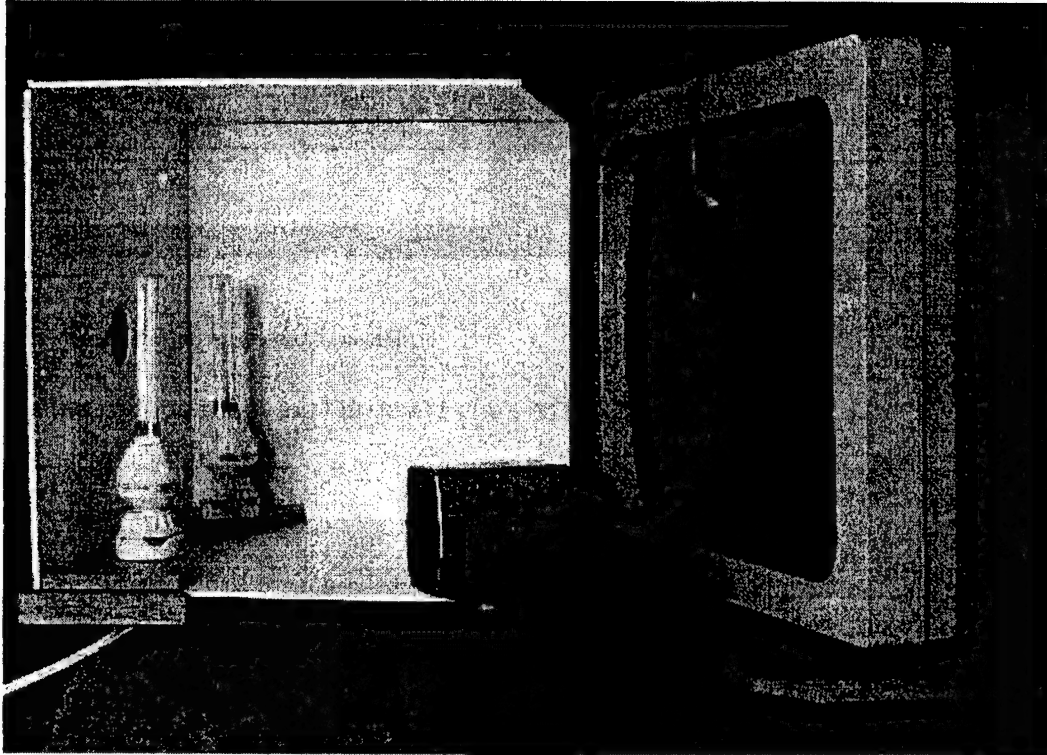


Figure 5.3: White reflective box measuring for diffuse reflection coefficients consisting of a 40x40x40 cm box with white reflective sides and two compact fluorescent lamps located at the back corners. The front side of the box has been removed for illustration purposes. Luminance is measured in a normal direction through a hole in the back of the box with a spot photometer. Illuminance is measured with a small illuminance probe placed on the surface of the display.

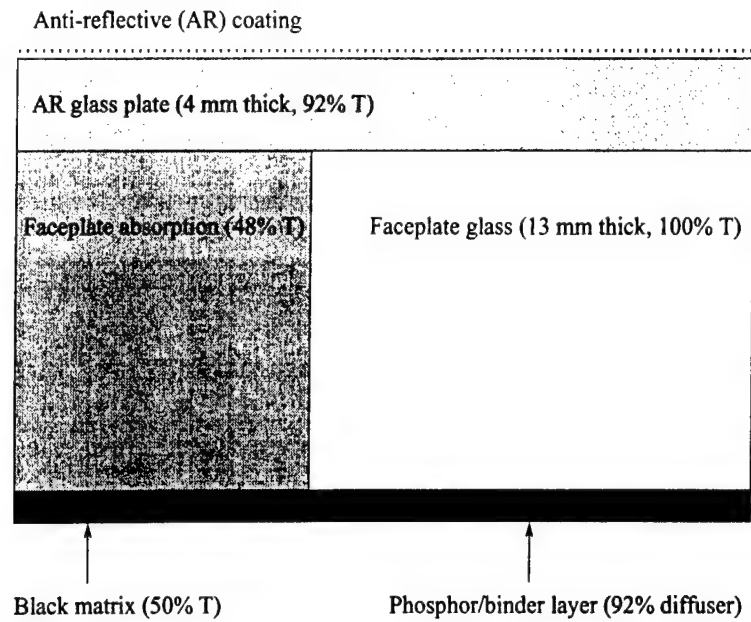


Figure 5.4: Model of the emissive structure for the CRT monitor.

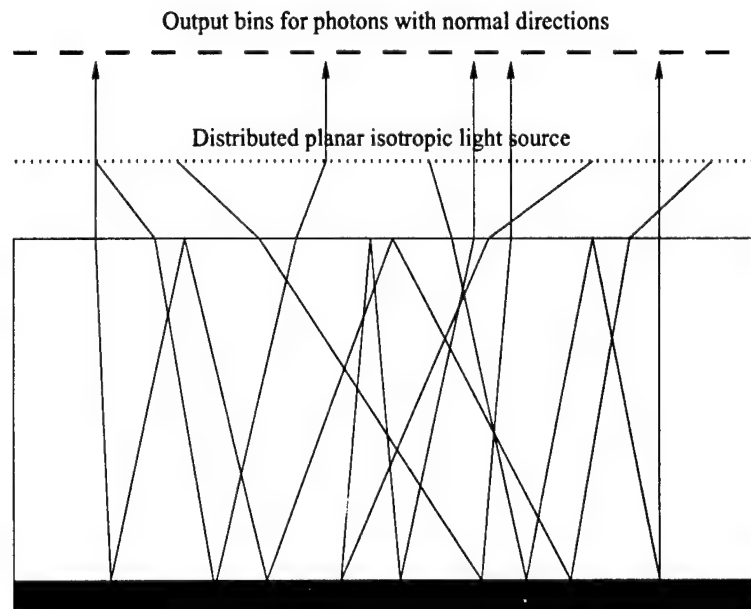


Figure 5.5: Binning of photon histories for simulations of diffuse reflections.

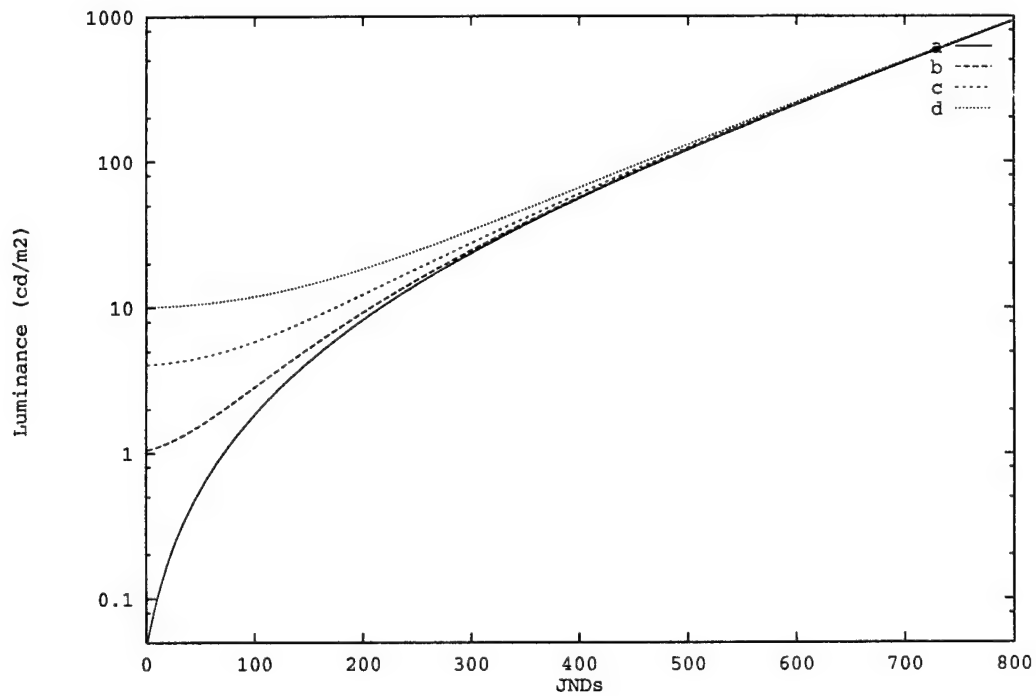


Figure 5.6: Standard display function curve (a) shown as log-luminance versus image value in units of just noticeable visual differences (JNDs) [3, 14]. A unit change in the JND variable causes a luminance change equal to the contrast threshold at the indicated luminance level. Curves (b), (c), and (d) depict the effect of adding a background luminance level of 1, 4, and 10 cd/m^2 . A significant reduction of contrast for small image values is indicated by the small slope of this curve for high background levels.

5.9 Tables

Table 5.1: Reflection coefficients for high performance display devices. The color CRT performs better due to an AR coating and to the black matrix in the phosphor layer. Low diffuse reflection coefficients for AMLCDs demonstrate that careful optical design of flat panels can achieve good performance. Random errors are estimated from the standard deviation of 10 consecutive measurements.

Display	R_S	R_D (1/sr)
<i>Film</i>		
Radiographic film (at OD = 2.8)	0.013 ± 0.001	0.020 ± 0.001
Radiographic film (at OD = 1.0)	0.024 ± 0.001	–
Radiographic film (at OD = 0.1) ^a	0.039 ± 0.001	–
Radiographic film (with chest image)	–	0.026 ± 0.001
<i>CRT</i>		
Monochrome CRT DS2000 HB ^b	0.0034 ± 0.0001^i	0.018 ± 0.001
Monochrome CRT Simomed HM54 ^c	0.0055 ± 0.0001^i	0.031 ± 0.001
Monochrome CRT DR80(25) ^d	0.010 ± 0.001^i	0.064 ± 0.001
Color CRT Superscan Elite 751 ^e	0.017 ± 0.001^i	0.025 ± 0.001
Monochrome CRT ML24 ^f	0.037 ± 0.001	0.058 ± 0.001
Monochrome CRT DR90(21) ^d	0.042 ± 0.001	0.032 ± 0.001
<i>AMLCD</i>		
Color AMLCD Akia 145 (black state) ^g	0.0019 ± 0.0001^i	0.024 ± 0.001
Color AMLCD Akia 145 (gray state)	0.0021 ± 0.0001^i	0.023 ± 0.001
Color AMLCD avionics (off state) ^h	–	0.005 ± 0.001^i

(a) From Eastman Kodak (Ekstascan HNC). (b) From Clinton Electronics Corp. (c) From Siemens AG. (d) From Data Ray Corp. (e) From Hitachi Ltd. (f) From Image Systems Corp. (g) AMLCD panel from Hosiden Corp. (h) From Optical Imaging Systems Inc. (i) Display devices with AR coating.

Table 5.2: Monte Carlo estimates of diffuse reflectance.

Display design	A	B	C	D ^a	E	F
Faceplate glass (13 mm, 100% T)	✓	✓	✓	✓	✓	✓
Faceplate absorption (48% T)		✓	✓	✓	✓	✓
AR plate glass (4 mm, 92% T)				✓		✓
AR coating			✓	✓		✓
Black matrix (50% absorption)					✓	✓
R_D (nit/lux)	0.109	0.029	0.032	0.018	0.016	0.008

^aCase D corresponds to the current model for monitor DS2000 from Clinton Electronics Corp. for which the experimentally measured R_D is 0.018 nit/lux.

Table 5.3: High fidelity specular reflection coefficient R_S for display devices having different minimum luminance L_{min} viewed under different illumination I .

L_{min} (cd/m ²)	C_t^a	I (lux)				
		1000	500	100	50	10
20	0.007	0.0005	0.001	0.005	0.01	0.05
10	0.008	0.00028	0.00056	0.0028	0.0056	0.028
4	0.012	0.00017	0.00033	0.0017	0.0033	0.017
2	0.017	0.00012	0.00024	0.0012	0.0024	0.012

^aContrast threshold is defined as $C_t = \Delta L / L_{min}$.

Table 5.4: High fidelity diffuse reflection coefficient R_D (in nit/lux) for display devices having different minimum luminance L_{min} viewed under different illumination I .

L_{min} (cd/m ²)	I (lux)				
	1000	500	100	50	10
20	0.005	0.01	0.05	0.1	0.5
10	0.0025	0.005	0.025	0.05	0.25
4	0.001	0.002	0.01	0.02	0.1
2	0.0005	0.001	0.005	0.01	0.05

5.10 References

1. 9241-7, Ergonomic requirements for office work with visual display terminals. Technical report, ISO, 1997.
2. M. E. Becker. Evaluation and characterization of display reflectance. *Displays*, 19:35–54, 1998.
3. H. Blume and B. M. Hemminger. Image presentation in digital radiology: perspectives on the emerging DICOM display function standard and its application. *Radiographics*, 17:769–777, 1997.
4. M. Born and E. Wolf. *Principles of optics*. Pergamon Press, 3rd. revised edition, 1965.
5. R. Brinkley, G. Xu, A. Abileah, et al. Wide-viewing-angle AMLCD optimized for gray-scale operation. *Proceedings of the Society for Information Display*, pages 471–474, 1998.
6. G. R. Jones, E. F. Kelley, and T. A. Germer. Specular and diffuse reflection measurements of electronic displays. *Proceedings of the Society for Information Display*, pages 203–206, 1996.
7. E. F. Kelley, G. R. Jones, and T. A. Germer. Display reflectance model based on the BRDF. *Displays*, 19:27–34, 1998.
8. M. Lindfors. Accuracy and repeatability of the ISO 9241-7 test method. *Displays*, 19:3–16, 1998.
9. C. J. Lloyd, M. Mizukami, and P. R. Boyce. A preliminary model of lightning-display interaction. *Journal of the Illuminating Engineering Society*, pages 59–69, 1996.
10. Y. Ono, Y. Ohtani, K. Hiratsuka, et al. A new antireflective and antistatic double-layered coating for CRTs. *Proceedings of the Society for Information Display*, 1992.
11. E. Peli, J. Yang, R. Goldstein, et al. Effect of luminance on suprathreshold contrast perception. *Journal of the Optical Society of America A*, 8:1352–1359, August 1991.
12. H. S. Tong and G. Prando. Hygroscopic ion-induced antiglare/antistatic coating for CRT applications. *Proceedings of the Society for Information Display*, 1992.
13. N. Umezu, Y. Nakano, T. Sakai, et al. Specular and diffuse reflection measurement feasibility study of ISO 9241 Part 7 method. *Displays*, 19:17–25, 1998.
14. ACR/NEMA Working Group XI. Greyscale display function standard, draft version 1.2. Technical report, ACR/NEMA, March 1997.

CHAPTER VI

CONCLUSIONS

This thesis focused on the image quality degradation by optical processes in electronic display devices. We showed that, although often overlooked, veiling glare and ambient light reflections can severely handicap the optical performance of devices. Moreover, we concluded that improvements are needed in the design of devices to achieve high fidelity. In medical diagnostic applications that use radiographic film for viewing images, such devices are needed to maintain diagnostic performance.

Improvements in CRT monochrome monitor design were shown using simulations, particularly with respect to the use of an absorptive black matrix that reduces veiling glare without sacrificing brightness. The computational predictions of structures with thin faceplates suggest that when compared to thick structures typical of cathode-ray tubes, flat panel devices are found to be capable of high quality due in part to more frequent absorption by the phosphor layer.

We also demonstrate in this work, that although having similar ambient light reflection coefficients to film, the performance is much worse due to the low luminance of current devices. In this respect, improvements in performance can be realized if the brightness of current designs was increased.

These conclusions point to 4 main future research directions that are most at-

tractive, and can have direct impact on the performance of electronic display devices in medical imaging and other high fidelity applications.

The first direction would address the implications on diagnostic performance of improved display quality. To substantiate further research in this area, solid results will have to show that the improved display designs can improve diagnostic efficacy in specific areas such as chest and skeletal radiology. Knowledge about the differential increase in observer performance for a given improvement in display optical quality will help the understanding of the relative importance of optical scattering degradation against all other parameters.

With the surge in improved AMLCD designs that is taking place, careful attention needs to be directed at understanding the peculiarities of these devices, and their impact on diagnostic performance. Issues that have not been addressed include the angular dependency of the grey-scale levels, and the measurement methods and figures of merit that are associated with such phenomenon. Another issue that needs to be examined is the degradation of contrast caused by electronic cross-talk in AMLCDs. Large size panels, higher resolution and gray-scale, and increased aperture ratio have been shown to worsen vertical and horizontal cross-talk artifacts in AMLCDs. Novel experimental methods to measure the small spot contrast ratio of the type described in this thesis might be needed to appropriately characterize the cross-talk effect.

Finally, the high efficiency reported for organic light-emitting devices merits the exploration of advanced designs that make use of the structure transparency to improve contrast through absorbing backing layers. From our discussion in Chapter IV and V, we can conclude that ideally, a device that controls the lateral diffusion of light within the emissive structures and absorbs all of the incident ambient light will

have high fidelity even when viewed in rooms with high illumination. Organic light-emitting display devices have demonstrate that highly transparent thin structures can be used to generate high brightness. The development of devices with very high luminance and black absorber in the back of the stack represent a logical direction of future research. Issues related to organic material such as stability and interface electronic properties, along with further knowledge on the processes of light generation and diffusion in stacks of organic and inorganic layers need to be addressed. A high fidelity display device for medical diagnostic applications with excellent performance even when used in bright areas, will definitely impact the practice of radiology. In addition, flat panel devices will save space in the clinics, and can have the added benefit of being portable monitor units.